

**STAR FORMATION IN SMALL CLUSTERS
ASSOCIATED WITH BRIGHT-RIMMED
CLOUDS AND H_{II} REGIONS**

THESIS

**Submitted for the degree of
DOCTOR OF PHILOSOPHY
(PHYSICS)**

to

Kumaun University, Nainital

By

NEELAM

**Aryabhata Research Institute of observational sciencES
(ARIES)**

Manora Peak, Nainital 263 129, India

March 2011

DECLARATION

I hereby declare that the work presented in this thesis is a result of the investigation carried out by me at the Aryabhata Research Institute of observational sciences (ARIES), Nainital, under the joint supervision of Dr. A. K. Pandey (Aryabhata Research Institute of observational sciences, Nainital) and Prof. P. S. Rawat (Department of Physics, Kumaun University, Nainital). This thesis has not been submitted for the award of any degree, diploma, associateship or fellowship of any University or Institute.

Place : Nainital

Date :

(Neelam)

CERTIFICATE FROM THE SUPERVISOR

This is to certify that

1. The synopsis of the thesis entitled “ **STAR FORMATION IN SMALL CLUSTERS ASSOCIATED WITH BRIGHT-RIMMED CLOUDS AND HII REGIONS**” for the award of the degree of Doctor of Philosophy in Physics was approved by the Kumaun University, Nainital.
2. This thesis embodies the work of Ms. Neelam herself.
3. Ms. Neelam worked under my supervision as a Research Fellow at the Aryabhata Research Institute of observational sciencES (ARIES), Nainital. She has put in more than 200 days of attendance at ARIES, Nainital during this period.
4. This thesis has not been submitted before for the award of any degree, diploma, associateship or fellowship of any University or Institute.

(Dr. A. K. Pandey)

ARIES

Nainital 263 129

Place: Nainital

Date:

CERTIFICATE FROM THE CO-SUPERVISOR

This is to certify that

1. The synopsis of the thesis entitled “**STAR FORMATION IN SMALL CLUSTERS ASSOCIATED WITH BRIGHT-RIMMED CLOUDS AND HII REGIONS**” for the award of the degree of Doctor of Philosophy in Physics was approved by the Kumaun University, Nainital.
2. This thesis embodies the work of Ms. Neelam herself.
3. Ms. Neelam worked under my supervision as a Research Fellow at the Aryabhata Research Institute of observational sciencES (ARIES), Nainital. She has put in more than 200 days of attendance at ARIES, Nainital during this period.
4. This thesis has not been submitted before for the award of any degree, diploma, associateship or fellowship of any University or Institute.

(Prof. P. S. Rawat)
Department of Physics,
Kumaun University,
Nainital 263 002
Place: Nainital
Date:

To,

My family

List of Publications

Publications in refereed journal

1. Age sequence in small clusters associated with bright-rimmed clouds
K. Ogura, Neelam Chauhan, A. K. Pandey, B. C. Bhatt, D. K. Ojha, Y. Itoh 2007, Publications of the Astronomical Society of Japan (PASJ), 59, 199
2. Triggered star formation and evolution of T-Tauri stars in and around bright-rimmed clouds
Neelam Chauhan, A. K. Pandey, K. Ogura, D. K. Ojha, B. C. Bhatt, S. K. Ghosh, P. S. Rawat, 2009, Monthly Notices of the Royal Astronomical Society (MNRAS), 396, 694
3. Star formation in bright-rimmed clouds and cluster associated with W5 E HII region
Neelam Chauhan, A. K. Pandey, K. Ogura, J. Jose, D. K. Ojha, M. R. samal, H. Mito 2011, Monthly Notices of the Royal Astronomical Society, accepted for publication
4. A multi-wavelength census of stellar contents in the young cluster NGC 1624
Jessy Jose et al. including Neelam Chauhan 2011, Monthly Notices of the Royal Astronomical Society, in press.
5. Stars at the tip of peculiar elephant trunk-like clouds in IC 1848E: A possible third mechanism of triggered star formation
Neelam Chauhan, K. Ogura, A. K. Pandey et al. 2011, Publications of the Astronomical Society of Japan, under review

-
6. Stellar content and star formation in NGC 281
Saurabh Sharma et al. including Neelam Chauhan 2011, Monthly Notices of the Royal Astronomical Society, under review

 7. Young population of the HII complex Sh2-294
M. R. Samal, A. K. Pandey, D. K. Ojha, Neelam Chauhan et al. 2011, Monthly Notices of the Royal Astronomical Society, under review

 8. Pre-main sequence population in NGC 1893 region
A. K. Pandey, M. R. Samal, Neelam Chauhan et al. 2011, to be submitted

Others

1. Star formation in bright-rimmed clouds and associated clusters
Neelam Chauhan, A. K. Pandey, K. Ogura, J. Jose 2010, in *ASI Conference Series, Vol. 1, Interstellar Matter and Star Formation : A Multi-wavelength Perspective*, ed. D. K. Ojha, 221

2. Multi-wavelength study of the young cluster NGC 1624
J. Jose et al. including Neelam Chauhan 2010, in ASI Conference Series, Vol. 1, Interstellar Matter and Star Formation : A Multi-wavelength Perspective, ed. D. K. Ojha, 233

Acknowledgments

Thanks are due to a number of people who have inspired me and offered their support in varying doses over the years. First and foremost I would like to thank my supervisor Dr. A. K. Pandey for offering me such an interesting and stimulating project. For providing me the right combination of support, guidance, encouragement, his valuable time and allowing me the opportunity to take such a project and run with it, to see where it would take me. I am indebted to my co-supervisor Prof. P. S. Rawat for his unwavering support and guidance.

I am also eternally thankful to Prof. Ram Sagar for his encouragement and support. I express my deepest gratitude to Prof. K. Ogura, whose contributions over the years do not go unappreciated. His support and stimulating discussions have greatly improved my understanding about the subject. My deep sense of gratitude to Dr. D. K. Ojha for helping me to explore the new techniques in research and his ever timely helps and fruitful discussions. I express my thanks to Prof. S. K. Ghosh for his guidance and discussions. I greatly benefited from their advises. I wish to express my appreciation to Dr. B. C. Bhatt for his support during the observations from the 2-m Himalayan Chandra telescope.

I thank Dr. Brijesh kumar for his informative discussions on various aspects of CCD photometric observations and data reductions. I also thank Dr. Biman J. Medhi and Dr. J. C. Pandey for their encouragement and timely helps. I would also like to thank Mrs. Medhi, and Sanskriti for all their love and care. Throughout my stay here at ARIES they made me feel at home. I also wish to extend a heartfelt thanks to Dr. Santosh Joshi, Dr. A. C. Gupta, Dr. Snehlata, Dr. Maheswar, Dr. Soumen Mondal, Dr. S. B. Pandey, Dr. Narendra Singh and members of academic committee at ARIES, for their helps and positive attitudes. I specially thanks to Dr. Humchand, Kavita and Dr. Atul Srivastava and Kamini for their affection and support.

It is a pleasure to acknowledge the invaluable supports and timely co-operation of the whole ARIES staff especially the library, the telescope and the computer section. I am thankful to Mr. Navin Kishor, Mr. Sanjit Sahu and Mr. Deep Pant for their helps in computer related problems. I express my gratitude to Abhishek Sharma for dealing with all the financial accounts of DST and CSIR.

I found an abundance of colleagues who encouraged throughout the past five years. I thank Raman and Arti for their everlasting friendship and lively company. I thank to Himali, Sanjeev, Madhu, Chhavi, Prashant, Amitava, Chrisphin for their friendship. I specially thanks to Saurabh for his help, encouragement and friendship. I am also thankful to my seniors Kuntal Mishra, U. C. Dumka, Bhuwan Joshi and Tejbir for their encouragement and motivation.

I shared an especial bond with Jessy. Being an office-mate, room-mate and friend, I found her very supportive and encouraging. I appreciate her determination and never ending high spirit. I thank to her and Lijo for their friendship and help and wish them a healthy little one. I also specially thank to my dear friend and brother Manash for his help during my thesis writing, suggestions and fruitful discussions. I cherish their friendship. I also express my sincere thanks to Bindu, who was my office-mate during the last stage of my PhD work and became one of my best friend. She has always motivated and helped me when I needed. The sweet memories of them will always remain a treasure for me.

I would like to thank Ramkesh, Ravi, Rupak, Rajesh, Pankaj, Eswar, Sumana, Akash, Brajesh, Aparajita, Narendra, Hema, Tapaswini, Haritma, Devesh, Archana, Rashmi, Rajeev, Sumit, Kishor, Krishna, Piyush, Jai Bhagwan, Pradip, Anuj and Subhash for their ever joyful company and for always making me feel at home.

I would like to thank my Maa and Papa for always supporting and encouraging me. I would like to thank my brothers, Ashok, who inspired me to develop an interest in research field, and Manoj for providing me all kind of support. I also extend my heartfelt thanks to my bhabhi and my loving 'Arnav' for all their faith and love. I am also grateful to my in-laws, relatives, nephews and niece for their interest, enthusiasm, prayers, blessings and good wishes for my work.

I would like to thank my husband Vinod who is a source of constant support. He has encouraged and motivated me at times when I needed it most. I could not have done this thesis without him. I know these words are not enough to express how much you have done for me. Lastly, but not by any means least of all, I am thankful to my Dadi and my daughter 'Yugantika (my loving Ishu)' who shared all my burdens with smiles and were the motivation to finish this work by time.

I sincerely acknowledge the financial support from Department of Science and Technology (DST) and Council of Scientific and industrial Research (CSIR), India

during my research period.

Lastly, and most importantly, I would like to thank the Almighty God for showering all His blessings on me. You have given me the power to believe in myself and pursue my dreams. I could never have done this without the faith I have in you.

Neelam

Contents

1	INTRODUCTION	1
1.1	Star Formation	1
1.1.1	From cloud to collapsing core	2
1.1.2	Pre-main sequence stages	3
1.1.2.1	Protostellar phase	4
1.1.2.2	T Tauri phase	4
1.1.2.3	Evolution in the HR-Diagram	6
1.1.2.4	Classification of YSOs	8
1.2	Star clusters and stellar evolution	11
1.3	Modes of Star Formation	12
1.3.1	Spontaneous star formation	13
1.3.2	Triggered star formation	14
1.4	Triggered star formation at the periphery of the HII regions	15
1.4.1	Formation and dynamics of HII region	15
1.4.2	Star formation processes in the HII regions	18
1.4.2.1	The collect and collapse model	18
1.4.2.2	Radiation driven Implosion (RDI) model	19
1.4.2.3	Hydrodynamic instability in the ionisation / shock fronts	20
1.5	Bright-Rimmed Clouds : RDI candidates	21
1.5.1	Formation and evolution of Bright-Rimmed Clouds	21
1.5.2	Morphological classification of BRCs	23
1.5.3	Star formation in BRCs : small scale Sequential star for- mation ?	24

1.6	Objectives of the present study	26
1.6.1	Examination of S^4F in BRCs	26
1.6.2	Disk evolution in T-Tauri Stars	26
1.6.3	Mass function	27
1.7	Thesis outline	27
2	CCD OBSERVATIONS, DATA REDUCTION AND ANALYSIS TECHNIQUES	29
2.1	Introduction	29
2.2	Optical Observations and Data Reduction	30
2.2.1	Telescopes used	30
2.2.2	The filters	30
2.2.3	The detector	31
2.2.4	CCD Observations	32
2.2.5	Data Reduction	33
2.2.5.1	Pre-processing	34
2.2.5.2	Processing	37
2.2.5.3	Post-processing	42
2.3	Grism slit Spectroscopy	44
2.3.1	Extraction of the optical spectrum	44
2.4	Archival datasets	45
2.4.1	Near-infrared data from 2MASS	45
2.4.2	Mid-infrared data from <i>Spitzer</i> Space Mission	46
2.4.2.1	Telescope and Instruments	46
2.4.2.2	Data Reduction	46
2.4.2.3	Mosaicking and Source Extraction	49
2.5	Basic Assumptions and Analysis Techniques Used	50
2.5.1	Basic parameters of the cluster	51
2.5.1.1	Determination of the cluster centre	51
2.5.1.2	Stellar radial density profile (RDP)	51
2.5.1.3	Reddening	53
2.5.1.4	$U - B, B - V$ colour-colour diagram	55
2.5.1.5	Colour magnitude diagrams (CMDs)	55
2.5.1.6	Distance Estimation	56

2.5.1.7	Determination of photometric completeness . . .	56
2.5.1.8	The sample to study the Mass Function	57
2.5.2	YSOs associated with BRC regions	57
2.5.2.1	H α emission	58
2.5.2.2	Near-infrared excess	58
2.5.2.3	Mid-infrared excess	59
2.5.3	Reddening and NIR excess determination for the YSOs in BRC regions	61
2.5.3.1	Determination of A_V	61
2.5.3.2	NIR Excess	61
2.5.4	Age determination of the YSOs	61
3	Star formation in the central cluster of W5 E HII region	65
3.1	Introduction	65
3.2	Observations and Data reductions	66
3.2.1	Optical CCD Observations	66
3.2.2	Grism Slit spectroscopy	69
3.3	Archival Data	69
3.3.1	Near-infrared data from 2MASS	69
3.3.2	Mid-infrared data from <i>Spitzer</i>	70
3.3.3	Slitless H α emission	71
3.4	Analysis of the associated cluster	71
3.4.1	Radial stellar surface density profile	71
3.4.2	Interstellar reddening	74
3.4.3	Spectral classification of ionising star in W5 E HII region .	75
3.4.4	Distance and optical colour-magnitude diagrams	75
3.5	Identification of pre-main sequence objects associated with the cluster	78
3.6	Reddening law in the cluster region	80
3.7	Initial mass function of the cluster	82
3.8	Star formation in the cluster region	85
3.9	Conclusions	86

4	SMALL SCALE SEQUENTIAL STAR FORMATION IN AGGREGATES ASSOCIATED WITH BRCs	87
4.1	Introduction	87
4.2	Observations and data reduction	88
4.3	Star Selection and Reddening Correction	89
4.4	Results	91
4.5	Discussion and Conclusion	95
5	<i>S</i> ⁴ <i>F</i> AND GLOBAL STAR FORMATION IN HII REGIONS ASSOCIATED WITH THE BRCs	99
5.1	Introduction	99
5.2	Observations and Data reductions	100
5.3	Archive Data	102
5.3.1	Near-infrared data from 2MASS	102
5.3.2	Mid Infrared data from Spitzer-IRAC	103
5.4	Description of the BRCs studied	103
5.5	Membership and Age determination of member stars	105
5.6	Star Formation Scenario in BRC Regions	114
5.6.1	Small-Scale Sequential Star Formation	115
5.6.2	Indication of Global Triggered Star Formation	120
5.6.3	Star Formation inside ‘A’-Type BRCs	129
5.7	Conclusions	130
6	DISK EVOLUTION AND CMF OF YSOs ASSOCIATED WITH HII REGIONS	131
6.1	Introduction	131
6.2	Evolution of H α EW and disk of T-Tauri stars associated with BRCs	133
6.3	Cumulative mass function of BRC aggregates	136
6.4	Disk evolution and CMFs of Class II and Class III YSOs associated with the cluster and BRCs in W5 E HII region	140
6.4.1	NIR-CC diagram of PMS stars associated with the BRCs	140
6.4.2	Evolution of disks of Class II and III sources associated with the Cluster and BRC regions	143

6.4.3	CMF of identified YSOs in the cluster and BRCs in W5 E HII region	145
6.5	Conclusions	147
7	STAR FORMATION IN THE W5 E HII REGION	149
7.1	Introduction	149
7.2	Reddening law in BRC regions	152
7.3	Star formation around BRC regions	152
7.3.1	Small scale sequential star formation (S^4F)	155
7.4	Nature and origin of the stars at the tip of ETLs	156
7.4.1	Target Selection, Observations and Data Reduction	156
7.4.2	Results	160
7.4.2.1	NIR colour-colour diagram	160
7.4.3	Optical colour magnitude diagram	160
7.4.3.1	SED fitting	160
7.4.4	Origin of Bright-Rimmed Clouds and Hydrodynamical In- stability of Ionization Fronts	164
7.4.5	Third Possible Mechanism of Triggered Star Formation	166
7.5	Conclusions	166
8	SUMMARY, CONCLUSIONS AND FUTURE WORK	169
8.1	Summary and conclusions	169
8.2	Strategies for the Future Work	172
8.2.1	Sample selection and observational Strategy	174
8.2.1.1	Deep Near-IR imaging	174
8.2.1.2	Mid-IR imaging from Spitzer-IRAC	174
8.2.1.3	X-ray data from Chandra	175
8.2.1.4	Slitless H α spectroscopy	175
8.2.1.5	Optical photometry	175
A	CHAPTER 5	177
	REFERENCES	206

List of Figures

1.1	Stages in the formation of a low-mass stars	5
1.2	Evolutionary paths in the HR-diagram for stellar masses ranging from 0.5 to 15 M_{\odot}	7
1.3	A schematic evolutionary sequence for the SEDs	9
1.4	Schematic diagram of conditions on the surface of a molecular cloud exposed to ionising and dissociating radiation from a sin- gle star	16
1.5	An Open Cluster and Emission Nebula in Cassiopeia	17
1.6	The collect and collapse process	19
1.7	Vishniac instability mechanism	21
1.8	A schematic description of three BRC morphologies	24
1.9	Small scale star formation in BRCs	25
2.1	A chart summarizing the whole data reduction procedure.	34
2.2	Radial distribution of the apparent surface density	53
2.3	Description of the method of measuring $E(B - V)$	54
2.4	Infra-red colour-colour diagrams	59
2.5	IRAC colour-colour diagrams	60
2.6	$V/(V - I)$ CMD for a region	62
3.1	The $\sim 50 \times 50$ arcmin ² DSS2-R band image of the W5 E region.	67
3.2	Radial density profiles for the cluster using the optical and 2MASS data.	72
3.3	$(U - B)/(B - V)$ CC diagram for the stars within the cluster radius.	73
3.4	Flux calibrated normalised spectrum of HD 18326.	76

3.5	CMDs for the stars within the cluster radius and nearby field region.	77
3.6	NIR $(J - H)/(H - K)$ CC diagrams for the stars within the cluster radius and in the reference field.	79
3.7	$V/(V - I)$ CMD for the clustered YSOs identified by Koenig et al. (2008) in the cluster region	80
3.8	$V/(V - I)$ CMDs for the YSOs selected in the presented study in the cluster region	81
3.9	TCDs for the diskless (Class III) sources in the cluster region. . .	82
3.10	Statistically cleaned $V/(V - I)$ CMD for stars lying within the cluster radius.	83
3.11	The MF in the cluster region derived using the optical data. . . .	84
3.12	age distribution for the YSOs in the cluster region	85
4.1	Finding charts for stars in BRC 11NE and BRC 37	90
4.2	$V_0/(V - I_c)_0$ CMD for the BRC 14 aggregate	94
5.1	$(J - H)/(H - K)$ colour-colour diagrams for BRCs 2, 11NE, 13, 14, 27 and 38	107
5.2	Spatial distribution of $H\alpha$ emission and NIR excess stars	108
5.3	$V_0/(V - I_c)_0$ CMDs for probable YSOs in BRCs 2, 11NE, 13, 14, 27 and 38	111
5.4	IRAC colour-colour diagrams for YSOs in BRCs 2, 27 and 13/14 .	117
5.5	Spatial distribution of Class 0/I sources and Class II sources in the BRC 2 and BRC 27 regions	118
5.6	Spatial distribution of Class 0/I sources and Class II sources in the BRCs 13 and 14 region	119
5.7	Spatial distribution of NIR excess stars in the IC 1848W region .	121
5.8	Spatial distribution of NIR excess stars in the IC 1848E region . .	122
5.9	Spatial distribution of NIR excess stars in the CMaR1 region . . .	122
5.10	Spatial distribution of NIR excess stars in the IC 1396 region . . .	123
5.11	Variation of NIR excess $\Delta(H - K)$ and A_V as a function of distance from HD 17505 toward BRC 11 region	125
5.12	Variation of NIR excess $\Delta(H - K)$ and A_V as a function of distance from HD 18326 toward BRC 14 region	126

5.13	Variation of NIR excess $\Delta(H - K)$ and A_V as a function of distance from HD 53974 of the CMaR1 region	127
6.1	EWs of $H\alpha$ emission stars in the BRCs as a function of stellar ages.	134
6.2	Cumulative distributions of CTTSs and WTTSs in BRCs as a function of stellar age.	135
6.3	Cumulative distributions of $H\alpha$ emission and NIR excess stars in the BRCs as a function of stellar age.	136
6.4	CMF of YSOs in the 7 BRCs	137
6.5	CMF of the ‘A’ type and ‘B/C’ type BRCs	138
6.6	The $(J - H)/(H - K)$ CC diagrams of the YSOs in the BRC NW, BRC 13 and BRC 14.	141
6.7	$V/(V - I)$ CMD for the YSOs selected (see the text) in BRC NW and BRC 13.	142
6.8	Cumulative age distribution of Class II (CTTSs) and Class III (WTTSs) sources in the cluster and BRC 14 region.	144
6.9	CMFs of YSOs in the cluster, BRC NW, BRC 13 and BRC 14 regions.	146
7.1	<i>Spitzer</i> pseudo-colour image of part of W5 E.	151
7.2	TCDs for the diskless (Class III) sources in the BRC NW, BRC 13 and BRC 14 regions.	153
7.3	Global distribution of YSOs in the W5 E HII region.	154
7.4	Variation of $\Delta(H-K)$ and A_V for the IR excess stars in the strip toward BRC NW.	155
7.5	NIR CC and $V/(V - I_c)$ CM diagrams for the <i>ETLS</i> stars.	161
7.6	The SEDs for a Class I, Class II and Class III sources among the <i>ETLS</i> stars.	163

List of Tables

1.1	Classical evolutionary PMS lifetimes together with more recently derived lifespans for low-mass stars (Schulz 2005).	8
2.1	A brief description of the telescopes used	30
2.2	Brief details about the detectors used	32
2.3	Summary of <i>Spitzer</i> Characteristics	47
2.4	Brief details about the detectors used	47
3.1	Log of observations	68
3.2	Completeness factor of photometric data in the cluster and field regions.	70
4.1	Log of observations	89
4.2	Results of dereddening and age estimation	92
4.3	Summary of results	95
5.1	Log of optical observations	101
5.2	The zero-point constants, colour- and extinction-coefficients	102
5.3	Dereddened magnitude, colours, age, and mass of the YSOs associated with the BRCs.	112
5.4	Average age of the YSOs associated with the inside/outside regions of the BRCs.	115
5.5	Correlation between radial distance and $\Delta(H - K)$, A_V	128
6.1	Mass function of BRC aggregates	139
6.2	CMF of the YSOs in the cluster and BRC regions	146

7.1 Mean age inside/on the rim and outside rim in BRCs associated with W5 E.	156
7.2 Stars at the tip of elephant trunk-like structures	157
7.3 Log of observations	158
7.4 Photometric data for the <i>ETLS</i> stars	159
7.5 Physical parameters for the <i>ETLS</i> stars based on the SED fitting	164
7.6 Comparison of modes of triggered star formation	167
A.1 B , V and I_c photometric data for the stars along with their positions, EWs and corresponding 2MASS data.	178
A.2 J , H and K magnitudes of the sources used in the analysis	183
A.3 IRAC photometric magnitudes of the disk bearing candidates in BRCs 2, 27 and 13/14	190

NOTATIONS AND ABBREVIATIONS

The most commonly used notations and abbreviations in the thesis are given below. If a symbol has been used in a different connection than listed here, it has been explained at the appropriate place.

Notations

A_V	total absorptions in the visual magnitude
l, b	galactic longitude and latitude as per revision for the epoch 1950.0
u, b, v, i	apparent instrumental magnitude in U, B, V and I filters respectively
$(u - b), (b - v), (v - i)$	apparent instrumental colours
X	airmass
u_o, b_o, v_o, i_o	apparent instrumental magnitude, corrected for atmospheric extinction, in filters U, B, V and I respectively
$(u - b)_o, (b - v)_o$	apparent instrumental colours, corrected for atmospheric extinction
$(v - i)_o$	apparent instrumental colour, corrected for atmospheric extinction
U, B, V, I	apparent standard magnitudes
J, H, K	apparent standard magnitude in J, H and K filters respectively
$(J - K), (H - K)$	apparent standard colours
$(U - B), (B - V), (V - I)$	apparent standard colours
$(U - B)_0, (B - V)_0, (V - I)_0$	intrinsic standard colours
$E(U - B), E(B - V),$	colour excesses in $(U - B), (B - V)$
$E(V - I)$	$(V - I)$
$E(B - V)_{max}$	maximum $(B - V)$ colour excess
$E(B - V)_{min}$	minimum $(B - V)$ colour excess
$\Delta E(B - V)$	difference between the maximum and minimum $E(B - V)$ colour excess
M_\odot	mass of the Sun
m	apparent visual magnitude

M_V	absolute visual magnitude
$(m - M)_o$	true distance modulus
pc	parsec (unit of distance)
$\rho(r)$	stellar surface density as a function of radius
R	ratio of total to selective absorption
r_c	cluster core radius
r_{cl}	cluster extent
d	distance to the cluster from earth
α	right ascension
δ	declination

Abbreviations

Be	Berkeley
CC	Colour-Colour (diagram)
CCD	Charge-Couple Device
CF	Completeness factor
CMD	Colour-Magnitude Diagram
DAOPHOT	Domanian Astrophysical Observatory Photometry.
DSS	Digitized Sky Survey
ESO	European Southern Observatory
FWHM	Full Width at Half Maximum
GMCs	Giant Molecular Clouds
HR	Hertzsprung-Russell
IC	Index Catalogue
IMF	Initial Mass Function
IR	Infra-Red
IRAF	Image Reduction and Analysis Facility
IRAS	Infrared Astronomical Satellite
HCT	Himalayan Chandra Telescope
HFOSC	Hanle Faint Object Spectrograph and Camera
SSC	<i>Spitzer</i> Science Center

LIST OF TABLES

ST	Sampurnanand Telescope
ISM	Interstellar Matter
RDI	Radiation Driven Implosion
SED	Spectral Energy Distribution
SFR	Star Forming Region
TTS	T Tauri Star
kpc	Kiloparsec(unit of distance)
K-S	Kolmogorov-Smirnov
LF	Luminosity Function.
mag	magnitude (stellar)
MIR	Mid-infrared
FIR	Far Infrared
MS	Main-Sequence
MF	Mass Function
MIDAS	Munich Image Data Analysis System
PHOT	Photometry
PMS	Pre-Main Sequence
PSF	Point Spread Function
yr	year/years
Myr	Million year
NGC	New General Catalogue
ZAMS	Zero-Age-Main-Sequence
PAH	Polycyclic Aromatic Hydrocarbons
PDR	Photo Dissociation Region
2MASS	Two Micron All Sky Survey
IRAC	InfraRed Array Camera
MIPS	Multiband Imaging Photometer for Spitzer
BCD	Basic Calibrated Data

Chapter 1

INTRODUCTION

1.1 Star Formation

Stars are the fundamental units of luminous matter in the universe which serve as primary tracers of the structure and evolution of the universe and its contents. A decade ago, it was thought that star birth was a thing of the past and their birth itself remained a mystery. Now we all know that star formation did not cease after the Bing Bang but it is also occurring now. Eventually we know that the stars twinkling in the night sky are the distant versions of our own sun. Consequently, it is very important in astrophysics to understand the origin of stars and their evolution. Today, with the revolution of technology which enabled us to make necessary observations, we have come out of many misleading beliefs and conflicting thoughts. Now we have better understanding about the dramatic life history of stars. Stars always born in the nurseries of molecular clouds in the darkness of cosmic dust hence, not visible to the human eyes. In fact, when a newborn star finally becomes visible, it has already crossed its toddler stage in terms of human age. It takes the most modern of observational techniques and the entire accessible bandwidth of the electromagnetic spectrum to peek into the hatcheries of stars. The formation and early evolution of stars today is a faster growing field of research than ever before and constitutes a frontier field of astronomy.

1.1.1 From cloud to collapsing core

Most of the galactic star formation occurs in giant molecular clouds (GMCs) which possess extended envelopes of HI gas. GMCs are observed to have a hierarchical substructure that is highly inhomogeneous, with density enhancements such as cores, clumps, and filaments on all observable scales, from ~ 100 pc down to ~ 0.1 pc. Cores have masses of a few solar masses, sizes of 0.1 pc and average H_2 densities of $\sim 10^4 \text{ cm}^{-3}$. Clumps are coherent regions in the clouds, with masses of $\sim 10^3 M_\odot$, sizes of parsecs and average H_2 densities of $\sim 10^3 \text{ cm}^{-3}$ (Mac Low & Klessen 2004; Williams et al. 2000). Thus clumps are sites where stellar cluster may form while cores are regions out of which single stars or binaries form and are assumed gravitationally bound. However, a large fraction of the GMC mass is in clumps, which are generally larger structures than cores. Specifically the more massive gravitationally bound clumps are thought to form stellar clusters. However, this also means that a large fraction of the mass occupies a relatively small volume compared with the total volume of the cloud. The process that governs the global structure from large-scale properties of the interstellar medium (ISM) to stars is called fragmentation. It is a hierarchical process in which parent clouds break up into sub-clouds, which may themselves break into smaller structures.

GMCs and their massive constituent cores are strongly self-gravitating and are supported against collapse by turbulence and magnetic fields. The internal velocity dispersions of the substructures in molecular clouds are found to scale with their sizes, with decreasing non-thermal support on the smallest scales (Goodman et al. 1998). Both the random motion of clumps and the pressure associated with an internal magnetic field prevent immediate gravitational collapse. The internal random motions in molecular clouds are often referred to as ‘turbulence’, even though their detailed nature remains unclear. Thermal pressure is unimportant in this regard. A convenient tool for analyzing molecular clouds, or any other self-gravitating structure, is the virial theorem. For a gas cloud in hydrostatic equilibrium, Virial theorem relates between potential energy and kinetic energy for a spherically symmetric gas cloud, where the atoms satisfy the ideal

gas condition :

$$E_{th} = -1/2 \times E_{pot} \tag{1.1}$$

i.e., on the collapse of a gas cloud due to self gravity, half of the potential energy changes into heat and other half is radiated away. A homogeneous, isothermal gas cloud will collapse to form a star if its gravitational potential energy is greater than the thermal kinetic energy. This implies that there is a critical radius for homogeneous cloud beyond which it will collapse. This necessary condition for the gravitational collapse is the Jeans criteria.

For an isothermal medium with a uniform density ρ and a constant temperature T which is fixed by radiative processes, the Jeans length λ_J can be expressed in terms of the density and the isothermal sound speed $c = (kT/m)^{1/2}$, where m is the average particle mass:

$$\lambda_J = \pi^{1/2} c / (G\rho)^{-1/2} \tag{1.2}$$

Similarly, the corresponding minimum mass for the cloud to be unstable and undergo collapse is called the ‘Jeans mass’ M_J , usually defined as $\rho\lambda_J^3$, is

$$M_J = 5.57c^3 / (G^{3/2}\rho^{1/2}) \tag{1.3}$$

In short we can say that $M_J \propto \rho^{-1/2}T^{3/2}$

According to a classical picture originally proposed by Fred Hoyle, a cloud or a part of a cloud with mass above the Jeans mass collapses under gravity. The Jeans mass decreases as the density increases provided the collapse remains isothermal. Therefore, each part will also fragment again and again. A hierarchy of cloud sizes is systematically created until the collapse ceases to be isothermal. At the point when the gravitational energy, released through compressive heating, cannot escape the system in the form of radiation, the temperature of the fragments rises.

1.1.2 Pre-main sequence stages

Stars of different masses are thought to form by slightly different mechanisms. The theory of low-mass star formation, which is well-supported by a plethora of observations, suggests that low-mass stars form by the gravitational collapse of

rotating density enhancements within molecular clouds. The collapse of a rotating cloud of gas and dust leads to the formation of an accretion disk through which matter is channeled onto a central protostar. However, for high mass stars ($M > 8 M_{\odot}$) the mechanism of star formation is not well understood. In the present work we will be primarily dealing with low-mass pre-main-sequence (PMS) stars. Figure 1.1 is a schematic diagram showing different steps of the star formation process.

1.1.2.1 Protostellar phase

Figures 1.1a and 1.1b show a molecular cloud with several dense cores and the first step of the collapse of a core, respectively. As the cloud collapses, its density and temperature increase. The temperature and density are highest at the center of the collapsing part of the cloud (i.e., a core), where a new star will eventually form. The object that forms at the center of the collapsing core is known as a protostar (or Class 0 object). Since the birth, a protostar ejects remarkable slender jets of gas which drive spectacular outflows to highly supersonic speeds. Many outflows turn out to be gigantic twin structures. Figure 1.1c shows a protostar with accreting material and outflows. The radiation from the protostar is absorbed by the dust surrounding it, causing the dust to warm up and radiate in the infrared (IR). Infrared studies of star forming regions give us important information about how stars are born and thus how our own Sun and Solar System were formed.

1.1.2.2 T Tauri phase

Protostars which are starting to blow away the gas and dust surrounding them are called T-Tauri stars (TTSs). These are the star being fed from a disk supplied from an envelope. TTSs are PMS stars of F, G, K, M spectral type and mass $\lesssim 2 M_{\odot}$. They are significantly more luminous than the main sequence (MS) stars of the same mass because their radii are larger. They are powered by gravitational energy released as the stars contract towards the MS. They are very active and variable. They are generally been divided into two subgroups, namely classical T-Tauri stars (CTTSs) and weak-line T-Tauri stars (WTTSs).

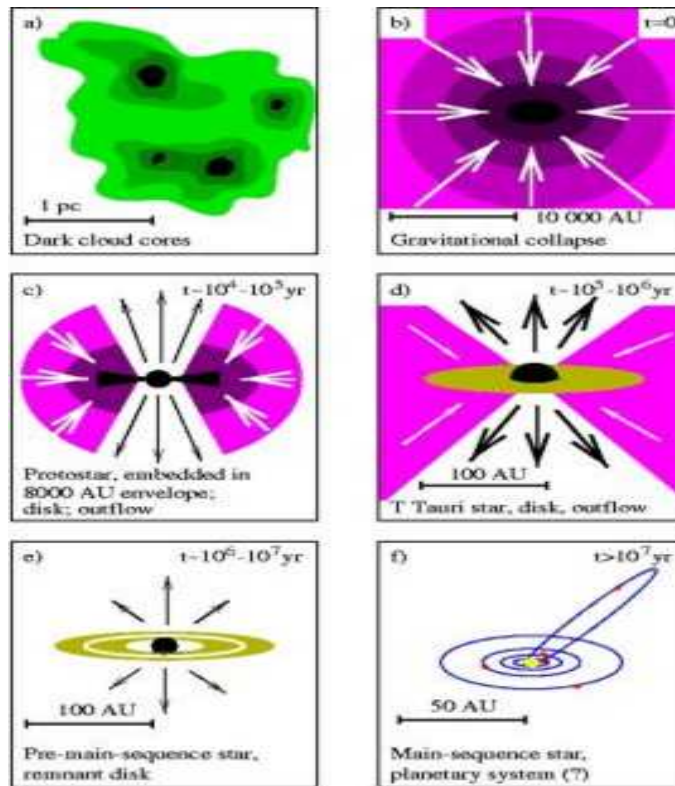


Figure 1.1: A sketched guide to the stages in the formation of a low-mass star like our Sun (a) Molecular cloud with several dense cores, (b) First steps of the collapse of a core, (c) Protostar with accreting material and outflows, (d) Accreting disk surrounding a protostar (CTT phase), (e) End of the CTT phase, (f) Planetary system built up with the remnant of the circumstellar disk. Credit : Hogerheijde (1998).

CTTSs have circumstellar disks, which in this case are called protoplanetary disks because they are probably the progenitors of planetary systems like the solar system. They possess strong magnetic field of order of a few kG. The matter free-falls along the magnetic field and is channeled onto the discrete regions of the stellar photosphere. The accreted material shocks as it impacts the stellar surface and radiates away its kinetic energy in the optical, UV and soft X-ray wave bands. A CTTS with an accretion disk is shown in Fig. 1.1d. However, the WTTSs are the PMS stars surrounded by a disk that is very low density or may not even exist. Traditionally, TTSs are classified as CTTSs or WTTSs based on

the H α equivalent width (EW). CTTSs show very strong H α emission in contrast to WTTSs. Thus CTTSs are stars with H α EW , $EW(H\alpha)$, greater than 10 Å, while WTTSs have $EW(H\alpha)$ less than 10 Å (Hamann & Persson 1992; Strom et al. 1989). Figs. 1.1e and 1.1f show the end of the T-Tauri phase and planetary system built up with the remnant of the circumstellar disk.

Analogous of TTSs in the higher mass range 2 - 8 M_{\odot} (A and B spectral type stars) are called Herbig Ae/Be stars. Stars massive than 8 M_{\odot} could not be observed in PMS stage because they evolve very quickly. Finally, the young star starts to resemble the adult (MS) star but with exaggerated behaviour.

1.1.2.3 Evolution in the HR-Diagram

It is well known that young stars can be identified by their location in the Hertzsprung-Russel (HR) diagram. The HR-diagram is a valuable tool to understand the stellar evolution. It takes advantage of the fact that in the course of stellar evolution only specific paths of luminosity and effective temperature occur. A nearly vertical track on the HR-diagram along which low-mass stars ($M \lesssim 2 M_{\odot}$) evolve during their early stages, is known as Hayashi track. The Hayashi track gives the location in the HR-diagram of completely convective stars (see, Fig. 1.2). The protostar may indeed be considered fully convective and this is usually where Hayashi tracks have their starting point (timeline labeled 1 in Fig. 1.2). When the opacity drops, the internal temperature rises and the convective zone recedes from the center. This causes the evolutionary path of the star in the HR-diagram to move away from the Hayashi track toward higher effective temperatures. The protostar is now on the radiative track of the HR-diagram. The location of the protostars of various phases are marked in the Fig. 1.2 (timelines 2-5 in Fig. 1.2). The classical evolutionary PMS lifetimes together with more recently derived lifespans for low-mass stars (Schulz 2005) are shown in Table 1.1.2.3. When young low-mass stars leave the main accretion phase (no infalling envelope anymore), and gain the main luminosity from gravitational contraction, the location in the HR-diagram where this happens is called the stellar birthline. Observationally, birthline is defined as the locus where stars first appear in the HR-diagram emanating from their dusty natal envelope. The determination of

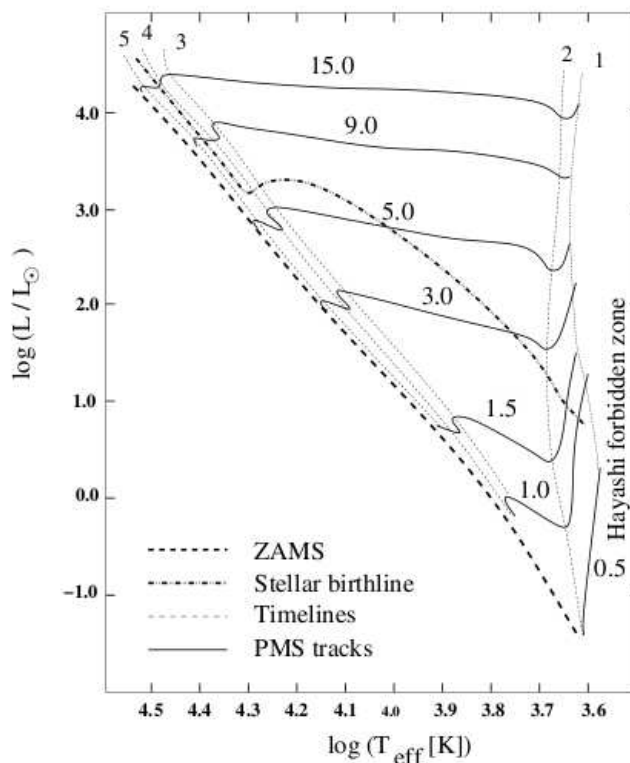


Figure 1.2: Evolutionary paths in the HR-diagram for stellar masses ranging from 0.5 to $15 M_{\odot}$. These paths are marked by thin hatched lines marking time periods labeled 1 to 5. The thick hatched line to the left approximately indicates the location of the ZAMS. The line across the tracks is the stellar birthline approximated (from Bernasconi 1996) for an accretion rate of $M_{acc} = 10^{-5} M_{\odot}/\text{yr}$ (taken from Schulz 2005).

the stellar birthline has two aspects. The first one is that it marks the end of the stellar collapse phase at which the protostar more or less has reached its final mass. It is thus sensitive to the mass accretion rate. The second aspect has to do with the fact that observationally there should not be any PMS star visible with effective temperatures and luminosities above this line. Figure 1.2 shows the approximate position of the birthline according for a thermal (constant) accretion rate of $10^{-5} M_{\odot}/\text{yr}$. For PMS stars with masses up to around $2 M_{\odot}$, the birthline cuts through the Hayashi track. Since TTSs are optically visible and possess only a very small or no fraction of their natal envelope, they are found beyond the

Table 1.1: Classical evolutionary PMS lifetimes together with more recently derived lifespans for low-mass stars (Schulz 2005).

M	1-2	2-4	4-5	t_{rad}	t_{ZAMS}
M_{\odot}	(Myr)	(Myr)	(Myr)	(Myr)	(Myr)
0.5	160	-	-	8.3	98
0.8	-	-	-	2.5	52
1.0	8.9	25	16	1.4	32
1.5	2.4	8.1	3.0	-	20
3.0	0.21	1.2	0.28	-	2.0
5.0	0.029	0.35	0.068	-	0.23
6.0	-	-	-	-	0.040

birthline on the Hayashi track in the HR-diagram.

The zero-age main sequence (ZAMS) is the end point of PMS evolution. At the end of the evolutionary track it represents the first time when energy generation by nuclear reactions in the stellar core fully compensates the energy losses due to radiation from the stellar photosphere. Finally, at above about $7 M_{\odot}$ the birthline attaches to the ZAMS indicating that these stars do not possess a PMS phase and may already be on the MS once they become visible.

The entire stellar systems throughout all evolutionary phases are called young stellar objects (YSOs). However, it is specifically used during the collapse phases and in the case of massive systems, where evolutionary phases can not easily be distinguished (Schulz 2005). Knowledge about intrinsic properties of YSOs relies almost entirely on theoretical stellar models. From these models ages, masses, and stellar radii can be derived if the brightness, distance, and effective temperature of the YSO are known. The so-determined ages constitute the only available evolutionary clocks for tracing the development of the star towards the MS.

1.1.2.4 Classification of YSOs

YSOs are frequently classified in the literature based on the shape of the emitted spectrum from near- to far-infrared spectral regions, which emphasizes the properties of circumstellar dust (Lada 1987; Lada & Wilking 1984). The emitted

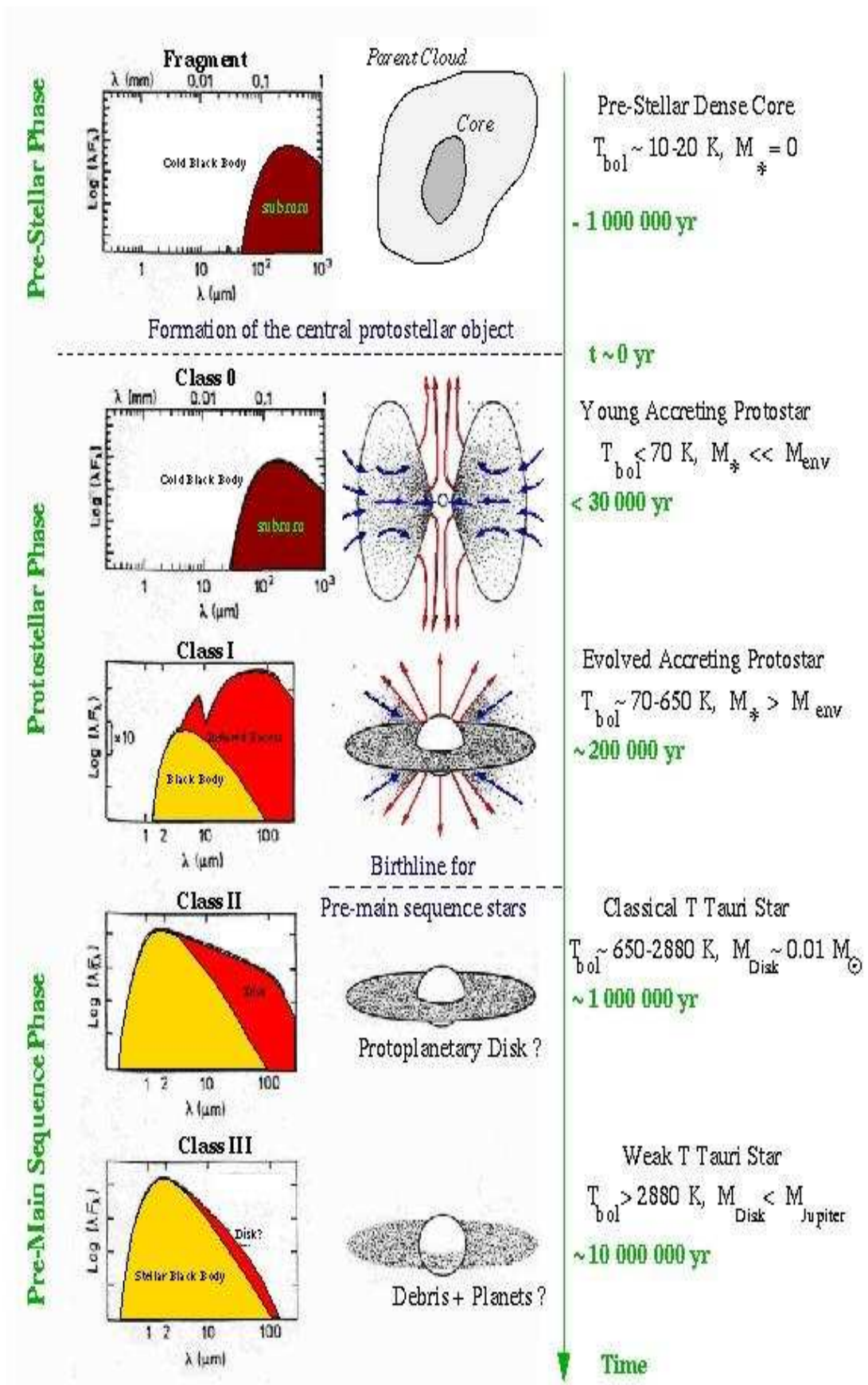


Figure 1.3: A schematic evolutionary sequence for the SEDs and components from embedded clumps to naked young stars. (Adopted from Smith 2004)

spectrum is usually discussed in terms of the “spectral energy distribution” or SED, which is a frequently used shorthand for either the flux distribution λF_λ observed at the Earth, or the luminosity distribution λL_λ , depending upon the context. The IR classification scheme depends upon the spectral index α of the emitted flux F of the object, $\nu F_\nu = \lambda F_\lambda \propto \lambda^\alpha$, typically measured between $2 \mu\text{m}$ and $50 - 100 \mu\text{m}$. A schematic evolutionary sequence for the SEDs is shown in Fig. 1.3. The classification of YSOs having masses in the range of $\sim 0.2 - 2.0 M_\odot$ on the basis of SEDs is discussed below;

Class 0 and I sources have $\alpha > 0$, indicating a rise in the SED all the way up to $\lambda \sim 100 \mu\text{m}$. The IR excess is very conspicuous and the SED is much broader than that of a single temperature blackbody function. From the evolutionary viewpoint, Class I sources are thought to represent accreting protostars, surrounded by luminous disks, with radii of $\sim 100\text{-}1000 \text{ AU}$, and by infalling, extended envelopes with sizes of $\sim 10^4 \text{ AU}$.

Class I protostars should be rather evolved protostars and Class 0 sources are their younger siblings. This perception comes from two observational results. One is that Class 0 sources seem to have significantly higher envelope masses than Class I sources. The other is that different outflow rates and morphologies exist in these sources.

Class II sources have $-2 < \alpha < 0$. The SED peak for these sources shifts towards shorter wavelengths but are still broad due to significant amount of circumstellar dust. A Class II sources results from the clearing of the circumstellar envelope, due to the action of a powerful stellar wind, and corresponds to a CTT or Herbig Ae/Be stars surrounded by a spatially thin, optically thick circumstellar disk of radius $\sim 100 \text{ AU}$.

Class III sources have $\alpha < -2$, and the SED resembles that of a normal, reddened stellar photosphere. The absence of an IR excess indicates the disappearance of the circumstellar structures, disks and envelopes, and the approach to the conditions of a normal MS star.

1.2 Star clusters and stellar evolution

It is believed that majority of the stars are formed in groups known as star clusters. Young open clusters (age ≤ 10 Myr), having just formed from gravitationally bound molecular clouds and still embedded in the parent nebulous regions, present an unique laboratory for understanding the process of star formation and its history (Stahler & Palla 2005). They contain YSOs of the same parental heritage but of differing mass and evolutionary states, therefore early evolution of stars over a wide mass range as well as the nature of interactions between young stars and the interstellar medium can be easily understood. The ages of young clusters (a few million years) are small in comparison to their dynamical evolution time (around 10^8 years). Consequently their study helps in understanding the process of star formation (Miller & Scalo 1979; Roberts 1957).

The question of cluster formation is a complex one that is intimately linked to the process of star formation. The star clusters born in molecular clouds and during their formation and early evolution therefore they are completely embedded in molecular gas and dust. These young clusters are known as embedded clusters.

Most stars within clusters lie along a band in the luminosity-temperature plane (where temperature is measured by spectral type or colour) of HR-diagram. The theory of stellar structure and evolution predicts fairly precisely the mass dependent evolution of stellar luminosities and temperatures with age. This enables the age of a stellar population to be determined by placing the stars on a HR-diagram. The locations of stars are then compared to the predictions of stellar-evolution theory. This has been proved to be a powerful tool to estimate the age of the intermediate age clusters whose more massive stars have finished their main hydrogen-burning stage and experience significant luminosity and temperature evolution. However, dating of young, embedded clusters is considerably more difficult. The reason for this is two-fold. First, the majority of stars in an embedded cluster are PMS stars, that is, stars that have not yet evolved to the point where nuclear burning commences in their interiors. For these stars, the theoretical trajectories on the HR-diagram can be highly uncertain, especially for

stars with ages of ~ 1 Myr or less. Second, it is difficult to estimate accurate luminosities and temperatures for PMS stars since they are obscured by interstellar dust, exhibit IR excess emission and are variable. The embedded-cluster phase of evolution lasts somewhere between 3 and 5 Myr (Lada 2010).

In older clusters, the MS terminates at fainter and cooler levels. Differences observed among stars away from the MS, such as in luminosity and temperature or in chemical composition, reflect changes to the stars during the end of their lives and provide laboratories for the study of stellar evolution.

Pandey et al. (2001, 2005) found that star formation in few young clusters may be a continuous process. For example, in the case of NGC 663, star formation seems to have taken place non-coevally in the sense that formation of low-mass stars precedes the formation of most massive stars. Whereas, in the case of NGC 654 and NGC 3603, formation of low-mass stars did not cease after the formation of most massive stars in the clusters. Another useful observable that is at least in principle possible to determine in the cluster is the time spread of star formation within a cluster, that is, the age difference between the oldest and youngest star in the given cluster. If this age spread is large (tens of Myr or longer) then we can conclude that the molecular cloud from which the cluster forms may be long-lived. However, it is difficult to evaluate the significance of age spreads and distributions estimated from colour-magnitude diagrams (CMDs) of young clusters because differential extinction, source variability, IR excess, binarity, and contamination by field stars can contribute significantly to the intrinsic scatter in the diagram (e.g., Hartmann 2001). But still it is a useful tool to get the preliminary age analysis of a cluster.

1.3 Modes of Star Formation

Star formation can be characterised by the degree to which external processes influence it. In general, there are two modes of star formation; Spontaneous star formation, and Triggered star formation. Spontaneous star formation occurs without external influence while triggered, or induced star formation is induced by the external events.

1.3.1 Spontaneous star formation

Star formation occurs as a result of the action of gravity on a wide range of scales, and different mechanisms may be important on different scales depending on the force opposing gravity. On the galactic scales, the tendency of the interstellar matter to condense under gravity into star-forming clouds is counteracted by galactic tidal forces, and star formation occur only where the gas becomes dense enough for its self gravity to overcome these tidal forces, for example in the spiral arms. On the intermediate scales of star-forming GMCs, turbulence and magnetic field may be the most important effect counteracting gravity, and star formation may involve the dissipation of turbulence and magnetic fields. On the small scales of individual prestellar cloud cores, thermal pressure becomes the most important force resisting the self-gravity, and it sets a minimum mass that a cloud core must have to collapse under gravity to form stars (Larson 2003).

In spontaneous star formation it is believed that huge molecular clouds become unstable and begin to collapse, falling inward towards a centre that would eventually become a protostar. Earlier spontaneous star formation was considered to be the result of the gradual cooling of the warm interstellar gas, bringing the thermal Jeans mass to a value lower than the mass of the cloud, at which point the collapse would occur. A cold cloud may be stabilized by turbulence or magnetic tension and pressure or rotation. A cloud collapse is presumed to begin when a cold cloud loses its turbulent energy via any dissipation mechanisms or magnetic field diffuse away or cloud's angular momentum is removed due to magnetic tension. In addition, a cloud that is stabilized by some combination of these three energies can accrete matter and go unstable due to mass change - without any loss of energy (Elmegreen 1998).

The mechanism for spontaneous star formation are dissipation-collapse scenarios. In each case, a cloud starts with a relatively low gravitational binding energy and lots of other energy. The other energy dissipates and, by the virial theorem, the gravitational binding energy increases. The dissipation-collapse scenario implies that the basic time scale for spontaneous star formation is the dissipation time scale, which is the slowest step in the star formation process.

1.3.2 Triggered star formation

In triggered star formation, the collapse of the core is initiated by an outside agent exerting pressure on the system. Once initiated, the collapse is expected to follow the same path as in the case of spontaneous star formation.

Triggering mechanisms are generally related to the high pressure events. These mechanism can be divided into three types depending on the impact of triggering on the star formation rate (Elmegreen 1998). In the case of **Strong triggering**, the star formation occurs where it would not have occurred otherwise. For example, when a diffuse cloud that is hit and compressed by a shock and then forms stars. **Moderate triggering** is when star formation is sped up in a region where it would have been occurred at slower pace. For example, in the case of a molecular cloud where spontaneous star formation is occurring but a shock compress the gas and star formation takes place on faster rate. **Weak triggering** is when the star formation moves from one place to another because of the bulk motion of the gas, but there is no change in the star formation rate. Triggering can also be divided into three size scales (see, Elmegreen 1998) as **small scale triggering**, which involves the direct squeezing of pre-existing cloud or globules by high pressure which nearly surrounds the whole cloud; **intermediate scale triggering**, which is the compression of a cloud from one side, leading to a dense ridge of gas which eventually collapses or retracts into denser cores in which stars form; and, **large scale triggering**, which is an accumulation of gas into an expanding shell or ring which partially surrounds the pressure source, a star or supernova. Triggering on all size scales can be the result of a gravitational instability caused by the density enhancement of a shock moving through a molecular cloud.

There may be different mechanisms for the triggering of star formation for example, triggering by supernova explosion, cloud-cloud collision, spiral arm triggering and triggering by HII regions formed through the strong ultraviolet radiation from massive stars.

1.4 Triggered star formation at the periphery of the HII regions

1.4.1 Formation and dynamics of HII region

Massive stars have extremely high luminosities often in excess of $10^5 L_{\odot}$. These stars produce intense extreme ultraviolet (EUV) radiation that ionises the star's surroundings, and intense far ultraviolet (FUV) radiation that can penetrate into regions of neutral gas. The volume of ionised gas surrounding a massive star is referred to as an "HII region", because the principal constituent of the region is ionised hydrogen. When a massive star turns on, a volume of gas around the star is rapidly ionised and heated to $\sim 10^4$ K. The resulting high pressure region then expands into surrounding molecular gas at roughly the speed of sound in the hot gas. At the same time, electrons and protons in this plasma recombine, creating new atomic hydrogen. Since each ionisation event deletes a photon from the beam, a star with a fixed output in ultraviolet radiation can only ionise a limited region in the surrounding cloud. If this matter has uniform density, the ionisation spreads isotropically and fills out a volume known as the 'Stromgren sphere'.

The moving edge of the HII region is known as the ionisation front (I-front). The resulting high pressure drives a photo-evaporative flow of photo-ionised material away from the surface of the molecular cloud into the HII region interior. At the same time, the pressure at the I-front drives a shock into the surrounding molecular cloud, compressing the molecular gas and driving up the pressure (e.g., Kahn 1958). The I-front and shock front (S-front) typically move into the molecular cloud at velocities of order a few km/sec. The interaction of HII region with the surrounding molecular cloud may trigger the next generation star formation in the cloud.

A photo-dissociation region (PDR) is the transition layer at the surface of a molecular cloud between the dense, cold molecular gas and the tenuous, warm, ionised gas; it is the region where the FUV photons in the range 912 - 1110 Å are either absorbed by H₂ or by dust. The sharp transition where molecular hydrogen turns mostly atomic is termed as the dissociation front (D-front). It

1.4 Triggered star formation at the periphery of the HII regions

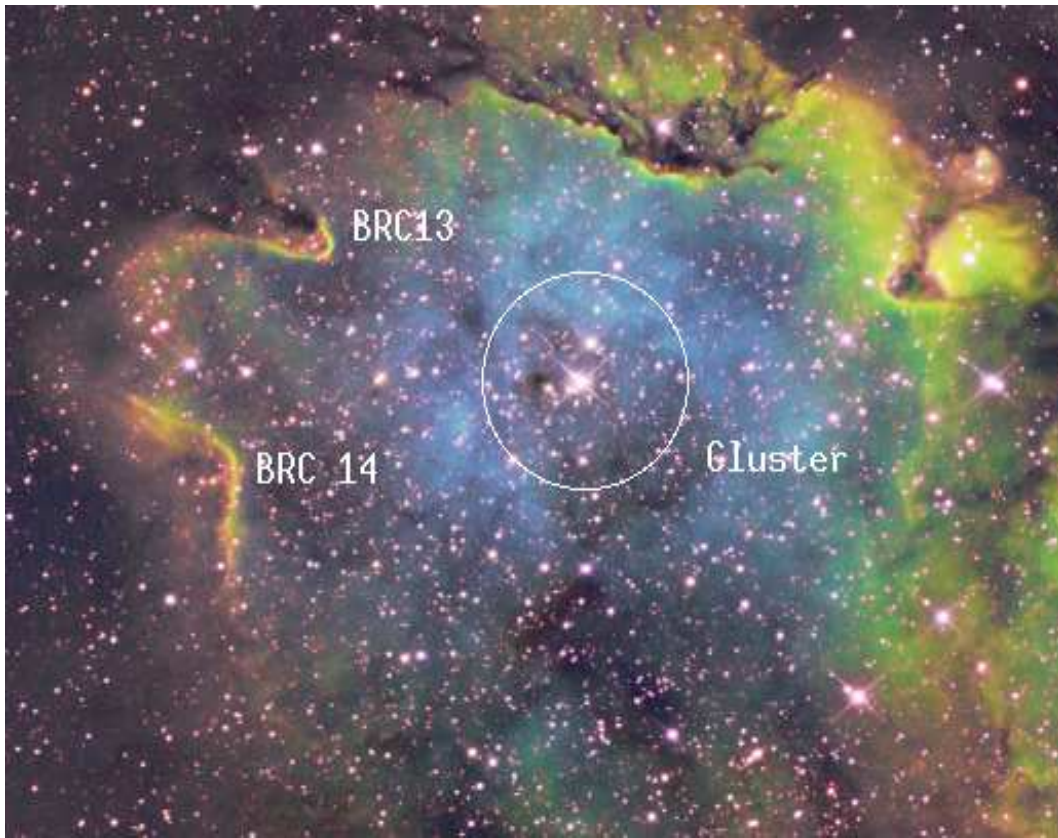


Figure 1.5: An SII , $\text{H}\alpha$, OIII colour-composite image of an open cluster and emission nebula in Cassiopeia (taken from <http://www.ruppel.darkhorizons.org/IMAGE>). The cluster and bright-rimmed clouds (BRCs) (cf. Sec. 1.5) associated with the region are marked.

such as CO can occur upstream of the H_2 D-front, and some of the characteristic emission associated with PDR (from e.g. O, C, or CI) may arise there (Bertoldi & Draine 1996). Fig. 1.4 shows the schematic diagram of conditions on the surface of a molecular cloud exposed to ionising radiation from a single star. The compressed gas layer between the I-front and S-fronts, in which the D-front is trapped, is also shown.

Models of the photo-dissociation of molecular clouds surrounding newly formed ‘O’ and early ‘B’ type stars (Hill & Hollenbach 1978; Roger & Dewdney 1992) show that the resulting HII will exist in a layered structure surrounding the star. A D-front will first rapidly move through the molecular cloud forming a broad HI

1.4 Triggered star formation at the periphery of the HII regions

region. As the HII region expands a layer of shocked HI will form just outside the I-front. Eventually the faster moving I-front will catch up with the D-front and all of the HI will be found in the shocked layer. The time when the I-front and D-front merge ranges from $10^5 - 10^6$ years depending upon the spectral type of the star and the density of the surrounding molecular material (Roger & Dewdney 1992).

Fig. 1.5 shows an example of HII region created by a massive star and its interaction. In Fig. 1.5 we can notice the curved rim like structures, which are the output of the interaction of the ionising radiation with the neighbouring cloud and the strong $H\alpha$ emission, which is likely to be the photo-evaporative flow of the ionised gas from the surface layer of the cloud. The massive star is at the center of HII region and is a member of the central cluster.

Thus, the above discussion shows the formation and dynamics of HII region. The interaction of expanding HII region with the surrounding molecular cloud may trigger the star formation in various processes which will be discussed in the following section.

1.4.2 Star formation processes in the HII regions

1.4.2.1 The collect and collapse model

This model was first proposed by Elmegreen & Lada (1977). During the expansion of an HII region, the I-front may be supersonic, and is preceded by a S-front on the neutral side. Neutral material accumulates between the two fronts, forming a layer of dense shocked material. Gravitational instabilities can develop on a long time scale, along the length of the layer. Due to the long time scale, the compressed layer becomes very massive and consequently leads to the formation of massive fragments. An observational signature of this process is the presence of a dense layer and massive condensations adjacent to an HII region (e.g. Deharveng et al. 2003). A schematic view of the collect and collapse process is shown in Fig. 1.6.

1.4 Triggered star formation at the periphery of the HII regions

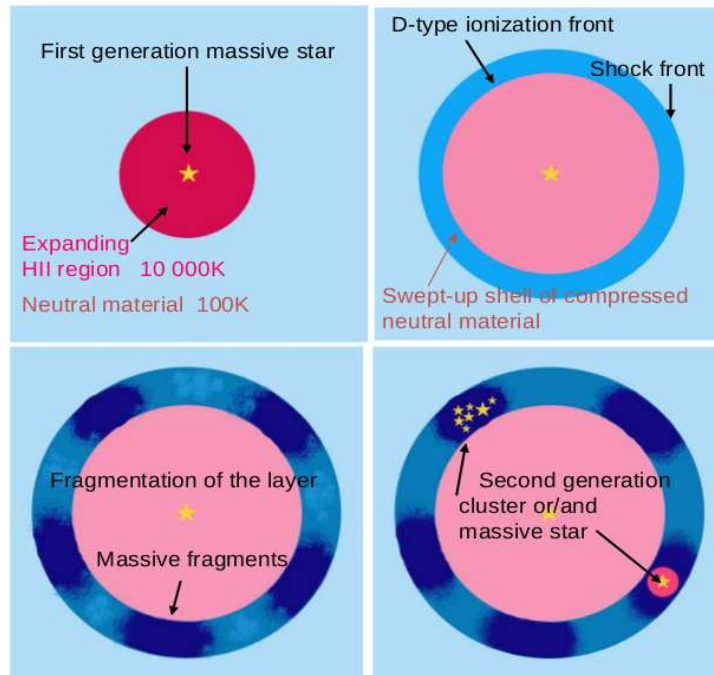


Figure 1.6: The collect and collapse process : credit A. Zavagno

1.4.2.2 Radiation driven Implosion (RDI) model

In this scenario the HII region expands in a medium containing pre-existing dense molecular clumps. The pressure exerted by the ionised gas on the surface of a clump can lead to its implosion, and to the formation of a ‘cometary globule’ surrounded by dense ionised gas forming a ‘bright rim’. Detailed model calculations of the RDI process have been carried out by several authors (e.g., Bertoldi 1989; Kessel-Deynet & Burkert 2003; Lefloch & Lazareff 1995; Miao et al. 2006). According to this model the evolution of the cloud is two phases, namely, compression phase and cometary phase. During the collapse phase, a S-front progresses into the clump and compresses it. The compression phase is rapid, lasting about 10% of the lifetime of the globule. Star formation is predicted to occur in this short compression phase. This compression phase is followed by a transient phase of re-expansion and then by a quasi-stationary cometary phase. During this last phase, the cloud represents a structure of a dense head and a long tail and moves

1.4 Triggered star formation at the periphery of the HII regions

slowly away from the ionising source by the rocket effect. The signature of the RDI process is the anisotropic density distribution of gas in a relatively small molecular cloud surrounded by a curved I-front (bright rim) as well as a small group of YSOs in front of it.

1.4.2.3 Hydrodynamic instability in the ionisation / shock fronts

The dynamical instability of radiative shocks is an oscillatory, unstable regime that produces undulations in the thin shells and deforms the shape of the S-front. For the case of the decelerating shells (i.e., evolving in increasing, constant, or mildly decreasing density gradients), the amplitudes of the unstable modes have a maximum, saturated value, and shell simply oscillates without any further growth. The maximum shell deformation corresponds to this saturated amplitude value. This instability was first described by Vishniac (1983) and is also oftenly referred to as the “Vishniac instability”.

The mechanism of the Vishniac instability can be understood by considering a thin, decelerating shell driven from within by a high-pressure region, as shown in Figure 1.7. From within it is confined by thermal pressure acting normal to the shell surface, as adjacent regions can communicate with each other by sound waves, while from outside it is confined by ram pressure acting parallel to the velocity of propagation, as the shell moves supersonically into the surrounding gas. In equilibrium, these two forces remain in balance. Should the shell be perturbed, however, the thermal pressure will continue to act normally, but the ram pressure will now act obliquely, giving a transverse resultant force that drives material from “peaks” into “valleys” of the shell. The denser valleys will be decelerated less than the rarefied peaks, however, so that the positions of peaks and valleys are interchanged after some time. Vishniac (1983) showed that this over-stable oscillation can grow as fast as $t^{1/2}$. It saturates when the transverse flows in the shell become supersonic and form transverse shocks, so that the end result of Vishniac instability is a shell with transonic turbulence and moderate perturbations (Mac Low & Norman 1993).

A two-dimensional simulation of this process is presented by Garcia-Segura & Franco (1996). According to these authors, the resulting structures are very

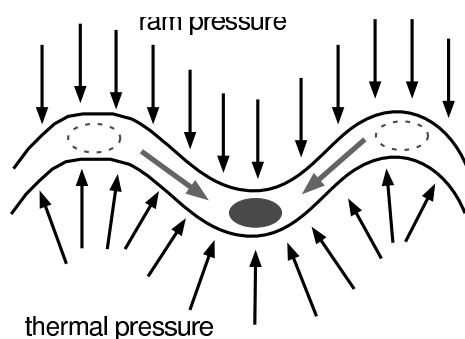


Figure 1.7: Vishniac instability mechanism (from Mac Low 1999)

similar to the bright rims and ‘elephant trunks’ observed at the periphery of HII regions. If confirmed, this process is interesting as it allows the formation of dense clumps in a formerly rather homogeneous medium. The hydrodynamic instability of an I-front accelerating into a molecular cloud, with imposed initial perturbations of different amplitudes is also investigated recently by Mizuta et al. (2006).

1.5 Bright-Rimmed Clouds : RDI candidates

BRCs are small isolated molecular clouds found at the boundary of the evolved HII regions (as can be seen with bright rims at the boundary of the HII region in Fig. 1.5). They are thought to be the remnants of recent star formation activity. Some of these clouds show evidence for star formation such as, Infrared Astronomical Satellite (IRAS) sources, $H\alpha$ emission stars, Herbig-Haro objects, molecular outflows. Thus they are also considered the potential sites of triggered star formation.

1.5.1 Formation and evolution of Bright-Rimmed Clouds

As the HII region surrounding an ionising star expands, it preferentially erodes away the nearby low-density material and uncovers the higher density clumps. The cloud structure and evolution is decided by the incoming ionising radiation. When the I-front reaches the cloud surface, the surface layers of the cloud are

photo-evaporated and drives a shock into the gas. This can lead to stars being induced to form inside the rims. Apart from the ionised rim, clear evidence of striated rays is seen as gas streams off the ionised boundary. As the surface layers of the clouds are photo-ionised, a recombination layer (or ionised boundary layer, hereby, IBL) develops on the side of the cloud facing the ionising star. The optically bright rim of the BRC is the result of recombination within the IBL.

The evolution of BRCs are primarily determined by two dimensionless parameters: the ratio of the ionised gas and the initial cloud's densities, and the fraction of UV photons absorbed in a thin ionised boundary layer at the front of the cloud. Additionally the dynamics of gas in the head of the globule will be influenced by the propagation of an isothermal shock. After about 10^5 years, a dense core forms inside the head and the compression continues deeper into the cloud, eventually forming small ansae along the major axis of the cloud (i.e. aligned with the direction of the illuminating stars responsible for the RDI). At this stage the density contrast between the core and the initial cloud material will be about one order of magnitude. Finally, the cloud enters a quasi-equilibrium state, when the cometary head becomes confined by over-pressure of the ionised gas. The globule, and its now well developed tail structure, will ultimately acquire a bulk velocity away from the external radiation source at velocities of typically 10 km/s.

The pressure balance between the hot ionised gas and molecular gas (internal pressure of the molecular gas is mostly due to turbulent motions but with a small thermal contribution) within the cloud can be used as the key diagnostic indicator of the impact of ionising radiation on the dynamics and future evolution of the cloud (Morgan et al. 2004). There may be three cases:

1. The ionisation photon flux is too weak and/or the pressure of the ionised gas is too small to compress the molecular gas, the radiation field is therefore unable to dynamically affect the cloud.
2. the ionising flux is too strong and/or the density of the molecular cloud is too small, the I-front is able to propagate supersonically with respect to the molecular gas, resulting in an almost instantaneous photo-ionisation of the

cloud. This is referred to as ionisation flash by Lefloch & Lazareff (1994) or cloud zapping by Bertoldi (1989).

3. The ionisation flux and the density of the molecular cloud is such that the whole evolution of the cloud is dominated by the propagation of a D-critical I-front that also act to drive an isothermal shock before it.

Evaporation of the cloud ensures that eventually the surface area of the cloud will decrease, leading to a relative increase in the IBL pressure. The overpressure of the hot, ionised surface layers with respect to cooler neutral gas leads to isothermal shocks being driven into the cloud.

1.5.2 Morphological classification of BRCs

Sugitani et al. (1991, hereafter SFO 91) and Sugitani & Ogura (1994) classified BRCs into three types depending on the curvature of the rim of the BRCs. Type ‘A’ cloud has moderately curved rim with a length to width ratio (l/b) of less than 0.5, type ‘B’ cloud with a rim displaying moderate curvature which sometimes is also described as elephant trunk with a length to width ratio (l/b) greater than 0.5 and type ‘C’ cloud with a tightly curved rim and a tail, which is also called cometary globule.

Lefloch & Lazareff (1994) presented a two-dimensional numerical simulation of the effect of UV radiation on the dynamical evolution of a molecular cloud based on the RDI model. The three rim types, A, B and C, closely match their model at 0.036, 0.126 and 1.3 Myr respectively. The shock induced model of Vanhala & Cameron (1998) as well as the observations of the expanding I-front of the Ori OB 1 associations (Ogura & Sugitani 1998) suggested that these morphological types of BRCs may actually be a time evolution sequence with cloud evolving from type ‘A’ through type ‘B’ to type ‘C’. Miao et al. (2006) incorporated self-gravity and thermal evolution in their simulation and produced the same morphological results as by Lefloch & Lazareff (1994). The first whole sky survey by SFO 91 and Sugitani & Ogura (1994) revealed that 61% of the observed BRCs are of type ‘A’. Recently Miao et al. (2009) developed a comprehensive RDI model in order to obtain a consistent description about the effect of UV radiation on the

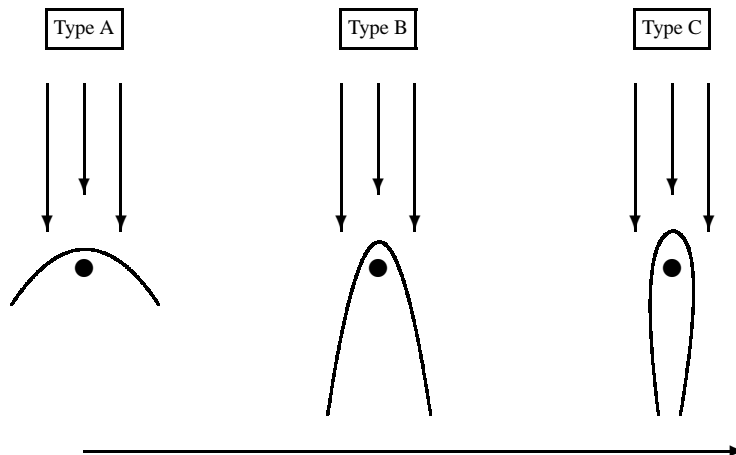


Figure 1.8: A schematic description of three BRC morphologies. The vertical arrows represent the incoming ionising photon flux and the horizontal arrow denotes the direction of the possible time evolution of the cloud complex under the influence of the ionising radiation flux. The three types A, B and C correspond to the three morphologies in three different stages over the evolution of the cloud complex (Miao et al. 2006).

dynamical evolution of a molecular cloud and to reveal the physical origin for the observed characteristics of BRCs' morphology formation. They concluded that depending on the initial gravitational state, a cloud could evolve to any one of the three type BRCs.

1.5.3 Star formation in BRCs : small scale Sequential star formation ?

Sugitani et al. (1995) carried out near infrared (NIR) imaging of 44 BRCs and revealed that an elongated, small cluster or aggregate of YSOs which are aligned along the direction toward the ionising star is often associated with them. These aggregates showed a tendency that 'redder' (presumably younger) stars tend to be located inside the BRCs, whereas relatively 'bluer' (presumably older) stars are found outside the clouds, suggesting an age gradient. Thus they advocated a hypothesis called '*small-scale sequential star formation (S^4F)*', i.e. the propaga-

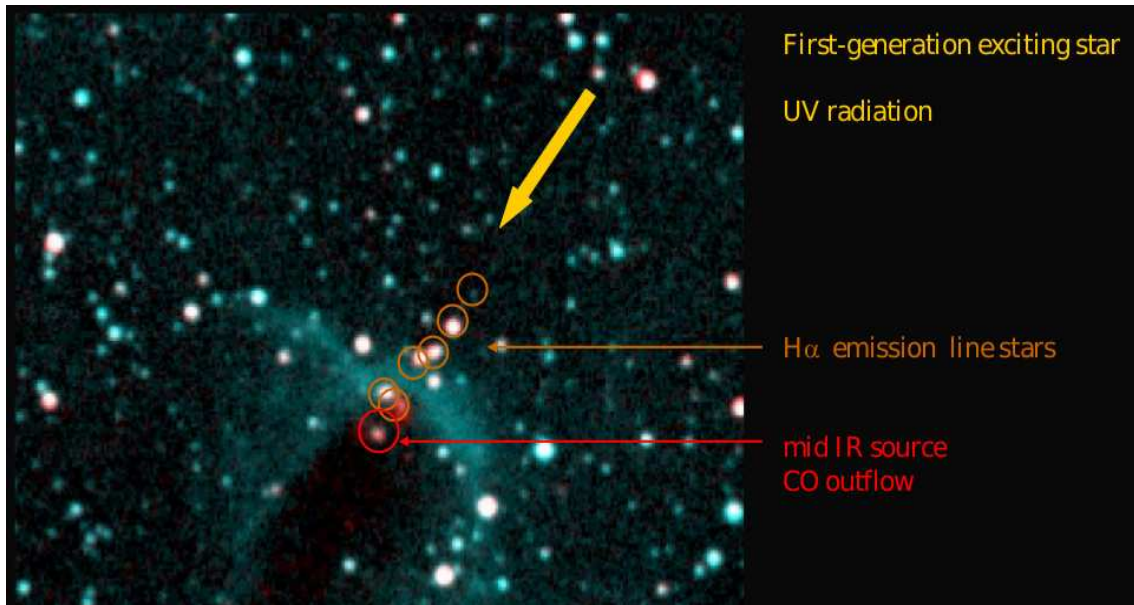


Figure 1.9: Small scale star formation in BRCs (taken from L. Deharveng)

tion of star formation along the axis of the BRCs as the I/S-front advances further and further into the molecular cloud (see, Fig. 1.9). The H α grism survey of 24 BRCs by Ogura et al. (2002) detected 460 H α emission stars (possibly, TTSs or Herbig Ae/Be stars) and 12 Herbig-Haro objects in their vicinities. Again these H α emission stars are found concentrated toward the head or just outside of the BRCs and aligned toward the exciting star(s) direction. Deep NIR photometry of BRC 14 by Matsuyanagi et al. (2006) revealed that three indicators of star formation, i.e., the fraction of YSOs among the sources, the amount of extinction and the near IR excesses of the YSOs, show a clear trend from outside to the inside of the rim indicating that the YSOs located near the rim are relatively younger than those located away from the rim. This result further strengthens the S^4F hypothesis.

1.6 Objectives of the present study

1.6.1 Examination of S^4F in BRCs

There has been qualitative evidence for the S^4F hypothesis such as an asymmetric distribution of probable TTSs (Ogura et al. 2002) and of the properties of NIR excess stars (Matsuyanagi et al. 2006) but there were no quantitative confirmation of the hypothesis in BRCs. Hence, the present study aims to examine quantitative evidences for S^4F in BRCs.

1.6.2 Disk evolution in T-Tauri Stars

TTSs are divided into two subclasses, CTTSs and WTTSs. As strong $H\alpha$ line emission is believed to be an indicator of the presence of an accretion disk in young stars, CTTSs are considered to be the PMS stars with $EW(H\alpha) \geq 10 \text{ \AA}$ and strong IR emissions, while WTTSs have $EW(H\alpha) < 10 \text{ \AA}$ and almost non-existing infra-red excess. This fact leads to the idea that CTTSs lose their disks and evolves into WTTSs (e.g., Duvert et al. 2000). However, there are many observational evidences which claimed that the CTTS and the WTTS are coeval and have indistinguishable age distribution (e.g., Gras-Velázquez & Ray 2005; Lawson et al. 1996; Walter et al. 1988). From the analyses of the HR-diagram of the CTTSs and WTTSs in Chamaeleon I, Lawson et al. (1996) concluded that some stars may be born even almost diskless or lose the disk at very early stages (age $< 1 \text{ Myr}$). However, in order to explain the co-existence and approximate coevality of CTTSs and WTTSs in a SFR, it is usually postulated that YSOs display a wide range of disk masses and their accretion activity and/or the dispersal of the disk takes place in a correspondingly wide range of time-scales (Bertout et al. 2007; Furlan et al. 2006). Recently, Bertout et al. (2007), by using new parallaxes for CTTS and WTTS in the Taurus-Auriga T association, concluded that their observed age and mass distribution can be explained by assuming that a CTTS evolves into a WTTS when the disk is fully accreted by the star.

Hence, it is still in debate whether CTT evolves to WTT or both are coeval. Here, in the present study we are examining the age distribution of YSOs, which are mainly TTSs, hence it will be useful to study the disk evolution in TTSs.

1.6.3 Mass function

The distribution of stellar masses at birth of a star formation event, known as the initial mass function (IMF), is one of the fundamental properties of a stellar system. The IMF is a key diagnostic in distinguishing between various regimes of star formation processes. The IMF has been estimated from low-mass brown dwarf to very massive stars (Kroupa 2002). Combining IMF estimates for different population in which stars can be observed individually unveils an extraordinary uniformity of the IMF. This apparent universality of the IMF is a challenge for star formation theory because elementary considerations suggest that the IMF ought to systematically vary with star-forming conditions. Therefore, it is important to identify the systematic variation of the IMF with different star-forming conditions. Identification of systematic variations of star formation would allow us to understand the physics involved in star formation (Kroupa 2002). The mass function (MF) is described by a power law and the slope of the MF, Γ , is defined as

$$\Gamma = d \log N(\log m)/d \log m,$$

where $N(\log m)$ is the number of stars per unit logarithmic mass interval. For the mass range $0.4 < M/M_{\odot} \leq 10$, the classical value of the MF slope derived by Salpeter (1955) is $\Gamma = -1.35$. The mass spectrum for “clumps” within GMCs is tend to follow a power law having $\Gamma = -0.54$ (Blitz 1993).

Since the universality of the IMF is still an open question therefore it will be useful to study the MF of the cluster and associated BRC regions to compare the star formation process/scenario in different regions.

1.7 Thesis outline

In this thesis, the optical and infra-red analysis of HII regions and associated BRCs are reported. The main aim of the study is to obtain the information about the evolutionary stages of the young stars in the regions in order to study the star formation in and around HII regions. Disk evolution in TTSSs associated with BRCs and cluster region is also analysed. A comparative study of MF in the BRC regions and associated cluster is also carried out.

For this purpose we have selected the target BRCs from the SFO 91 catalogue which are within ~ 2 kpc distance. Also, to study the influence of ionising radiation from massive star on the star formation activity in the immediate vicinity and neighbouring cloud, we have used W5 E HII region as a template.

The organisation of this work is as follows.

Chapter 1 describes a brief understanding of the subjects of the present study.

Chapter 2 presents the observations and data reduction procedures used in this work. Data analysis techniques are also discussed briefly.

Chapter 3 presents the results of our study on the central cluster of W5 E HII region. The cluster parameters and IMF of the cluster associated with the region are also discussed.

Chapter 4 describes the S^4F in four BRC aggregates using optical and NIR JHK_s photometry.

Chapter 5 describes the results of optical, near- and mid-infrared photometry of six BRC regions. It also describes the star formation in and around BRCs and global star formation in the associated HII region.

Chapter 6 Chapter 6 illustrates the disk evolution and cumulative mass function (CMF) of YSO associated with six BRCs as well as central cluster of the W5 E HII region.

Chapter 7 describes the large scale star formation scenario in the W5 E HII region.

Chapter 8 summarises the results of the present work and a brief out line of the future plans.

Chapter 2

CCD OBSERVATIONS, DATA REDUCTION AND ANALYSIS TECHNIQUES

2.1 Introduction

Deep optical observations are the most efficient way to characterise the properties of the YSO population in a SFR. However, in the case of deeply embedded SFRs, the diagnosis of the YSOs only on the basis of the optical observations is difficult. Therefore, the complementary IR observations are also useful to detect and identify the YSOs associated with such regions. The present work deals with the star formation activity and properties of YSOs in the BRCs and cluster associated with HII region, using optical and IR observations. In this chapter the various observations, data reduction and analysis techniques are discussed. A brief description of telescopes, filters and detectors used are given in sections 2.2.1, 2.2.2 and 2.2.3, respectively. In sections 2.2.4 and 2.2.5, the observation strategy, reduction procedure and calibration methods have been discussed. In addition to this, in section 2.3 and 2.4 the spectroscopic and archival near/mid -IR data sets are discussed. The basic assumptions and analysis techniques employed in the present work are described in section 2.5.

2.2 Optical Observations and Data Reduction

Table 2.1: A brief description of the telescopes used

Telescope	Sampurnanand Telescope (ST)	Himalayan Chandra Telescope (HCT)	Kiso Schmidt Telescope (KST)
Place	ARIES, Nainital, India	Hanle, IIA, Bangalore, India	Kiso Observatory, Japan
Longitude	79°27'24''(E)	78°57'51''(E)	137°37'42''(E)
Latitude	29°21'42''(N)	32°46'46''(N)	35°47'39''(N)
Altitude	1951 m	4500 m	1130 m
System	Ritchey-Chretien	Ritchey-Chretien	Schmidt
Effective Diameter of primary mirror	104 cm	201 cm	105 cm
Focus	Cassegrain	Cassegrain	Prime
f-Ratio	f/13	f/9	f/3.1

2.2 Optical Observations and Data Reduction

2.2.1 Telescopes used

The objects studied in the present study are observed using three optical telescopes, i.e., Sampurnanand Telescopes (ST) of ARIES, Himalayan Chandra Telescope (HCT) of IIA, India and Kiso Schmidt telescope (KST) of Kiso observatory Japan. The ST is a 1.04-m aperture Veb Carl Zeiss reflector with f/13 Cassegrain and f/31 Coude foci. KST is a 1.05-m telescope with f/3.1 Schmidt focus. HCT of the Indian Astronomical Observatory (IAO) is a 2.01-m reflector with f/9 Cassegrain focus. The details of the site can be found at the HCT web-site (<http://www.crest.ernet.in>). The brief description of the telescopes is given in table 2.1.

2.2.2 The filters used

Filters are used either to reduce the overall intensity or to restrict the wavelengths of electromagnetic radiation (EMR) that hit the detector. Imaging without a filter results in no information about the colour of objects. As the detectors available now, invariably have a wider wavelength response and/or improved sensitivity than earlier detectors (viz. photographic plate), the role of filters becomes more important in the sense that now with proper choice of these, standard pass bands

are sampled for the total flux from the astronomical sources at different wavelengths providing information about temperature, luminosity etc. Photometry using different filters is needed to measure the magnitude of the stars to a standard, internationally agreed system with a good precision. In our observations of BRCs and clusters taken from ARIES, broad-band photometric standard filters of Johnson and Morgan (*UBV*) and Kron - Cousins (*I*) were used. The observation taken from HCT were in Bessell *UBVI* system.

2.2.3 The detector used and its function

Throughout the history of the telescope the detector at the focal point has been recognized as vital. We have used **Charge Coupled Device (CCD)** detector for our observations. Though the CCD is still not the panacea, but it has quickly won over the astronomical community as it combines the advantages of both photographic plates and photomultiplier tubes, i.e. two dimensional detection in an integrating mode, good linear response, high quantum efficiency which permits to venture much fainter in much less time and large dynamic range recording of objects over vastly different levels of brightness. *This device, which replaces the camera loaded with film — is ultra-sensitive, silicon semiconductor, ‘chip’-based optical detector, composed of an array of thousands or millions of individual, tiny picture elements that almost touch each other and are called ‘pixels’.* Each pixel acts as a little detector of light (may be square or rectangular, normally ranges between 6 to 30 μm in size) and receives a signal which converts the faint glow into electrons, typically at a quantum efficiency (QE) of 80% (at $\lambda \sim 6900 \text{ \AA}$).

The CCD operation is based on **photoelectric effect** and can be described as follows. The photons which are coming from the source hit the silicon chip within a pixel and are easily absorbed. The photon absorption causes the silicon to give up a valence electron and move it into the conduction band. The photons in the energy range 1.1 to 4 eV generate a single electron-hole pairs, whereas those of higher energy produce multiple pairs. Once electrons have been freed to the conduction band, they are collected and held in a place until readout occurs. When the exposure is over, CCD readout begins, such that the charge stored within each pixel is electronically shifted in a serial fashion along columns from

Table 2.2: Brief details about the detectors used

CCD Attached to	Sampurnanand Telescope	Himalayan Chandra Telescope	Kiso Schmidt Telescope
Size	2048×2048 pixel ²	2048×4096 pixel ²	2048×2048 pixel ²
Type	SI424AB-2	SITe ST-002	TK2048E
Pixel size	24×24 μ ²	15×15 μ ²	24×24 μ ²
Operating Temp.	160 K	173K	~ 150 K
Readout noise	13.7 e ⁻ (high speed) 5.3 e ⁻ (slow speed)	4.8 e ⁻	23 e ⁻
Camera gain	10 e ⁻ /ADU	1.22 e ⁻ /ADU	3.4 e ⁻ /ADU
Dark current	< 10 ⁻⁵ e ⁻ /pixel/sec	< 10 ⁻⁴ e ⁻ /pixel/sec	1 e ⁻ /pixel/60 min
Field of view	~ 13' × 13' at Cassegrain focus	~ 10' × 10' at Cassegrain focus	~ 50' × 50' at Schmidt prime focus

one CCD pixel to another throughout the array. The charge collected within each pixel is measured as a voltage and converted into an output digital number within a device called an analog-to-digital converter. The output digital number are usually stored in computer memory.

CCD must be cooled if the integration time is more than a few seconds to avoid the silicon's self-generated dark signal filling the potential well. CCDs used for the present observations were cooled to about -110°C in a liquid nitrogen dewar. A brief description about the CCD detectors used for the observations is given in Table 2.2. The output of the CCD is in digital form and hence it can be stored, copied and transported, thus these can be processed and analysed with the help of computers.

2.2.4 CCD Observations

In order to ensure the quality of the data, the observations were carried out only when the sky was cloud free and weather conditions were stable. We observed target BRCs and associated cluster when their elevations exceeded 30 degree. Efforts were made to observe each image within one or two hours of the meridian to minimize the effect of atmospheric extinction. Majority of the observations were obtained while the sources were higher than 45 degree above the horizon. In the same conditions we also observed standard star frames to calibrate the photometric observations. Bias frames were acquired at regular intervals during

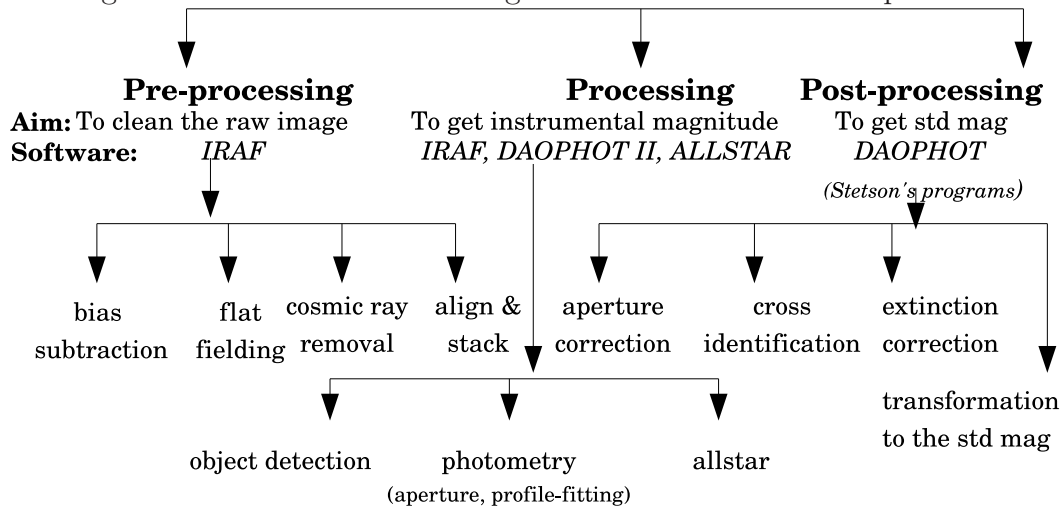
the observational nights. We also procured flat fields on each night using the dawn/dusk observations in the case of ST and HCT, and dome flats in the case of KST. To ensure, that all the measurements taken from the images fall in the “linear” response region of the CCD, we tried to set the exposure times in each filter in such a way that brightest star recorded had pixel intensities less than about 50% of the saturation level of CCD. But in some long exposure frames where our aim was to achieve the deepest photometry we exceeded the above mentioned limit. We also observed many short exposure frames to obtain the photometry of those bright stars that were saturated in long exposures. We took some images at a number of air-masses to determine the nightly extinction coefficients. In the case of cluster region to determine the contamination due to the field stars, a nearby field region is also observed along with the cluster region. To improve the S/N ratio, observations at the ARIES, Nainital were taken in the 2×2 binning mode.

2.2.5 CCD Data Reduction Strategy

CCD images as received directly from the telescope are raw images. These images need to be reduced (also called processing) to extract useful information like position, luminosity and image shape of the objects present on the frame. This reduction of CCD data is necessary because the combination of atmosphere, telescope, the CCD itself and its associated electronics tend to degrade the image. Strong atmospheric turbulence, poor focusing or the presence of charge diffusion in the detector can cause image spread. The optical system can also deform the image (geometric distortion). Moreover, the CCD is affected by different noises which are superimposed on the image. Extracting useful information from this kind of environment is one of the main purposes of image reduction.

The basic operation of data reduction involves mathematical manipulations like: addition, subtraction, multiplication or division of a frame by another frame or by a constant and numerous other manipulations like logarithms, statistics, smoothing, contouring and magnitude calculations etc. To carry out these tasks several image processing (data reduction) packages have been developed worldwide to name a few, *MIDAS*, *IRAF*, *DAOPHOT* etc.

Figure 2.1: A chart summarizing the whole data reduction procedure.



In following subsections the data reduction methods used for the interpretation of CCD images have been discussed. There are three basic stages of image processing in the case of photometric measurements, which may be called **Pre-processing**, **Processing** and **Post-processing**. The whole procedure of data reduction can also be summarized in the form of chart as given in Fig. 2.1

2.2.5.1 Pre-processing

The procedure of rectification of raw data (which may contain blemishes, bad pixels or columns or tiny specks due to cosmic rays) from the detector into something which represents actual intensity measurement is called pre-processing and is a highly interactive process that necessitates the image to be displayed at each step. We have used IRAF package for pre-processing. The various steps involved are :

I. Bias subtraction

The CCD has a d-c offset voltage which gets recorded along with the image.

Bias is a zero exposure image with camera shutter closed, also called Zero-frame which contains information of the d-c voltage applied to the CCD chip. The purpose of the bias frame is to allow the user to determine the underlying level within each data frame. The bias value in a CCD image is usually a low spatial frequency variation throughout the array, caused by the CCD on-chip amplifiers. A bias frame contains both the DC offset level and the variations on that level. A single bias frame will not sample these variations well in a statistical fashion, therefore number of bias frames were acquired at regular intervals and then they are combined to make master bias frame by averaging and simultaneously using a rejection algorithm to reject cosmic ray events. To remove the d-c voltage from the images, the master bias frame was subtracted from the each flat and program frame.

II. Flat Fielding

All the pixels in the CCD do not necessarily have the same response, though ideally all pixels are supposed to have the same sensitivity. Thus the resulting images present spatial noise because adjacent pixels do not react in a similar way to identical incident fluxes. Pixel to pixel variations in the sensitivity can be of the order of 10 to 20% of the mean sensitivity. Correction of non-uniform sensitivity is obtained by acquiring an image made on a uniform background (either on sky or dome), known as a flat field and then dividing the program frame by this flat field frame after normalization. Buil (1991) shows if $I(x, y)$ is the image to be corrected for non-uniformity and if $F(x, y)$ is the flat-field, then the processed image will be $E(x, y) = K(I(x, y)/F(x, y))$ where the multiplier coefficient, K , allows us to approximately find the initial level of the processed image. The value of K is equal to the average intensity of the flat field. It is absolutely essential that the uniform image to be acquired under conditions identical to those of the image to be processed, i.e., the same CCD, the same telescope and the same filter.

Flat field calibration frames are needed for each wavelength and different instrumental setup Flat field exposures are used to correct for pixel to pixel variations in the CCD response. In order to reduce statistical fluctuations at

least 5 or more flat field frames are taken and median averaged to produce the final flat used for image calibration.

The simplest and safest method to acquire flat-fields was to point the telescope at the sky background during twilight hours because at this hour the sky was just right to give dense flat image with a few seconds exposure. The ideal time period within which the flat fields could be observed always remained short because the twilight duration is no longer than half an hour. If it is too dark, the exposure times are long and stars start appearing. Some times when sky was already dark, a few stars also appeared on the flat-field. To overcome this problem, we took several flat-field observations each time displacing the telescope by a few arcsecs in a random way to change the stellar field and kept the telescope drive on to avoid the trailing of stars. These stars were eliminated by combining flat field frames using median option. Flat-fields in a given filter having approximately similar levels of counts were averaged after subtracting bias and then normalized to make a master flat. These master flats are then used to flat field the program images.

III. Dark correction

Like other detectors, CCDs also generate some charges due to thermal fluctuations. The counts registered on the CCD with its shutter closed for the same exposure time as that of object frame is called the dark counts. Since the thermal dark current undergoes a very rapid decay with decreasing temperature, a drastic reduction in dark current can be achieved by cooling the CCD to a temperature somewhere between those of dry-ice and liquid Nitrogen. Hence, the CCD was kept in an evacuated dewar, which was cooled by a liquid nitrogen to $\sim -120^\circ$ C. At this temperature, the thermal dark was found to be less than a few counts for an exposure of 30 min, which was considered negligible. Therefore the dark correction is not applied in the present study.

IV. Removal of cosmic Rays

On displaying the object frame we usually notice a few bright specks in addition to stars. These are cosmic ray events and their removal is the next step in pre-processing. Its intensity profile is different from the stellar profile and this property is used for their removal by the software.

V. To align and combine program images

In order to increase signal to noise ratio, we combined images of program field in each filter. But before combining, we had to align them with respect to a reference image. The *IRAF* software uses the center co-ordinates of common stars in two images and calculates the transformation co-efficients. This transformation was then applied to align the images which were to be combined. Images were combined by taking the corresponding pixels in all the images.

The pre-processing described so far resulted in a final combined clean images which we used for further processing. Utmost care had been taken to obtain clean images as any blemishes left on the frame would be carried over in to further reduction and might affect the photometric quality. The cleaned images were displayed and closely scrutinized for any blemishes or bad pixels. Before proceeding further, they were removed.

2.2.5.2 Processing

After removing the CCD characteristics and getting a clean image using pre-processing steps, the second stage would be the main processing which may be termed as photometry and involves the extraction of stellar positions and magnitudes from a given CCD image. DAOPHOT II is used to perform the photometry of individual stellar images recorded on the object frames. DAOPHOT II is the revised version of Dominion Astrophysical Observatory Photometry software by Stetson (1987). The different steps involved in processing are as follows

I. Object Detection

The primary task which we performed was to detect star like objects above a certain detection level, rejecting bad pixels, rows and columns etc in the frame. This can be done interactively if there are only a few stars in the frame. But as our frames were very crowded, we used automatic detection algorithm of DAOPHOT package called 'FIND' which:

1. Detects and locates small, positive brightness enhancement within an image.
2. Distinguishes stellar images from random noise peaks in the data, images of galaxies or other extended objects and cosmic rays or any high energy particles.
3. Recognizes when a seemingly extended object consists of two or more overlapping stellar images.

FIND routine convolves the image to locate a star in a pixel by fitting an analytic Gaussian profile (whose full width at half maximum (FWHM) is equal to the FWHM of the objects) to the brightness values of surrounding sub-array of pixels. It tries to locate stars by going through pixel by pixel and looking for locations where the Gaussian profile fit is good, i.e., where the central height of the best fitting model Gaussian profile achieves a large, positive value probably lies near the center of star image. In this way FIND identified the X and Y position of stars in the frame and cataloged then in a file.

II. Photometry

Next step involves doing the photometry which gives instrumental magnitude of the stars detected by FIND routine as mentioned above. Photometry is the process of obtaining quantitative (numerical) values for the brightness of objects. Two basic procedures for obtaining photometric data from CCD are : Aperture Photometry and Profile Fitting Photometry.

Aperture photometry

The total amount of counts belonging to the star gives the magnitude of that star. For bright uncrowded stars this can be accomplished by aperture photometry where the counts in a given box centered around the star are integrated and the counts in an equal area near the vicinity of the star (star free area) are subtracted from the former. The resulting counts corresponding to the particular star can be easily converted to magnitude. We have performed aperture photometry using the ‘PHOT’ routine of DAOPHOT II. The routine allows to specify a series of 12 increasing concentric apertures and an annulus to evaluate the sky. The sky value (i_{sky}) per pixel determined was an estimate of the mode of the intensity values of pixels in the annulus. The magnitude of the star corresponding to any aperture was determined by summing the data inside that aperture and from the relation, $m = zpt - 2.5\log I$, where zpt is the arbitrary zero-point and $I = (\sum I_{ij} - n_{pix}i_{sky})$ is the intensity of star. A plot of derived instrumental magnitude versus the radius of aperture yields a curve of growth. Faint objects are best measured with a small aperture but bright stars usually need a larger aperture. The final instrumental mag achieved by curve of growth was obtained using DAOGROW routine. The aperture photometric technique is unable to provide accurate magnitudes of faint as well as overlapping stars and thus can not be used for precise photometry of stars in cluster field. For the Landolt (1992) standard field aperture photometry was performed because most of the standard stars are bright and isolated.

Profile Fitting Photometry

In star clusters where crowding is more, it may not be possible to define an aperture which is large enough to contain all of a star’s flux while entirely excluding the flux of neighbors. For dealing with faint stars against noisy background and stars in crowded regions model-profile fitting offers the best possible recovery of photometric information for stellar objects. Point spread function (PSF) represents the actual recorded shape of a point source, on the detector. The method relies on modeling the image rather than summing over the image. In a given CCD frame where all the stars are observed at same time and in identical

2.2 Optical Observations and Data Reduction

observing conditions they would have the same profile and same form and differ from one another only in intensity by a scaling ratio. This property of the image is the basic principle of profile fitting photometry. In the case of a perfect telescope and in the absence of atmosphere (e.g., in the case of space telescope) the image can be represented by profile emerging from diffraction pattern. However, in ground based observations the stellar image is affected by the irregularities of the instrument (telescope observations, tracking errors, camera optics etc.) and the seeing. So the approach is to determine a point spread function from the stars themselves in a given frame. A number of approaches are used to determine the PSF.

The profiles of astronomical point sources that are imaged on two dimensional arrays are commonly referred to as PSFs. In order to perform measurements on such images, the method is profile fitting. PSFs can be modeled by a number of mathematical functions, in particular following three have been found to be useful in describing the stellar brightness profile (Stetson 1989). They are

$$\text{Gaussian} \quad G(r; a) \propto e^{-\frac{r^2}{2a^2}},$$

$$\text{modified Lorentzian} \quad L(r; a, b) \propto \frac{1}{1+(r^2/a^2)^b},$$

$$\text{and Moffat} \quad M(r; a, b) \propto \frac{1}{(1+r^2/a^2)^b},$$

representations, where r is the radius and a and b are fitting parameters (Stetson 1989).

These types of functional forms can be used to define the PSF for a star within an image by the assumption that they provide a good representation of the data itself and the method is called analytical. For our CCD frame, we used Gaussian analytical function because the χ^2 value in fitting this function is less than 0.05. This analytical method has the advantage of integrating numerically over the entire stellar image but the problem being that the function used to fit the profile can only be approximated. The other PSF method is known as empirical where it is possible to simply store the observed profile of several bright stars as a data array $O(i, j)$. The empirical method has the advantage that it uses

the observed profile, but the drawback in this case is that near the central region of the stellar image, the brightness varies too rapidly between the adjacent pixels to be interpolated correctly. Therefore, the better results can be obtained by combining both the methods. In the present analysis, we have used **ALLSTAR** program of **DAOPHOT** where PSF is determined by a combination of both empirical and analytical methods (for details see Stetson 1987).

To determine point spread function for our frames we used Gaussian PSF routine of DAOPHOT. Using this routine we first identified a few fairly isolated bright stars in the frame and determined the PSF iteratively by detecting and deleting the neighbors present inside the PSF radius. We repeated the procedure till we got the few isolated stars devoid of neighbors. With the help of these stars final PSF was determined and we took utmost care in selecting such stars because a star should not be used to define PSF if there is either a neighbor within one fitting radius or bad pixels within the profile of the star.

Photometry of all the stars present in a frame

The PSF obtained by the above method was applied to all the stars with aperture photometry using the routine ALLSTAR. This technique uses deconvolution procedure for magnitude determination of overlapping stellar images. It is therefore effectively used accurate photometric work in star clusters. In order to ascertain whether all the stars have been detected and measured, the measured stars were subtracted from the frame by using the option of ALLSTAR. This option uses the PSF file and the above file obtained after PSF photometry and outputs an image display. If there were stars still left in the picture then we detected them manually and repeated the whole procedure of photometry till we got the clean residual image. The output of ALLSTAR gave us the final x and y pixel positions of the stars, their magnitudes with errors, sharpness, roundness value and χ value of PSF fitting. The estimated errors in the magnitude determination were used to reject the bad measurements.

2.2.5.3 Post-processing

Now, the astronomical images obtain during our CCD run has been reduced to a list of stars with known positions and their apparent instrumental magnitudes relative to an arbitrary zero point. They need to be converted to the standard magnitude indices. Essential steps related to this are as following:

I. Aperture correction

Aperture photometry is performed for several selected, bright, isolated stars in each CCD frame using a series of apertures of increasing size. In profile fitting photometry, the instrumental magnitude of a star comes from the height of a model point-spread function for that frame scaled to the intensity values recorded inside the stars image. This magnitude is restricted to the aperture chosen and has to be corrected for the counts left out in the wings of the stellar profile. The correction from profile fitting magnitudes to aperture magnitudes were carried out by the process of determining aperture growth curve. This correction is known as **aperture correction** and applied to the PSF magnitudes to get the aperture instrumental magnitudes. This is done by **DAOGROW** routine (see Stetson 1990 for details).

II. Cross Identification

For determining the standard magnitudes and colours, we have to cross-identify the stars of different frame and different filter. For this purpose, **DAO-MATCH** programme is available in **DAOPHOT II**. This programme attempts to recognize triangles of stars, exploiting the fact that while their positions, orientations and sizes may change triangles won't change shape as they are translated, rotated and scaled. It considers brightest star first, since these are the most detectable objects in the field. This programme consider only 30 brightest stars between the two frames and provides the coordinate transformation equations between the various frames with respect to a reference frame. In this way, it is

not possible to cross-identify each star in a field. Therefore another programme **DAOMASTER** is used to identify all stars. This programme accepts the approximate transformation equation provided by **DAOMATCH**, reads in all the star lists for that field and cross-matches all stars by spatial proximity: if after transformation to the coordinate system of the master frame, a star lies within the specified distance of a star in the master list, it is provisionally identified with that star; if it lies near no star in the master list it is added to the list as a possible new detection.

III. Transformation to the standard system

Now, we have to transform the instrumental magnitudes to the standard magnitudes. For this purpose the transformation equations are as follows.

$$\begin{aligned}
 u_{CCD} &= U + a_0 + a_1(U - B) + a_2X \\
 b_{CCD} &= B + b_0 + b_1(B - V) + b_2X \\
 v_{CCD} &= V + c_0 + c_1(B - V) + c_2X \\
 i_{CCD} &= I + e_0 + e_1(V - I) + e_2X
 \end{aligned}$$

Where a_0 , b_0 , c_0 , d_0 and e_0 are the zero points; a_1 , b_1 , c_1 , d_1 and e_1 are the colour coefficients; a_2 , b_2 , c_2 , d_2 and e_2 are the earth's atmospheric extinction coefficients and X is the airmass. U , B , V , R and I are the standard magnitudes and u_{CCD} , b_{CCD} , v_{CCD} , r_{CCD} and i_{CCD} are the aperture instrumental magnitudes. We have ignored the second order colour correction terms as they are generally small in comparison to other errors present in the photometric data reduction.

For calibration purpose, we observed standard fields of Landolt (1992) The stars used for calibrations cover a wide range in brightness as well as colour. The standard field are also observed in U , B , V , R and I filters at different air-masses to obtain a reliable estimate of the atmospheric extinction coefficients. Using the transformation equations and **CCDSTD** routine in **DAOPHOT II**, we determined the values of transformation coefficients.

Using the transformation coefficients and the standard values from Landolt (1992), we generate secondary standards in the cluster frames. For generating

the secondary standards, we used **CCDAVE** routine in **DAOPHOT II**. In this way, a list of secondary standards are created to transform the cluster stars. The final transformation of all the cluster stars is done by the **FINAL** routine. This routine redetermine the photometric zero points of each frame from the local standard stars. By re-correcting all frames to a single consistent zero point, one can find an accurate photometry. In this way, we have a list of number of stars having positions, standard magnitudes and colours which are present in our CCD frame.

2.3 Grism slit Spectroscopy

Optical spectrum of a star is obtained using HFOSC of HCT, Hanle in a two-dimensional array. The long slit spectroscopic data consists of bias frames, flat frames, calibration frames and object frames. The object frames contain the spectral image of the star focused at a slit. This image is made to disperse on the CCD along a particular direction known as the *dispersion axis*, which is parallel to the slit width direction when the CCD axis is properly aligned with the slit axis. In order to avoid any degradation of resolution as well as the sky background contribution, the slit widths are usually kept equal to the full width at half maxima of the star's seeing limited image. The pixel along the *dispersion axis* are measured in wavelengths units, while the pixels along the spatial axis in photon counts. In order to convert these pixels and counts in wavelength and flux respectively, calibration frames are required. Arc frames and standard star frames are required for wavelength and flux calibration respectively.

2.3.1 Extraction of the optical spectrum

Spectroscopic data reduction has been done using *IRAF*. The pre-processing steps like bias subtraction, flat fielding and cosmic ray rejection are similar to those discussed in the case of photometric data reduction. The one dimensional spectra are extracted using *APALL* task in *IRAF*, which is based on the extraction algorithm by Horne (1986). This task eliminates the sky noise, delivers

maximum possible signal-to-noise ratio and takes care of the effects of moderate geometric distortion.

The one dimensional spectrum is in the form of intensity versus pixel number. In order to calibrate the pixel number in terms of wavelength, it is necessary to take spectra of a laboratory standard source (e.g., Fe-Ar and Fe-Ne arc lamp). For such a standard source, wavelength of different spectral features such as emission is known. The wavelength calibration is done using *IDENTIFY*, *HEDIT* and *DISPCOR* tasks in *IRAF*. Usually a high order polynomial is employed to fit the identified pixels against wavelength. Flux calibration is performed using the tasks *STANDARD*, *SENSFUNC* (used to fit a polynomial to the observed magnitude as a function of wavelength after applying extinction correction in the standard and programme star spectra) and calibrated.

2.4 Archival datasets

2.4.1 Near-infrared data from 2MASS

The near-IR data are taken from the digital Two Micron All Sky Survey (2MASS) available at web site <http://www.ipac.caltech.edu/2MASS>. This survey has been carried out with two identical highly-automated 1.3-meter aperture, open-tube, equatorial fork-mount telescopes. One is the northern telescope which is located at 2306 meters elevation in Arizona (N 31° 40' 50".8, W 110° 52' 41".3) and second one is the southern telescope which is at 2171 meters elevation in Chile (S 30° 10' 3".7, W 70° 48' 18".3). Both telescopes have Cassegrain focus mount for the infrared cameras. During survey mode the telescope moves continuously in declination at approximately 57"/second, while tracking in hour angle at the sidereal rate.

Each telescope is equipped with a three-channel camera. Each camera consists of a liquid nitrogen cryostat which contains three NICMOS3 arrays. During the observations each array views the same region of the sky. The detailed description of the 2MASS camera optical design is given in Milligan et al. (1996). In the 2MASS survey three band-passes are used namely *J* (1.11-1.36 μm), *H* (1.50-1.80 μm) and *K_s* (2.00-2.31 μm). When camera mounted on the 2MASS telescopes

each pixel subtends approximately $2''.0$ on the sky. The gain of the 2MASS electronic is approximately 8 electrons per analog-to-digital count and read out noise is 40 electrons.

The 2MASS data base provides photometry in the near infrared J , H and K_s bands to a limiting magnitude of 15.8, 15.1 and 14.3 respectively, with a signal to noise ratio (S/N) greater than 10. We retain only those sources for which the error in each band is less than 0.1 mag to ensure better photometric accuracy.

2.4.2 Mid-infrared data from *Spitzer* Space Mission

2.4.2.1 Telescope and Instruments

Spitzer space telescope is the fourth mission in Nasa's 'Great observatories program'. Launched in space in August 2003, it has 0.85-m telescope equipped with 3 cryogenically- cooled science instruments operating in wavelengths between 3 to 160 μm . The three instruments on board are : the Infrared Array Camera (IRAC, Fazio et al. 2004) operating at four wavelengths (3.6, 4.5, 5.8, 8.0 μm , called 'channels 1, 2, 3, 4' respectively), the Multiband Imaging Photometer (MIPS, Rieke et al. 2004) at 24, 70 and 160 μm and the infrared Spectrograph (IRS, Houck et al. 2004) have four separate modules working at low and high resolution mode. The brief description of the telescope and the instrument used is given in table 2.3 and table 2.4, respectively.

IRAC provides images at 3.6, 4.5, 5.8 and 8.0 μm , with two adjacent $5.2' \times 5.2'$ fields of view. One field of view images simultaneously at 3.6 and 5.8 μm and the other at 4.5 and 8.0 μm via diachronic beam splitters. All four detector arrays are 256 x 256 pixels with 1.2 arcsecond square pixels.

2.4.2.2 Data Reduction

The IRAC images were processed by the *Spitzer* Science Center (SSC) using a standard pipeline to produce basic calibrated data (BCD) images. The SSC pipeline produces BCD images that have subtracted the dark and bias levels from the raw data, followed by flat-fielding and sky subtraction. In the BCD images, any instrumental signatures, bad pixels (those with a typical sensitivities), and pixels saturated by very bright sources have been identified within mask files.

Table 2.3: Summary of *Spitzer* Characteristics

Aperture (diameter)	85 cm
Orbit	Solar (Earth-trailing)
Cryogenic Lifetime	5.5 years (est.); 5.7 years actual
Wavelength Coverage (passband centers)	3.6 – 120 μm (imaging) 5.3 – 40 μm (spectroscopy) 55 – 95 μm (SED)
Diffraction Limit	5.5 μm
Image Size	1".5 at 6.5 μm
Pointing Stability (1, 200s, when using star tracker)	<0".1
As commanded pointing accuracy (1 radial)	<0".5
Pointing reconstruction (required)	<1".0
Field of View (of imaging arrays)	$\sim 5' \times 5'$ (each band); at 160 μm a single field of view 0".053 x 5".33
Telescope Minimum Temperature	5.6 K (cryo); 27.5 K (post-cryo)
Maximum Tracking Rate	1'.0/ sec
Time to slew over 90	~ 8 minutes

Table 2.4: Brief details about the detectors used

λ (μm)	Array type	$\lambda/\Delta\lambda$	Field of view	Pixel size (arcsec) confusion)	Sensitivity (μJy) (5 σ in 500 sec, including
3.6	InSb	4.7	5'.21x5'.21	1.2	1.6 (3.4)
4.5	InSb	4.4	5'.18x 5'.18	1.2	3.1 (4.3)
5.8	Si:As(IBC)	4.0	5'.21x5'.21	1.2	20.8 (21)
8.0	Si:As(IBC)	2.8	5'.18x5'.18	1.2	26.9 (27)

Overall flux calibration, expressed in physical units of MJy/sr/Å, is estimated by the SSC to be accurate to within 10%. With each astronomical observation request (AOR), the SSC releases two mask files (*pmask* and *imask*) that identify most pixels affected by various peculiarities. The purpose of the *pmask* is to identify pixels that are permanently damaged, that exhibit dark currents or sensitivities that are consistently either too variable or extreme to be reliable. The purpose of the *imask*, on the other hand, is to identify pixels that are affected by various peculiarities, some of which do not render a pixel non-usable or “bad”. One *pmask* is sufficient for each band in an AOR, while a *imask* is released for each IRAC BCD image.

The BCDs is downloaded from the *Spitzer* archive using *Spitzer* Science Center’s software *Leopard*. Three artifacts occurring near moderately bright sources, **muxbleed**, **pulldown**, and **banding features**, are corrected to the extent possible in the image processing.

Muxbleed: These effects appear in InSb arrays when a bright source is read out and the readout multiplexers in the cold electronics do not return to their quiescent state for a considerable length of time. The result is a ghosting along the pixel readout channels, and appears that a pixel bleeds only as a result of the light falling onto it. The muxbleed flux is not real, so can be corrected by knowing the readout order of the pixels, by correcting all pixels downstream from the first pixel, and then move on to the next pixel. The generalized solution is to correct this effect by a look up table.

Bandwidth Effect: The bandwidth effect appears in IRAC channels at 5.8 and 8.0 μm . It looks like a decaying trail of pixels 4, 8, and 12 columns to the right of a bright or saturated spot. Due to the design of the IRAC electronics, there is a maximum rate at which they can react to changes in pixel intensity during readout. The effect is nonlinear except in the weakest cases. Currently, there is no correction for this effect. Hence, it is recommended to use small apertures (< 4 pixels) for photometry of bright sources at 5.8 and 8 μm .

Column Pull-down/Pull-up : When a bright star or cosmic ray on the array reaches a level of approximately 35,000 data number (DN), there is a change in the intensity of the column in which the signal is found. In channels at 3.6 μm and 4.5 μm , the intensity is reduced throughout the column (thus the term

“column pull-down”). When the effect occurs, it shifts the intensities of the pixels above and below the position of the “guilty” source, within the same column. Column pull down has been corrected in the cryogenic IRAC data BCD files. The code estimates the “true” sky value for the affected pixels and fits a DC offset, which is in general a different constant above or below the offending bright source. There are also other minor effects such as: Full Array Pull-up, Persistent Images, Stray or Scattered Light, Optical Banding and Internal Scattering and Optical Ghosts. These effects are also taken care by IRAC pipelines. For more information, see IRAC Data Instrument Handbook (Reach et al. 2005). While the pipeline-reduced BCD files are mostly artifact-free, some residual artifacts may remain.

Muxbleed occurs in the rows on which these sources are positioned in band 1 and band 2 images; banding occurs in the rows in band 3 and band 4 images. Pulldown, primarily seen in band 1 and band 2 images, occurs in the columns containing moderately bright sources and is corrected in all IRAC bands.

2.4.2.3 Mosaicking and Source Extraction

To create mosaics from individual BCDs the SSC’s “Mosaicking and point source extractor (Mopex)” software suite (Makovoz & Marleau 2005) is used. This is comprised of a number of modules that are typically used sequentially from Perl scripts. The overlap module is used to determine the best common background value at points of overlap between frames (because the precise background level in IRAC frames is uncertain due to the lack of contemporaneous dark frames and inoperability of the IRAC shutter). The outlier detection modules, together with the natural redundancy in the data set is used to mask out all but the faintest radiation hits. The mosaics are produced with a 1:1 pixel ratio (i.e., native pixel size of 1.2") relative to the input BCD frames.

Since, the IRAC pipeline returns the individual exposures calibrated in physical units of surface brightness (MJy/Sr), mosaicked image is converted to DN by applying the flux conversion factor which is given in the individual BCDs header. A number of astronomical standard stars are observed in each instrument campaign to obtain a relative flux calibration. Stars with a range of spectral indices

2.5 Basic Assumptions and Analysis Techniques Used

and fluxes are observed at a number of positions across the array and many times throughout the mission to monitor any changes that may occur. To calculate Vega magnitudes from the calibrated IRAC images, the zero-magnitude fluxes 277.5, 179.5, 116.6, and 63.1 Jy are used for channels 1, 2, 3, and 4, respectively. These fluxes were calculated from the IRAC throughput values and the absolute spectra at IRAC wavelengths (Cohen et al. 2003).

For all the data presented here, the threshold is set such that the faintest objects typically had a signal-to-noise ratio, $S/N > 7$. The final source extraction list is produced in a two-step process, first running *DAOFIND* task of *IRAF* on the relevant mosaic and then using the extraction list from that step as an input to *PHOT* task to obtain the positions and fluxes of the sources that are found from the mosaic with its higher S/N. The zero point magnitudes for the IRAC data were adopted for the standard aperture radius ($12''$) and background annulus of ($12''.2 - 22''.4$) of 19.67, 18.93, 16.85 and 17.39 in the channels 1, 2, 3 and 4, respectively.

The short integration frames are used to replace likely saturated sources in the longer integration frames. Avoiding background contamination is particularly important in IRAC 3.6 and 8.0 μm bands, because the polycyclic aromatic hydrocarbon (PAH) emissions are highly structured. Hence we prefer smaller aperture. Also the objects studied are crowded fields therefore in order to avoid contaminating flux from other nearby sources, a smaller source aperture with a radius of 3 pixels and annuli of 4 pixels are used. *PHOT* task of *IRAF* software is used for the aperture photometry of the studied objects. The resulting photometry was calibrated using large aperture in-flight measurements of standard stars, with an appropriate aperture correction in each channel to correct for the smaller apertures used in our study.

2.5 Basic Assumptions and Analysis Techniques Used

In this section, the basic assumptions made in order to determine the memberships, reddening, NIR of the YSOs and basic parameters of the cluster associated

with HII region has been discussed.

In section 2.5.1 the procedure to determine the structural parameters of the cluster and in the section 2.5.2, the methods to identify YSOs in BRC regions using H α emission and near- to mid-infrared observations and also their membership criteria have been discussed. Section 2.5.3 describes the method to determine A_V and NIR excess $\Delta(H - K)$ of the individual YSO candidate using NIR $(J - H)/(H - K)$ colour-colour (CC) diagram.

2.5.1 Basic parameters of the cluster

2.5.1.1 Determination of the cluster centre

To study the shape of the cluster, the first necessary step is to identify the cluster center. Various authors define and calculate the center in different ways. The point where the number density is the maximum is called the density center of the cluster and where the luminosity density is maximum is called the mass center. To calculate the density center, weighted average of the positions of all stars is considered by von Hoerner (1960, 1963) and marginal distribution of all measured stars by Kassis et al. (1996). Moitinho et al. (1997) estimates center by convolving a Gaussian kernel with the star distribution and taking center to be the point of maximum number density. Sagar et al. (1988) choose the cluster center as the point of maximum stellar number density in the stellar density versus α and δ plots and conclude that number density center differs by mass density center by an arcmin or less, which may be the maximum error in locating the center.

In the present study, to derive the center we assume a spherical symmetry for the cluster. The center of the cluster is determined using the stellar density distribution of stars in a ± 100 pixels wide strip along both X and Y directions around an eye estimated center. The point of maximum density, obtained by fitting a Gaussian curve, is considered as the center of the cluster. An error of few arcsecs is expected in locating the cluster center.

2.5.1.2 Stellar radial density profile (RDP)

To determine the radial surface density, the cluster was divided into a number of concentric circles with respect to the above estimated cluster-center in such a way

2.5 Basic Assumptions and Analysis Techniques Used

that each zone contains a statistically significant number of stars (generally more than 20). Projected radial stellar density in each concentric circle was obtained by dividing the number of stars in each annulus by its area. The stellar surface density ρ_i in the i th zone is defined as:

$$\rho_i = \frac{N_i}{A_i} = \frac{N_i}{\pi(R_i^2 - R_{i-1}^2)} \quad (2.1)$$

where N_i is the number of stars in the i 'th annulus, A_i is the area of i 'th annulus whose outer and inner radii are R_i and R_{i-1} respectively. The errors were calculated assuming that the number of stars in a zone is governed by Poisson statistics.

King (1962, 1966) has shown from theory and observations that three parameters are required to describe the structure of a cluster : a core radius, a limiting (tidal) radius and a richness factor that represents the internal energy of the system while the tidal radius is set by external tidal forces.

In Fig. 2.2, the solid continuous curve represents projected radial distribution of the apparent surface density $\rho(r)$ of a typical star cluster. Broken curve represents field star density (ρ_f). Because of the low S/N ratio in the star counts of open clusters, it is not an easy task to constrain the tidal radius of clusters using the empirical model of King (1962) therefore to parametrize the radial density profiles, we follow the approach by Kaluzny & Udalski (1992). We describe radial density $\rho(r)$ as

$$\rho(r) \propto \frac{\rho_o}{1 + \left(\frac{r}{r_c}\right)^2}; \quad (2.2)$$

where r_c is the core radius (the radius at which the surface density falls to half of the central density ρ_o). We fit above function to the observed radial density profile of stars. The best fit is obtained by χ^2 minimization technique. We have also used these profiles to calculate the extent of cluster ' r_{cl} ' which is defined as the point at which the radial density becomes constant and merges with the field density. The region between the cluster extent and the core region is called the corona of the cluster.

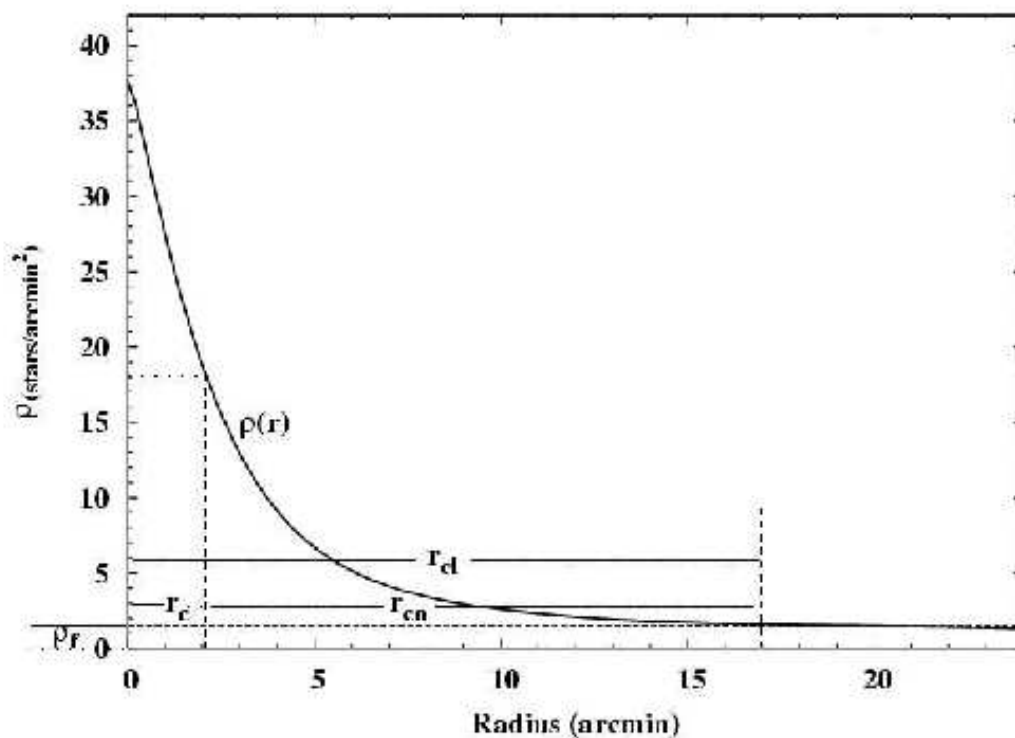


Figure 2.2: Radial distribution of the apparent surface density $\rho(r)$ of a typical star cluster (solid curve). Field star density is denoted by ρ_f . The r_c, r_{cn}, r_{cd} are core radius, corona and cluster extent respectively.

2.5.1.3 Reddening

A knowledge of interstellar reddening is necessary to determine intrinsic properties of the cluster stars. Reddening occurs because of absorption and scattering in the ISM. The effect of absorption and scattering is, in general, more efficient for shorter wavelengths. Thus red light is less extinguished than blue light in the transmitted beam coming from the stars, whereas the scattered component is predominantly blue.

The extinction in star cluster arises due to two distinct sources: (1) the general ISM in the foreground of the cluster [$E(B - V)_{min}$], and (2) the localized cloud associated with the cluster [$\Delta E(B - V) = E(B - V)_* - E(B - V)_{min}$], where $E(B - V)_*$ is the reddening of the star embedded in the parent cloud. The former component is characterized by the ratio of the total to the selective extinction

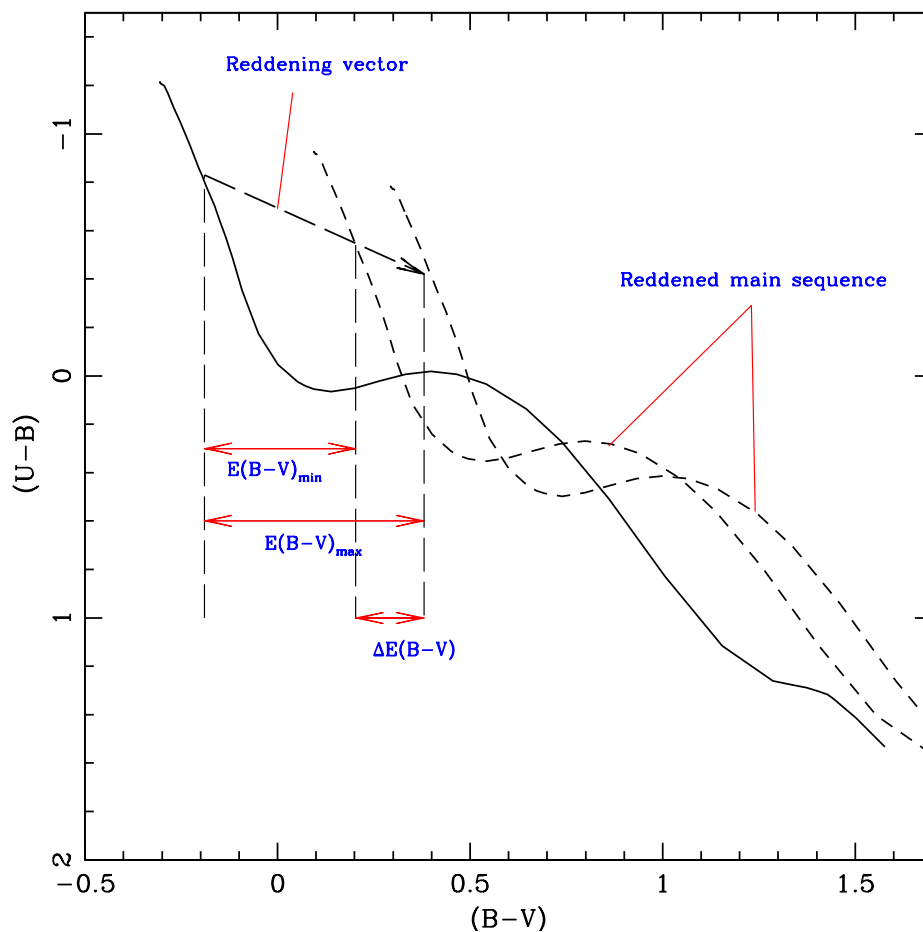


Figure 2.3: Schematic description of the method of measuring $E(B - V)$ in the $(U - B, B - V)$ diagram.

$R_V [= A_V/E(B - V)] = 3.1$ (He et al. 1995; Wegner 1993; Winkler 1997), whereas for the intra-cluster regions of young clusters embedded in dust and gas cloud the value of R_V varies significantly (Pandey et al. 2003; Tapia et al. 1991). However, HII regions associated with a large amount of gas and dust often show larger values of R_V (Chini & Wargau 1990; Forte 1978; Pandey et al. 2000; The & Groot 1983).

2.5.1.4 $U - B, B - V$ colour-colour diagram

In the absence of spectroscopic observations, the interstellar extinction $E(B - V)$ toward the cluster region can be estimated using the $(U - B)/(B - V)$ diagram (cf. Becker & Stock 1954). The reddened stars are found displaced with respect to unreddened stars of the same intrinsic colours in the direction of the reddening vector, given by the ratio of the colour excesses, i.e. $E(U - B)/E(B - V) = 0.72$ (cf. Johnson & Morgan 1953).

Therefore on comparing the $(U - B, B - V)$ CC diagram of MS stars for a reddened cluster with that of unreddened MS stars, one would expect that a reddened MS of the cluster stars is displaced from the unreddened MS in the direction of the reddening vector by an amount which is equal to the colour excess $E(B - V)$ in abscissa and the colour excess $E(U - B)$ in ordinate, as shown schematically in Fig. 2.3. Thus the interstellar reddening for the observed clusters can be determined using the slide-fit method. The photometric sequences of open clusters in the CC diagram exhibit different dispersions from one case to another. The causes of dispersion in the cluster sequence are differential interstellar reddening, stellar evolution, stellar duplicity, stellar rotation, difference in chemical composition, dispersion in distances, presence of non-member stars and the inaccuracies in data (Burki 1975). If one considers only the MS stars of the clusters, the various effects mentioned above (apart from differential reddening) can produce differential reddening $\Delta E(B - V) [\equiv E(B - V)_{max} - E(B - V)_{min}] < 0.11$ mag for the MS cluster stars having spectral types earlier than A0. Thus $\Delta E(B - V) > 0.11$ indicates the presence of non uniform extinction across the cluster. The minimum ($E(B - V)_{min}$) and maximum ($E(B - V)_{max}$) colour excesses are determined using the slide fit method as shown schematically in Fig. 2.3. The total visual absorption A_V is calculated using the relations:

$$A_V = R \times E(B - V), \quad (2.3)$$

where $R [\equiv \frac{A_V}{E(B - V)}]$ is total to selective absorption ratio having normal value 3.1.

2.5.1.5 Colour magnitude diagrams (CMDs)

The main tool used to study open clusters is the HR-diagram in which the star's luminosity is plotted as a function of its temperature. The original form of

the HR-diagram, based on the absolute magnitude and the spectral types, is equivalent to a photometric diagram of star cluster which displays the apparent magnitude as a function of colour index and the diagram is known as CMD. A colour index represents the ratio of the fluxes measured through two filters: for example, the widely used $(B - V)$ colour index results from the ratio of the fluxes in the blue B and visible V parts of the stellar energy distribution. Several photometric colour indices are closely related to the effective temperature and apparent magnitude which are in turn related to the luminosity of the stars.

2.5.1.6 Distance Estimation

The apparent V magnitude differs from the absolute magnitude by a constant which is called the distance modulus of the cluster. This quantity, denoted by $m - M$, is related to the distance d , expressed in pc, by the simple relation

$$V - M_V = 5 \log d - 5 + A_V, \quad (2.4)$$

where A_V represents the correction for the interstellar absorption in visual band. Assuming that stars of a cluster are situated approximately at the same distance, the distance modulus is obtained by fitting standard ZAMS on to the observed CMD of the cluster. Once the distance modulus and A_V are known, the distance 'd' to the cluster (in pc) can be calculated using the above equation.

2.5.1.7 Determination of photometric completeness

The photometric data may be incomplete due to various reasons e.g. crowding of the stars. The incompleteness correction is necessary if we want to analyze the luminosity function (LF)/ MF of the stars in the cluster. To determine the completeness factor we use the ADDSTAR routine of DAOPHOT II. This method has been used by various authors (cf. Pandey et al. 2005 and references therein). Briefly, the method consists of randomly adding artificial stars of known magnitude and position into the original frame. The frames are re-reduced using the same procedure used for the original frame. The ratio of the number of stars recovered to those added in each magnitude interval gives the completeness factor, CF, as a function of magnitude. In practice we added artificial stars to

both V and I images in such a way that they have similar geometrical locations but differ in I brightness according to mean $(V - I)$ colours of the MS stars. The luminosity distribution of artificial stars has been chosen in such a way that more stars are inserted into the fainter magnitude bins. In total about 15% of the total stars are added so that the crowding characteristics of the original frame do not change significantly. To have satisfactory statistics for the determination of CF, a number of independent sets of artificial stars are inserted into a given data frame. The minimum value of the CF of the pair thus obtained is used to correct the data for the incompleteness (cf. Sagar & Richtler 1991).

2.5.1.8 The sample to study the Mass Function

To study the LF/MF, it is first necessary to remove field-star contamination from the sample of stars in the cluster region. In the absence of a proper-motion study, we used a statistical criterion to estimate the number of probable member stars in the cluster region. Only on the basis of a single passband, we cannot decide whether the star is really a member of the cluster. Two passbands, such as V and I , are required to identify the cluster members. We used the $V/(V - I)$ CMD to estimate the number of probable members in the cluster region and to construct the LF of the cluster. To remove contamination of field stars from the MS and PMS sample, we statistically subtracted the contribution of field stars from the CMD of the cluster region using a nearby reference field. For a star in the $V, (V - I)$ CMD of the field region, the nearest star in the cluster's $V, (V - I)$ CMD within $V \pm 0.125$ and $(V - I) \pm 0.065$ of the field star is removed. While removing stars from the cluster CMD, necessary corrections for incompleteness of the data samples as well of the areas were taken into account. This statistically cleaned dereddened CMD is used to study the mass function of the cluster region.

2.5.2 YSOs associated with BRC regions

The aggregates associated with BRCs are very loose and are composed of a small number of stars. Since BRCs are found at low galactic latitudes, the fields can be significantly contaminated by foreground/background stars. To understand star formation in BRCs it is necessary to identify stars directly related to them. Since

2.5 Basic Assumptions and Analysis Techniques Used

embedded clusters are very young stellar systems, independent indicators of stellar youth, such as presence of circumstellar disks, variable emission lines, etc., can be employed to ascertain membership of individual stars. Spectroscopic surveys can be used to identify the members in the regions, however, such observation can be time consuming and even prohibitive for faint members. Circumstellar disks can be detected directly with infrared broad-band photometry as a readily measurable excess above the expected emission from a normal stellar atmosphere. We selected probable members associated with the BRCs using the following criteria.

2.5.2.1 $H\alpha$ emission

The spectra of some PMS stars, specifically TTs, show emission lines, among which usually $H\alpha$ is the strongest. Therefore, $H\alpha$ emission stars can be considered as good candidates for PMS stars associated with BRCs. In the present study we used $H\alpha$ emission stars found by Ogura et al. (2002) in the vicinity of BRCs.

2.5.2.2 Near-infrared excess

Since many PMS stars also show NIR excesses caused by circumstellar disks, NIR photometric surveys have also emerged as a powerful tool to detect low-mass PMS stars. To identify NIR excess stars from the 2MASS PSC, we used NIR $(J - H)/(H - K)$ CC diagram (cf. Fig. 2.4). The thin and long-dashed curves in Fig. 2.4 represent the unreddened MS and giant branches (Bessell & Brett 1988), respectively. The dotted line indicates the locus of intrinsic CTTSs (Meyer et al. (1997)). The curves are also in the CIT system. The parallel dashed lines are the reddening vectors drawn from the tip (spectral type M4) of the giant branch (“upper reddening line”), from the base (spectral type A0) of the MS branch (“middle reddening line”) and from the tip of the intrinsic CTTS line (“lower reddening line”). The extinction ratios $A_J/A_V = 0.265$, $A_H/A_V = 0.155$ and $A_K/A_V = 0.090$ have been adopted from Cohen et al. (1981). We classified sources into three regions in the NIR-CC diagrams (cf. Ojha et al. 2004a). ‘F’ sources are located between the upper and middle reddening lines and are considered to be either field stars (MS stars, giants) or Class III sources and Class II sources with small NIR excesses. ‘T’ sources are located between

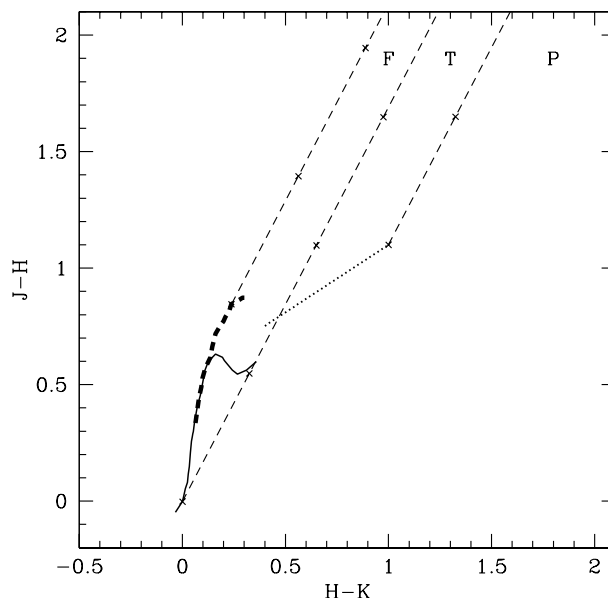


Figure 2.4: NIR $(J - H)/(H - K)$ CC diagram. The sequences for dwarfs (solid curve) and giants (thick dashed curve) are from Bessell & Brett (1988). The dotted line represents the locus of TTSs (Meyer et al. 1997). Broken straight lines represent the reddening vectors (Cohen et al. 1981). The crosses on the dashed lines are separated by $A_V = 5$ mag.

the middle and lower reddening lines. These sources are considered to be mostly CTTSs (Class II objects). There may be an overlap in NIR colours of Herbig Ae/Be stars and CTTSs in the ‘T’ region (Hillenbrand et al. 1992). ‘P’ sources are those located in the region redward of the ‘T’ region and are most likely Class I objects (protostar-like objects; Ojha et al. 2004b). So, objects falling in the ‘T’ and ‘P’ regions of NIR-CC diagrams are considered to be NIR excess stars and hence are probable members of the cluster. These sources are included in the analysis of the present study in addition to $H\alpha$ emission stars. It is worthwhile, however, to note that Robitaille et al. (2006) have recently shown that there is a significant overlap between protostars and CTTSs in the NIR-CC space.

2.5.2.3 Mid-infrared excess

Excess due to circumstellar disks and envelopes are most robustly measured at longer infrared wavelengths. In recent years, the *Spitzer* Space Telescope, oper-

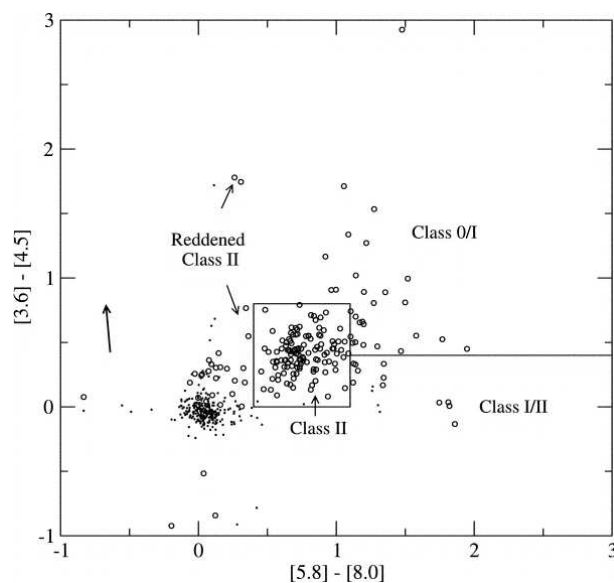


Figure 2.5: IRAC $[5.8] - [8.0]/[3.6] - [4.5]$ colour-colour diagram.

ating at mid- to far-infrared wavelengths, has provided the capability to survey and measure infrared excesses and circumstellar-disk emission with unprecedented sensitivity across the complete mass range of stars in the highly extinguished regions (e.g., Allen et al. 2007). YSOs occupy distinct regions in the IRAC colour plane; this makes MIR colour- colour diagram a very useful tool for the classification of YSOs. Whitney et al. (2003a) and Allen et al. (2004) presented independent model predictions for IRAC colours of various classes of YSOs. Fig. 2.5 presents a sample IRAC ($[5.8]-[8.0]$ versus $[3.6]-[4.5]$) CC diagram. The sources within the box represents the location of Class II objects (Allen et al. 2004; Megeath et al. 2004). The sources located around $[5.8]-[8.0]=0$ and $[3.6]-[4.5]=0$ are foreground/background stars, as well as diskless PMS stars (Class III objects). Sources with $[3.6]-[4.5]$ 0.8 and/or $[5.8]- [8.0]$ 1.1 have colours similar to those derived from models of protostellar objects with in-falling dusty envelopes (Allen et al. 2004). These are Class 0/I sources.

2.5.3 Reddening and NIR excess determination for the YSOs in BRC regions

2.5.3.1 Determination of A_V

Since BRCs are associated with the recent star forming activity. The presence of variable amount of reddening due to the dust and gas in the BRC and/or HII regions makes the reddening correction a difficult task. YSOs have peculiar colour indices, in particular $U-B$ colour due to ultraviolet excess (UV excess). Therefore the $U-B/B-V$ CMD cannot be used to estimate the amount of reddening for YSOs. In the case of $B-V/V-I_c$ CC diagram, the intrinsic line is nearly parallel to the reddening vector. Hence the $B-V/V-I_c$ CMD is practically not usable to estimate the amount of reddening. In order to overcome this difficulty we used the $J-H/H-K_s$ CC diagram, where A_V value for each star has been measured by tracing back to the intrinsic lines along the reddening vector found in Meyer et al. (1997). The E_{V-I_c} and E_{B-V} values from A_V values have been estimated using the following relations,

$$A_V = R \times E(B - V) \quad (2.5)$$

$$E(V - I)/E(B - V) = 1.25 \quad (2.6)$$

2.5.3.2 NIR Excess

NIR excess ($\Delta(H - K)$) of each YSO candidate is derived from the NIR CC diagram. $\Delta(H - K)$ is defined as the horizontal displacement of the NIR excess stars from the middle reddening vector in $(J - H)/(H - K)$ CC diagram (see Fig. 2.4).

2.5.4 Age determination of the YSOs

The age of each YSO was estimated by referring to the isochrones. In our analysis we have estimated age and mass of the YSOs using the $V/(V - I_c)$ CMD as discussed in Pandey et al. (2008). As an example, a $V/(V - I_c)$ CMD of young cluster Be 59 used for the age, mass estimation of the YSOs by Pandey et al. (2008) is shown in Fig. 2.6. Here, we would like to point out that the estimation of the age of the PMS stars by comparing the observations with the theoretical

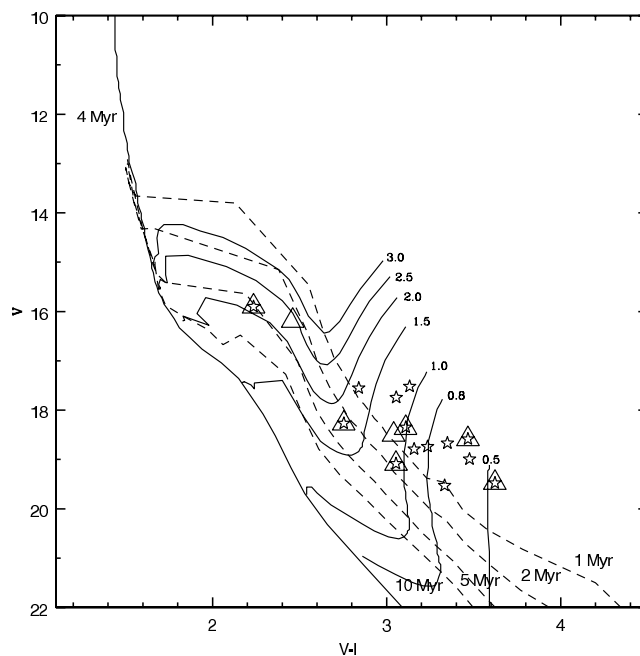


Figure 2.6: $V/(V - I)$ CMD for $H\alpha$ (star symbol) and NIR excess stars in Be 59 (Pandey et al. 2008). PMS isochrones for 1, 2, 5, 10 Myr (dashed line) along with evolutionary tracks of different mass stars by Siess et al. (2000) are also shown. All the isochrones are corrected for distance and reddening of the region.

isochrones is prone to two kinds of errors; random errors in observations and systematic errors due to the variation between the predictions of different theoretical evolutionary tracks (see e.g., Hillenbrand 2005; Hillenbrand et al. 2008). The effect of random errors in determination of age and mass was estimated by propagating the random errors to their observed estimation by assuming normal error distribution and using Monte-Carlo simulations. The use of different PMS evolutionary models give different ages and hence an age spread in a cluster (e.g., Sung et al. 2000). In the present study, we have used the models by Siess et al. (2000) only for all the BRCs and the cluster region, therefore our age and mass estimations are not affected by the systematic errors. However, the use of different sets of PMS evolutionary tracks will introduce a systematic shift in age determination. The presence of binaries may be another source of errors in the age determination. Binarity will brighten the star, consequently the CMD will

2.5 Basic Assumptions and Analysis Techniques Used

yield a lower age estimate. In the case of equal mass binaries we expect an error of $\sim 50 - 60\%$ in the age estimation of the PMS stars.

Chapter 3

Star formation in the central cluster of W5 E HII region

3.1 Introduction

Since most of the stars form in clusters or groups and mostly all the massive stars form in the cluster mode, it is interesting to study the star formation in clusters and effect of massive star on the cluster as well as on the remaining parental cloud. The W5 HII region is an extended HII region with relatively simple morphology and shows indications of triggered star formation. It is a part of the large W3/W4/W5 cloud complex in the Perseus arm and consists of two adjacent circular HII regions, W5 E and W5 W. W5 E is primarily ionised by a centrally located O7V star HD 18326. There are many studies on this region. There are many studies on this region. Karr & Martin (2003) discussed triggered star formation in W5 using multi-wavelength archival data. Based on the timescales of the expansion of the HII region and the age of the YSOs, they obtained the timescale of the interaction between the molecular clouds and the HII region, $t \sim 0.5 - 1.0$ Myr. Using the *Spitzer* Space Telescope imaging with IRAC and MIPS, Koenig et al. (2008) noticed dense clusters of YSOs, centered around the O stars HD 17505, HD 17520, BD +60 586 and HD 18326. The HII region W5 E is primarily ionised by HD 18326. The W5 E HII region has two

¹The results presented in this chapter have been accepted for publication (Chauhan et al. 2011, MNRAS)

BRCs, namely BRCs 13 and 14 (SFO 91) at its periphery. Based on the column densities of ^{13}CO and the spatial distribution of YSO candidates, Niwa et al. (2009) identified a BRC candidate in the north-western part of the W5 E HII region. We refer this BRC candidate as BRC NW. Hence W5 E is an interesting region to study the triggered star formation.

In this chapter, the photometric studies of the stellar contents of the newly identified cluster by using the optical, NIR and MIR data have been discussed. The properties of the YSOs associated with cluster have used to understand the star formation scenario in this central cluster of the W5 E HII region. The influence of the ionizing source on the remaining molecular cloud and the BRCs associated with HII region will be discussed in the chapter 7.

3.2 Observations and Data reductions

The 50×50 arcmin² area containing the cluster around the O7 star HD 18326 noticed by Koenig et al. (2008) and Chauhan et al. (2009), reproduced from the DSS2-R image, is shown in Fig. 3.1. As evident from the figure, the cluster is embedded in an HII region W5 E. Towards the eastern side BRCs 13 and 14 are located, whereas BRC NW detected by Niwa et al. (2009) can be seen towards the north-west direction of the cluster. In the ensuing subsections we describe the observations carried out to study the region in detail.

3.2.1 Optical CCD Observations

The $UBVI_c$ CCD optical observations of W5 E were carried out using the 2048×2048 pixel² CCD camera mounted at f/3.1 Schmidt focus of the 1.05-m telescope of Kiso Observatory, Japan. The instrument details are given in section 2.2.3. The average FWHM of the star images during the observations was $\sim 3''$.

The $UBVI_c$ CCD observations of the central region of W5 E have also been carried out using the 2048×2048 pixel² CCD camera mounted on the 1.04-m ST of the ARIES, Nainital, India. To improve the signal-to-noise ratio (S/N), the observations were carried out in a binning mode of 2×2 pixel². The instrument is discussed in section 2.2.3. The average FWHM of star images was $\sim 2''.5$. The

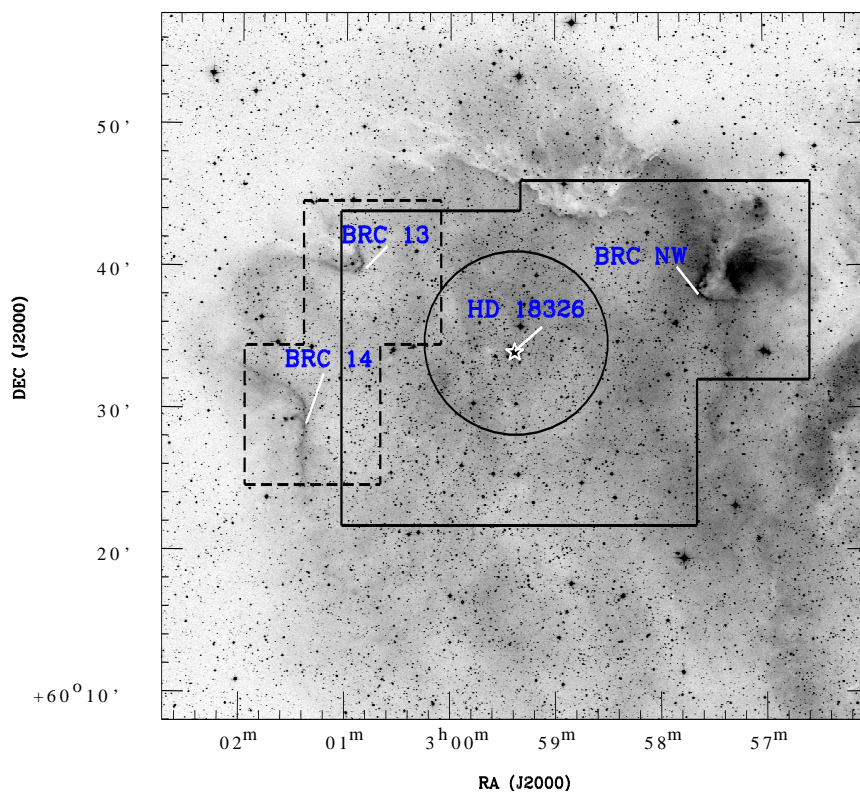


Figure 3.1: The 50×50 arcmin² DSS2-R band image of the W5 E region. The area marked with thick lines is the region for which deep images are taken in V and I_c bands. The circle represents the boundary of the cluster. The abscissa and the ordinates are RA and DEC for the J2000 epoch. The dashed lines represent the boundaries of the region for which deeper observations have been carried out using the HCT (for details; see chapters 5 & 6.) to study the BRCs 13 and 14.

observations of the central region of W5 E were standardised on 2009 October 13 by observing standard stars in the SA 92 field (Landolt 1992). Deep imaging of a nearby field region towards the north from the cluster centre ($\alpha_{2000} = 02^h 59^m 34^s$; $\delta_{2000} = +61^\circ 05' 28''$), was also carried out in V and I_c bands using the ST. The magnitudes of bright stars which were saturated in deep exposure frames have been taken from short exposure frames. A number of bias and twilight frames were also taken during the observing runs. The log of the observations is tabulated in Table 3.1.

The pre-processing of the data frames was done using the various tasks avail-

3.2 Observations and Data reductions

Table 3.1: Log of observations

$\alpha_{(2000)}$ (h:m:s)	$\delta_{(2000)}$ (d:m:s)	Filter & Exposure(sec) \times no. of frames	Date of observations (yr-mm-dd)
KISO 02:59:22.60	+60:33:48.7	U:180 \times 9,30 \times 6; B:60 \times 9,10 \times 6; V:60 \times 9,10 \times 6; I:60 \times 9,10 \times 6	2007-10-20
ST 02:59:22.60	+60:33:48.7	U:240 \times 2,10 \times 1; B:180 \times 2,5 \times 1; V:100 \times 2,4 \times 1; I:60 \times 2,4 \times 1	2009-10-13
02:59:22.60	+60:33:48.7	U:900 \times 1,300 \times 1; B:600 \times 5; V:360 \times 9; I:120 \times 10	2006-12-16
03:00:08.34	+60:39:19.3	V:600 \times 5;I:300 \times 5	2007-10-13
02:58:38.78	+60:39:06.1	V:600 \times 5;I:300 \times 5	2007-10-13
03:00:03.49	+60:27:59.6	V:600 \times 5;I:300 \times 5	2007-10-13
02:58:33.34	+60:28:47.2	V:300 \times 10;I:300 \times 5	2007-11-06
02:57:44.41	+60:38:29.1	V:180 \times 2;I:100 \times 2	2009-10-13
02:57:44.41	+60:38:29.1	V:600 \times 6;I:300 \times 8	2009-10-15
02:59:34.13	+61:05:28.4	V:300 \times 10;I:300 \times 5	2006-12-15
HCT 02:59:23.83	+60:34:00.0	Gr7/167I:300 \times 1	2009-11-16

able under the *IRAF* data reduction software package. The photometric measurements of the stars were performed using the *DAOPHOTII* software package (Stetson 1987). The point spread function was obtained for each frame using several uncontaminated stars.

The instrumental magnitudes of the central region observed on 2009 October 13 with ST were converted into the standard system using least-square linear regression procedures outlined by Stetson (1992). The photometric calibration equations used are as follows:

$$u = U + (7.858 \pm 0.007) + (0.596 \pm 0.024)X + (0.124 \pm 0.008)(U - B),$$

$$b = B + (5.464 \pm 0.006) + (0.336 \pm 0.010)X + (0.134 \pm 0.006)(B - V),$$

$$v = V + (5.088 \pm 0.006) + (0.188 \pm 0.011)X + (0.032 \pm 0.007)(V - I_c),$$

$$i = I_c + (5.320 \pm 0.012) + (0.121 \pm 0.019)X + (0.106 \pm 0.011)(V - I_c)$$

where U, B, V and I_c are the standard magnitudes; u, b, v and i are the instrumental magnitudes obtained after time and aperture corrections and X is the airmass. We have ignored the second-order colour correction terms as they are generally small in comparison to other errors present in the photometric data reduction. The standard deviations of the standardisation residuals, Δ , between the standard and transformed magnitudes and colours of the standard stars, are found to be $\Delta V = 0.008$, $\Delta(B - V) = 0.017$, $\Delta(V - I_c) = 0.020$ and $\Delta(U - B) = 0.011$.

The photometric accuracies depend on the brightness of the stars, and the typical *DAOPHOT* errors in B , V and I_c bands at $V \sim 18$ are smaller than 0.01 mag. Near the limiting magnitude of $V \sim 21$, the *DAOPHOT* errors increase to 0.06, 0.04 mag in the V and I_c bands, respectively. The Kiso data were standardised using the secondary standards obtained from the central region observations as mentioned above.

To study the luminosity function/ mass function of the cluster region we have used VI_c data taken with 1.04-m ST. It is necessary to take into account the incompleteness in the observed data that may occur for various reasons (e.g., crowding of the stars). A procedure to determine the completeness factor is illustrated in the section 2.5.1.7. Briefly, we randomly added artificial stars to both V and I_c images in such a way that they have similar geometrical locations but differ in I_c brightness according to the mean $(V - I_c)$ colour ($=1.5$ mag) of the data sample. The minimum value of the CF of the pair (i.e., V and I_c band observations) for the two sub-regions, given in Table 3.2, is used to correct the data for incompleteness. The incompleteness of the data increases with increasing magnitude as expected, however it does not depend on the area significantly.

3.2.2 Grism Slit spectroscopy

We obtained a low resolution optical spectrum of the exciting star of W5 E, HD 18326, on 2009 November 16 using HFOSC on HCT, with a slit width of 2 arcsec and Grism 7 ($\lambda = 3800 - 6840 \text{ \AA}$, dispersion = 1.45 \AA/pixel). One dimensional spectrum was extracted from the bias subtracted and flat-field corrected image in the standard manner using IRAF. The wavelength calibration of the spectrum was done using a FeAr lamp source. The standard star G191-B2B is used for the standardisation and flux calibration.

3.3 Archival Data

3.3.1 Near-infrared data from 2MASS

NIR JHK_s data for point sources within a radius of $25'$ around the central cluster have been obtained from the 2MASS Point Source Catalog (PSC) (Cutri et al.

Table 3.2: Completeness factor of photometric data in the cluster and field regions.

V range (mag)	cluster region		field region
	$r \leq 3'$	$3' < r \leq 6'$	
13.5 - 14.0	1.00	1.00	1.00
14.0 - 14.5	1.00	1.00	1.00
14.5 - 15.0	0.99	0.99	1.00
15.0 - 15.5	0.98	0.98	0.99
15.5 - 16.0	0.98	0.98	0.98
16.0 - 16.5	0.96	0.97	0.98
16.5 - 17.0	0.97	0.96	0.98
17.0 - 17.5	0.97	0.96	0.98
17.5 - 18.0	0.95	0.95	0.96
18.0 - 18.5	0.93	0.94	0.95
18.5 - 19.0	0.91	0.92	0.94
19.0 - 19.5	0.88	0.90	0.91
19.5 - 20.0	0.85	0.84	0.89
20.0 - 20.5	0.81	0.82	0.84
20.5 - 21.0	0.72	0.71	0.77
21.0 - 21.5	0.51	0.54	0.57

2003). Sources having uncertainty less than 0.1 mag ($S/N \geq 10$) in all the three bands were selected to ensure high quality data. The JHK_s data were transformed from the 2MASS system to the CIT system.

3.3.2 Mid-infrared data from *Spitzer*

The near- and mid-infrared data (3.6 to 24 μm) from the *Spitzer* Space telescope have provided the capability to detect and measure the infrared excesses due to circumstellar disk emission of the YSOs. In order to study the evolutionary stages of the YSOs detected using the *Spitzer*, we used the IRAC (3.6 μm , 4.5 μm , 5.8 μm and 8.0 μm) and MIPS (24 μm) photometry taken from Koenig et al. (2008).

3.3.3 Slitless H α emission

The H α emission stars for the cluster region have been taken from Nakano et al. (2008).

3.4 Analysis of the associated cluster

3.4.1 Radial stellar surface density profile

The radial extent is one of the important parameters to study the dynamical properties of clusters. To estimate this we assumed a spherically symmetric distribution of stars in the cluster.

In order to determine the cluster centre, we derived the highest peak of stellar density by fitting Gaussian profile to the star counts in strips along both the X and Y axes around the eye estimated cluster centre. The cluster centre from the optical data has turned out to be at $\alpha_{2000} = 02^h59^m22^s \pm 1^s.0$; $\delta_{2000} = +60^\circ34'37'' \pm 12''$. We repeated the same procedure using the 2MASS data to estimate the cluster centre and obtained it to be $\sim 12''$ away from the optical co-ordinates. However, this difference is within the uncertainty. Henceforth, we adopt the optical centre.

We estimated the RDP (see section 2.5.1.2) to study the radial structure of the cluster. We divided the cluster into a number of concentric circles. Projected stellar density in each concentric annulus was obtained by dividing the number of stars by the respective annulus area. Stars brighter than $V = 19.5$ mag and $K = 14.7$ mag were considered for estimating the RDPs from the optical and 2MASS data, respectively. The densities thus obtained are plotted as a function of radius in Fig. 3.2. The error bars are derived assuming that the number of stars in each annulus follows the Poisson statistics.

The horizontal dashed line in the plot shows the field star density, which is obtained from a region $\sim 25'$ away towards the north from the cluster center ($\alpha_{2000} = 02^h59^m34^s$; $\delta_{2000} = +61^\circ05'28''$). Based on the radial density profile, we find that the cluster extent, r_{cl} , is about $6'$ for stars brighter than $V = 19.5$ mag. Almost the same value for the cluster extent is obtained for the 2MASS data.

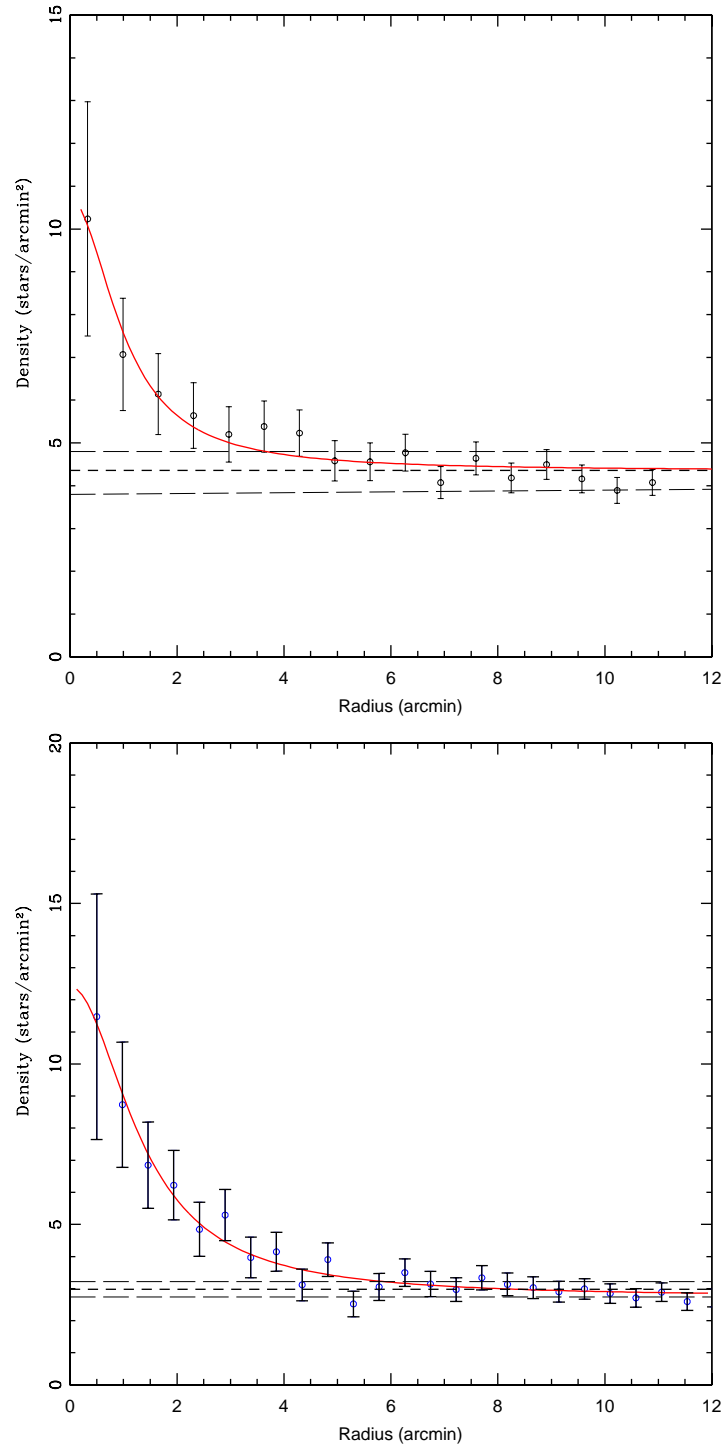


Figure 3.2: Radial density profiles for the cluster using the optical (upper panel) and 2MASS (lower panel) data. Thick dashed line represents the mean density level of the field stars and thin dashed lines are the error limits for the field star density. The continuous curve shows the least-squares fit of the King (1962) profile to the observed data points. The error bars represent $\pm\sqrt{N}$ errors.

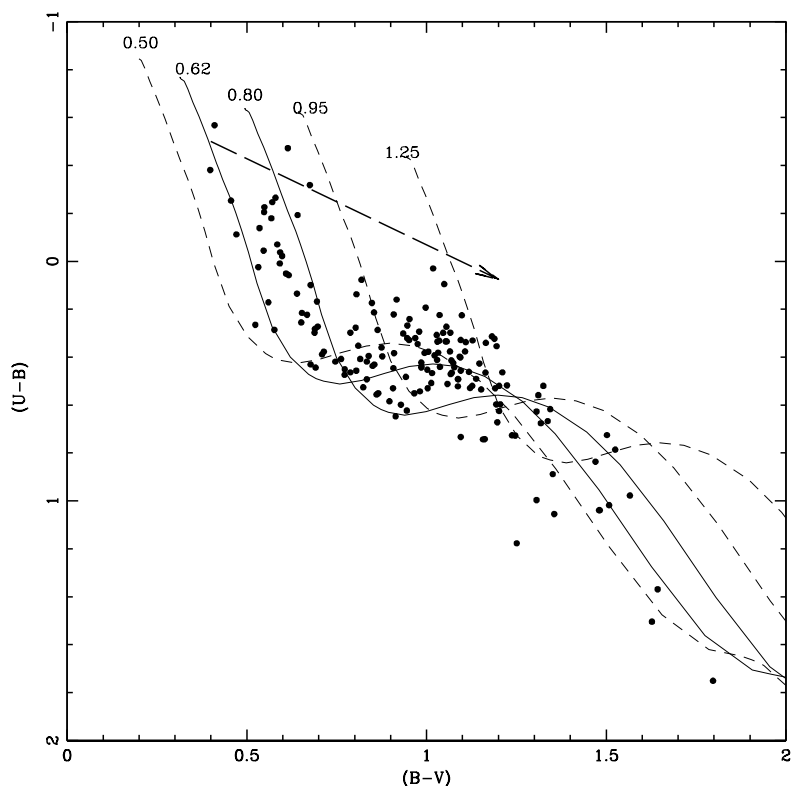


Figure 3.3: $(U - B)/(B - V)$ CC diagram for the stars within the cluster radius ($r_{cl} \leq 6'$). The continuous curves represent the ZAMS by Girardi et al. (2002) shifted along the reddening slope of 0.72 (shown as dashed arrow) for $E(B - V) = 0.62$ mag and 0.80 mag, respectively. The dashed curves represent the ZAMS reddened by $E(B - V) = 0.50$ mag, 0.95 mag and 1.25 mag, respectively to match the probable foreground and background populations (see the text for details).

We adopted a radius of $6'$ for this cluster to obtain the cluster parameters such as reddening, distance, IMF etc.

To parametrise the RDP of the cluster, we fitted the observed RDP with the empirical model of King (1962) as described in section 2.5.1.2. The core radius thus estimated is $1'.01 \pm 0'.12$.

3.4.2 Interstellar reddening

The ratio of the total-to-selective extinction $R_V [= A_V / E(B - V)]$ for the intra-cluster regions of young clusters embedded in a dust and gas cloud may vary significantly (Chini & Wargau 1990; Pandey et al. 2000; Tapia et al. 1991). The value of R_V affects the distance determination significantly, and consequently the age determination of stars. Since the W5 E cluster and the BRCs are associated with the HII region, it will be interesting to examine the reddening law in these objects. The ratio of total-to-selective extinction R_V is found to be normal in the cluster region (cf. section 3.6 for details).

Since spectroscopic observations are not available, the interstellar reddening $E(B - V)$ toward the cluster region is estimated using the $(U - B)/(B - V)$ CC diagram. The CC diagram of the cluster region is presented in Fig. 3.3. Since the cluster is very young, a variable reddening within the cluster region is expected. In Fig. 3.3, the continuous lines represent the intrinsic ZAMS by Girardi et al. (2002) which are shifted by $E(B - V) = 0.62$ and 0.80 mag respectively, along the normal reddening vector (i.e., $E(U - B)/E(B - V) = 0.72$) to match the observations of probable cluster members. Fig. 3.3 thus yields a variable reddening with $E(B - V)_{min} = 0.62$ mag to $E(B - V)_{max} = 0.80$ mag in the cluster region. The star lying within these two reddened ZAMSs may be probable members of the cluster. Reddening of individual stars having spectral classes earlier to A0 have been computed using the reddening free index, Q (Johnson & Morgan 1953). Assuming a normal reddening law we calculated $Q = (U - B) - 0.72 \times (B - V)$. The value of Q for stars earlier than A0 will be < 0 . For main sequence (MS) stars, the intrinsic $(B - V)_0$ colour and colour excess can be obtained by the relations; $(B - V)_0 = 0.332 \times Q$ and $E(B - V) = (B - V) - (B - V)_0$, respectively. Fig. 3.3 also indicates a large amount of contamination due to field stars. The probable late type foreground stars having spectral types later than A0 may follow the ZAMS reddened by $E(B - V) = 0.50$ mag. A careful inspection of Fig. 3.3 indicates the presence of further reddened background populations. The reddening $E(B - V)$ for the background population is found out to be in the range of $\sim 0.95 - 1.25$ mag. This population may belong to the blue plume (BP) of the Norma-Cygnus arm (cf. Pandey et al. 2006). The estimated $E(B - V)$

values for the background population are comparable to the $E(B - V)$ value of the BP population around $l \sim 130^\circ$ (cf. Pandey et al. 2006).

3.4.3 Spectral classification of ionising star in W5 E HII region

We obtained a slit spectrum of the brightest source to study its evolutionary nature. In Fig. 3.4, we present the flux calibrated, normalized spectrum of HD 18326, which is the ionising source of the HII region, in the wavelength range 4000 – 5000 Å. The important lines have been identified and labeled. HD 18326 is identified as an O7V and O7V(n) type star by Conti & Leep (1974) and Walborn (1973), respectively. The ratio of HeI $\lambda 4471$ / HeII $\lambda 4542$ is a primary indicator of the spectral class of early type stars. The ratio we found for this star is ~ 1 , which indicates that it is an $O7 \pm 0.5$ star. With the present resolution of the spectrum, luminosity assessment is quite difficult, however due to the presence of strong absorption in HeII $\lambda 4686$, we design the luminosity class V.

3.4.4 Distance and optical colour-magnitude diagrams

The spectral class of the ionising source yields an intrinsic distance modulus of 11.2 which corresponds to a distance of 1.74 kpc. Here, it is worthwhile to mention that the M_V for an O7V star in the literature varies significantly; e.g., $M_V = -5.2$ (Schmidt-Kaler 1982) to -4.9 (Martins & Plez 2006). This star is also reported as a variable star and a suspected spectroscopic binary (Turner et al. 2008; ?). Hence, the distance estimation based only on the O-type star alone may not be reliable. We also estimated the individual distance modulus of other probable MS stars. The intrinsic colours for each star were estimated using the Q-method as discussed in section 3.4.2. We estimated corresponding M_V values for each star using the ZAMS by Girardi et al. (2002). The average value of the intrinsic distance modulus, obtained using 24 probable MS members, comes out to be 11.65 ± 0.57 , corresponds to a distance of 2.1 ± 0.3 kpc. This distance estimate is in agreement with those obtained by Becker & Fenkart (1971, 2.2 kpc), Georgelin & Georgelin (1976, 2.0 kpc) and Hillwig et al. (2006, 1.9 kpc).

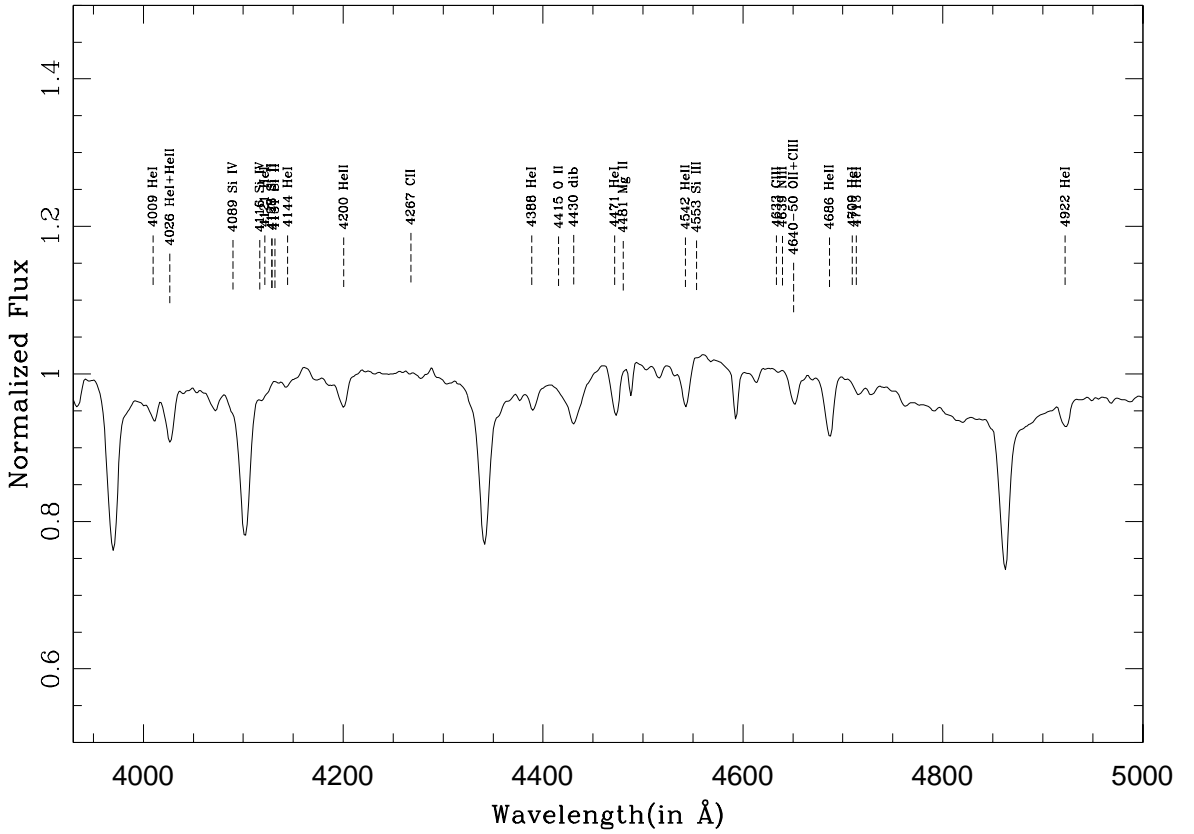


Figure 3.4: Flux calibrated normalised spectrum of HD 18326.

We used the optical CMDs to derive the fundamental parameters of the cluster, such as age, distance etc. The $V/(B - V)$ and $V/(V - I)$ CMDs for stars lying within $6'$ radius are shown in Figs. 3.5a and 3.5b. Fig. 3.5c shows the $V/(V - I)$ CMD for a nearby field region (see section 3.4.1). A 4 Myr isochrone for $Z = 0.019$ by Girardi et al. (2002) and the PMS isochrones for 1 Myr and 5 Myr by Siess et al. (2000) have also been plotted for $(m - M_V) = 13.5$ mag and $E(B - V) = 0.62$ mag and assuming $E(V - I) = 1.25 \times E(B - V)$, $R = 3.1$. A comparison of the CMDs of the cluster region with the field region reveals an unambiguous population of PMS sources along with a significant contamination due to field star population.

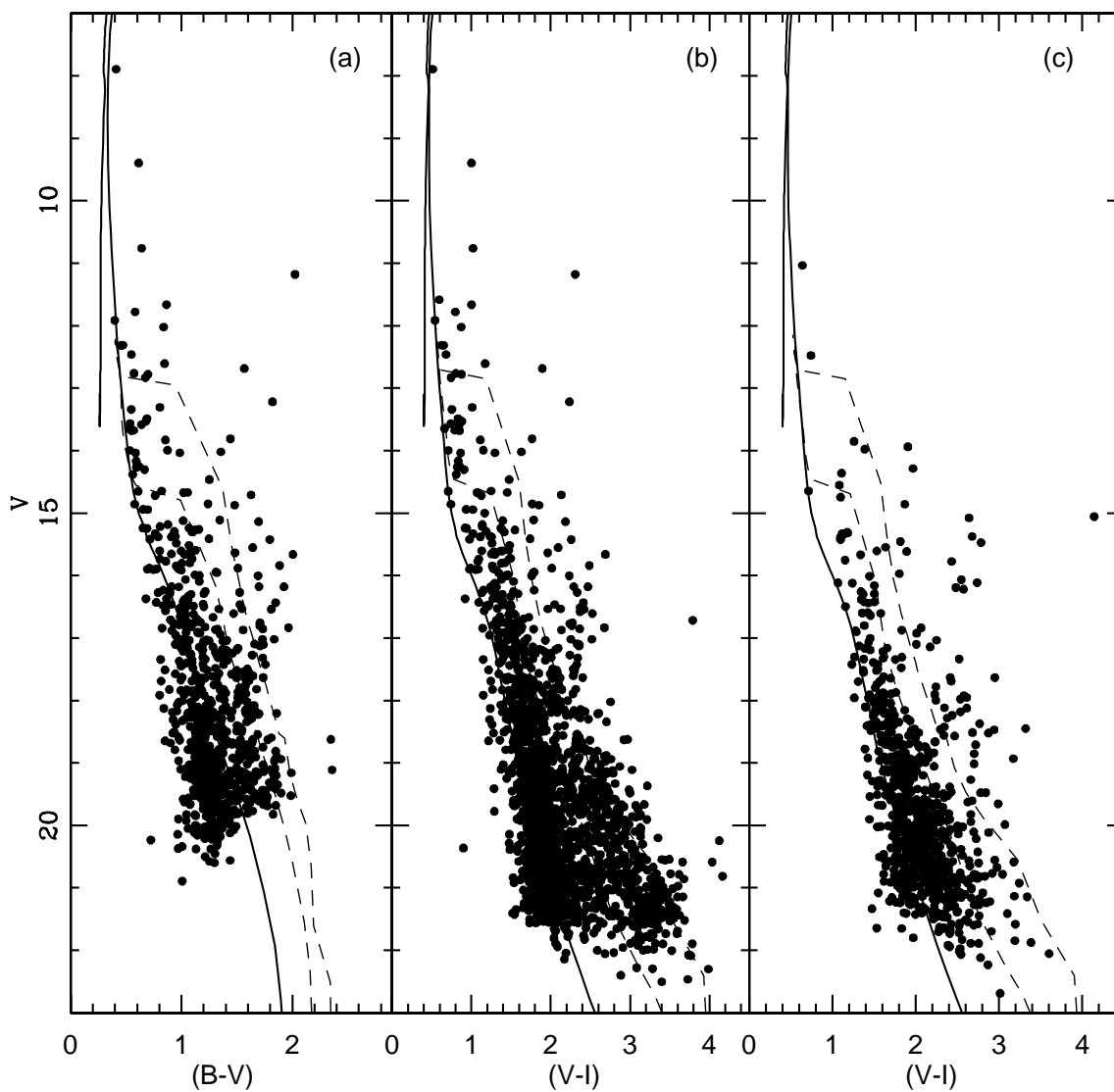


Figure 3.5: (a) and (b): The $V/(B-V)$ and $V/(V-I)$ CMDs for the stars within the cluster radius; (c): $V/(V-I)$ CMD for stars in the field region having same area as in (a) and (b). The continuous line is the isochrone of 4 Myr from Girardi et al. (2002) and dashed lines are 1 Myr and 5 Myr PMS isochrones from Siess et al. (2000). The isochrones are corrected for the cluster distance of 2.1 kpc and reddening $E(B-V) = 0.62$ mag.

3.5 Identification of pre-main sequence objects associated with the cluster

Since W5 E region is located at a low galactic latitude, the region is significantly contaminated by foreground/background stars as discussed above. In order to understand star formation in the region we selected probable PMS members associated with the region using the criteria described in section 2.5.2.

In the present study, we use $H\alpha$ emission stars in the W5 E HII region found by Nakano et al. (2008) in the W5 E HII region. Since many PMS stars also show NIR/ MIR excesses caused by circumstellar disks, NIR/ MIR photometric surveys are also powerful tool to detect low-mass PMS stars. We have also used the YSOs identified by Koenig et al. (2008) in the W5 E HII region using the *Spitzer* IRAC and MIPS photometry. Fig. 3.6a shows the NIR $(J - H)/(H - K)$ colour-colour (NIR-CC) diagram of all the sources detected in the 2MASS catalogue along with the YSOs identified by Koenig et al. (2008) in the cluster region, whereas Fig. 3.6b shows the NIR-CC diagram for the sources in the nearby reference field.

The $V/(V - I)$ CMD for the YSOs taken from the catalogue by Koenig et al. (2008) for the cluster region ($r_{cl} = 6'$) is shown in Fig. 3.7. Here the well-known age-with-mass trend that higher mass stars look older than lower mass stars (Hillenbrand et al. 2008) is evident. In addition a few sources, having $V \gtrsim 15$, classified as Class III objects are located near the MS. They are also located on the MS in the NIR-CC diagram and hence could be field stars. This indicates that part of Class III objects by Koenig et al. (2008) are not YSOs, but rather stars found in the W5 *Spitzer* photometric sample that appear to have photospheric colours in the 3 to 24 μm bands and thus appear as Class III SEDs. Thus, the listed Class III objects by Koenig et al. (2008) may be heavily contaminated by foreground and background field populations. A comparison of the NIR-CC diagram of the cluster region and nearby field region indicates that the YSOs identified by Koenig et al. (2008) and having $(J - H) > 0.7$ mag and $(H - K) > 0.3$ mag can be safely considered as YSOs associated with the region.

Fig. 3.8 shows the $V/(V - I)$ CMDs of the YSOs selected using the NIR-CC diagram in the cluster region. Again the CMDs indicate that practically all of them are PMS stars, but at the same time reveal a significant scatter in

3.5 Identification of pre-main sequence objects associated with the cluster

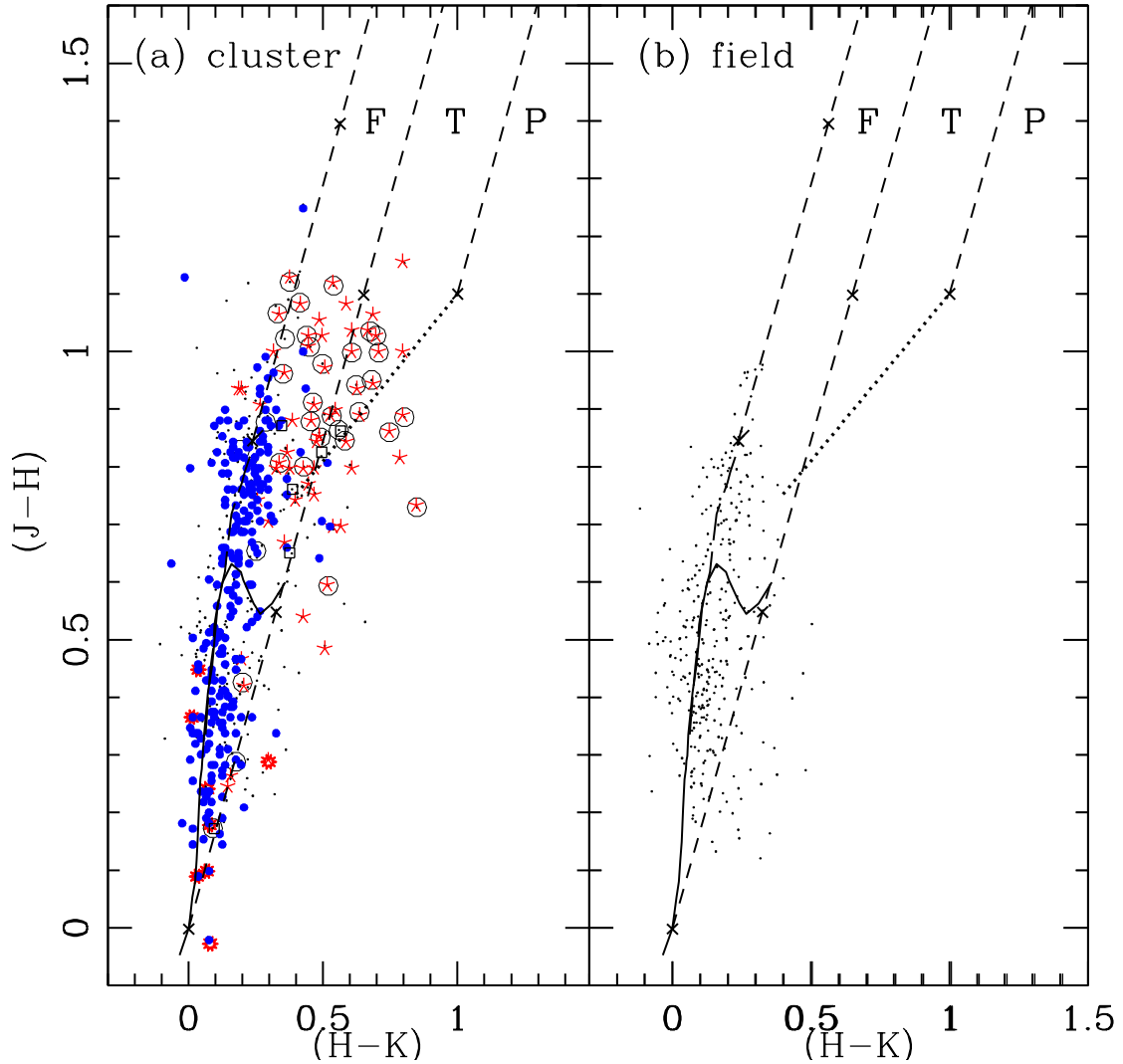


Figure 3.6: NIR $(J-H)/(H-K)$ CC diagrams for the stars (a) within the cluster radius and (b) in the reference field. Small dots represent 2MASS sources and open circles represent $H\alpha$ sources from Nakano et al. (2008). Class II, Class III and transition sources from the *Spitzer* photometry are shown by asterisks, filled circles and open squares, respectively. Dashed straight lines represent the reddening vectors (Cohen et al. 1981). The crosses on the dashed lines are separated by $A_V = 5$ mag.

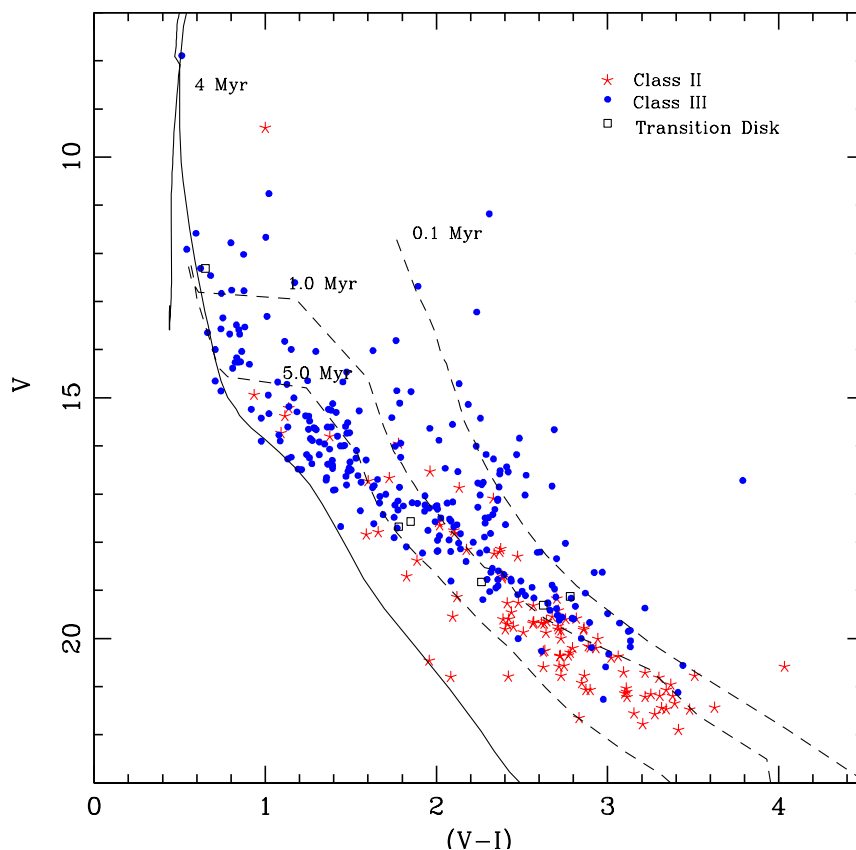


Figure 3.7: $V/(V - I)$ CMD for the clustered YSOs identified by Koenig et al. (2008) in the cluster region. The continuous line is the isochrone of 4 Myr from Girardi et al. (2002) and dashed lines are the 0.1 Myr, 1 Myr and 5 Myr PMS isochrones from Siess et al. (2000). The isochrones are corrected for the cluster distance of 2.1 kpc and reddening $E(B - V) = 0.62$ mag

their ages. The age and mass of the YSOs was estimated using the $V/(V - I_c)$ CMD. However, the estimation of the age of the PMS stars by comparing the observations with the theoretical isochrones is prone to errors as discussed in section 2.5.4 .

3.6 Reddening law in the cluster region

To study the nature of the extinction law in the region, we used two colour diagrams (TCDs) as described by Pandey et al. (2003). The TCDs of the form

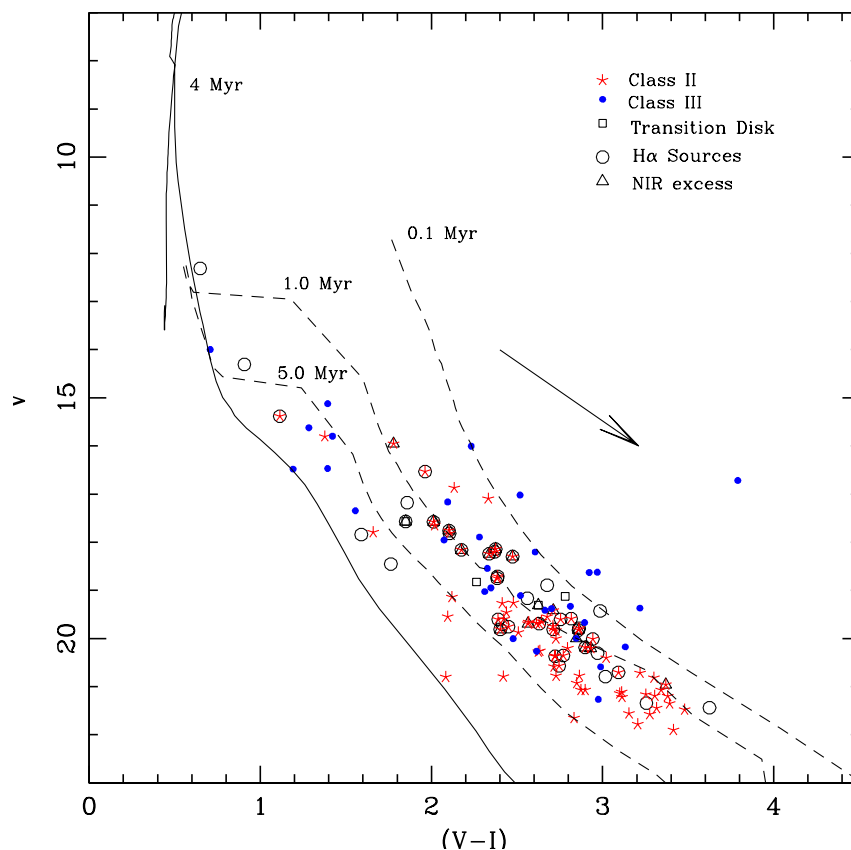


Figure 3.8: $V/(V - I)$ CMDs for the YSOs selected in the presented study (see the text) in the cluster region. The continuous line is the isochrone of 4 Myr from Girardi et al. (2002) and dashed lines are 0.1, 1 and 5 Myr PMS isochrones from Siess et al. (2000). The isochrones are corrected for the distance and reddening of the respective regions. The arrow represents the reddening vector.

of $(V - \lambda)$ vs. $(B - V)$, where λ is one of the broad-band filters (R, I, J, H, K, L), provide an effective method for separating the influence of the normal extinction produced by the diffuse interstellar medium from that of the abnormal extinction arising within regions having a peculiar distribution of dust sizes (cf. Chini & Wargau 1990; Pandey et al. 2000).

The TCDs for the diskless (Class III) YSOs associated with the cluster and BRC regions are shown in Fig. 3.9. In order to avoid IR excess stars, we have used all the *Spitzer* Class III sources having $V < 17$ mag. The slopes of the distributions are given in the figure. The ratio of total-to-selective extinction

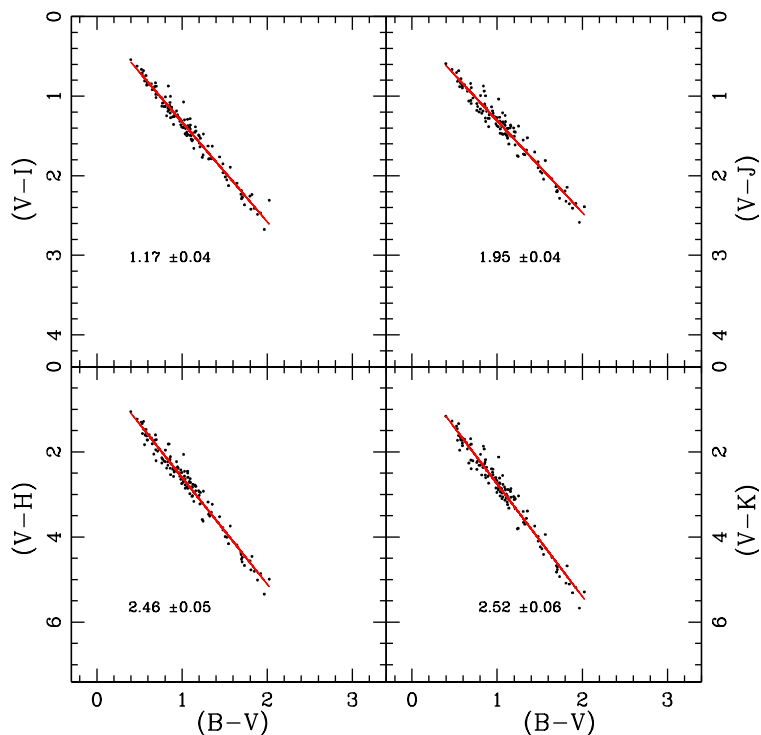


Figure 3.9: TCDs for the diskless (Class III) sources in the cluster region.

‘ R ’ in the regions is estimated using the procedure as described in Pandey et al. (2003). The R values in the cluster region is estimated to be $R_{cluster} = 3.14 \pm 0.12$. The value of $R_{cluster}$ indicates a normal reddening law in the cluster region.

3.7 Initial mass function of the cluster

The IMF is the distribution of the masses of stars at the time of a star formation event. Young clusters are preferred sites to IMF studies as their MFs can be considered as IMFs, since they are too young to lose significant number of members either due to dynamical evolution or stellar evolution. The IMF is defined as the number of stars per unit logarithmic mass interval, and is generally represented by a power law having a slope,

$$\Gamma = d \log N(\log m) / d \log m,$$

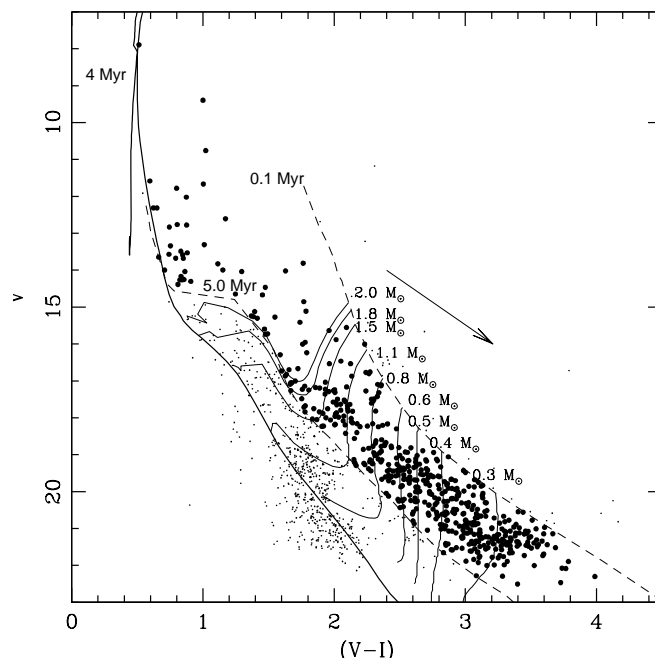


Figure 3.10: Statistically cleaned $V/(V-I)$ CMD for stars lying within the cluster radius. The stars having PMS age ≤ 5 Myr are considered as representing the statistics of PMS stars in the region and are shown by filled circles. The isochrone for 4.0 Myr age by Girardi et al. (2002) and PMS isochrones of 0.1, 5.0 Myr along with evolutionary tracks for different masses by Siess et al. (2000) are also shown. All the isochrones are corrected for the cluster distance and reddening. The corresponding values of masses in solar mass are given at the right side of each track. Points shown by small dots are considered as non-members. The arrow represents the reddening vector.

where $N(\log m)$ is the number of stars per unit logarithmic mass interval. For the mass range $0.4 < M/M_{\odot} \leq 10$, the classical value derived by Salpeter (1955) is $\Gamma = -1.35$.

To remove the contamination due to field stars from the MS and PMS sample, we statistically subtracted the contribution of field stars from the observed CMD of the cluster region using the procedure as described in section 2.5.1.8. For any star in the $V/(V-I)$ CMD of the control field (Fig. 3.5c), the nearest star in the cluster's $V/(V-I)$ CMD (Fig. 3.5b) within $V \pm 0.125$ and $(V-I) \pm 0.065$ was removed. The statistically cleaned CMD is shown in Fig. 3.10, which clearly

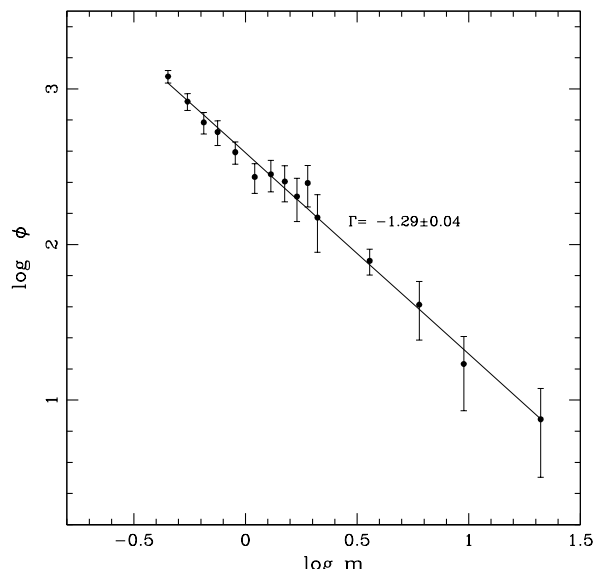


Figure 3.11: The MF in the cluster region derived using the optical data. The ϕ represents $N/d \log m$. The error bars represent $\pm\sqrt{N}$ errors. The continuous line shows least-squares fit to the mass ranges described in the text. The value of the slope obtained is mentioned in the figure.

shows a sequence of PMS stars. PMS isochrones by Siess et al. (2000) for ages 0.1 and 5 Myr (dashed lines) and 4 Myr isochrone by Girardi et al. (2002) (continuous line) are shown in Fig. 3.10. The evolutionary tracks by Siess et al. (2000) for different masses are also shown which are used to estimate the masses of PMS stars. Here we would like to point out that the points shown by filled circles in Fig. 3.10 may not represent the actual members of the clusters. However the filled circles should represent the statistics of PMS stars in the region and the statistics has been used to study the MF of the cluster region.

We used the statistics of the sources having age $0.1 \leq \text{age} \leq 5$ Myr in the statistically cleaned CMD (Fig. 3.10) to study the IMF of the cluster region. We used the ADDSTAR routine of DAOPHOT II to determine the completeness factor (CF) as describe in section 2.5.1.7. Since the MS age of the most massive star in the cluster is < 4 Myr, the stars having $V < 14.7$ mag ($M > 3 M_{\odot}$) have been considered on the MS. In order to obtain the MF for MS stars, the LF is converted to MF using the theoretical model of Girardi et al. (2002). The MF

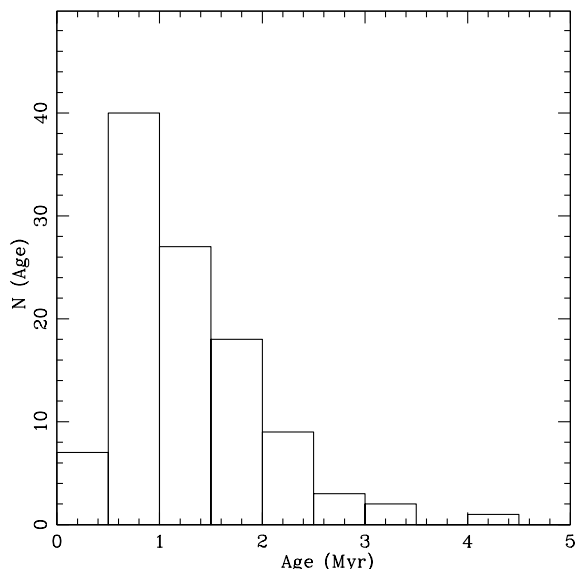


Figure 3.12: Histogram of the age distribution for the YSOs in the cluster region.

of the PMS stars was obtained by counting the number of stars in different mass bins (for details see Jose et al. 2008; Pandey et al. 2008). Fig. 3.11 shows the MF of the cluster in the mass range $0.4 < M/M_{\odot} < 30$. A single slope for the MF in the mass range $0.4 < M/M_{\odot} < 30$ can be fitted with $\Gamma = -1.29 \pm 0.03$, which is comparable to the Salpeter value (-1.35).

3.8 Star formation in the cluster region

The CMD of the identified YSOs (Fig. 3.8) and the statistically cleaned CMD (Fig. 3.10) reveal a non-coeval star formation in the cluster region. The age distribution is shown in Fig. 3.12. The mean age of the YSOs is estimated to be 1.26 ± 0.69 Myr. This is smaller than the average age of the YSOs obtained by Nakano et al. (2008), age ~ 4 Myr. Nakano et al. (2008) have used only $H\alpha$ emission stars while the present sample is larger, including NIR and MIR excess stars in addition. To estimate the age of the $H\alpha$ emission stars, Nakano et al. (2008) used PMS isochrones by Palla & Stahler (1999), whereas we have used those by Siess et al. (2000). The use of different PMS evolutionary models can introduce a systematic shift in the age estimation.

3.9 Conclusions

In this chapter the results of VI_c photometric studies of the newly identified central cluster of W5 E has been presented. NIR data from 2MASS and MIR data from IRAC/MIPS of the *Spitzer* telescope have also been used to study the properties of the cluster. The main conclusions of the present chapter are as follows:

The central cluster has a distance of ~ 2.1 kpc, a radius of $6'$ and a mean age of ~ 1.3 Myr. The reddening law is found to be normal. The star formation in the cluster region is found to be non-coeval, with an age spread of ~ 5 Myr. The slope of the IMF within the cluster region in the mass range $0.4 \leq M/M_\odot \leq 30$ is found to be $\Gamma = -1.29 \pm 0.03$, which is comparable to the Salpeter value.

Chapter 4

SMALL SCALE SEQUENTIAL STAR FORMATION IN AGGREGATES ASSOCIATED WITH BRCs

4.1 Introduction

In the previous chapter we studied the basic parameters of the central cluster of W5 E HII region. In this chapter the age sequence in the four BRCs namely 11NE, 12, 14 and 37 which are associated with different HII regions are studied. The “ S^4F hypothesis” suggests that a BRC undergoes a few or several star formation events due to the RDI at its head part, which is located closer to the exciting stars(s) first, but then recedes outward in the HII region as the the star formation proceeds, leaving groups of stars aligned in an age sequence. With the aim to strengthen the S^4F hypothesis, Ogura et al. (2002) made grism surveys of 24 BRCs for $H\alpha$ emission stars. Altogether 460 $H\alpha$ emission stars and 12 Herbig-Haro objects were detected in their vicinities. Presumably, these $H\alpha$ emission stars are mostly TTSs, although practically no follow-up observations were carried out. These objects are found concentrated toward the head or just outside of BRCs on the side of the exciting star(s). One may suspect that there might be just as many such stars farther inside the BRCs, but concealed by the higher

¹The results presented in this chapter have been published in Ogura K., Chauhan Neelam et al. (2007)

extinction. However this does not appear likely, because, as we see in section 4.4, the A_V values of the $H\alpha$ emission stars inside, e.g., BRC 14 are not much larger than those outside it. In addition in figures 1a to 1z of Ogura et al. (2002) we do not find many faint ($H\alpha$ emission) stars inside BRCs. So we think that the observed concentration of $H\alpha$ emitters toward the heads of the BRCs supports the S^4F hypothesis, although it may be exaggerated to some extent by the opacity effect. Here we also add that as for the very rich AFGL 4029 IR cluster embedded in somewhat eastern part of BRC 14 (e.g., Deharveng et al. 1997), we believe that it formed spontaneously, not as a result of RDI; it is located too far away from the head of the BRC 14 for the effects of RDI to propagate. Recently, Matsuyanagi et al. (2006) analyzed their deep JHK photometry of the BRC 14 region and showed that three indicators of star formation, i.e., the fraction of YSO candidates, the amount of extinction of all sources, and near-IR excesses of the YSO candidates, all showed a clear sequence from outside to inside the bright rim. This result further strengthens the S^4F hypothesis.

The best way to quantitatively testify the hypothesis is to estimate of the ages of the aggregate members and to compare them between different regions with respect to the bright rim. So we undertook BVI_c photometry of BRC aggregates. We constructed reddening-corrected CMDs for each BRC aggregate. The age of each star has been determined on the $V_o/(V-I_c)_o$ CMDs, and its spatial distribution has been examined. The result seems to confirm the S^4F hypothesis.

4.2 Observations and data reduction

The imaging observations of the four BRCs in the BVI_c bands were carried out on the 2.0-m HCT of the Indian Astronomical Observatory. HCT is located at Mt. Saraswati (altitude 4500m above sea level) in the Himalayan region, but is remotely operated from CREST, Hosakote near Bangalore, via a satellite link. The instrument used is HFOSC in the imaging mode. The observations were made on 25 and 27 Sep, 2005 and a log of the observations is given in Table 4.1. The sky conditions at the time of the observations were satisfactory with the seeing size of about $1''.5$.

4.3 Star Selection and Reddening Correction

Table 4.1: Log of observations

BRC	Date of Obs.	Exposure Times (sec) × No. of Frames
11NE	05/9/27	$I_c: 60 \times 4$ $V: 120 \times 4$ $B: 300 \times 4$
12	05/9/27	$I_c: 60 \times 4$ $V: 100 \times 4$ $B: 240 \times 4$
14	05/9/27	$I_c: 50 \times 4$ $V: 120 \times 4$ $B: 300 \times 4$
37	05/9/25	$I_c: 60 \times 6$ $V: 200 \times 6$ $B: 300 \times 6$

The data reduction was carried out at ARIES, India. The initial processing of the data frames was made using the IRAF data reduction package. The photometric measurements were done using DAOPHOT II Stetson (1987). The PSF was obtained for each frame using several uncontaminated stars. The photometric accuracies depend on the brightness of the stars, and the typical DAOPHOT errors of our target stars ($V \sim 18$ mag) are: 0.003 mag in I_c , 0.005 mag in V , and 0.007 mag in B for BRCs 11NE, 12 and 37. However they are a little bit larger for BRC 14: 0.005, 0.005 and 0.007, respectively. The standard deviation of the residuals of the transformed V magnitude and $B-V$ and $V-I_c$ colours of the standard stars were 0.010, 0.005 and 0.012, respectively. Near the limiting magnitude of $V \sim 20.5$, the DAOPHOT errors increase to ~ 0.03 in all colour bands.

4.3 Star Selection and Reddening Correction

The aggregates associated with the BRCs are very loose and composed of a small number of stars. In addition, their Galactic latitudes are low, the aggregates may be contaminated by field star population. Therefore we selected the targets from such BRCs that the associated aggregate contains relatively many stars. BRCs 11NE, 12 and 14 belong to the HII region IC 1848 and BRC 37 to IC 1396. For each BRC the $H\alpha$ emission stars of Ogura et al. (2002) have been selected as the member stars. In the case of BRC 11NE and BRC 37, however, only a few $H\alpha$ stars are available. But, as one sees in figures 1f and 1p of Ogura et al.

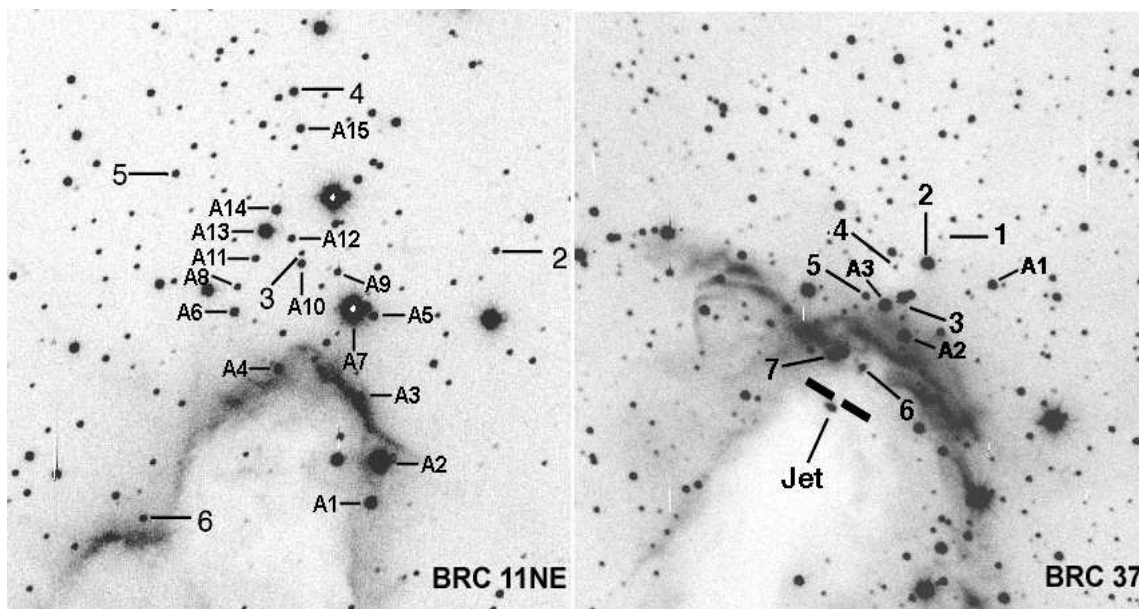


Figure 4.1: Finding charts for stars in BRC 11NE and BRC 37. Stars with prefix “A” are non-H α emission stars, and those without the prefix are H α emitters of Ogura et al. (2002). They are reproduced from their figures 1f and 1p, and are 2.5’ by 2.5’ wide each with north up and east to the left. In BRC 37 “jet” is part of the Herbig-Haro object HH 588 (see, Ogura et al. 2002) and the pair of thick tick marks indicate the nominal IRAS position. BRC 11NE does not harbor any IRAS point sources.

(2002), a relatively clear aggregate of stars can be noticed that appears to be associated with the BRCs; these aggregates show up more prominently in the 2MASS images. We, therefore, have added the stars having 2MASS counterparts from the aggregates, and they are indicated with “A” (*additional stars*) in the finding charts, Fig 4.1. In BRCs 12 and 14 we deal only with the H α stars of Ogura et al. (2002), so see the finding charts therein.

The difficulty of extinction correction is solved by adopting procedure mentioned in section 2.5.3.1. We adopted the intrinsic line of TTSs given by Meyer et al. (1997) and that of dwarfs of Bessell & Brett (1988). The former is used for H α stars. The latter, used for non-emission stars, has been converted into the CIT JHK_s system according to the equation given in Bessell & Brett (1988). For BRCs 11NE, 12 and 37 the JHK_s data have been taken from the 2MASS cata-

log and converted into the CIT JHK_s system. Only stars with the photometric qualities ‘AAA’ have been adopted. For BRC 14 we have adopted the JHK_s data used in Matsuyanagi et al. (2006), which were obtained with the infrared camera SIRIUS on the University of Hawaii 2.2-m telescope atop Mauna Kea. The identifications of the target stars between the HCT data and the 2MASS catalog or the SIRIUS data have been made on the basis of the J2000.0 coordinates within an accuracy of $2''$. From the A_V values thus obtained we have calculated the colour excesses E_{V-I_c} and E_{B-V} according to the ratio given by Munari & Carraro (1996).

4.4 Results

The photometric results for each star in each BRC aggregate are given in Table 4.2. The second and third columns give the extinction-corrected V magnitude and $V-I_c$ colour, respectively. The last column gives the location of the star with respect to the bright rim. Note that “outside/inside BR” (BR stands for bright rim) are the inside/outside of the HII region. We cannot tell the accuracies of the values in Table 4.2, since the amounts of reddening corrections depend on several factors whose reliability is difficult to quantify. For each BRC a $V_0/(V-I_c)_0$ CMD was constructed, where overlaid are the isochrones of Siess et al. (2000) with $Z = 0.02$ and no overshooting, which are corrected for the distance given in Table 4.2. These distances are taken from the SFO 91. The age of each star has been determined according to these isochrones. In view of the limited page space we show as an example the $V_0/(V-I_c)_0$ CMD for BRC 14 in Fig. 4.2. There are many stars which lie above the youngest isochrone of 1 Myr and their ages are estimated by extrapolation. The resultant ages appear to be reasonable, ranging from 0.1 to a few Myr (with only a few exceptions), which compare well with TTSs’ lifetime of a few tenths to a few Myr. From this we would say that all the stars in our sample are probably aggregate members with practically no foreground/background stars mixed-in. The mass of the stars ranges from ~ 0.3 to $\sim 2 M_\odot$ (for the 1 Myr isochrone), which is again reasonable. With these ages and masses the TTS nature of the $H\alpha$ emission stars is almost confirmed. $V_0/(B-V)_0$ CMDs yield similar results.

Table 4.2: Results of dereddening and age estimation

Star	V_0	$(V-I_c)_0$	$(B-V)_0$	A_V (mag)	Age (Myr)	Location
BRC 11NE (1.9 kpc)						
H α -6	17.99	1.84	1.23	1.46	1.7	on BR
A1	15.45	1.57	1.22	1.41	0.3	"
A2	14.56	1.57	1.41	0.00	0.1	"
A3	17.44	2.00	1.40	0.71	0.7	"
A4	16.25	1.34	0.80	2.26	1.5	"
A5	17.91	1.75	-0.21	0.69	1.9	outside BR
A6	17.01	1.67	1.29	0.78	1.0	"
A7	13.13	0.85	0.53	0.00	1.0	"
A8	19.13	2.24	1.65	0.78	1.9	"
A9	17.27	1.61	-0.65	2.16	1.8	"
A10	15.56	1.58	1.06	3.09	0.3	"
A11	17.92	1.8	1.32	1.55	1.8	"
A12	16.84	1.45	1.11	2.29	1.9	"
A13	15.52	1.54	1.30	0.00	0.3	"
A14	16.26	1.63	1.21	1.42	0.6	"
H α -5	18.32	2.08	1.52	0.73	1.4	"
A15	17.24	1.82	1.35	1.38	0.8	"
H α -4	18.09	2.05	1.37	0.61	1.2	"
BRC 12 (1.9 kpc)						
H α -1	16.19	1.61	1.06	2.61	0.6	outside BR
H α -5	17.88	1.52	1.09	0.00	6.0	"
H α -10	19.79	2.22	0.97	0.00	4.0	"
H α -17	17.96	1.88	1.29	1.06	1.6	"
H α -19	16.34	1.70	1.09	0.94	0.35	"
H α -09	16.34	1.95	1.18	1.62	0.17	on BR
H α -11	17.18	2.10		2.36	0.35	"
H α -14	14.81	1.57	0.99	1.73	0.1	"
H α -16	16.9	1.83	1.13	1.41	0.4	"
H α -20	15.24	1.29	0.64	3.54	0.5	inside BR

BRC 14 (1.9 kpc)						
H α -5	16.99	1.84	1.50	2.18	0.5	outside BR
H α -12	16.51	1.46	1.35	3.40	1.3	"
H α -16	17.85	1.85		3.37	1.5	"
H α -18	19.07	2.11		2.42	2.5	"
H α -20	17.29	1.62		3.14	1.7	"
H α -23	16.94	1.39		3.23	3.0	"
H α -24	18.93	2.55		2.14	1.0	"
H α -32	15.2	1.36	1.15	3.22	0.4	on BR
H α -33	17.87	1.77		2.87	1.9	"
H α -35	16.76	1.82	1.47	2.70	0.4	on BR
H α -31	15.6	1.39		3.99	0.5	"
H α -34	16.46	1.39	0.88	4.17	1.7	"
H α -38	17.68	1.97		2.65	0.8	inside BR
H α -39	17.22	1.89		2.87	0.5	"
H α -40	15.04	1.37		5.47	0.3	"
H α -42	17.14	1.95		3.04	0.4	"
BRC 37 (0.75 kpc)						
A1	16.07	1.63	1.23	2.04	4.5	outside BR
H α -2	14.10	1.49	1.12	2.27	0.6	"
H α -3	14.13	1.46		3.71	0.7	"
A2	14.65	2.00	1.01	2.52	0.25	on near BR
A3	15.11	1.62	1.20	2.07	1.5	"
H α -7	14.39	1.49	0.68	3.21	1.0	on BR

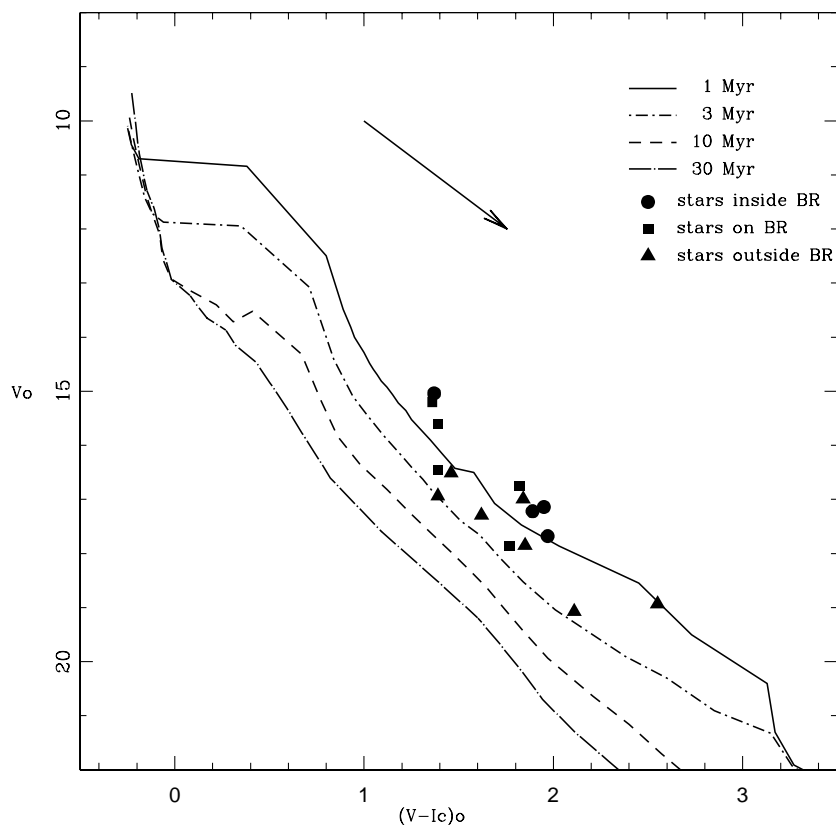


Figure 4.2: $V_0/(V-I_c)_0$ CMD for the BRC 14 aggregate. Stars, which are all $H\alpha$ emitters in this case, are plotted with different symbols according to their locations with respect to the bright rim. The isochrones of Siess et al. (2000) with $Z = 0.02$ and no overshooting are drawn with the correction for the distance of 1.9 kpc. The arrow indicates the reddening vector.

In each aggregate the locations of the stars with respect to the bright rim are grouped into two or three (only in the case of BRC 14) regions. The grouping is chosen so that there are at least four stars in each region with the exception of BRC 37 where we have altogether only six stars. The mean age and A_V of the stars in each region are summarized in Table 4.3. It shows that the mean age of the stars inside or on the bright rim is *always* younger than that outside it, although the scatter is very large. The age difference is particularly significant in BRCs 12 and 14 where we have stars inside the bright rim. Moreover in BRC 14 the mean age constantly decreases from outside to inside the bright rim.

Table 4.3: Summary of results

BRC	Region	No. of stars	Mean age \pm st dev (Myr)	Mean A_V \pm st dev (mag)
11NE	outside BR	13	1.26 ± 0.60	1.21 ± 0.88
	on BR	5	0.86 ± 0.71	1.17 ± 0.85
12	outside BR	5	2.51 ± 2.43	0.93 ± 1.07
	inside & on BR	5	0.30 ± 0.17	2.13 ± 0.86
14	outside BR	7	1.64 ± 0.86	2.84 ± 0.57
	on BR	5	0.98 ± 0.75	3.39 ± 0.66
	inside BR	4	0.50 ± 0.22	3.51 ± 1.32
37	outside BR	3	1.93 ± 2.22	2.67 ± 0.91
	on & near BR	3	0.92 ± 0.63	2.60 ± 0.57

Therefore our results appear to confirm the S^4F hypothesis.

From Table 4.3 we see that stars inside the bright rim have larger A_V values than those outside it in the case of BRCs 12 and 14, although the scatters are large again. This confirms the result of Matsuyanagi et al. (2006) for BRC 14 (but with a smaller difference between the regions in our case). It is natural in view of the above general trend of the stellar ages. In the case of BRCs 11NE and 37, however, no difference is found between the two regions.

4.5 Discussion and Conclusion

Lee et al. (2005) argued that the presence of TTSs only near and/or outside the surface of BRCs would clearly indicate the evidence for triggered star formation, and in their study of BRCs in the Orion region they actually found TTSs only between the BRCs and the OB stars. In the present study we locate some TTSs inside the bright rim. But their A_V values show that they are not deeply embedded in the BRC. Therefore their apparent location may be due to a projection effect and they may actually be located near the front surface of the BRC, so in reality similar to the “on BR” stars. The difference between Lee et al. (2005)’s

result and ours is probably due to the fact that our study is deeper and more small-scaled.

The regions in each BRC aggregate show big scatters of the ages of the member stars in spite of a clear trend of the mean ages. The reason for this is not clear, but we suspect that it is caused by the proper motions of newly born stars. Jones & Herbig (1979) showed that young stars in the Taurus molecular cloud have velocity dispersions of 1-2 km/s in one coordinate. If this value is applicable to BRC aggregates, the stars must have moved 2 pc or so (in projection) from their birth place in 1 Myr. Since the size of the BRC aggregates is ~ 0.2 pc (BRC 37) to ~ 2 pc (BRC 12), this is sufficiently large for some of the stars which formed 1 Myr ago to move into the (projected) inside of the present bright rim. We suspect that many stars in HII regions have their origin in already dispersed BRC aggregates except for the case where a rich cluster exists.

The stars outside a BRC (i.e., inside the HII region) have similar ages irrespective of the (projected) distance from the bright rim. It is our position that they essentially formed there inside the BRC that has since retreated to its present position. Then the above fact suggests that they were formed in the (first) collapse phase of the evolution of BRCs Lefloch & Lazareff (1994). Presumably BRCs may have a second (or, even third) collapse phase due to their clumpiness or as the exciting O star(s) evolve(s) and increase(s) its (their) UV photon emission, or somehow they give birth to stars after this phase (i.e., in the cometary phase); and the stars on or near the bright rim, which generally are younger, may correspond to such origin. It is interesting to note that among the aggregate regions in Table 4.3, those having the youngest mean age (i.e., inside/on BR of BRCs 12 and 14) show the smallest age scatter.

The age estimate from CMDs depends on the adopted distance; if we use a larger distance we get younger ages. For some BRCs in the SFO 91 the distances are not well determined. However, since the results given in Tables 4.2 and 4.3 are in a reasonable range and do not show any systematic differences between the BRCs, the distances adopted here are not in big error, presumably. Anyway, what is important in the present study is the relative ages among the stars in a BRC, and they are not changed by the error of the adopted distance. Another factor which affects the age estimation is duplicity of stars. On a CMD an unresolved

binary star can be placed at an elevated position (by up to 0.75 mag), which results in a younger age. Some of the stars which fall above the 1 Myr isochrone (see Figure 4.2) might be such stars. However, unresolved binaries must not be limited to this location, but exist among all the stars more or less equally on the CMDs. Therefore our main conclusion remain unchanged by this effect. We therefore conclude that our photometry of the BRC aggregates confirms the S^4F hypothesis.

Chapter 5

S^4F AND GLOBAL STAR FORMATION IN HII REGIONS ASSOCIATED WITH THE BRCs

5.1 Introduction

In chapter 4 sequential star formation on small scale in four BRC regions was studied. It will be interesting to study the global star formation scenario in the HII regions associated with the BRCs. In this chapter we have studied the star formation in six BRC regions using the spatial distribution of the YSOs and the variation of A_V and NIR excess from the ionising source(s) of the HII regions. As is discussed in chapter 4, S^4F hypothesis in four BRC regions was studied using the YSOs which were detected only through $H\alpha$ survey. Since many PMS stars also show NIR excess (as discussed in chapter 2) caused by the circumstellar disks, NIR photometric surveys have also emerged as a powerful tool to detect low mass PMS stars. Hence, we supplemented YSOs sample by including infrared excess stars from 2MASS survey. We have also used MIR photometry to identify deeply embedded YSOs to study the spatial distribution of the Class I and Class II sources.

¹The results presented in this chapter have been published in Chauhan et al. (2009)

Since, the best way to quantitatively testify the hypothesis is to estimate the ages of the aggregate members and to compare them between different regions with respect to the bright rim. Based on the BVI_c photometry of four BRC aggregates (BRCs 11NE, 12, 14 and 37) in chapter 4, we have shown that the stars inside or on the bright rim tend to have younger ages than those outside it, which is exactly what is expected from the S^4F hypothesis. To further confirm it and to investigate the star formation scenario in/around the BRCs, in this chapter we have extended BVI_c photometry to four more BRCs, namely BRCs 2, 13, 27 and 38. In addition to them BRCs 11NE and 14 were re-observed and analysed to obtain deeper data.

The information about the observations and archival data is given in sections 5.2 and 5.3, respectively. Section 5.4 describes the BRCs studied in the present work. The procedure to estimate age and mass of the YSOs is described in section 5.5. The star formation scenario in the BRC regions is studied in section 5.6. In section 5.7 the conclusions of this chapter are summarised.

5.2 Observations and Data reductions

BVI_c CCD observations of BRCs 2, 11NE, 13, 14 and 27 were carried out using the 2048×2048 pixel² CCD camera mounted on 2.0-m HCT, Hanle, India on 2006 October 27 and 28. The instrument HFOSC was used in the imaging mode. The sky at the time of observations was photometric with a seeing size (FWHM) of $\sim 1''.5$. The observations of the BRCs 2, 13, 27 were standardised on same night by observing standard stars in the SA113 field (Landolt 1992). The observations of BRCs 11NE and 14 were transformed to the standard system by using the BVI_c magnitudes given in chapter 4.

The BVI_c observations of BRC 38 were obtained by using the 2048×2048 pixel² CCD camera mounted at f/13 Cassegrain focus of the 1.04-m ST at ARIES, Nainital, India. The details of the CCD camera can be found in section 2.2.3. To improve the signal to noise ratio, the observations were carried out in a binning mode of 2×2 pixels. During the observations the seeing was about $2''.1$. SA98 field of (Landolt, 1992) was observed on 2006, October 26 to standardise the observations. The log of the HCT and ST observations is tabulated in Table 5.1.

5.2 Observations and Data reductions

Table 5.1: Log of optical observations

Region	Telescope	filter; exposure time(sec)×No. of frames	date of observations
BRC 2	HCT, Hanle	B : 600×4; V : 300×4; I _c : 180×4	2006.10.27
BRC 11	HCT, Hanle	B : 600×4; V : 300×4; I _c : 180×4	2006.10.28
BRC 13	HCT, Hanle	B : 600×4; V : 300×4; I _c : 180×4	2006.10.27
BRC 14	HCT, Hanle	B : 600×4; V : 300×4; I _c : 180×4	2006.10.27
BRC 27	HCT, Hanle	B : 600×4; V : 300×4; I _c : 180×4	2006.10.28
BRC 38	ST, Nainital	B :1800×4; V : 300×8; I _c : 600×3	2006.10.26

A number of bias and twilight flat frames were also taken during the observing runs.

The data analysis was carried out at ARIES, Nainital, India. The initial processing of the data frames was done using various tasks available under the IRAF data reduction software package. The photometric measurements of the stars were performed using DAOPHOT II software package (Stetson 1987). The PSF was obtained for each frame using several uncontaminated stars. Aperture photometry was carried out for the standard stars to estimate the atmospheric extinction and to calibrate the observations. The following transformation equations were used to calibrate the observations:

$$(B - V) = m_1(b - v) + c_1$$

$$(V - I_c) = m_2(v - i) + c_2$$

$$V = v + m_3(v - i) + c_3$$

where b , v , i are the instrumental magnitudes corrected for the atmospheric extinctions, and B , V , I_c are the standard magnitudes; c_1 , c_2 , c_3 and m_1 , m_2 , m_3 are zero-point constants and colour-coefficients, respectively. The values of the zero-point constants and the colour-coefficients are given in Table 5.2.

The standard deviations of the standardization residuals, Δ , between the standard and transformed magnitudes and colours of the standard stars, are found to be $\Delta V = 0.006$, $\Delta(B - V) = 0.007$ and $\Delta(V - I_c) = 0.007$ for the HCT data, whereas for the ST observations these values are 0.001, 0.010 and 0.002 respectively. The photometric accuracies depend on the brightness of the stars, and the typical DAOPHOT errors in B, V and I_c bands at $V \sim 18$ are smaller

Table 5.2: The zero-point constants, colour-coefficients and extinction-coefficients

Parameters	HCT	ST
Zero-point constants		
c1	-0.344 ± 0.024	-0.305 ± 0.011
c2	0.101 ± 0.005	0.541 ± 0.009
c3	-0.799 ± 0.017	-3.394 ± 0.010
colour-coefficients		
m1	0.855 ± 0.017	0.981 ± 0.008
m2	1.063 ± 0.005	0.990 ± 0.011
m3	0.078 ± 0.015	0.031 ± 0.009
Extinction-coefficients		
K_b	0.219 ± 0.009	0.301 ± 0.010
K_v	0.122 ± 0.007	0.199 ± 0.009
K_i	0.056 ± 0.008	0.088 ± 0.010

than 0.01 mag. Near the limiting magnitude of $V \sim 21$, which is practically the same for HCT and ST, the DAOPHOT errors increase to 0.11, 0.05, 0.02 mag in the B , V and I_c bands, respectively. The B , V and I_c photometric data for the stars along with their positions, equivalent widths (EWs) and corresponding 2MASS data are given in Table A.1.

5.3 Archive Data

5.3.1 Near-infrared data from 2MASS

NIR JHK_s data for the stars in the BRC regions have been obtained from the 2MASS Point Source Catalog (PSC) (Cutri et al., 2003). Sources having uncertainty ≤ 0.1 mag ($S/N \geq 10$) in all the three bands were selected to ensure high quality data. For BRC 14 we have adopted the JHK_s data by Matsuyanagi et al. (2006), which were obtained with the infrared camera SIRIUS mounted on the University of Hawaii 2.2-m telescope.

5.3.2 Mid Infrared data from Spitzer-IRAC

We have also used archived MIR data from IRAC of the *Spitzer* telescope. We obtained BCD using the software Leopard. Mosaicking was performed using the MOPEX software. Details of the telescope and instrument are given in section 2.4.2.1. All of our mosaics were built at the native instrument resolution of $1''.2/\text{pixel}$ with the standard BCDs. We used the standard IRAF photometry routines in the *apphot* package to detect sources and perform aperture photometry in each IRAC band. The FWHM of every detection is measured and all detections with $\text{FWHM} > 3''.6$ are considered resolved and removed. The detections are also examined visually in each band to remove non-stellar objects and false detections. The sources with photometric uncertainties ≤ 0.2 mag in each band were considered as good detections. The photometry was done using an aperture radius of $3''.6$ and the background estimation was done within a concentric sky annulus of the inner and outer radii of $3''.6$ and $8''.4$, respectively. We adopted the zero-point magnitudes for the standard aperture radius ($12''$) and background annulus of ($12''$ - $22''.4$) of 19.67, 18.93, 16.85 and 17.39 in the 3.6, 4.5, 5.8 and $8.0 \mu\text{m}$ bands, respectively. Aperture corrections were made using the values described in the IRAC Data Handbook (Reach et al. 2006).

5.4 Description of the BRCs studied

A brief description of BRCs studied is given below.

BRC 2 : Sharpless 171 (= NGC 7822) is a large HII region associated with the Cepheus OB4 association (Yang & Fukui 1992). This region contains three BRCs, BRCs 1-3 (SFO 91). A star cluster Be 59, containing nine O7-B3 stars, is located at the centre of the HII region. Recently, Pandey et al. (2008) have made photometric studies of Be 59 and its surrounding region in detail. The distance to the cluster was estimated to be 1.0 kpc. The age of these massive stars is found to be about 1-4 Myr with an average of ~ 2 Myr. It was also found that the stars around BRC 1, which is located about 3 pc towards west of Be 59, are younger than those in the cluster. This seems to support triggered star formation in the BRC 1 region due to the massive stars in Be 59.

BRC 2 is located about 17 pc north of Be 59. On the basis of MIR observations by IRAC of the *Spitzer Space Telescope*, Megeath et al. (2004) have reported a cluster of young stars near the edge of BRC 2. The distribution of YSOs suggests that their formation is triggered by a photo-evaporation driven shock propagating into the BRC 2 cloud.

BRCs 11NE, 13 and 14 : The large HII region IC 1848 = S199, associated with the radio source W5, is located in the Perseus arm at the distance of about 1.9 kpc (SFO 91). In fact it is composed of two adjacent HII regions namely, IC 1848W and IC 1848E (Karr & Martin 2003; Koenig et al. 2008; Vallee et al. 1979). IC 1848W is ionised by HD 17505 (O6V) and HD 17520 (O9V), whereas IC 1848E is ionised by HD 18326 (O7V). The former harbours a young cluster (age ~ 1 Myr; Feinstein et al. 1986). Carpenter et al. (2000) reported several deeply embedded star forming sites in the W3/W4/W5 region and put forward the notion of triggered star formation in this complex. Based on a multi-wavelength study of the W5 star forming region, Karr & Martin (2003) investigated the star formation scenario and supported triggered star formation in this region.

SFO 91 lists four BRCs, BRCs 11 - 14 around IC 1848. BRC 11 is situated near the southern edge of IC 1848W, BRC 12 near its northern edge and BRCs 13 and 14 at the eastern edge of IC 1848E. There are two more BRCs in the vicinity of BRC11, which are designated as BRC 11NE and BRC 11E, respectively, by Ogura et al. (2002). They are not listed in SFO 91 because of the lack of associated IRAS point sources. However, Ogura et al. (2002) found several H α emission stars in the vicinity of BRC 11NE in contrast to one or two in and around BRC 11 and BRC 11E. Moreover BRC 11NE appears to be associated with a more or less clear aggregate of young stars just outside its tip. So BRC 11NE was selected as one of the target BRCs in chapter 4 to show an age gradient. In the present study we have aimed to increase the sample stars for age determination by reaching a deeper limiting magnitude.

BRC 14 is associated with the molecular cloud IC 1848A to its east, which harbours a bright infrared young cluster AFGL 4029 (Deharveng et al. 1997). The optical and NIR study by these authors revealed that AFGL 4029 is an active star formation site. A deeper NIR survey of the BRC 14 region by Matsuyanagi et al. (2006) supports sequential star formation in this region propagating from

the west. In chapter 4 we determined the ages of the stars associated with BRC 14 and found a quantitative evidence for the S^4F hypothesis. We are repeating the study with deeper data for this BRC too.

BRC 27 : BRC 27 is located at the outer edge of S296 at a distance of 1.15 kpc (SFO 91) and associated with the active star forming region Canis Major R1 (CMa R1). The location of S296 coincides with the boundary of an expanding neutral hydrogen shell. Shevchenko et al. (1999) have estimated the ages of the stellar contents of CMa R1 ranging from < 1 Myr to 8 Myr. Herbst & Assousa (1977) suggested that the star formation in the CMa R1 region could have been triggered by a supernova explosion.

BRC 38 : Cepheus OB2, located at a distance of ~ 870 pc Contreras et al. (2002), is a complex of a stellar aggregate and a bubble-shaped structure of atomic and molecular gas (Patel et al. 1998, 1994). The clusters NGC 7160 and Tr 37 are located near the centre of the bubble and near its edge, respectively. There is evidence that the star formation at the edge of the bubble was triggered by a supernova explosion which took place near the centre of the bubble (Sicilia-Aguilar et al. 2004, 2005). Tr 37 harbours an O6 star HD 206267, which excites the relatively evolved HII region IC 1396. The age of Tr 37 is estimated as ~ 3 -5 Myr (Contreras et al. 2002). IC 1396 has a rich population of BRCs including BRCs 32-42 (SFO 91), among which BRCs 37 and 38 have been studied extensively (see, e.g., Getman et al. 2007; Ikeda et al. 2008). In particular, chapter 4 reported quantitative evidence for S^4F in BRC 37, and Ikeda et al. (2008) confirmed sequential star formation in this region. Getman et al. (2007) provided detailed qualitative discussion on S^4F based on the *Chandra* X-ray data for BRC 38.

5.5 Membership and Age determination of member stars

Since BRCs are found at low galactic latitudes, the fields can be significantly contaminated by foreground/background stars. To understand star formation in

5.5 Membership and Age determination of member stars

BRCs we selected probable members associated with the BRCs using the following criteria.

In the present study we use $H\alpha$ emission stars found by Ogura et al. (2002) in the vicinity of BRCs. However, some of them may not be directly associated with the BRCs (see section 6.2).

To identify NIR excess stars from the 2MASS PSC, we used NIR $(J - H)/(H - K)$ NIR-CC diagrams as discussed in section 2.5.2.2. Figure 5.1 shows NIR-CC diagrams for the studied BRCs. However, we selected only those $H\alpha$ emission stars, as probable members associated with the BRCs, that lie rightward of the upper reddening line. It is worthwhile, however, to mention that Robitaille et al. (2006) have recently shown that there is a significant overlap between protostars and CTTSs in the NIR-CC space.

The spatial distribution of the probable YSOs (i.e., $H\alpha$ emission and NIR excess stars) for each BRC is shown in Fig. 5.2. In Fig. 5.2 we have also demarcated the two regions for each BRC, i.e., on/inside and outside the bright rim. The NIR-CC diagrams (Fig. 5.1) were used to estimate A_V for each of these stars by tracing back to the intrinsic CTTS line of Meyer et al. (1997) along the reddening vector (for details see section 2.5.3.1). The A_V for stars lying in the ‘F’ region is estimated by tracing them back to the extension of the intrinsic CTTS line. Fig. 5.3 shows dereddened $V_0, (V - I_c)_0$ CMDs for those stars.

In Fig. 5.3 the post-main sequence isochrone for 2 Myr by Girardi et al. (2002), which is practically a ZAMS line, and PMS isochrones for 1, 3, 10, 30 Myr for the solar metallicity by Siess et al. (2000) are also plotted. The distances are taken from SFO 91 barring for BRC 38. In the case of BRC 38 a distance of 870 pc has been adopted from Contreras et al. (2002). The age of each YSO was estimated by referring to the isochrones. The mass of the YSOs was estimated using the $V_0/(V - I_c)_0$ CMD as discussed in Pandey et al. (2008). The resultant A_V values, ages and masses are given in Table 5.3.

The ages range from 0.1 to a few Myr (with some exceptions) which are comparable with the lifetime of T-Tauri stars (TTSs). The masses of these YSOs, range from ~ 0.1 - $2.0 M_\odot$, further indicate that they are probable TTSs and their siblings.

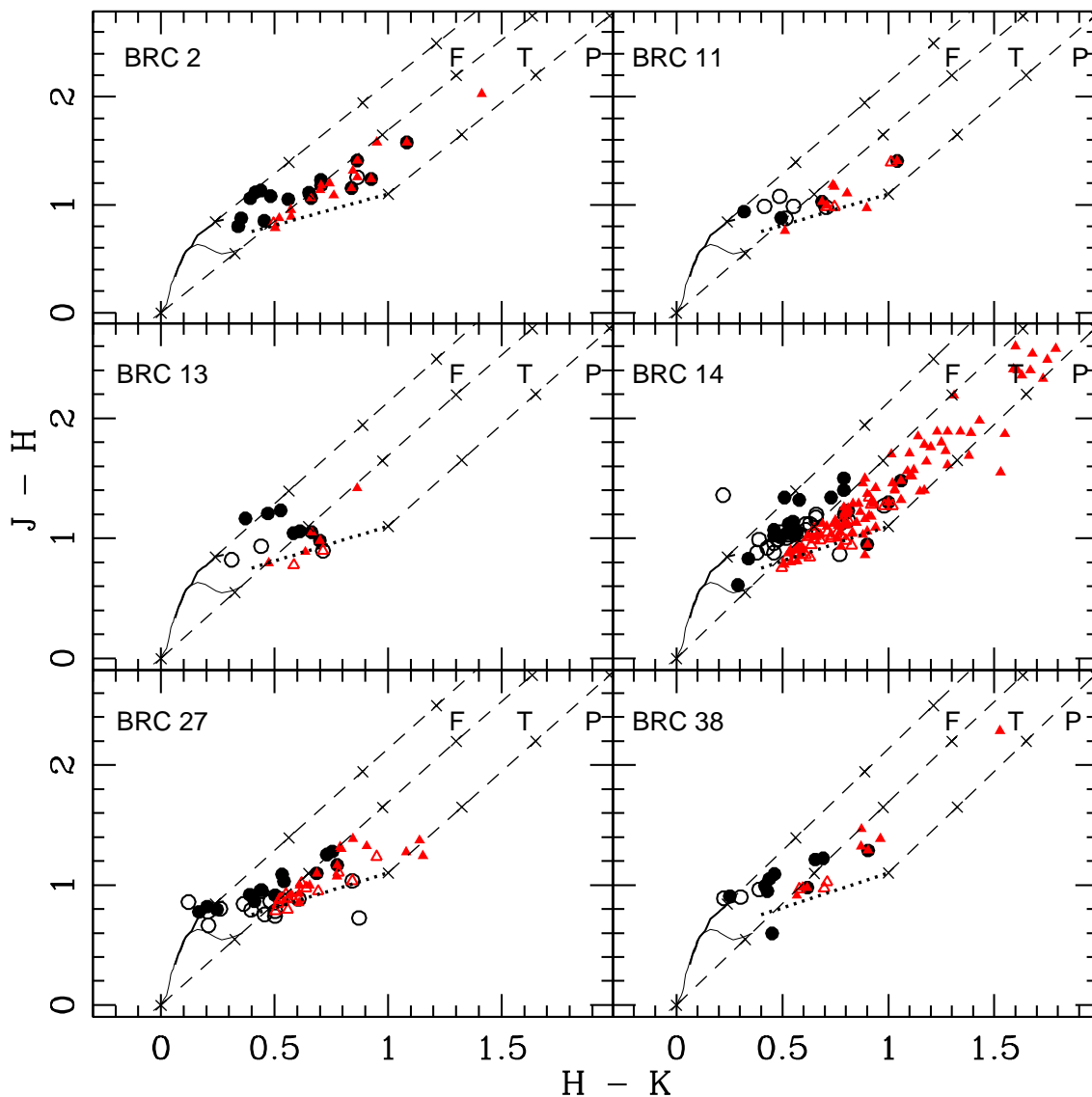


Figure 5.1: $(J - H)/(H - K)$ colour-colour diagrams for BRCs 2, 11NE, 13, 14, 27 and 38. The sequences for dwarfs (thin solid curve) and giants (thick solid curve) are from Bessell & Brett (1988). The dotted line represents the intrinsic locus of CTTSs (Meyer et al. 1997). The three parallel dashed lines represent the reddening vectors. The crosses on the dashed lines are separated by $A_V = 5$ mag. The open and filled circles are $H\alpha$ emission stars lying in outside and on/inside the bright rims (see Fig. 5.2) respectively. The open and filled triangles are NIR excess stars lying in outside and on/inside the bright rims respectively.

5.5 Membership and Age determination of member stars

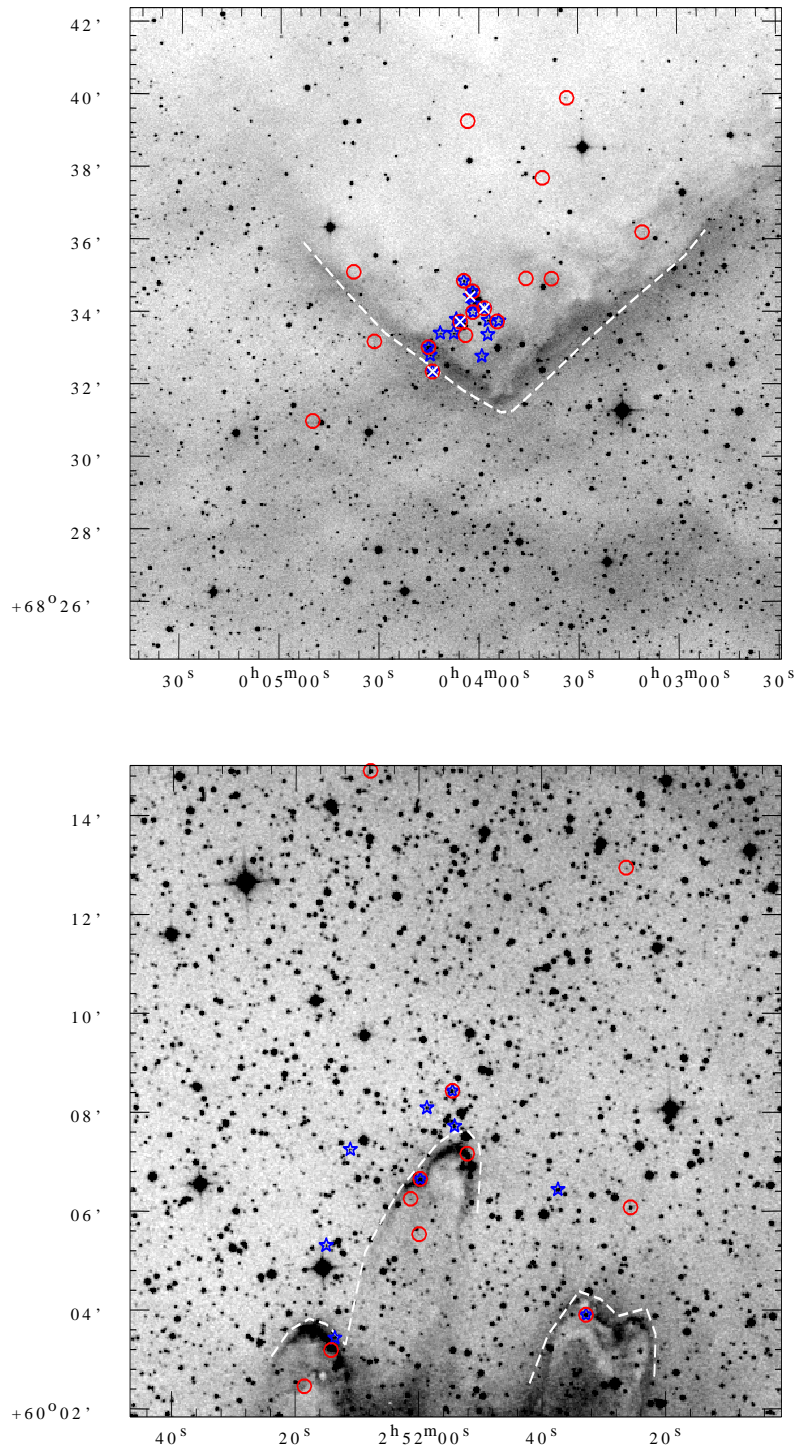


Figure 5.2: Spatial distribution of H α emission (star symbol) and NIR excess (open circle) stars overlaid on DSS2 R-band image of BRC 2 (*upper panel*); and BRC 11NE (*lower panel*). Dashed line demarcates the regions on/ inside and outside bright-rims. White crosses represent H α emission stars having ages larger than 5 Myr (see, section 6.2 and Fig. 6.1).

5.5 Membership and Age determination of member stars

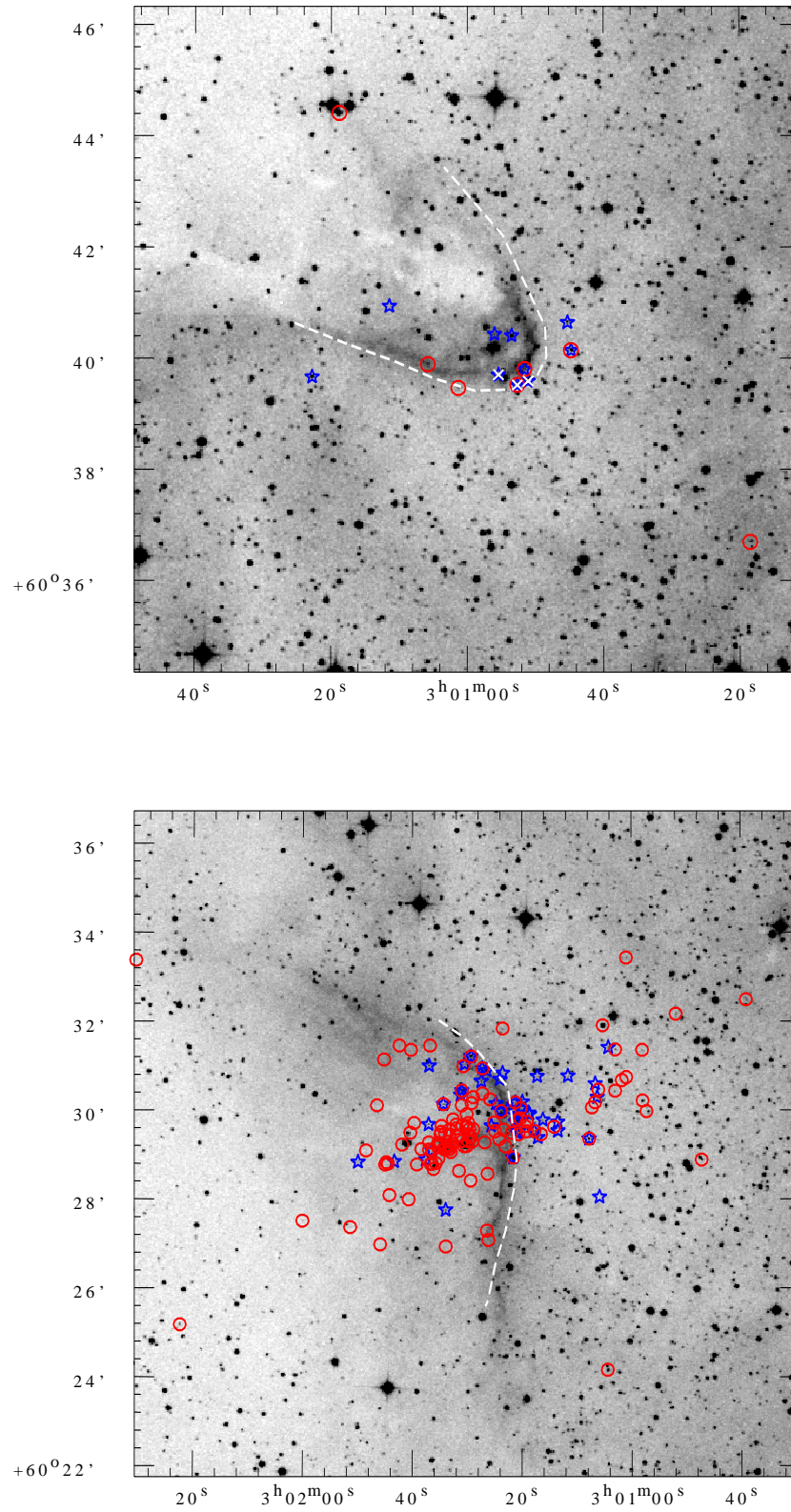


Figure 5.2 cont. BRC 13 (*upper panel*); BRC 14 (*lower panel*).

5.5 Membership and Age determination of member stars

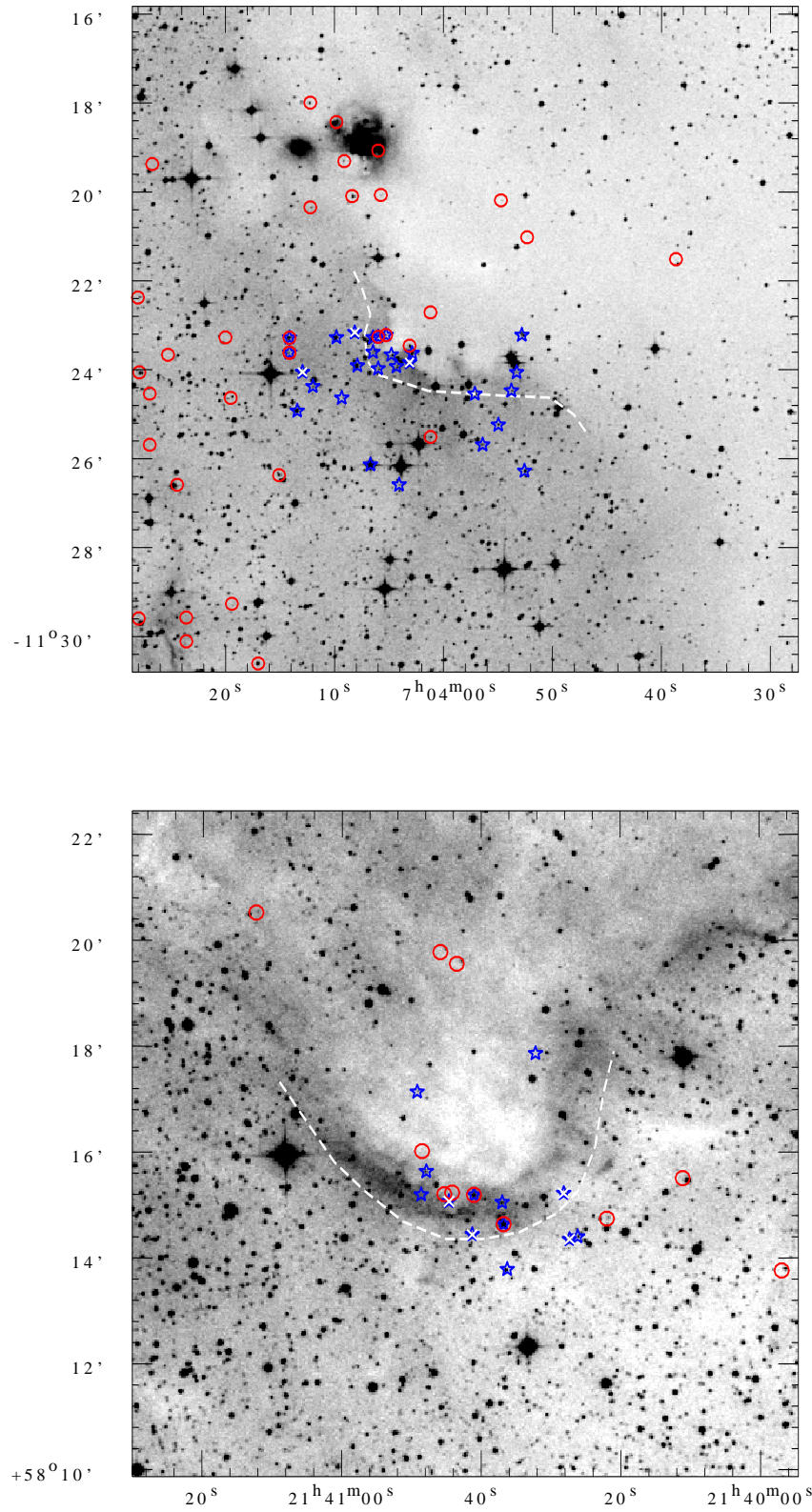


Figure 5.2 cont. BRC 27 (*upper panel*); BRC 38 (*lower panel*).

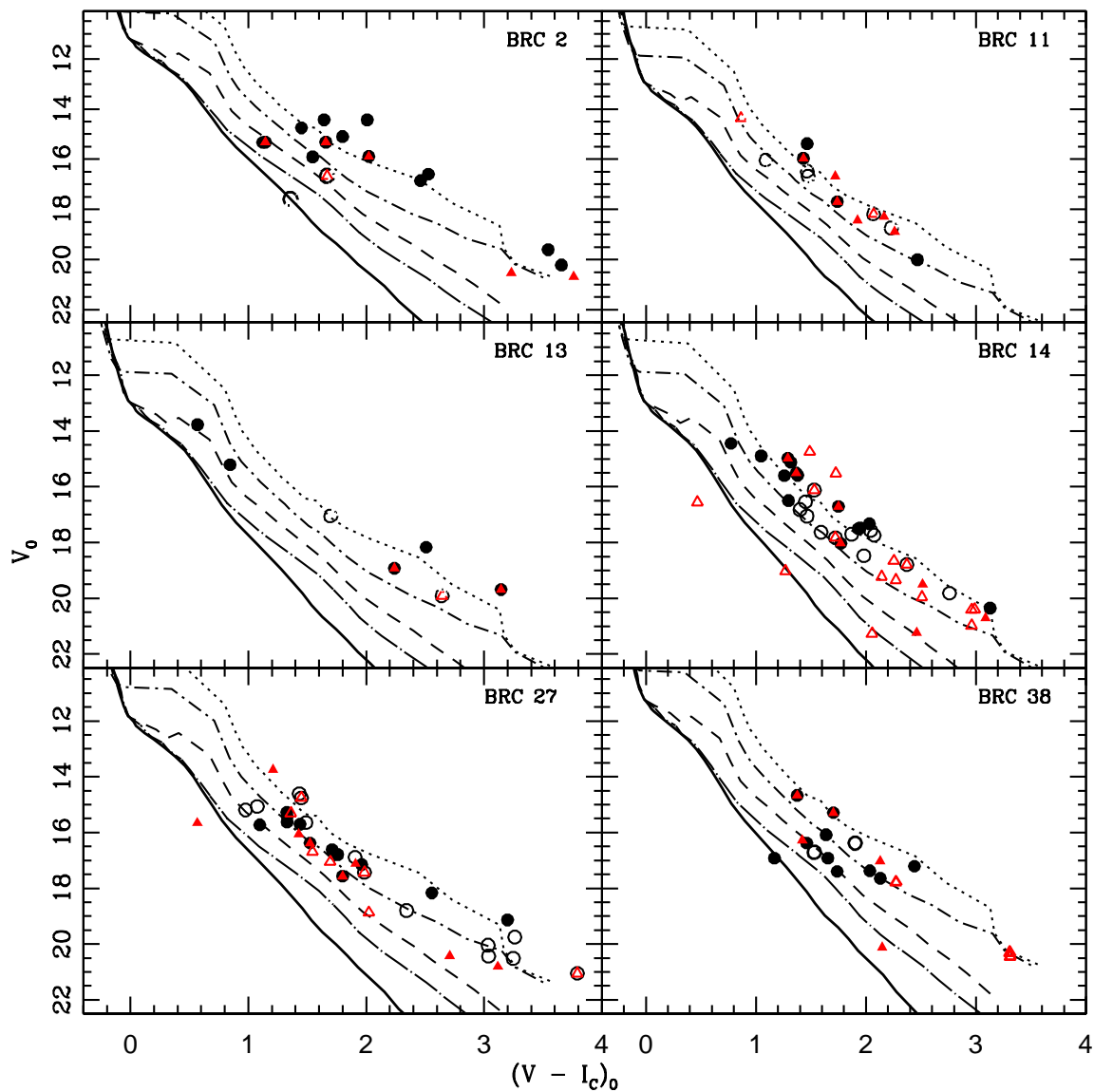


Figure 5.3: $V_0/(V - I_c)_0$ colour-magnitude diagrams for probable YSOs in BRCs 2, 11NE, 13, 14, 27 and 38. The 2 Myr isochrone (thick curve) by Girardi et al. (2002) and PMS isochrones of 1 (dotted), 3 (dashed-dotted), 10 (dashed), 30 (large dashed-dotted) Myr by Siess et al. (2000) are also shown. All the isochrones are corrected for the distances of the respective BRCs. The symbols are same as in Fig. 5.1.

5.5 Membership and Age determination of member stars

Table 5.3: Dereddened magnitude, colours, age, and mass of the YSOs associated with the BRCs.

S.No.	RA (2000)	DEC (2000)	V_0 (mag)	$(B-V)_0$ (mag)	$(V-I)_0$ (mag)	$A_V \pm \sigma$ (mag)	Age $\pm \sigma$ (Myr)	Mass $\pm \sigma$ (M_\odot)	ID (Ogura et al. 2002)
BRC 2									
1	00 03 57.1	+68 33 46.4	15.101	1.149	1.800	3.0 \pm 0.4	0.7 \pm 0.0	0.52 \pm 0.01	5
2	00 03 57.3	+68 33 23.0	19.604	-	3.543	2.9 \pm 0.5	0.3 \pm 0.0	0.14 \pm 0.01	6
3	00 03 59.1	+68 32 47.4	20.219	-	3.656	0.9 \pm 0.5	0.3 \pm 0.0	0.11 \pm 0.01	8
4	00 04 01.6	+68 34 14.2	15.911	-	1.546	2.1 \pm 0.5	4.0 \pm 0.9	0.78 \pm 0.06	9
5	00 04 01.8	+68 34 00.1	16.857	-	2.460	5.9 \pm 0.5	1.1 \pm 0.1	0.30 \pm 0.02	10
6	00 04 01.8	+68 34 34.3	14.431	1.246	2.008	2.5 \pm 0.6	0.1 \pm 0.0	0.47 \pm 0.01	12
7	00 04 02.6	+68 34 26.0	15.329	-	1.123	4.2 \pm 0.6	16.1 \pm 3.0	1.11 \pm 0.04	14
8	00 04 07.6	+68 33 24.8	14.750	0.995	1.451	4.9 \pm 0.4	1.2 \pm 0.1	0.85 \pm 0.03	21
9	00 04 11.7	+68 33 25.2	16.596	-	2.527	3.9 \pm 0.4	0.2 \pm 0.1	0.29 \pm 0.00	22
10	00 04 15.2	+68 33 01.8	14.428	1.170	1.643	2.2 \pm 0.4	0.6 \pm 0.0	0.63 \pm 0.01	25
11	00 03 58.4	+68 34 06.6	15.320	-	1.144	5.4 \pm 0.4	12.3		7
12	00 04 04.6	+68 34 52.0	15.891	1.298	2.022	3.5 \pm 0.4	0.9 \pm 0.0	0.40 \pm 0.01	16
13	00 04 05.6	+68 33 44.3	15.319	-	1.658	2.0 \pm 0.4	1.2 \pm 0.1	0.63 \pm 0.02	19
14	00 03 38.0	+68 34 55.6	20.526	-	3.231	0.7 \pm 0.6	4.5 \pm 0.2	0.14 \pm 0.02	
15	00 03 54.5	+68 33 43.2	20.680	-	3.761	2.2 \pm 0.4	1.0	0.09 \pm 0.01	
16	00 04 14.0	+68 32 21.5	16.680	0.921	1.665	3.2 \pm 0.5	6.7 \pm 1.1	0.68 \pm 0.03	23
17	00 04 14.7	+68 32 48.8	17.600	-	1.355	4.3 \pm 0.4	>30		24
BRC 11NE									
18	02 51 37.4	+60 06 26.6	16.495	1.028	1.463	2.0 \pm 0.6	1.5 \pm 0.2	0.91 \pm 0.01	1
19	02 51 54.5	+60 08 26.6	18.196	1.485	2.065	0.6 \pm 0.6	1.3 \pm 0.1	0.44 \pm 0.01	4
20	02 51 58.7	+60 08 05.8	18.760	1.421	2.226	0.7 \pm 0.5	1.5 \pm 0.1	0.35 \pm 0.01	5
21	02 52 11.1	+60 07 15.2	16.047	0.674	1.087	3.8 \pm 0.7	4.5 \pm 0.8	1.45 \pm 0.05	7
22	02 52 15.1	+60 05 18.5	16.692	0.557	1.471	3.1 \pm 0.6	1.5 \pm 0.2	0.83 \pm 0.04	8
23	02 51 54.2	+60 07 43.5	15.384	0.927	1.465	3.2 \pm 0.5	0.5 \pm 0.0	0.96 \pm 0.03	3
24	02 51 59.7	+60 06 39.3	17.693	1.172	1.739	1.5 \pm 0.6	1.7 \pm 0.2	0.58 \pm 0.02	6
25	02 51 52.1	+60 07 10.0	16.677	1.157	1.720	1.7 \pm 0.4	0.7 \pm 0.1	0.59 \pm 0.03	
26	02 52 01.3	+60 06 15.3	18.891	-	2.261	3.0 \pm 0.7	1.7 \pm 0.1	0.34 \pm 0.01	
27	02 51 59.9	+60 05 32.0	18.437	-	1.924	3.3 \pm 1.1	2.1 \pm 0.5	0.46 \pm 0.03	
BRC 11									
28	02 51 32.8	+60 03 54.3	15.967	-	1.431	3.9 \pm 0.4	0.9 \pm 0.1	0.97 \pm 0.03	1
29	02 51 25.6	+60 06 04.8	14.372	0.353	0.860	4.0 \pm 0.5	2.7 \pm 0.3	2.2 \pm 0.08	
BRC 11E									
30	02 52 13.6	+60 03 26.2	20.008	-	2.468	1.0 \pm 0.9	2.9 \pm 0.3	0.27 \pm 0.01	1
31	02 52 14.2	+60 03 11.7	18.291	0.347	2.165	0.8 \pm 0.5	1.2 \pm 0.1	0.36 \pm 0.01	
BRC 13									
32	03 00 51.1	+60 39 36.3	15.917	0.887	-	2.6 \pm 0.6	8.0 \pm 1.3	1.45 \pm 0.04	6
33	03 00 51.6	+60 39 48.9	19.684	-	3.144	2.00 \pm 0.6	0.1 \pm 0.0	0.19 \pm 0.01	7
34	03 00 52.7	+60 39 31.6	18.923	1.371	2.239	0.7 \pm 0.6	1.7 \pm 0.1	0.34 \pm 0.01	10
35	03 00 53.6	+60 40 24.9	13.770	0.492	0.569	5.9 \pm 0.6	8.6 \pm 0.8	1.72 \pm 0.04	11
36	03 00 55.4	+60 39 42.7	15.210	-	0.845	5.6 \pm 0.9	8.0 \pm 1.4	1.41 \pm 0.05	12
37	03 00 56.0	+60 40 26.3	18.169	-	2.508	2.5 \pm 0.7	0.1 \pm 0.0	0.29 \pm 0	13
38	03 00 44.8	+60 40 09.1	19.923	1.974	2.640	0 \pm 0.5	2.2 \pm 0.1	0.36 \pm 0.00	2
39	03 00 45.3	+60 40 39.5	17.059	1.329	1.695	1.7 \pm 0.5	1.0 \pm 0.1	0.60 \pm 0.02	3
BRC 14									
40	03 01 24.0	+60 30 42.2	17.480	-	1.947	3.9 \pm 0.1	0.9 \pm 0.0	0.45 \pm 0.02	29
41	03 01 24.7	+60 30 09.6	15.586	-	1.379	6.4 \pm 0.1	0.7 \pm 0.1	0.98 \pm 0.08	30
42	03 01 25.6	+60 29 39.0	15.597	-	1.258	4.1 \pm 0.1	1.1 \pm 0.1	1.20 \pm 0.01	31
43	03 01 26.4	+60 30 53.9	15.126	1.068	1.317	3.2 \pm 0.1	0.5 \pm 0.0	1.10 \pm 0.0	32
44	03 01 27.2	+60 30 56.9	18.031	-	1.771	2.9 \pm 0.3	2.3 \pm 0.2	0.56 \pm 0.02	33
45	03 01 27.4	+60 30 39.7	16.498	0.899	1.295	4.2 \pm 0.1	2.7 \pm 0.3	1.11 \pm 0.04	34
46	03 01 29.3	+60 31 13.6	15.511	1.001	1.366	2.8 \pm 0.1	0.7 \pm 0.1	0.99 \pm 0.01	35
47	03 01 34.0	+60 27 45.6	17.503	1.428	1.931	2.9 \pm 0.1	0.9 \pm 0	0.45 \pm 0.01	39
48	03 01 34.4	+60 30 08.5	14.977	-	1.290	5.5 \pm 0.1	0.5 \pm 0.0	1.19 \pm 0.03	40
49	03 01 36.4	+60 29 06.1	16.706	-	1.749	4.8 \pm 0.1	0.7 \pm 0.0	0.55 \pm 0.03	41
50	03 01 37.0	+60 31 00.2	17.326	-	2.031	3.1 \pm 0.1	0.7 \pm 0.0	0.39 \pm 0.01	42
51	03 01 37.1	+60 29 41.2	20.355	-	3.128	0 \pm 0.2	0.3 \pm 0.0	1.80 \pm 0.00	43
52	03 01 43.3	+60 28 51.5	14.893	-	1.047	7.2 \pm 0.1	1.4 \pm 0.3	1.79 \pm 0.11	46

5.5 Membership and Age determination of member stars

Table 5.3 cont.

53	03 01 50.0	+60 28 50.5	14.444	-	0.773	7.3 ± 0.1	5.6 ± 1.7	1.90 ± 0.18	47
54	03 01 04.2	+60 31 25.3	16.820	-	1.400	3.8 ± 0.1	2.4 ± 0.2	0.94 ± 0.03	1
55	03 01 06.2	+60 30 17.6	17.572	0.763	2.043	3.1 ± 0.1	0.9 ± 0.1	0.29 ± 0.01	3
56	03 01 06.6	+60 30 36.0	19.819	-	2.760	2.5 ± 0.3	1.5 ± 0.3	0.26 ± 0.01	4
57	03 01 07.7	+60 29 21.8	16.119	1.233	1.530	2.2 ± 0.1	0.8 ± 0.0	0.75 ± 0.00	5
58	03 01 11.5	+60 30 46.3	18.474	-	1.981	2.4 ± 0.3	1.8 ± 0.2	0.42 ± 0.04	6
59	03 01 13.4	+60 29 31.9	17.696	-	1.871	4.1 ± 0.1	1.2 ± 0.1	0.48 ± 0.02	8
60	03 01 16.1	+60 29 47.1	17.738	-	2.075	3.4 ± 0.1	0.9 ± 0.0	0.38 ± 0.01	10
61	03 01 17.0	+60 29 23.2	16.532	1.359	1.451	3.4 ± 0.1	1.3 ± 0.1	0.85 ± 0.02	12
62	03 01 20.3	+60 30 02.3	17.826	-	1.723	2.5 ± 0.1	2.1 ± 0.1	0.59 ± 0.01	18
63	03 01 20.6	+60 29 31.7	17.630	0.904	1.592	3.1 ± 0.1	3.1 ± 0.3	0.72 ± 0.02	20
64	03 01 21.2	+60 29 44.3	17.052	-	1.464	3.3 ± 0.1	2.4 ± 0.2	0.85 ± 0.03	23
65	03 01 21.2	+60 30 10.5	18.789	-	2.372	2.2 ± 0.1	1.3 ± 0.0	0.33 ± 0.01	24
66	03 01 32.0	+60 29 36.3	21.235	-	2.460	0.7 ± 0.3	9.0 ± 1.2	0.23 ± 0	
67	03 01 21.9	+60 29 29.5	19.493	-	2.515	1.1 ± 0.9	1.7 ± 0.2	0.28 ± 0.01	
68	03 01 51.4	+60 27 22.7	20.701	-	3.087	1.6 ± 0.9	0.9 ± 0.7	0.17 ± 0.01	
69	03 01 19.4	+60 29 38.9	21.266	-	2.055	0.7 ± 0.2	>30		
70	03 00 47.1	+60 28 53.6	19.343	-	2.273	1.0 ± 0.7	2.3 ± 0.2	0.33 ± 0.01	
71	03 01 20.3	+60 29 49.3	14.746	1.183	1.490	0 ± 0.4	0.3 ± 0.1	0.89 ± 0.04	
72	03 01 23.5	+60 31 50.6	19.226	-	2.143	1.6 ± 1.2	2.6 ± 0.5	0.36 ± 0.02	
73	03 01 14.1	+60 29 37.4	21.553	-	2.357	0 ± 0.1	>15		
74	03 01 01.1	+60 30 45.2	19.026	-	1.269	2.0 ± 0.1	>30		
75	03 00 58.0	+60 30 13.4	18.655	-	2.253	1.1 ± 0.6	1.4 ± 0.1	0.35 ± 0.01	
76	03 01 00.9	+60 33 26.7	20.402	-	2.989	0.3 ± 1.1	1.8 ± 0.4	0.21 ± 0.01	
77	03 01 02.9	+60 31 22.4	20.978	-	2.961	0.1 ± 1.3	2.8 ± 0.3	0.17 ± 0.02	
78	03 00 57.9	+60 31 21.7	20.406	-	2.961	0.4 ± 0.0	1.8	0.19	
79	03 00 51.8	+60 32 10.8	19.960	-	2.510	0.8 ± 1.3	2.6 ± 0.4	0.27 ± 0.01	
80	03 01 05.2	+60 31 55.4	15.523	1.334	1.727	0.8 ± 0.3	0.1 ± 0.0	0.61 ± 0.01	
BRC 27									
81	07 03 52.8	-11 23 13.2	15.278	0.860	1.326	2.2 ± 0.6	2.0 ± 0.5	1.05 ± 0.09	2
82	07 03 53.8	-11 24 28.4	18.164	-	2.557	1.9 ± 0.6	1.4 ± 0.1	0.29 ± 0.01	4
83	07 03 57.1	-11 24 32.8	16.618	0.920	1.711	2.5 ± 0.4	1.9 ± 0.2	0.60 ± 0.01	7
84	07 04 02.9	-11 23 37.3	15.426	0.642	1.330	3.6 ± 0.6	2.3 ± 0.5	1.03 ± 0.08	8
85	07 04 03.1	-11 23 50.6	15.726	-	1.097	4.5 ± 0.7	11.2 ± 1.1	1.19 ± 0.01	10
86	07 04 04.3	-11 23 55.7	17.151	0.637	1.962	2.5 ± 0.6	1.5 ± 0.2	0.44 ± 0.01	12
87	07 04 04.8	-11 23 39.8	15.620	0.920	1.329	2.7 ± 0.5	3.0 ± 0.5	1.06 ± 0.55	14
88	07 04 05.3	-11 23 13.2	16.378	0.660	1.523	2.7 ± 0.9	3.4 ± 0.8	0.80 ± 0.05	15
89	07 04 06.0	-11 23 58.9	16.791	1.188	1.758	1.4 ± 0.4	1.9 ± 0.2	0.56 ± 0.02	16
90	07 04 06.0	-11 23 15.7	17.568	-	1.800	2.5 ± 0.7	4.5 ± 0.8	0.54 ± 0.03	17
91	07 04 06.5	-11 23 36.2	19.134	-	3.199	1.5 ± 0.6	0.2 ± 0.0	0.18 ± 0.01	18
92	07 04 06.5	-11 23 16.4	15.700	0.933	1.439	2.4 ± 0.7	1.9 ± 0.3	0.88 ± 0.04	19
93	07 03 52.6	-11 26 16.8	15.064	0.907	1.076	1.8 ± 0.4	5.3 ± 0.4	1.43 ± 0.02	1
94	07 03 55.0	-11 25 14.5	16.887	1.067	1.906	1.9 ± 0.5	1.4 ± 0.1	0.47 ± 0.01	5
95	07 03 56.4	-11 25 41.5	20.435	-	3.039	0 ± 0.9	3.2 ± 1.4	0.14 ± 0.01	6
96	07 04 04.1	-11 26 35.5	20.515	-	3.247	0 ± 0.8	0.9	0.11 ± 0.01	11
97	07 04 08.2	-11 23 54.6	15.644	1.136	1.488	0.3 ± 0.5	1.5 ± 0.1	0.81 ± 0.02	22
98	07 04 08.2	-11 23 09.6	18.795	1.066	2.343	1.5 ± 1.1	3.2 ± 0.5	0.30 ± 0.01	23
99	07 04 09.4	-11 24 38.1	21.053	-	3.792	0 ± 0.6	0.3 ± 0.1	0.10 ± 0.00	24
100	07 04 09.8	-11 23 16.4	14.759	1.039	1.449	0.4 ± 0.3	0.6 ± 0.1	0.85 ± 0.02	25
101	07 04 12.0	-11 24 23.0	19.751	-	3.261	0.6 ± 0.7	0.3 ± 0.0	0.14 ± 0.00	27
102	07 04 13.0	-11 24 03.2	15.189	0.744	0.976	2.4 ± 0.7	9.4 ± 2.5	1.34 ± 0.07	28
103	07 04 13.4	-11 24 55.8	14.604	1.043	1.432	0.9 ± 0.3	0.6 ± 0.1	0.89 ± 0.02	29
104	07 04 14.2	-11 23 17.2	17.430	1.365	1.985	0.2 ± 0.3	1.9 ± 0.1	0.42 ± 0.01	31
105	07 04 14.2	-11 23 37.3	20.043	-	3.034	0.8 ± 0.8	2.9 ± 0.3	0.18 ± 0.01	32
106	07 04 08.4	-11 20 05.3	17.122	1.258	1.909	1.7 ± 0.4	1.7 ± 0.1	0.46 ± 0.01	
107	07 04 03.1	-11 23 27.6	13.749	-	1.209	5.2 ± 0.5	0.6 ± 0.1	1.38 ± 0.06	
108	07 03 54.7	-11 20 11.0	20.425	-	2.709	1.0 ± 1.0	6.3 ± 0.9	0.2 ± 0.01	
109	07 03 52.3	-11 21 01.1	20.808	-	3.117	1.4 ± 0.9	4.0 ± 0.4	0.11 ± 0.01	
110	07 04 12.2	-11 20 20.8	15.657	-	0.567	4.7 ±	>30		
111	07 04 05.8	-11 20 03.8	16.059	-	1.428	4.4 ± 0.6	3.5 ± 1.2	0.92 ± 0.09	
112	07 04 16.8	-11 24 32.4	16.685	0.669	1.545	0.3 ± 0.4	4.7 ± 0.5	0.79 ± 0.02	
113	07 04 15.1	-11 26 22.6	15.313	0.868	1.362	1.9 ± 0.4	1.7 ± 0.2	0.97 ± 0.05	
114	07 04 19.9	-11 22 22.4	17.050	0.979	1.695	1.2 ± 0.3	3.7 ± 0.4	0.63 ± 0.02	
115	07 04 15.1	-11 23 39.8	18.869	-	2.023	1.8 ± 1.0	8.9 ± 2.4	2.02 ± 0.02	

5.6 Star Formation Scenario in BRC Regions

Table 5.3 cont.

BRC 38									
116	21 40 26.2	+58 14 24.7	16.917	1.035	1.168	3.3 ±0.8	>30		1
117	21 40 28.1	+58 15 14.4	16.375	-	1.460	3.8 ±0.5	11.3 ±1.9	0.87 ±0.03	3
118	21 40 31.7	+58 17 55.3	16.082	1.119	1.637	4.2 ±0.4	3.1 ±0.4	0.67 ±0.02	4
119	21 40 37.0	+58 14 38.0	15.288	1.382	1.704	1.4 ±0.4	0.9 ±0.0	0.59 ±0.02	6
120	21 40 37.0	+58 15 03.2	17.644	1.086	2.130	2.5 ±0.5	3.0 ±0.3	0.36 ±0.01	7
121	21 40 41.3	+58 15 11.5	14.673	0.917	1.374	3.4 ±0.4	1.5 ±0.2	0.95 ±0.04	9
122	21 40 41.5	+58 14 25.8	17.398	0.913	1.738	3.2 ±0.4	12.3 ±1.8	0.61 ±0.02	10
123	21 40 44.9	+58 15 03.6	16.921	-	1.653	4.3 ±0.5	9.5 ±2.1	0.7 ±0.04	11
124	21 40 48.0	+58 15 37.8	17.209	1.005	2.441	3.3 ±0.4	1.3 ±0.1	0.3	12
125	21 40 49.0	+58 17 09.6	17.374	-	2.035	4.2 ±0.5	2.9 ±0.4	0.39 ±0.02	15
126	21 40 27.4	+58 14 21.5	16.709	0.625	1.530	3.0 ±0.5	11.9 ±2.5	0.8 ±0.02	2
127	21 40 36.5	+58 13 46.2	16.379	1.331	1.902	2.8 ±0.4	1.5 ±0.1	0.47 ±0.01	5
128	21 40 42.7	+58 19 37.6	17.030	-	2.129	4.1 ±0.4	1.7 ±0.1	0.37 ±0.01	
129	21 41 12.0	+58 20 33.7	20.125	-	2.148	1.6 ±1.2	>30		
130	21 40 45.1	+58 19 50.2	16.277	-	1.421	6.1 ±0.4	10.2	0.84 ±0.03	
131	21 39 49.2	+58 14 37.0	20.312	1.930	3.308	0.8 ±0.4	3.1 ±0.3	0.13 ±0.01	
132	21 39 56.4	+58 13 47.7	17.783	1.584	2.274	1.3 ±0.4	2.5 ±0.2	0.33 ±0.01	
133	21 40 21.8	+58 14 45.6	20.447	1.749	3.312	0.7 ±0.5	3.6 ±0.5	0.13 ±0.01	

Here we would like to point out that the estimation of the ages of the PMS stars by comparing the observations with the theoretical isochrones is prone to errors as discussed in section 2.5.4. Here we would like to point out that we are interested mainly in the *relative* ages of the aggregate members, in particular, the spatial differences with respect to the bright rim.

5.6 Star Formation Scenario in BRC Regions

Propagating star formation, where energetic activity of massive stars compresses the surrounding gas and triggers the formation of new generation of stars at the peripheries of HII regions (see e.g. Elmegreen 1998), is quite common in the Galaxy. Some different triggering mechanisms may work in such regions. Briefly, the process which has been frequently supported by the observations is RDI, which takes place in small remnant clouds such as BRCs. The signature of star formation due to RDI is the presence of bright rims and embedded IR sources just inside the dense head. The collect-and-collapse model is another mechanism proposed by Elmegreen & Lada (1977). The signature of this process are the presence of a collected, dense layer adjacent to the I-front and the presence of massive condensations in it (e.g. Deharveng et al. 2003).

5.6 Star Formation Scenario in BRC Regions

Table 5.4: Average age of the YSOs associated with the inside/outside regions of the BRCs.

BRC	Region	No. of stars	Mean age \pm std dev (Myr)	Mean A_V \pm std dev (mag)
Only Hα stars				
BRC 2	On/Inside BR	11	1.0 ± 1.0	3.1 ± 1.4
	Outside BR	-	-	-
BRC 11	On/Inside BR	4	1.5 ± 1.1	2.4 ± 1.4
	Outside BR	5	2.1 ± 1.4	2.1 ± 1.4
BRC 13	On/Inside BR	3	0.6 ± 0.9	1.7 ± 0.9
	Outside BR	2	1.6 ± 0.9	1.7
BRC 14	On/Inside BR	13	1.0 ± 0.7	3.9 ± 1.8
	Outside BR	12	1.6 ± 0.7	3.0 ± 0.6
BRC 27	On/Inside BR	11	2.2 ± 1.1	2.3 ± 0.6
	Outside BR	12	2.2 ± 2.5	0.7 ± 0.7
BRC 38	On/Inside BR	6	2.1 ± 1.0	3.2 ± 1.1
	Outside BR	1	1.5	2.8
Hα and NIR excess stars				
BRC 2	On/Inside BR	13	1.0 ± 1.0	3.0 ± 1.4
	Outside BR	-	-	-
BRC 11	On/Inside BR	8	1.5 ± 0.8	2.3 ± 1.2
	Outside BR	6	2.1 ± 1.3	2.4 ± 1.5
BRC 13	On/Inside BR	3	0.6 ± 0.9	1.8 ± 0.9
	Outside BR	2	1.6 ± 0.8	1.7
BRC 14	On/Inside BR	15	1.1 ± 0.7	3.6 ± 1.9
	Outside BR	21	1.7 ± 0.8	2.0 ± 1.3
BRC 27	On/Inside BR	15	2.3 ± 1.2	2.7 ± 1.2
	Outside BR	14	1.9 ± 1.4	0.7 ± 0.7
BRC 38	On/Inside BR	7	2.1 ± 0.9	3.3 ± 1.0
	Outside BR	4	2.7 ± 0.9	1.4 ± 1.0

5.6.1 Small-Scale Sequential Star Formation

As for the S^4F hypothesis on the RDI star formation, there has been only qualitative evidence such as an asymmetric distribution of probable TTSs (Ogura et al. 2002) and of properties of NIR excess stars (Matsuyanagi et al. 2006). In chapter 4 S^4F hypothesis is quantitatively verified by using BVI_c photometry of four BRCs. In the present chapter we follow the approach as given in chapter 4. We have divided the YSOs (H α stars and NIR excess stars) associated with BRCs into two groups: those lying on/inside and outside of the rims (see Fig. 5.2). Mean ages and mean A_V values have been calculated for these regions. Some of the stars in Table 5.3 show ages older than 5 Myr. Since the ages of

5.6 Star Formation Scenario in BRC Regions

the associated ionising sources of BRCs studied here have maximum ages of 4-5 Myr, therefore the TTSs having ages greater than this can not be expected as products of triggered star formation. We suspect that they may have formed spontaneously in the original molecular cloud prior to the formation of the HII region (see section 6.2). Some of them may be background stars; larger distances make them look older in the CMD. So while calculating the mean ages we have not included those stars. The results are given in Table 5.4, which shows that in almost all the BRCs the YSOs lying on/inside the rim are younger than those located outside it, whereas the mean A_V is higher on/inside the bright rim than outside it. The only exception for the mean age is BRC 27. The above results are exactly the same as those obtained in chapter 4. Therefore, the present results further confirm the S^4F hypothesis. As in chapter 4, we again find a big scatter in the stellar ages for each region of all BRCs in spite of a clear trend of the mean ages. Possible reasons for the scatter include photometric errors, errors in extinction correction, light variation of young stars, their proper motions, binarity of the stars, etc. Photometric errors and light variation as big as 0.5 mag would affect stellar ages by ~ 0.25 dex, so they do not seem to be the major reason for the scatter. As to the extinction correction, it probably does not affect the results much again, because in the $V_0, (V - I_c)_0$ CMD the isochrones are nearly parallel to the reddening vector. The adopted evolutionary models and distances of the BRCs causes systematic shifts in ages of the stars, but will not introduce scatters. As discussed in chapter 4, we speculate that the proper motions of the newly born stars may probably be the main cause of the scatter.

Since stars inside the rim are often deeply embedded, MIR observations through the *Spitzer Space Telescope* can provide a deeper insight into the embedded YSOs. YSOs occupy distinct regions in the IRAC colour plane; this makes MIR CC diagram a very useful tool for the classification of YSOs. Whitney et al. (2003a) and Allen et al. (2004) presented independent model predictions for IRAC colours of various classes of YSOs. Fig. 5.4 presents [5.8]-[8.0] versus [3.6]-[4.5] CC diagrams for the sources lying in the BRCs 2, 27 and 13/14 regions. The sources within the box represents the location of Class II objects (Allen et al. 2004; Megeath et al. 2004). The sources located around [5.8]-[8.0]=0 and [3.6]-[4.5]=0 are foreground/background stars, as well as diskless PMS stars (Class

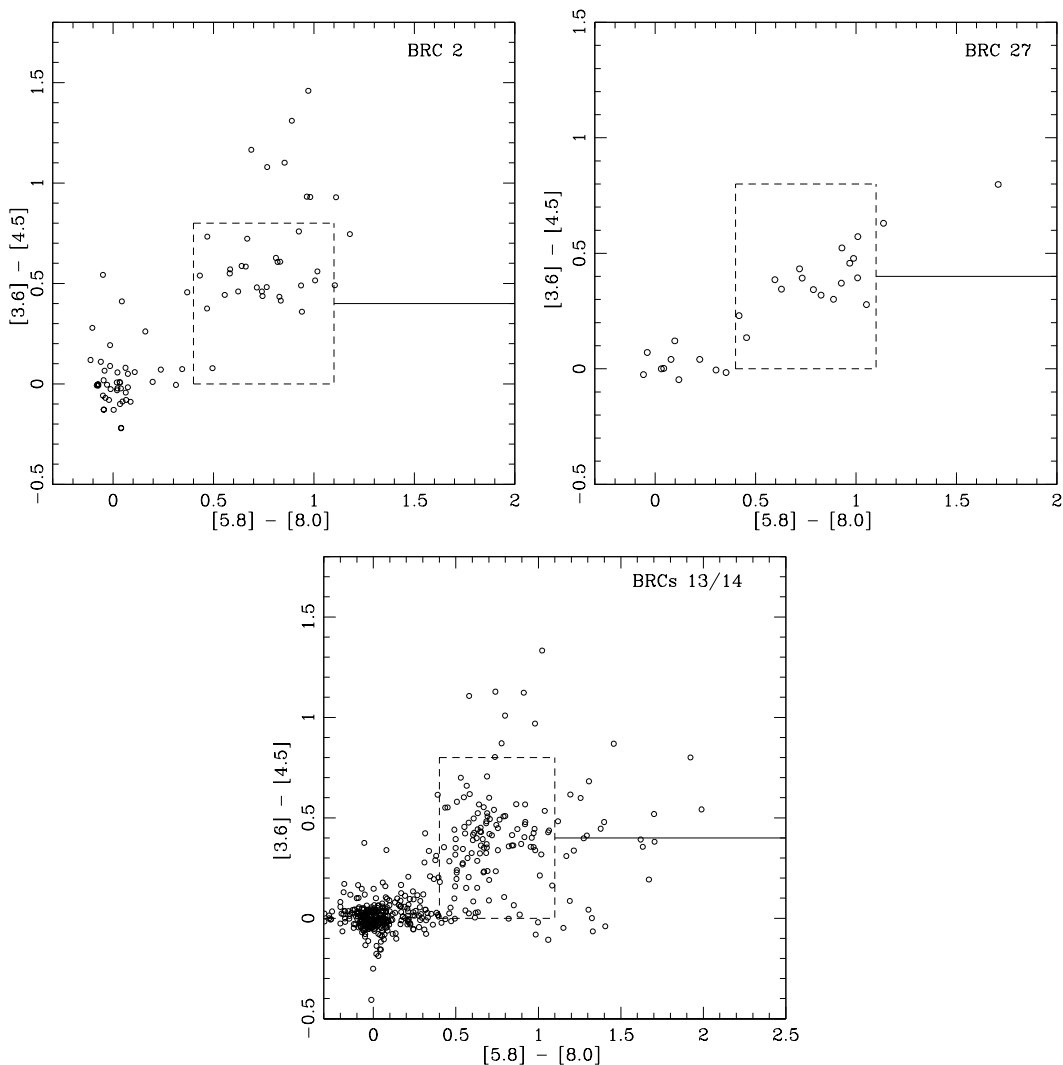


Figure 5.4: IRAC colour-colour diagrams for YSOs in BRCs 2, 27 and 13/14. The sources lying within the box are Class II sources. The sources located around $[5.8]-[8.0] \sim 0$ and $[3.6]-[4.5] \sim 0$ are the field/ Class III stars. Sources with $[3.6]-[4.5] \geq 0.8$ and/or $[5.8]-[8.0] \geq 0.8$ represent Class 0/I sources. The horizontal continuous line shows the adopted division between Class I and Class I/II sources (see Megeath et al. 2004.)

5.6 Star Formation Scenario in BRC Regions

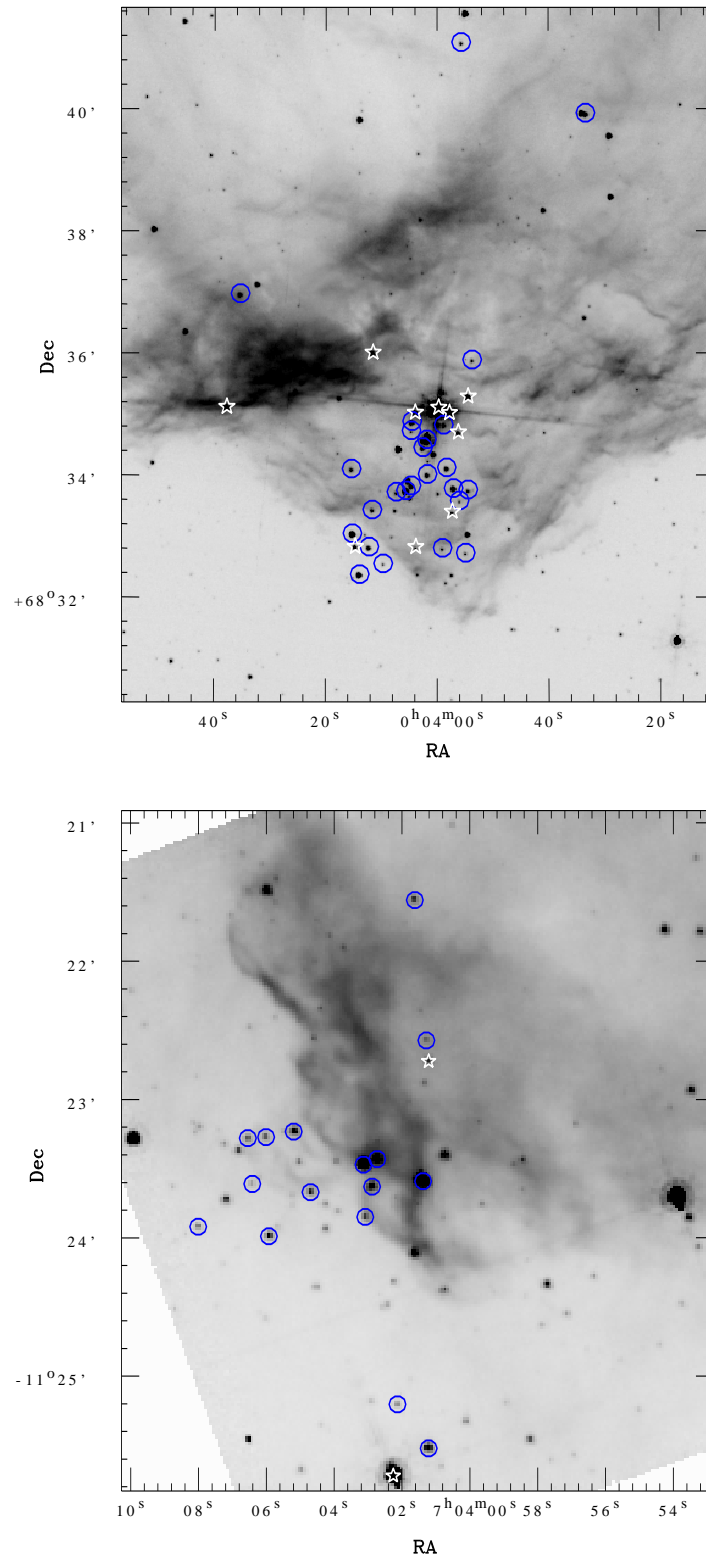


Figure 5.5: Spatial distribution of Class 0/I sources (star symbols) and Class II sources (open circles) in the BRC 2 (left panel) and BRC 27 (right panel) regions.

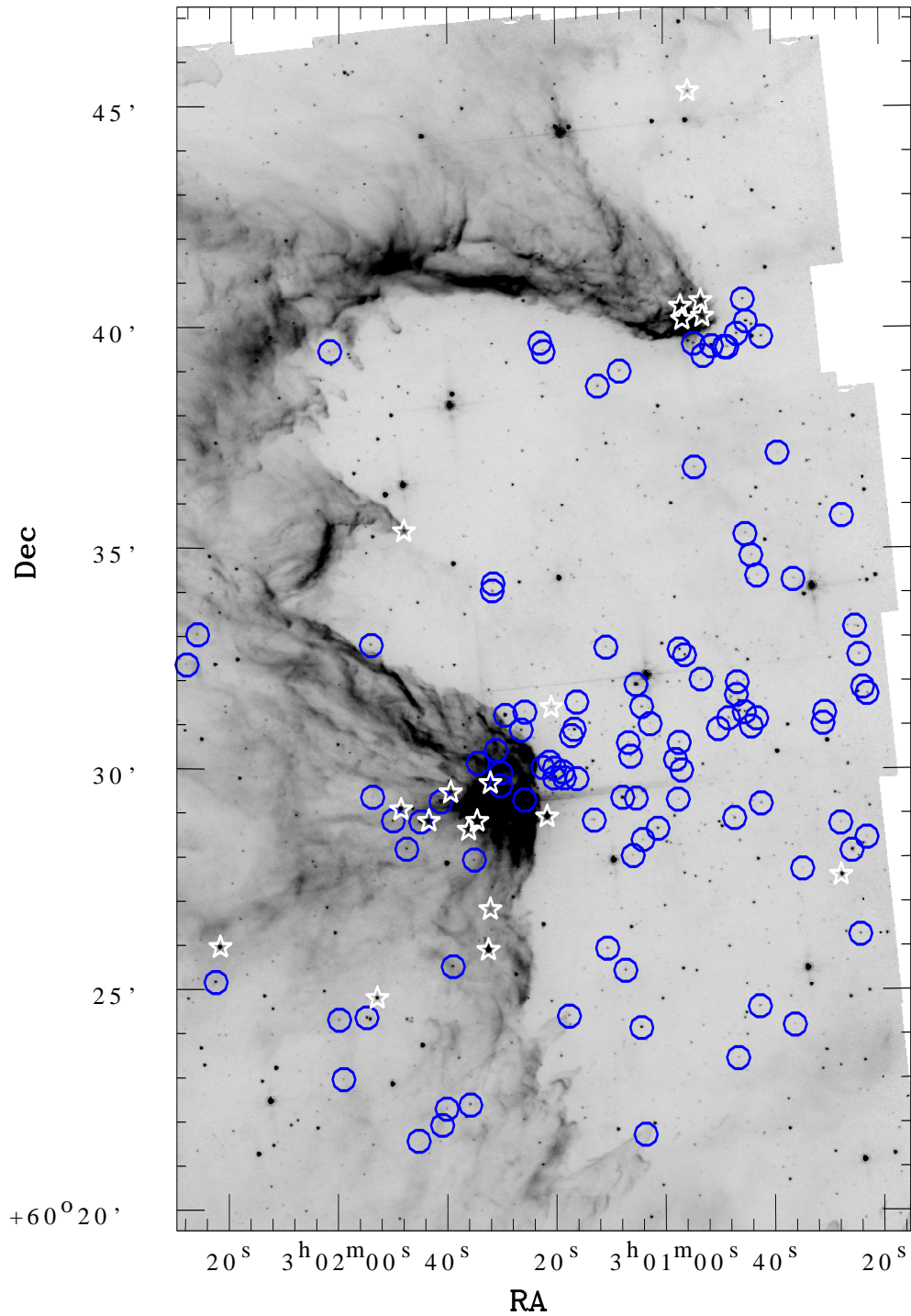


Figure 5.6: Spatial distribution of Class 0/I sources (star symbols) and Class II sources (open circles) in the BRCs 13 and 14 region identified in the *Spitzer/IRAC* data.

III objects). Sources with $[3.6]-[4.5] \geq 0.8$ and/or $[5.8]-[8.0] \geq 1.1$ have colours similar to those derived from models of protostellar objects with in-falling dusty envelopes (Allen et al. 2004). These are Class 0/I sources.

On the basis of the initial results from the *Spitzer* young cluster survey, Megeath et al. (2004) found a cluster of young stars near the edge of BRC 2 along with a group of Class I sources at the northern apex of the cluster. Table A.3 summarises the IRAC magnitudes of the disk bearing candidates of BRCs 2, 27 and 13/14. We reproduce the spatial distribution of the Class I and Class II sources in the BRCs 2 and 27 regions in Fig. 5.5. The upper panel for BRC 2 shows that the majority of the Class I sources are preferentially located away from the ionisation sources (which lies downward in Fig. 5.5) as compared to the Class II sources. If we divide the BRC into two regions at $Dec. \geq 60^{\circ}34'.5$, the fraction of Class 0/I sources in the northern region (which is away from the ionising source) is found to be 0.55 (6 Class 0/I and 5 Class II sources), which is significantly higher than that (0.16, 3 Class 0/I and 16 Class II sources) in the southern region (towards the ionising source). This distribution further manifests a small scale age sequence in the BRC 2 region.

In the cases of BRCs 13 and 14, Allen et al. (2005) reported that the Class I protostars are tightly clustered on the edge of the molecular clouds, coincident with the interface of the ionised and molecular gas, whereas the Class II stars are more widely distributed. The distribution of YSOs detected using the IRAC data is reproduced in Fig. 5.6, where again Class 0/I sources are found concentrated inside the BRCs, which is in accordance with the S^4F hypothesis. In the IC 1396N = BRC 38 region, Getman et al. (2007) found an elongated spatial distribution of YSOs with the youngest stars (Class 0/I) deeply embedded inside the cloud and relatively older stars aligned toward the exciting star, which again supports propagation of small-scale triggered star formation in that region.

5.6.2 Indication of Global Triggered Star Formation

BRCs are considered to be a sort of remnants originated from dense part (cores) in an inhomogeneous giant molecular cloud. So, if the original cloud was big, the resultant BRC could have undergone a series of RDI events, leaving an elongated

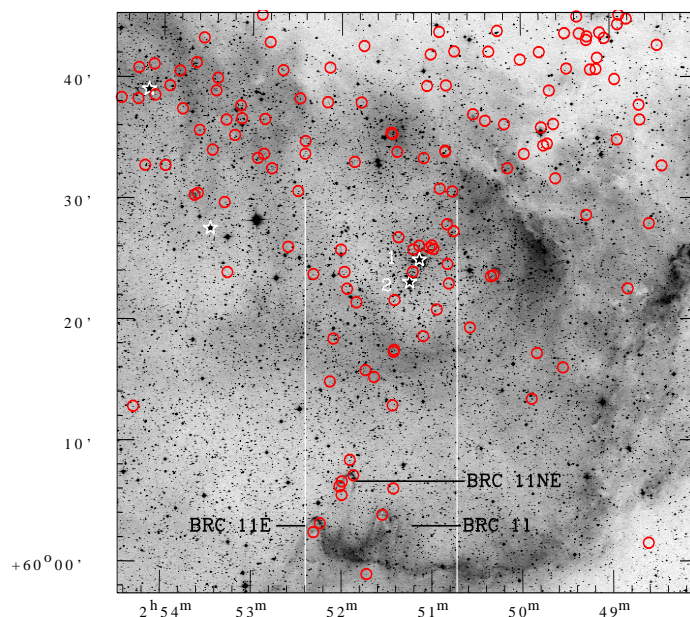


Figure 5.7: Spatial distribution of NIR excess stars (open circles) overlaid on DSS2 R-band image of the IC 1848W region. Star symbols indicate O type stars. The stars marked as ‘1’ and ‘2’ are HD 17505 (O6 V) and HD 17520 (O9 V) respectively. The variation of NIR excess $\Delta(H-K)$ and A_V for the stars within the strip as a function of distance from HD 17505 is shown in Fig. 5.11.

distribution of young stars; the distribution of such YSOs and its morphological details could be used to probe the star formation history in the OB association. With this expectation we have searched for NIR excess stars by using 2MASS PSC in the whole HII regions where the studied BRCs are located. Figs. 5.7 to 5.10 show spatial distribution of NIR excess stars in the IC 1848W, IC 1848E, CMaR1 and IC 1396 regions which contain BRCs 11NE, 13/14, 27 and 38 respectively. Figures 5.11 to 5.13 show radial variation of $\Delta(H - K)$ and A_V , for the stars located within the strip shown in Figs. 5.7 to 5.10. The NIR data along with $\Delta(H - K)$ and A_V values are given in Table A.2.

Fig. 5.7 shows that the NIR excess stars are aligned loosely towards the direction of BRC 11NE from the cluster IC 1848W which contains the ionising sources (HD 17505, O6 V; HD 17520, O9V) of the HII region. A very recent study (while the present study was in the reviewing process) based on *Spitzer*

5.6 Star Formation Scenario in BRC Regions

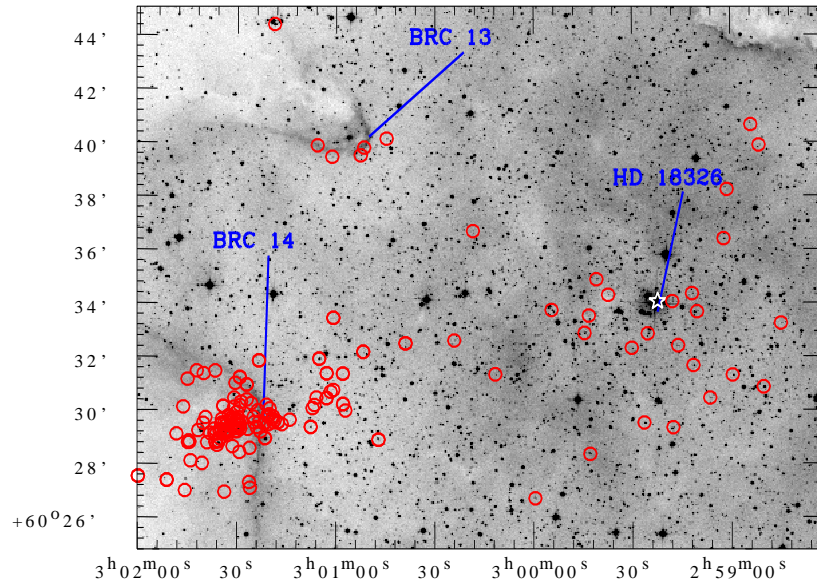


Figure 5.8: Same as Fig. 5.7 but for IC 1848E region.

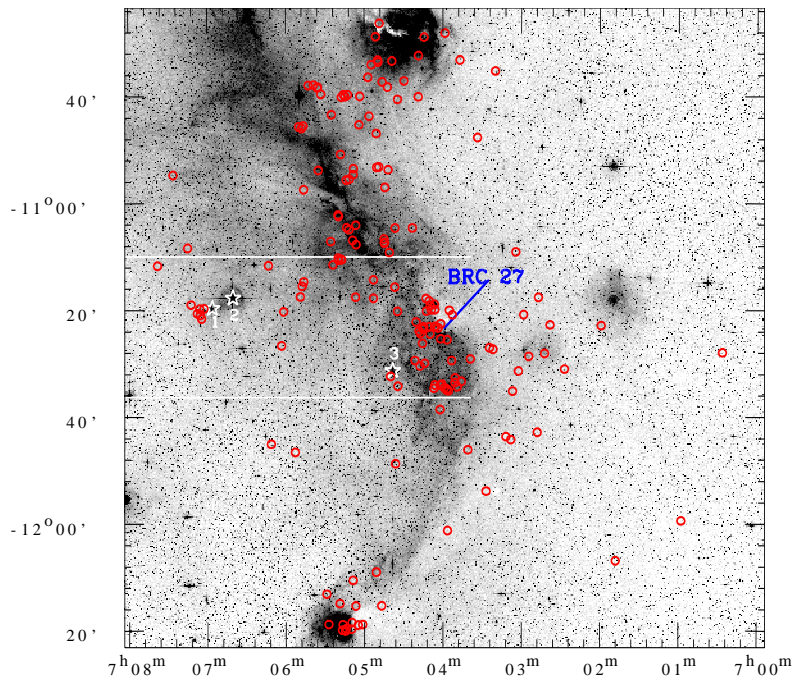


Figure 5.9: Same as Fig. 5.7 but for CMaR1 region. Stars marked as '1', '2' and '3' are HD 54025 (B1 V); HD 53974 (B0.5 IV) and HD 53456 (B0 V) respectively.

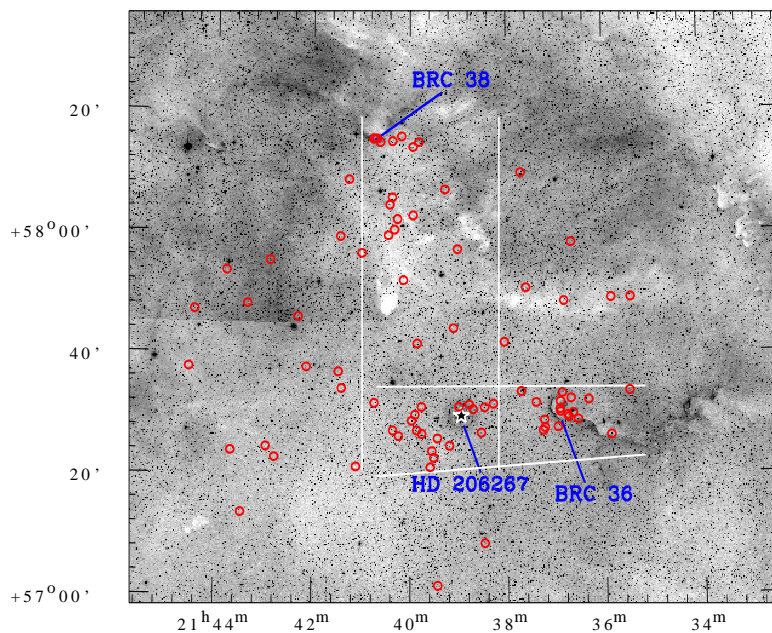


Figure 5.10: Same as Fig. 5.7 but for IC 1396.

observations by Koenig et al. (2008) also shows a nice alignment of Class II stars towards the direction of the BRC 11NE region from the ionising source(s) (see their Fig. 10). Figs. 5.11a and 5.11b show radial variation of $\Delta(H - K)$ and A_V , for the stars in the BRC 11NE region located within the strip shown in Fig. 5.7, as a function of radial distance from HD 17505. $\Delta(H - K)$ is defined as the horizontal displacement from the middle reddening vector (see Fig. 5.1). The distribution of the NIR excess $\Delta(H - K)$ values shows an increasing trend as we move towards the BRC 11NE region. For the whole sample shown in Fig. 5.11a, the Kendall's tau test gives a positive correlation at a confidence level of about 85%. The two extreme points at radial distance $\sim 28'$ have small $\Delta(H - K)$ values with small A_V (0.24 and 0.84) values. We presume that these sources are not embedded inside the rim and lying on the outer region of the cloud. The two stars at radial distance $\sim 5'$ and $\sim 9'$ shows relatively higher value of $\Delta(H - K)$ in comparison to nearby stars. Exclusion of these four points gives a probability of $\sim 97\%$ for a positive correlation between radial distance and $\Delta(H - K)$. Table 5.6.2 summarizes the results of the correlation analysis using the Kendall's tau

test.

On the basis of the pressure of the ionised boundary layer (IBL) and that of the molecular cloud, Thompson et al. (2004) have concluded that the cloud is in pressure balance with the exterior ionised gas and photo-ionisation induced shocks are propagating in the cloud. They also concluded that overall morphology of the cloud is similar to that predicted by RDI models (Bertoldi 1989; Lefloch & Lazareff 1994). They have also estimated the duration over which the BRC 11NE region might have been exposed to the UV flux. Assuming that the rims are located at a distance of ~ 22 pc from the ionising sources, an ionisation front expanding into a medium of homogeneous density at a speed of 11.4 km/s will take about 1.5 Myr to reach the rims. The mean age of the YSOs ($H\alpha$ stars and NIR excess stars) associated with BRC 11NE (both inside and outside the bright rim) is found from Table 5.3 to be 1.7 ± 1.0 Myr. Thus the sum of these two values yields a time scale of ~ 3.2 Myr, which is comparable to the MS lifetime (~ 4.0 Myr) of HD 17505 (Landolt 1992; Schaller et al. 1992). The above facts seems to support the triggered star formation scenario in the IC 1848W region.

Figure 5.8 shows that the distribution of the NIR excess stars in the IC 1848E region. We see they are aligned beautifully from the vicinity of the O7 star HD 18326 to the direction of BRC 14. A more impressive alignment of the Class II sources can be seen in Fig. 5.12 of Koenig et al. (2008). This spatial distribution of NIR excess stars resembles that in NGC 1893, where a similar nice distribution of NIR excess stars is noticed from the centre of the cluster containing several OB stars to the direction of the cometary globules Sim 129 and 130 (see Fig. 22 of Sharma et al. 2007). In the case of NGC 1893 evidence for triggered star formation due to RDI is also found. In Fig. 5.12a (upper panel) we plot the amount of NIR excess $\Delta(H - K)$ for the stars shown in Fig. 5.8 as a function of radial distance from the center of the cluster. Fig. 5.12a manifests an increase in NIR excess near BRC 14. A similar trend is noticed for the spatial distribution of A_V (Fig. 5.12b). Kendall's tau test yields a positive correlation for the radial variation of $\Delta(H - K)$ and A_V at a confidence level of better than 99.9%. As discussed in Matsuyanagi et al. (2006), these features indicate that stars located near BRC 14 should be younger than the rest of the stars.

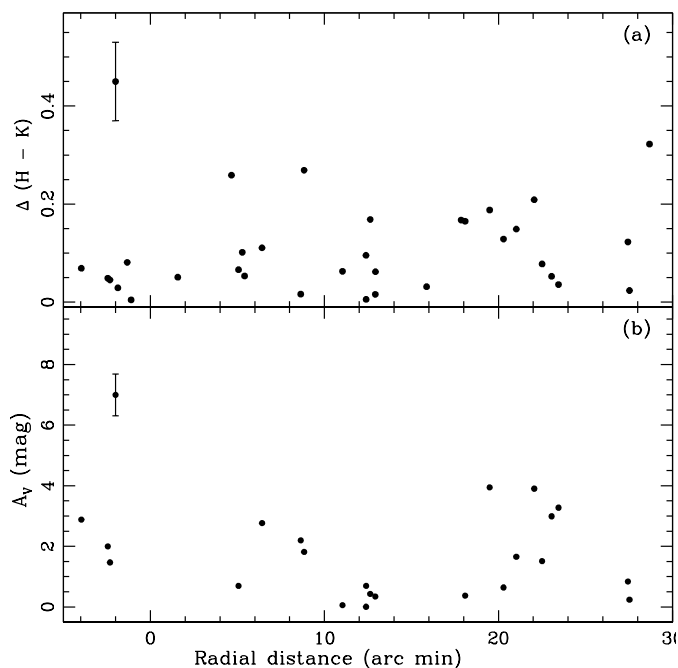


Figure 5.11: Variation of (a) NIR excess $\Delta(H - K)$ and (b) A_V for the stars within the strip shown in Fig. 5.7 as a function of distance from HD 17505 toward BRC 11 region. Average error bar is shown at the upper-left corner of the plot.

In Fig. 5.8 a loose clustering is also clearly visible around HD 18326. To our knowledge this clustering has not been designated so far as a known cluster¹. $J/(J - H)$ CM diagram of the cluster region yields an age of ~ 2 Myr. This cluster will be studied in detail in a forthcoming paper. On the other hand, the mean age of the YSOs associated with BRCs 13 and 14 (again, both inside and outside of the rims) is derived from Table 5.3 to be 1.0 ± 0.9 Myr and 1.5 ± 0.9 Myr, respectively, which are younger than the age of the cluster. Recently Nakano et al. (2008) reached the same conclusion, obtaining the ages of 4 Myr and 1 Myr for a groups of $H\alpha$ emission stars around HD 18326 and that near eastern edge of the HII region, respectively. This again indicates that the star formation in the BRCs 13/14 region is triggered by the O star in the cluster region. Thus all the above mentioned evidences clearly support a series of RDI processes which took

¹In a very recent study based on **Spitzer** observations, Koenig et al. (2008) have also identified this cluster.

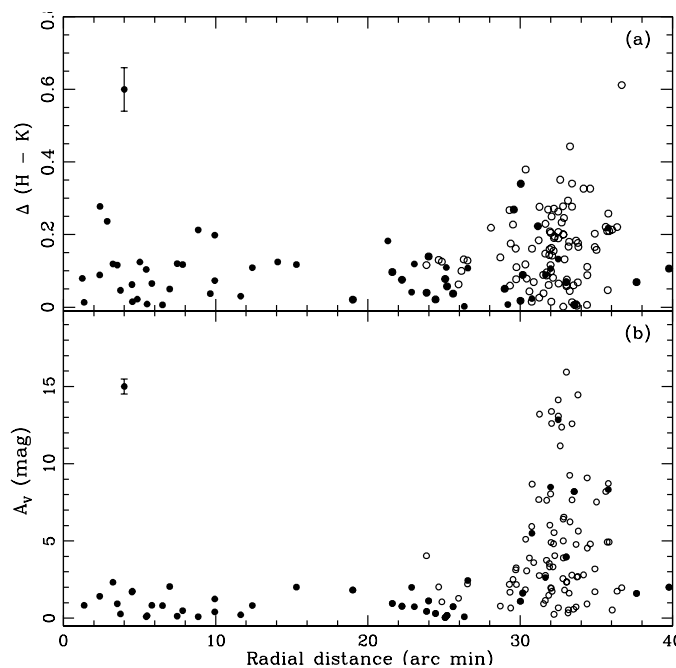


Figure 5.12: Variation of (a) NIR excess $\Delta(H - K)$ and (b) A_V as a function of the distance from HD 18326 toward BRC 14. Filled and open circles represents the data taken from the 2MASS catalogue and Matsuyanagi et al. (2006), respectively. Average error bar is shown at the upper-left corner of the plot.

place in the past starting from the vicinity of the O star.

The spatial distribution of the NIR excess stars in the BRC 27 region is shown in Fig. 5.9. Assuming that B0.5IV (HD 53974; marked as ‘2’) and B1V (HD 54025; marked as ‘1’) stars are the ionising sources for the BRC 27 region, the $\Delta(H - K)$ and A_V distribution for the sources lying within the strip marked in Fig. 5.9 as a function of radial distance from HD 54025 is shown in Fig. 5.13, which indicates relatively higher NIR excess and A_V near the BRC 27 region. The Kendall’s tau test for the entire sample indicates a positive correlation between radial distance and $\Delta(H - K)$ and A_V at a confidence level of $\sim 80\%$ and $\sim 95\%$, respectively. The sources having radial distance $> 43'$ show small value of A_V as well as $\Delta(H - K)$ as compared to the sources lying around $40' - 41'$. We presume that these sources are not embedded inside the rim and are lying on the outer periphery of the cloud. Exclusion of these points gives a probability of

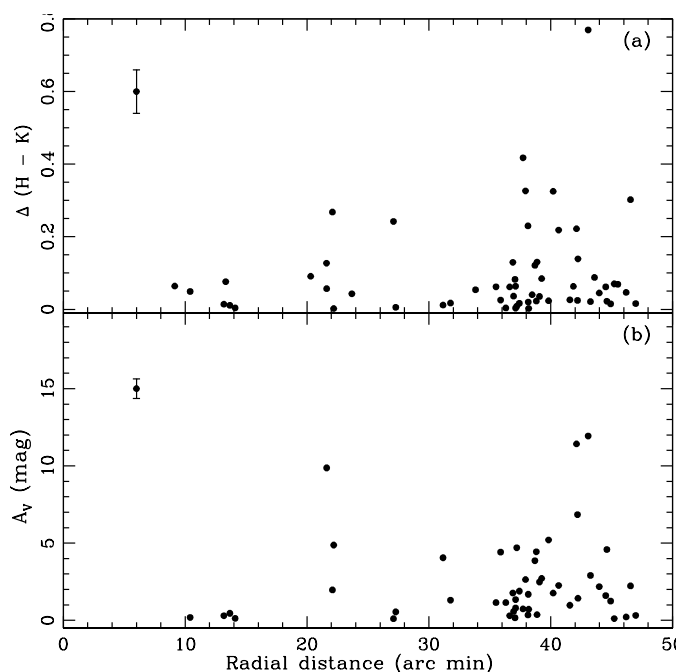


Figure 5.13: Variation of (a) NIR excess $\Delta(H - K)$ and (b) A_V for the stars within the strip shown in Fig. 5.9 as a function of distance from the probable ionising source (HD 53974) of the CMaR1 region. Average error bar is shown at the upper-left corner of the plot.

$\sim 98\%$ or better and 99.9% for a positive correlation between radial distance and $\Delta(H - K)$; and A_V , respectively. If the B1V/ B0.5 IV star(s) is (are) actually the ionising source(s) for the region, the maximum MS life-time of the star(s) is ~ 10 Myr (Landolt 1992; Schaller et al. 1992), whereas the mean age of the YSOs associated with BRC 27 is estimated as 2.1 ± 1.3 Myr, which is not in contradiction with that star formation in the BRC 27 region may be initiated by the UV-radiation from these star(s).

Sicilia-Aguilar et al. (2004) have shown that in the case of the Tr 37/ IC 1396 Globule region, CTTSs are found to be aligned towards the direction of IC 1396 Globule from the ionising source, HD 206267 (O6). Sicilia-Aguilar et al. (2005) found that most of the younger (~ 1 Myr) members appear to lie near or within the IC 1396 Globule. They concluded that it can be indicative of the triggered star formation. Fig. 5.10 shows distribution of NIR excess stars in the

5.6 Star Formation Scenario in BRC Regions

Table 5.5: Correlation between radial distance and $\Delta(H - K)$, A_V . The probability $P(0)$ indicates that no correlation is found with the generalized non-parametric Kendall's tau statistics.

Radial distance from the ionising source (arc min)	P (0) $\Delta(H-K)$	P (0) A_V	comment
BRC 11			
5 - 30	0.150	-	
5 - 30	0.026	-	Excluding Outliers (see text)
BRC 14			
0 - 40	< 0.00	< 0.00	
BRC 27			
0 - 48	0.230	0.04	
0 - 43	0.025	0.001	(see text)

Tr 37/IC 1396 Globule/BRC 38 region, where they seem to align loosely towards the direction of IC 1396 Globule and BRC 38. Their radial distribution of NIR excess $\Delta(H - K)$ and A_V does not show any trend, however. By using the ages of the YSOs near IC 1396 Globule given by Sicilia-Aguilar et al. (2005) we obtained their mean age of $\sim 1.8 \pm 1.1$ Myr, whereas for the YSOs near BRC 38 the mean age is estimated from Table 5.3 to be $\sim 2.2 \pm 0.9$ Myr. The upper main-sequence turn off age of Tr 37 is found to be ~ 3 Myr (Contreras et al. 2002). Thus the aligned distribution of YSOs from the ionising source HD 206267 towards IC 1396 Globule and BRC 38 and their younger age as compared to the central cluster Tr 37 suggest a triggered star formation scenario in the region.

We conclude that the global distribution of YSOs, their radial distribution of the amount of NIR excess $\Delta(H-K)$ as well as of A_V in each HII region studied here clearly show evidence that a series of RDI processes proceeded in the past from near the central O star(s) towards the peripheries of the HII region.

5.6.3 Star Formation inside ‘A’-Type BRCs

The *Spitzer* IRAC data on BRC 2, BRC 13 and BRC 14 manifest that the Class 0/I sources are concentrated inside the rim. The SCUBA imaging survey of sub-millimeter continuum emission from BRCs by Morgan et al. (2008) has shown that the embedded cores are likely to contain Class 0 protostars. On the basis of combination of the observed submillimeter flux excess and high dust temperature they concluded that star formation may be on-going within the BRCs. They have further concluded that the majority of the sources have $L_{bol} > 10L_{\odot}$, indicating that the sources are intermediate to high-mass stars. Some of the higher luminosity sources (e.g. in BRCs 13 and 14) may be proto-clusters. The *Spitzer* IRAC data manifest that in fact these two BRCs host a proto-cluster (cf. Fig. 5.11).

Morgan et al. (2008) did not find evidence for interaction of the external ionisation field with the star formation inside ‘A’ type BRCs (for the morphological types of BRCs we refer to SFO 91) and concluded that the star formation in these clouds is not subjected to the RDI process. The present work includes four BRCs of the ‘A’ type, namely, BRCs 2, 14, 27 and 38 and provides strong evidence for star formation due to RDI occurring in BRCs, however. As we have seen in section 5.6.1, BRCs 2, 14 and 38 show such age gradients that stars located on/inside the rim are younger than those located outside it, i.e., toward the ionising source, evidencing the most recent RDI phenomenon. In addition, our results in section 5.6.2 as well as recent study based on *Spitzer* observations by Koenig et al. (2008) manifest a nice, global alignment of NIR excess stars in IC 1848E from the O7 star HD 18326 to BRCs 13 and 14. The spatial distribution of H α emission stars found by Nakano et al. (2008) also revealed a similar alignment. Thus the ages of the YSOs and their spatial distribution in the region clearly support a series of RDI processes which have been taking place in the past until very recently. These results do not support the notion of Morgan et al. (2008) that star formation in/around ‘A’-type BRCs is not subjected to the RDI triggering process.

5.7 Conclusions

On the basis of the present optical and NIR analysis of six BRC aggregates we reached the following conclusions.

We estimated the ages of individual stars associated with BRCs from the reddening-corrected $V_0, (V - I_c)_0$ CM diagrams. By comparing the average ages of the stars on/inside and outside the bright rim, we again found quantitative age gradients in almost all the studied BRCs (the only exception being BRC 27), although the number of the sample stars are small and their age scatters are large. The results are quite similar to the results reported in chapter 4. In addition the youngest objects, obtained from *Spitzer* MIR data, are found to be deeply embedded inside the BRCs, supporting the above conclusion. These results further confirm S^4F hypothesis.

The distribution of NIR-excess stars in the studied HII regions indicates that they are aligned from the ionising source to the BRC direction. The age indicators, viz., infrared excess ($\Delta(H - K)$) and A_V as well as the age itself of the YSOs manifest an age gradient toward the ionising source. This global distribution indicates that a series of triggered star formation took place in the past from near the central O star(s) towards the peripheries of the HII region.

Chapter 6

DISK EVOLUTION AND CMF OF YSOs ASSOCIATED WITH HII REGIONS

6.1 Introduction

H α emission and IR excess are important signatures of young PMS stars. These signatures in CTTSs indicate the existence of a well-developed circumstellar disk actively interacting with the central star. Strong H α emission ($EW \geq 10 \text{ \AA}$) in CTTSs is attributed to the magnetospheric accretion of the innermost disk matter onto the central star (Edwards et al. 1994; Hartmann et al. 1994; Muzerolle et al. 2001 and references therein). On the other hand the weak H α emission ($EW < 10 \text{ \AA}$) in WTTSs, which lack disks (or, at least inner disks), is believed to originate from their chromospheric activity (e.g., Martín 1998; Walter et al. 1988). In 1990s a large number of WTTSs were found in and over wide areas around T associations by X-ray surveys with ROSAT, which aroused active studies on the nature of the so-called dispersed WTTSs.

As for the relation of the WTTS to the CTTS, the “standard model” (Kenyon & Hartmann 1995) postulates that the latter evolves to the former by losing the circumstellar disk (or, at least its inner part). Actually analysis of the age

¹The results presented in this chapter have been published in Chauhan et al. (2009) and Chauhan et al. (2011, accepted for publication in MNRAS).

distribution derived from the HR diagram of, e.g., the Taurus region indicated that the WTTSs are systematically older than the CTTSs, but the statistical significance was low (Armitage et al. 2003; Hartmann 2001; Kenyon & Hartmann 1995).

On the other hand, there also have been many observations which claimed that the CTTS and the WTTS are coeval and have indistinguishable stellar properties (e.g., Gras-Velázquez & Ray 2005; Lawson et al. 1996; Walter et al. 1988). From the analyses of the HR diagram of the CTTSs and WTTSs in Chamaeleon I, Lawson et al. (1996) concluded that some stars may be born even almost diskless or lose the disk at very early stages (age < 1 Myr). However, in order to explain the co-existence and approximate coevality of CTTSs and WTTSs in a star forming region, it is usually postulated that YSOs display a wide range of disk masses and their accretion activity and/or the dispersal of the disk takes place in a correspondingly wide range of time-scales (Bertout et al. 2007; Furlan et al. 2006). Based on L-band surveys of clusters of various ages, Haisch et al. (2001) reached the quantitative conclusion that the disk fraction is initially very high ($\geq 80\%$) and that one half the stars lose their disks in ~ 3 Myr and almost all in ~ 6 Myr. Armitage et al. (2003) obtained similar results that around 30% of stars lose their disks within 1 Myr, while the remainder have disk lifetimes that are typically in the 1 - 10 Myr range. Recently, Bertout et al. (2007), by using new parallaxes for CTTS and WTTS in the Taurus-Auriga T association, concluded that their observed age and mass distribution can be explained by assuming that a CTTS evolves into a WTTS when the disk is fully accreted by the star.

As discussed in Sec. 1.6.3 that the IMF is an important tool to study the star formation process. Morgan et al. (2008), using SCUBA observations, have estimated the masses of 47 dense cores within the heads of 44 BRCs. They concluded that the slope of the MF of these cores is significantly shallower than that of the Salpeter MF. They also concluded that it depends on the morphological type of BRCs (for the morphological description of BRCs we refer to SFO 91): ‘A’ type BRCs appear to follow the mass spectrum of the clumps in the Orion B molecular cloud, whereas the BRCs of the ‘B’ and ‘C’ types have a significantly shallower MF. So, it would be worthwhile to compare the MF of protostars given by Morgan et al. (2008) with that of BRC aggregates.

In the present study we have estimated the ages of a significant number of TTSs, hence we can study the evolution of the disk properties of TTSs. It would also be worthwhile to compare the MF of YSOs associated with the BRCs. Hence, in this chapter we discuss the evolution of protoplanetary disks of the TTSs and CMFs of the YSOs associated with BRCs and cluster region.

6.2 Evolution of H α EW and disk of T-Tauri stars associated with BRCs

In Chapters 4 & 5 we have derived the ages of 93 H α emission stars, hence we can study the evolution of the H α emission activity in TTSs. The H α EWs are taken from Ogura et al. (2002); however the values reported as EWs in their Table 5 are values in pixels. To convert these values into Å we multiply the reported values by a factor of 3.8 (see Ikeda et al. 2008).

In Fig. 6.1 we plot the EWs of H α emission stars as a function of age to explore possible evolutionary trends. Although, the dispersion around younger side is quite large, still in general there seems to be a decreasing trend in EW with the age. Here it is worthwhile to mention that a rather similar trend in the EWs of H α emission line of HAe/Be stars is reported by Manoj et al. (2006). The distribution of EWs in Fig. 6.1 indicates that the accretion activity in the TTSs associated with BRCs drops substantially by 5 Myr. In Fig. 6.1, there seems to be a small group of H α emission stars having far larger ages (≥ 5 Myr) and a relatively elevated level of EWs. The masses of these stars lie in the range $0.6 \geq M/M_{\odot} \geq 1.9$, whereas the majority of the YSOs having age ≤ 5 Myr have masses in the range $0.1 \geq M/M_{\odot} \geq 1.2$. If we take their ages at their face values, they presumably are not products of triggering. Since the ages of the ionizing sources of BRCs studied here have maximum age of 4-5 Myr, stars having ages greater than ~ 5 Myr can not be expected as results of triggered star formation, but must have formed spontaneously prior to the formation of the HII region. The stars with ages ≥ 5 Myr seems to born with large disk masses and spent a substantial part, say, half of their ages unexposed to UV radiation from O stars, the long lifetime of their accretion activity may be understood. Johnstone

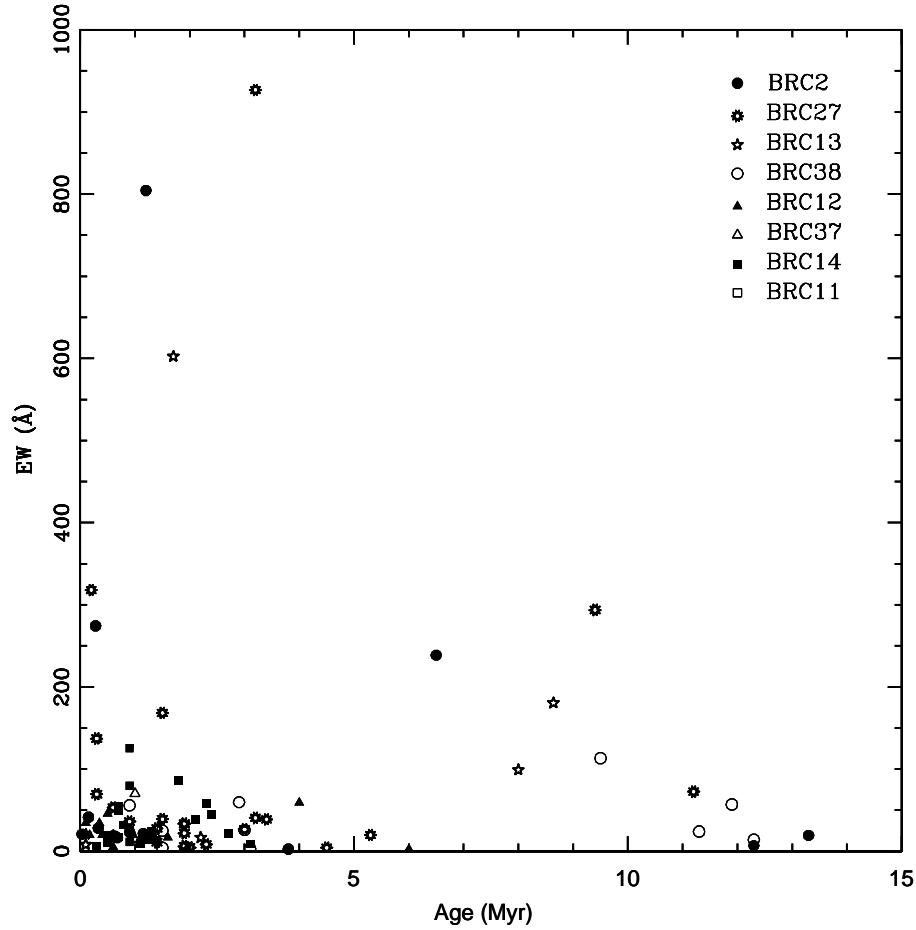


Figure 6.1: EWs of H α emission stars in the BRCs as a function of stellar ages (see section 6.3).

et al. (2004) have reported that the far-UV radiation from nearby massive star(s) may cause photo-evaporation of YSO disks resulting in short ($\sim 10^6$ yr) disk lifetimes. However, Fig. 5.2, where these stars are marked with crosses, shows that they are located both inside and outside the bright rims mixed with H α stars of younger ages. So their origin remains a mystery. But in the case of BRC 38, which contributes four to this group of altogether eleven stars, Getman et al. (2007) recognized, apart from young stars associated with the BRC, an older population of PMS stars dispersed in IC 1396. We suspect the above four stars may belong to this population and formed in the original molecular cloud prior to

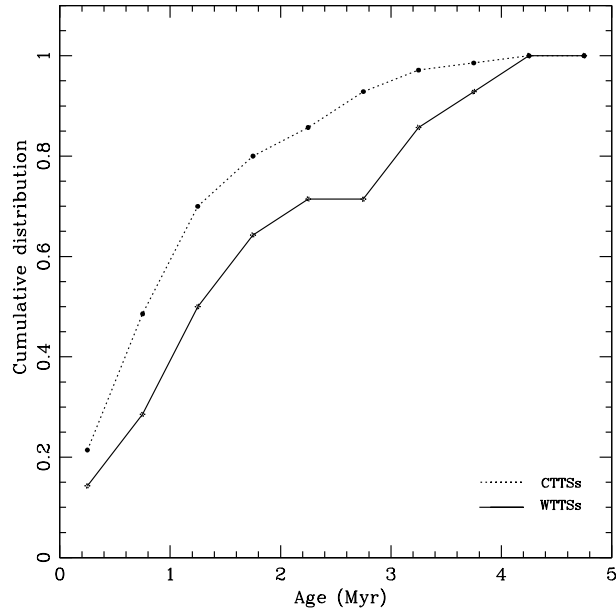


Figure 6.2: Cumulative distributions of CTTSs and WTTSs in BRCs as a function of stellar age (see text).

the formation of HD 206267. In Fig. 5.2 they look concentrated along the bright rim, but note that the H α survey by Ogura et al. (2002) is limited down to +58 13 35, which is only a few arcmin south of the bright rim. Here it is worthwhile to mention that in the case of cluster Tr 37 (age 1-5 Myr), Sicilia-Aguilar et al. (2005) have found a few stars having age > 5 Myr. They pointed out that in some clusters intermediate-mass stars seem older than low-mass stars and this effect seems to be related to a problem defining the birth line for intermediate-mass stars (Hartmann 2003).

Figure 6.2 shows the cumulative distribution of CTTSs ($EW \geq 10\text{\AA}$) and WTTSs ($EW < 10\text{\AA}$) (for stars having age ≤ 5 Myr) as a function of age. Fig. 6.2 manifests that CTTSs are relatively younger than WTTSs. A Kolmogorov-Smirnov test confirms the statement that the cumulative distributions of CTTSs and WTTSs are different at a mean confidence level of $\sim 70\%$ with minimum and maximum confidence level (obtained using the Monte Carlo simulations) of $\sim 55\%$ and $\sim 90\%$, respectively. This result is in agreement with that of Bertout et al. (2007) for the Taurus-Auriga T-association, that WTTSs are older than CTTSs

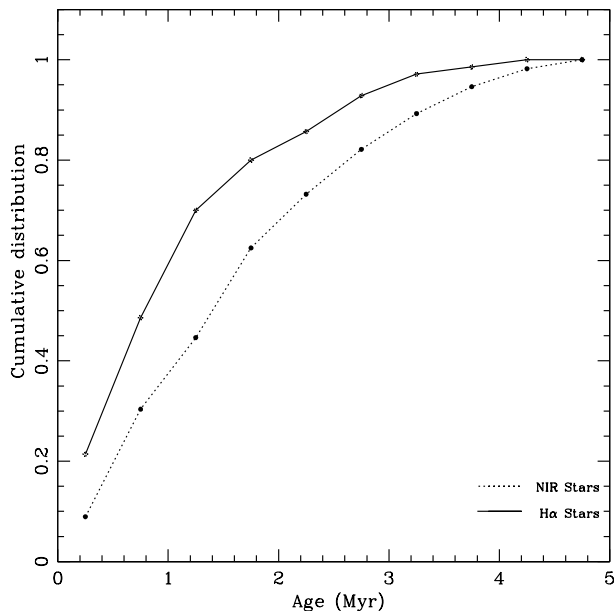


Figure 6.3: Cumulative distributions of H α emission and NIR excess stars in the BRCs as a function of stellar age (see text).

and CTTSs evolve into WTTSs. In Fig. 6.3 we plot cumulative age distribution of H α emission stars ($EW \geq 10\text{\AA}$) and of NIR excess stars. Fig. 6.3, at a mean confidence level of $\sim 98\%$ (with a minimum and maximum confidence level of $\sim 92\%$ and $\sim 99.4\%$) indicates that YSOs exhibit NIR excess for a relatively longer time as compared to accretion activity. Although our sample is small and the age span is very short, the obtained CTTS fraction (from Tables A.1 and 5.3) in BRCs seems to follow the trend of TTSs in the Taurus region as given by Armitage et al. (2003).

6.3 Cumulative mass function of BRC aggregates

To compare the MF of the cores given by Morgan et al. (2008) with that of the YSOs in the BRCs, we have used the masses of the YSOs given in Table 5.3. In Fig. 6.4 we plot CMF of the YSOs in 7 BRCs, namely BRCs 2, 11NE, 12, 13, 14,

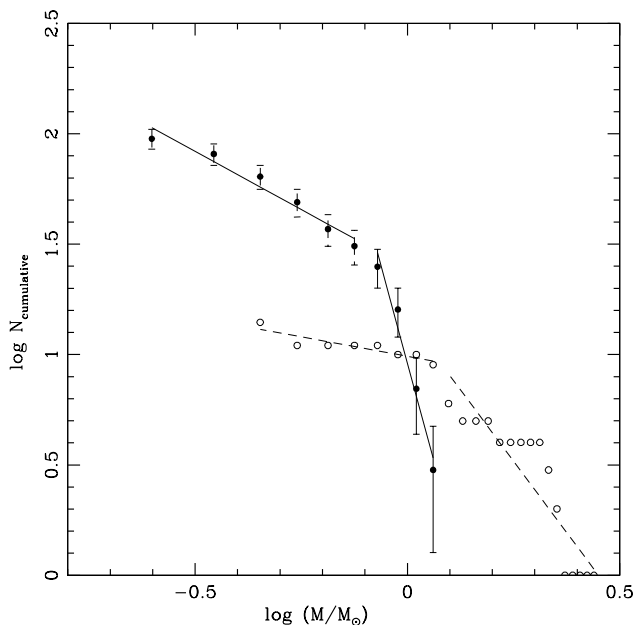


Figure 6.4: CMF of YSOs in the 7 BRCs (filled circles). Error bars represent $\pm\sqrt{N}$ errors. Open circles represent the CMF for the cores by Morgan et al. (2008).

27 and 38, in the mass range of $0.2 \leq M/M_{\odot} \leq 1.2$. The CMF of the dense cores by Morgan et al. (2008) is also plotted for comparison.

It is interesting to notice that both CMFs show a roughly similar shape with a break in power law. Obviously a detailed comparison manifests differences. In the case of the YSOs we find a break in the slope of the CMF at $\sim 0.8 M_{\odot}$. In the mass range $0.8 \leq M/M_{\odot} \leq 1.2$ the slope of the CMF is -7.1 ± 0.9 and it becomes shallower (-1.0 ± 0.1) for masses $0.2 \leq M/M_{\odot} \leq 0.8$, whereas the CMF of the cores can be represented by a power law with a shallower slope of -0.4 ± 0.1 in the mass range $0.4 \leq M/M_{\odot} \leq 1.2$. The core CMF becomes steeper for masses $\geq 1.2 M_{\odot}$ (slope = -2.6 ± 0.3). Morgan et al. (2008) have reported that their sample is complete down to $0.5 M_{\odot}$. Our sample toward lower mass may be affected by incompleteness, however the correction due to incompleteness will further steepen the CMF slope of the YSOs. The shallower CMF slopes in the case of dense cores than those for YSOs indicates that the star formation in the next sequence/ generation favours formation of relatively massive stars.

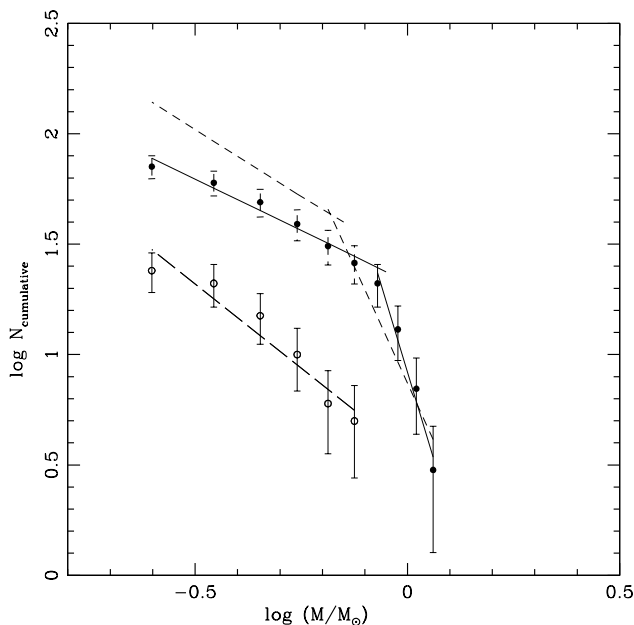


Figure 6.5: CMF of the ‘A’ type (filled circles) and ‘B/C’ type BRCs (open circles). Error bars represent $\pm\sqrt{N}$ errors. The CMF for the standard MF is shown by short dashed lines (see the text).

If the star formation within the BRCs depends on morphology of the clouds, as suggested by Morgan et al. (2008), it would be interesting to study the CMF of YSOs by separating the target BRCs on the basis of the morphology of BRCs. Here we assign type A to BRC 38 rather than type B given in SFO 91. BRC 11NE, which is not included in SFO 91, is classified as type B. In Fig. 6.5 we plot the CMFs of the YSOs in 4 ‘A’ type BRCs, namely BRCs 2, 14, 27 and 38, and of those in 3 ‘B/C’ type BRCs, namely BRCs 11NE, 12 and 13. In the YSO mass range $0.2 \leq M/M_{\odot} \leq 0.8$ the slope of the CMF for the ‘B/C’ type BRCs is found to be -1.5 ± 0.2 which is steeper than that (-0.9 ± 0.1) obtained for ‘A’ type BRCs. This is in contradiction with the results reported by Morgan et al. (2008). They reported a shallower MF slope for ‘B/C’ type BRCs in comparison to that of ‘A’ type BRCs (see their Figure 11); however a close inspection of their figure 11 manifests that in the mass range $0.5 \leq M/M_{\odot} \leq 3.0$, the MF slope of the cores of ‘A’ type BRCs is definitely shallower than that for ‘B/C’ type BRCs. This suggests that ‘A’ type rims, in the mass range $0.4 \leq M/M_{\odot} \leq 1.2$, appear to

6.3 Cumulative mass function of BRC aggregates

Table 6.1: Mass function of BRC aggregates. The maximum and minimum value of the slopes are estimated by propagating the random errors using the Monte Carlo simulations.

Mass Range (M_{\odot})	Mean value of the slope	Maximum value of the slope	Minimum value of the slope
All BRCs			
0.2 - 0.8	-0.97 ± 0.14	-0.99 ± 0.15	-0.95 ± 0.15
0.8 - 1.2	-7.08 ± 0.89	-8.17 ± 0.86	-6.40 ± 0.62
A-type BRCs			
0.2 - 0.8	-0.92 ± 0.09	-0.96 ± 0.10	-0.87 ± 0.11
0.8 - 1.2	-6.40 ± 0.78	-7.60 ± 0.74	-5.60 ± 0.55
B/C-type BRCs			
0.2 - 0.8	-1.53 ± 0.20	-1.63 ± 0.20	-1.20 ± 0.17

follow a MF that is more biased toward formation of relatively massive stars in comparison to that in case of ‘B’ and ‘C’ type BRCs.

In Fig. 6.5 we have also plotted the CMF generated for a sample aggregate having an average Galactic IMF, i.e., $\Gamma = -1.35$ for $0.6 \leq M/M_{\odot} \leq 1.2$, and $\Gamma = -0.3$ for $0.2 \leq M/M_{\odot} \leq 0.6$ (Kroupa 2001, 2002). The slope of the CMF in the mass range $0.2 \leq M/M_{\odot} \leq 0.6$ comes out to be $\sim -1.1 \pm 0.1$, which is close to the slope of the CMF (-0.9 ± 0.1) of the YSOs ($0.2 \leq M/M_{\odot} \leq 0.8$) in the ‘A’ type BRCs. Whereas, the CMF slope for YSOs in the ‘B/C’ type BRCs is significantly steeper (-1.5 ± 0.2) than the standard MF. This suggests that in the mass range $0.2 \leq M/M_{\odot} \leq 0.8$ the YSOs in ‘A’ type BRCs follow the standard form of MF, whereas aggregates in ‘B/C’ type BRCs is more biased towards relatively less massive objects. We have also estimated the effect of errors on estimation of MF. The results are given in Table 6.1 which indicate an insignificant effect on the MF slopes.

6.4 Disk evolution and CMFs of Class II and Class III YSOs associated with the cluster and BRCs in W5 E HII region

In section 6.2 YSOs used to study the disk evolution of TTSs associated with BRCs were selected on the basis of $H\alpha$ emission only. Since data for individual BRCs were not statistically significant, we combined the data of different types of BRCs lying in different star forming regions. The star formation and evolution of TTSs associated with BRCs may depend on the prevailing conditions in the region, it will be worthwhile to investigate the disk evolution properties and the mass distribution of YSOs associated with individual BRCs of the same HII region. Since many PMS stars also show NIR/MIR excess caused by circumstellar disks, NIR/MIR photometric surveys are powerful tools to detect the low-mass PMS stars. We have carried out deep optical observations of the BRCs and cluster region in W5 E HII region (see Chapter 3), we can study the evolution and MFs of the YSOs associated with the BRCs and cluster region. The identification of PMS stars on the basis of $H\alpha$ emission, NIR and MIR excess emission associated with the cluster region, their age and mass estimates already have been carried out in Chapter 3. Here we identify the YSOs associated with the BRC regions using optical, NIR and MIR photometry using the procedure discussed in section 3.5.

6.4.1 NIR-CC diagram of PMS stars associated with the BRCs

The NIR-CC diagrams for the identified YSOs (with $H\alpha$ emission stars from Ogura et al. 2002, NIR excess stars from 2MASS photometry and MIR excess stars from Koenig et al. 2008) in the BRC NW, BRC 13 and BRC 14 are shown in Figs. 6.6a, 6.6b and 6.6c, respectively. The NIR-CC diagrams were used to estimate A_V for each of these YSOs by tracing them back to the intrinsic CTTS locus of Meyer et al. (1997) along the reddening vector (for details; see 2.5.3.1). The A_V for the stars lying in the ‘F’ region is estimated by tracing them back

6.4 Disk evolution and CMFs of Class II and Class III YSOs associated with the cluster and BRCs in W5 E HII region

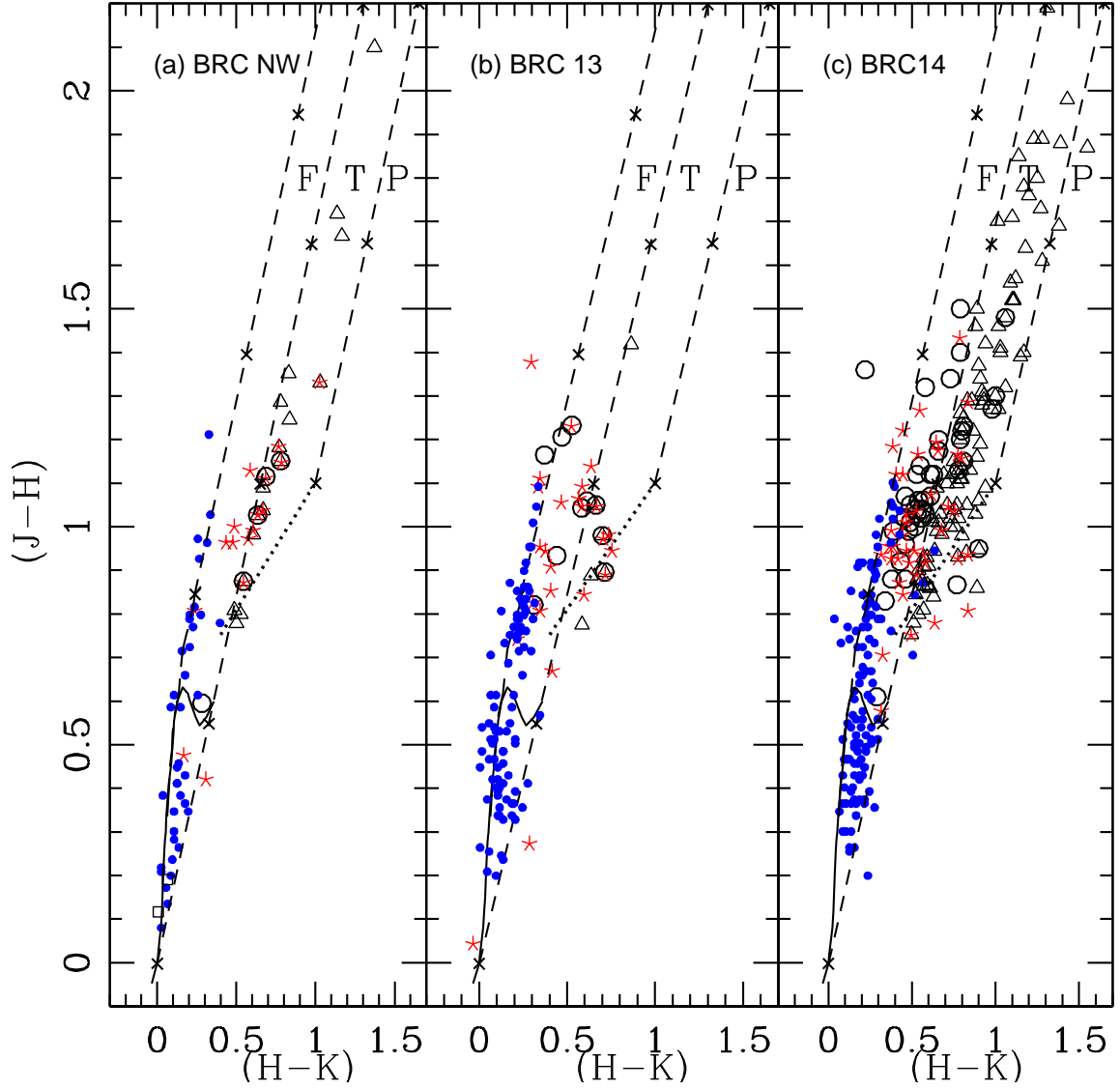


Figure 6.6: The $(J - H)/(H - K)$ CC diagrams of the YSOs in the BRC NW, BRC 13 and BRC 14. Class I, Class II, Class III and transition sources from *Spitzer* photometry are shown by filled triangles, asterisks, filled circles and open squares, respectively. NIR excess sources from 2MASS and Matsuyanagi et al. (2006) (in case of BRC 14) are shown by open triangles and $H\alpha$ sources from Ogura et al. (2002) are shown by open circles.

6.4 Disk evolution and CMFs of Class II and Class III YSOs associated with the cluster and BRCs in W5 E HII region

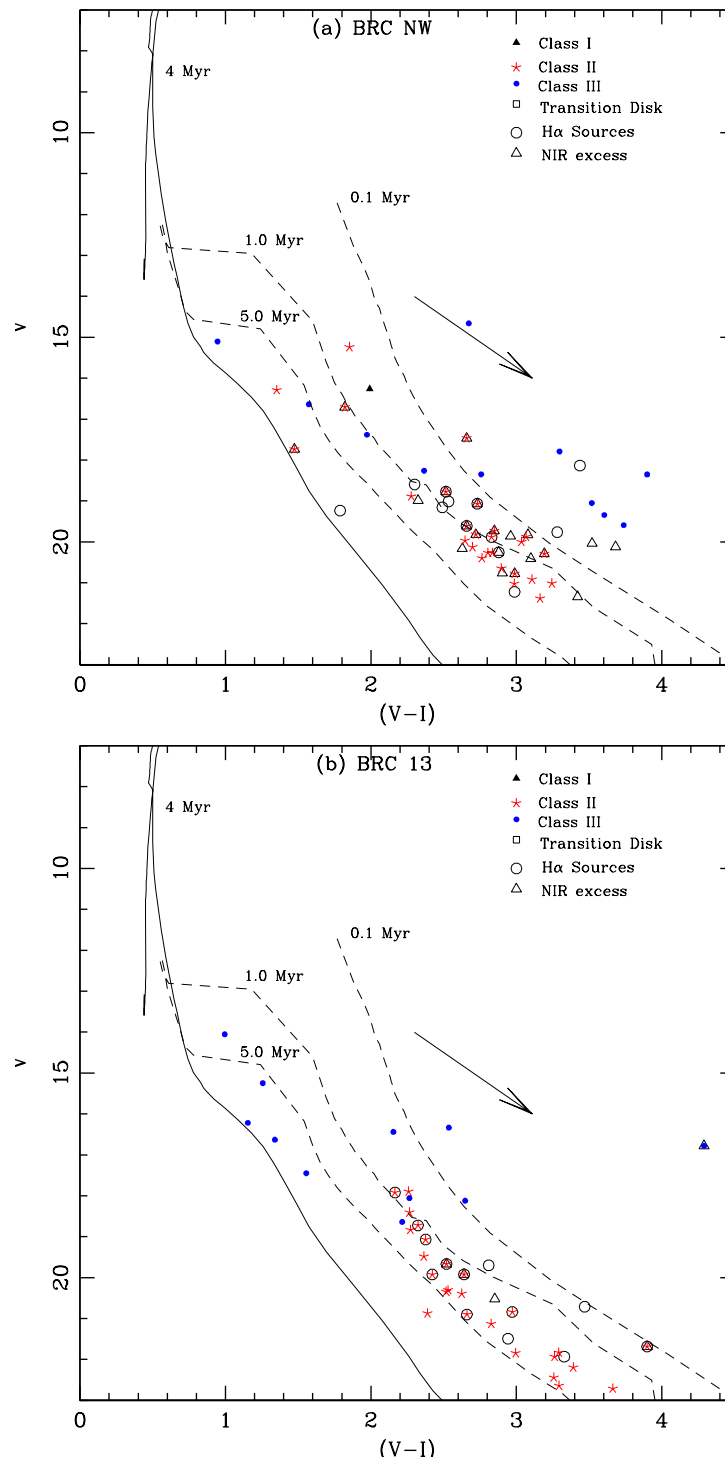


Figure 6.7: $V/(V - I)$ CMD for the YSOs selected (see the text) in BRC NW and BRC 13. The continuous line is the isochrone of 4 Myr from Girardi et al. (2002) and dashed lines are 0.1, 1 and 5 Myr PMS isochrones from Siess et al. (2000). The isochrones are corrected for the distance and reddening of the respective regions. The arrow represents the reddening vector.

6.4 Disk evolution and CMFs of Class II and Class III YSOs associated with the cluster and BRCs in W5 E HII region

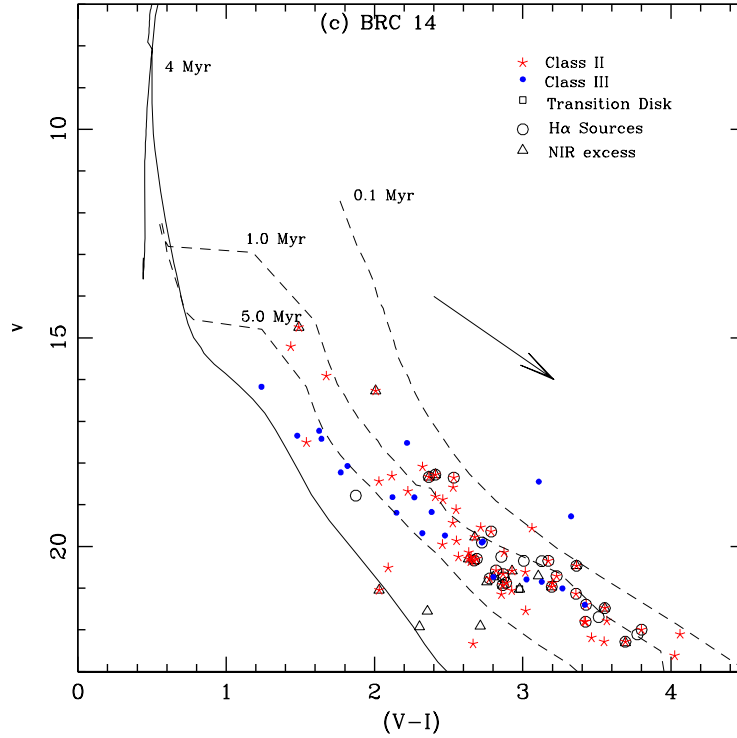


Figure 6.7 cont. $V/(V - I)$ CMD for the YSOs selected (see the text) in BRC 14. .

to the extension of the intrinsic CTTS locus. The mean reddening for each BRC region is calculated. The mean A_V values for BRC NW, BRC 13 and BRC 14 are found to be 2.26 mag, 2.33 mag and 3.05 mag, respectively. Fig. 6.7 shows the $V/(V - I)$ CMDs of the YSOs selected using the NIR-CC diagram in the three BRC regions (see section 3.5). Again, the CMDs indicate that practically all of them are PMS stars but, at the same time reveal a significant scatter in their age.

6.4.2 Evolution of disks of Class II and III sources associated with the Cluster and BRC regions

We have derived the age of 79, 26, 29, 59 Class II and 28, 5, 5, 17 Class III sources in the cluster, BRC NW, BRC 13, BRC 14 regions, respectively. Assuming that all the identified Class II and Class III stars are CTTSs and WTTSs respectively, we can study the possible evolution of the TTSS. The advantage of the above sample

6.4 Disk evolution and CMFs of Class II and Class III YSOs associated with the cluster and BRCs in W5 E HII region

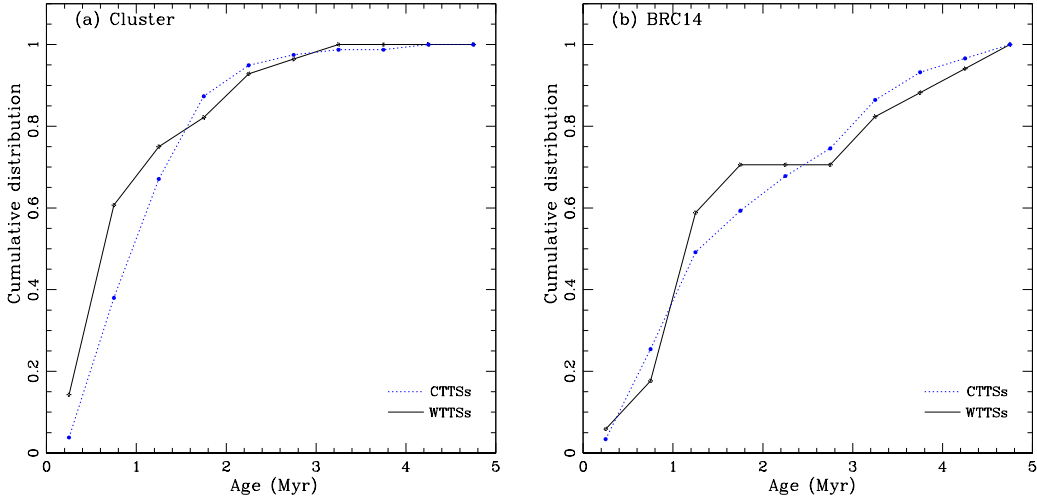


Figure 6.8: Cumulative age distribution of Class II (CTTSs) and Class III (WTTSs) sources in the (a) cluster and (b) BRC 14 region.

in addressing this issue is that the stars are spatially, i.e., three-dimensionally, very close to each other, so there should be no problem of distance difference, contrary to extended T associations. Here we would like to caution the readers that although we have attempted to clean the Class III sample from sources not belonging to W5, however, to confirm the WTTSs nature of these sources in the absence of spectral information such as measurement of the Lithium absorption line is difficult.

Since data for Class III sources in the BRC NW and BRC 13 regions are not statistically significant, in Fig. 6.8 we show the cumulative distribution of Class II and Class III sources in the cluster and BRC 14 region only. Fig. 6.8 indicates that both the Class III and Class II sources have rather similar distribution. A KS-test for the combined sample of the cluster and BRC 14 region confirms the statement that the cumulative distributions of Class II sources (CTTSs) and Class III sources (WTTSs) are different only at a confidence level of 50%. Hence, we can conclude that both the samples have rather similar distribution with practically indistinguishable age distribution. This result is in contradiction with that of Bertout et al. (2007) for the Taurus-Auriga T-association and that of presented in Sec. 6.2, that WTTSs are older than CTTSs and CTTSs evolve

6.4 Disk evolution and CMFs of Class II and Class III YSOs associated with the cluster and BRCs in W5 E HII region

into WTTSs; and it is in agreement with those which claim that the CTTSs and WTTSs are coeval and have indistinguishable properties. Here we have to keep in mind that the classification of CTTS and WTTS in this section is based on the Spitzer MIR observations whereas in Sec. 6.2 and in Bertout et al. (2007), the classification was based on the EWs of H α emission stars. H α surveys may fail to detect Class III sources which have smaller EWs whereas, those sources can be identified using the MIR observations. Here it is worthwhile to point out that the Class III sources by Koenig et al. (2008) were identified on the basis of all four *Spitzer* IRAC bands (3.6, 4.5, 5.8 and 8.0 μm). The detection of Class III sources would be suppressed because of less sensitivity at 5.8 and 8.0 μm bands and also because of the very bright, variable background at these wavelengths in W5. Koenig et al. (2008) have stated that their photospheric sample is only 90% complete to 2 M_{\odot} in general in W5, and to 8 M_{\odot} on regions of bright background emission (e.g., the BRCs studied in this paper). This fact is evident in $V/(V - I)$ CMD (Fig. 6.7) by comparing the number of Class II sources to the number of Class IIIs fainter than 20th magnitude in V band.

6.4.3 CMF of identified YSOs in the cluster and BRCs in W5 E HII region

Fig. 6.9 compares the CMFs of the YSOs in the BRC regions and the cluster associated with the W5 E region, presuming that the biases (if any) in all the four samples are the same. It is interesting to mention that the CMFs of the three BRCs show a break in the slope at $\sim 0.8 M_{\odot}$. The slopes of the CMFs are given in Table 6.2, which indicate that in the case of three BRCs, the slopes in the mass range $0.8 \leq M/M_{\odot} \leq 1.2$ are almost the same. However, in the mass range $0.2 \leq M/M_{\odot} \leq 0.8$, the slopes in the BRCs 13 and 14 are found to be similar, whereas CMF in the central cluster and BRC NW are biased towards lower mass in comparison to BRCs 13 and 14 regions. The average Galactic IMF in the mass range $0.2 \leq M/M_{\odot} \leq 0.6$, i.e., $\Gamma = -0.3$ (Kroupa 2001, 2002) corresponds to the slope of the CMF of -1.1 ± 0.1 . This fact also indicates that the cluster region and BRC NW have relatively more low mass YSOs in the mass range $0.2 \leq M/M_{\odot} \leq 0.8$.

6.4 Disk evolution and CMFs of Class II and Class III YSOs associated with the cluster and BRCs in W5 E HII region

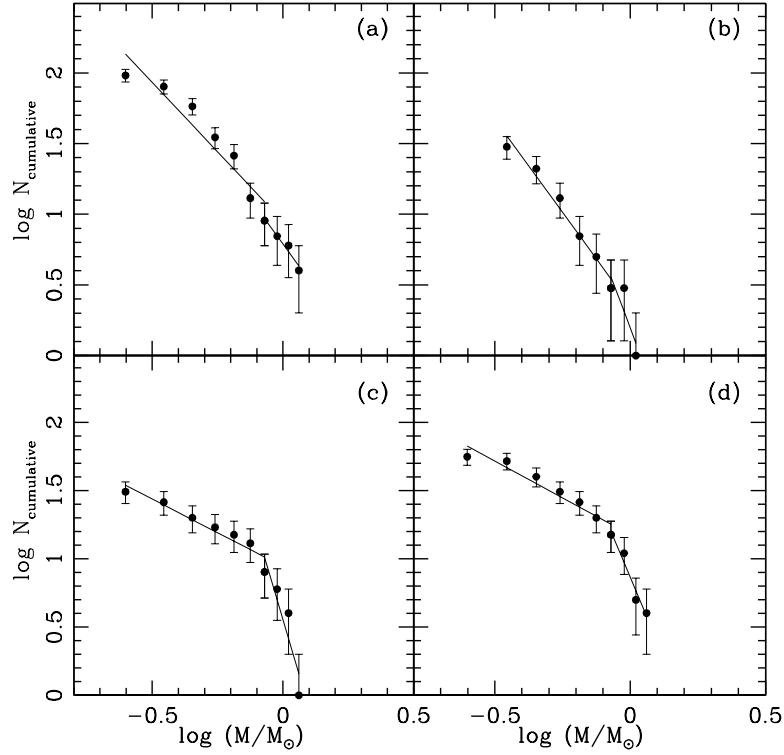


Figure 6.9: CMFs of YSOs in the (a) cluster, (b) BRC NW, (c) BRC 13 and (d) BRC 14 regions. Error bars represent $\pm\sqrt{N}$ errors.

Table 6.2: CMF of the YSOs in the cluster and BRC regions

Region	CMF in the mass range	
	$0.8 \leq M/M_{\odot} \leq 1.2$	$0.2 \leq M/M_{\odot} \leq 0.8$
Cluster	-2.54 ± 0.40	-1.97 ± 0.28
BRC NW	-5.06 ± 3.18	-2.63 ± 0.21
BRC 13	-6.45 ± 2.01	-0.98 ± 0.14
BRC 14	-4.69 ± 0.75	-1.08 ± 0.14

6.5 Conclusions

On the basis of the optical and NIR analysis of six BRC aggregates presented in section 6.2 & 6.3, we reached to the following conclusions:

It is found that the EW of $H\alpha$ emission in TTSs associated with the BRCs decreases with age. We found some $H\alpha$ emission stars that are significantly older than those TTSs associated with the BRCs. They apparently must have formed spontaneously before the main star formation event which gave birth to the massive stars in the region; however their origin is not clear. We found that in general WTTSs are older than CTTSs. It is also found that the fraction of CTTSs among the TTSs associated with the BRCs is found to decrease with age, as found in Taurus region by Armitage et al. (2003). These facts are in accordance with the conclusion by Bertout et al. (2007) that CTTSs evolve into WTTSs.

The CMF of ‘A’ type BRCs seems to follow a MF similar to that found in young open clusters, whereas ‘B/C’ type BRCs have a significant steeper CMF, indicating that BRCs of the latter type tend to form relatively more low mass YSOs of the mass range $0.2 \leq M/M_{\odot} \leq 0.8$.

The main conclusions of our study of the Class II and Class III YSOs (identified on the basis of optical, NIR and MIR data) of BRCs and cluster associated with the W5 E HII region are as follows;

It is found that the age distributions of the Class II and Class III sources are the same. This result is in accordance with the results which claimed that the CTTS and the WTTS are coeval and have indistinguishable age distribution (e.g., Gras-Velázquez & Ray 2005; Lawson et al. 1996; Walter et al. 1988). In the mass range of $0.2 \leq M/M_{\odot} \leq 0.8$; the CMFs of the YSOs associated with the three BRCs show a break in the slope at $\sim 0.8 M_{\odot}$. The CMFs indicate that the cluster region and BRC NW have relatively more low mass YSOs in the mass range $0.2 \leq M/M_{\odot} \leq 0.8$.

Chapter 7

STAR FORMATION IN THE W5 E HII REGION

7.1 Introduction

The W5 E region (see Fig. 3.1) is an excellent example of triggered star formation. The presence of central O7 MS star HD 18326 and several bright-rim like structures makes this region an interesting object to study triggered star formation. This region contains two of the BRCs catalogued in SFO 91. The millimeter line study by Niwa et al. (2009) has revealed the presence of a ^{13}CO cloud and C^{18}O cores on the eastern and northern sides of the region but there is no evidence for clouds on the southern side. They also found high density clumps in the BRC NW region. Karr & Martin (2003) concluded that the exciting O stars and YSOs along the edges of the whole W5 E HII region belong to two different generations. Based on the expansion velocity of the HII region and the evolutionary stages of the IRAS YSOs, they concluded that the timescale is consistent with the triggering by the RDI process.

In chapters 4 & 5, we have studied the star formation scenario in and around BRCs using the YSOs selected on the basis of $\text{H}\alpha$ emission and NIR excess and found evidence for triggered star formation around BRCs 13 and 14. Nakano et al. (2008) detected several $\text{H}\alpha$ emission stars in the W5 E region. They found

¹The results presented in this chapter have been accepted for publication (Chauhan et al. 2011) and communicated to PASJ (Chauhan et al. 2011)

that the young stars near the exciting stars are systematically older (~ 4 Myr) than those near the edge of the HII region (~ 1 Myr) and concluded that the formation of stars proceeded sequentially from the centre of the HII region to the eastern bright rims.

On the basis of the large-scale distribution of YSOs selected using *Spitzer* data, Koenig et al. (2008) found that the ratio of Class II to Class I sources within the whole W5 HII region cavity is ~ 7 times higher compared to the regions associated with the molecular cloud. They attributed this difference to an age difference between the two locations and concluded that there exist at least two distinct generations of stars in the region. They stated that the triggering is a plausible mechanism to explain the multiple events of star formation and suggested that the W5 HII region merits further investigation.

Earlier works studying the star formation scenario in the region were often qualitative (e.g., Karr & Martin 2003; Koenig et al. 2008). Some were quantitative studies, but they were based on a smaller sample of stars (e.g., Chauhan et al. 2009; Nakano et al. 2008; Ogura et al. 2007). Since in the present work we have a larger database, it will be worthwhile studying the global scenario of star formation in the region.

Recent high-resolution images of the IC 1848 (= W5) HII region taken with the *Spitzer Space Telescope* show a wealth of intricate structures inside/on its boundaries (See, e.g., Figure 4 of Koenig et al. 2008). Some of them are BRCs cataloged in SFO 91. But others are morphologically much different from usual BRCs, suggesting that they are genetically different from BRCs. We will discuss this point in Sect. 7.3, but briefly, we suspect that, whereas BRCs are mostly originated from pre-existing clouds left-over in evolved HII regions, some of them may have resulted from the hydrodynamical instability of the I-fronts of the expanding HII regions. Of particular interest is a concentration of thin and long elephant trunk-like structures (hereafter abbreviated as *ETLSs*) in the southeastern part of W5 E. Figure 7.1 is a contrast-enhanced pseudo-colour image of part of W5 E taken by the *Spitzer Space Telescope* (blue: $3.6\mu\text{m}$, green: $8.0\mu\text{m}$, red: $24.0\mu\text{m}$). Note that all these *ETLSs* point to HD 18326, the exciting O star of W5 E. Very interestingly, some of them have a star/a few stars at their very tip, as marked in Fig. 7.1. This led us to suspect that they gave birth to these stars

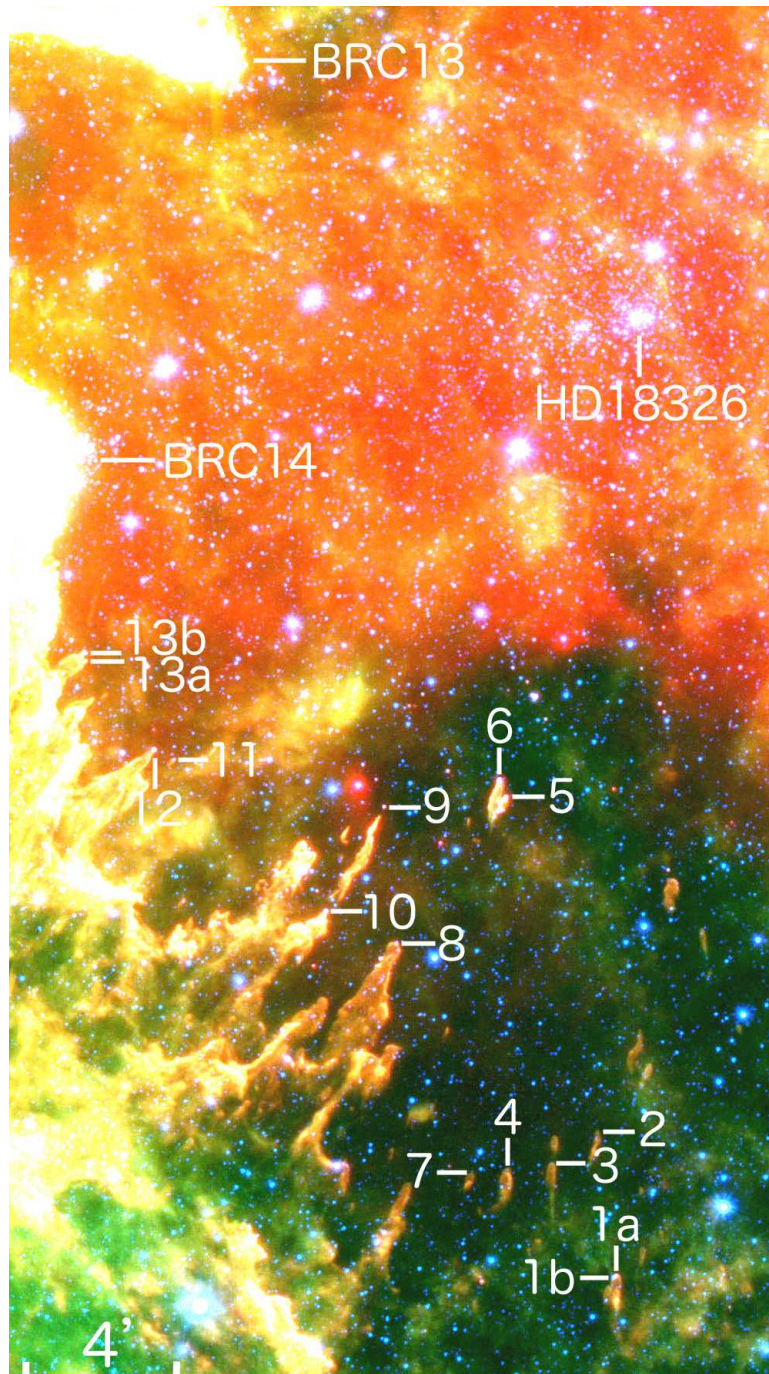


Figure 7.1: Contrast-enhanced *Spitzer* pseudo-colour image of part of W5 E taken from the NASA Spitzer Space Telescope website. Stars at the tip of elephant trunk-like structures are marked together with two bright-rimmed clouds and the exciting star of W5 E. The scale is shown. North is up, east to the left.

under the compressing effects of the HII gas. Zavagno et al. (2007) found two intrusions of similar morphology with a star at their tip in RCW 120 (see their Fig. 12). We further suspect that the hydrodynamical instability of the ionization fronts creating *ETLSs* makes a third mechanism of triggered star formation associated with HII regions, in addition to the *collect-and-collapse* process of the shell accumulated around an expanding HII region and *radiation-driven implosion* of BRCs.

In this chapter we shall discuss the large scale star formation scenario in the W5 E HII region using the identified YSOs in the region

7.2 Reddening law in BRC regions

To study the nature of the extinction law in the BRC regions, we used TCDs as described by Pandey et al. (2003) (see Section 3.6). The TCDs for the Class III YSOs associated with the cluster and BRC regions are shown in Figs. 7.2a - 7.2c. In order to avoid IR excess stars, we have used all the *Spitzer* Class III sources having $V < 17$ mag. The slopes of the distributions are given in the figure. The ratio of total-to-selective extinction ‘ R_V ’ in the regions is estimated using the procedure described in Pandey et al. (2003). The R_V values in the BRC regions, i.e., BRC NW, BRC 13 and BRC 14 are estimated to $R_{BRCNW} = 3.46 \pm 0.20$, $R_{BRC13} = 3.41 \pm 0.03$ and $R_{BRC14} = 2.75 \pm 0.12$, respectively. The higher values of R_{BRCNW} and R_{BRC13} indicate a larger grain size in the BRC NW and BRC 13 regions, whereas the smaller value of R_{BRC14} suggests a smaller grain size in the case of BRC 14. This indicates that the evolution of dust grains in the W5 E region has not taken place in a homogeneous way.

7.3 Star formation around BRC regions

BRCs are considered to be a sort of remnant clouds originating from the dense parts (cores) in an inhomogeneous molecular cloud. So, if the original core was big enough, the resultant BRC could have undergone a series of RDI events (Kessel-Deynet & Burkert 2003), leaving an elongated distribution of young stars. The distribution and evolutionary stages of such YSOs could be used to probe the star

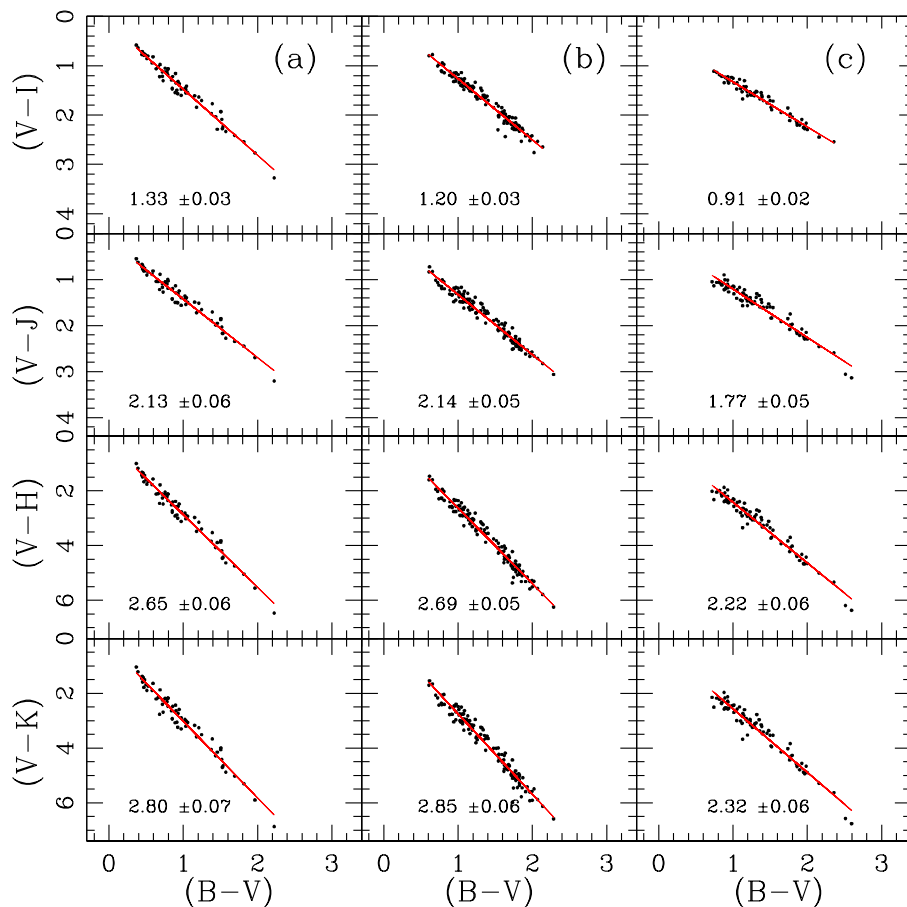


Figure 7.2: TCDs for the diskless (Class III) sources in the (a) BRC NW, (b) BRC 13 and (c) BRC 14 regions.

formation history in the HII regions. Using *Spitzer* observations Koenig et al. (2008) have identified clustered and distributed population of YSOs in W5 (see their figure 12). The clustered population shows a nice alignments of Class II sources towards the directions of BRCs from the ionization sources. In Chapter 5, we also examined the global distribution of YSOs, the radial distribution of A_V as well as the amount of NIR excess $\Delta(H - K)$, in the BRCs 13 and 14 regions. On the basis of these distributions, star formation was found to have propagated from the ionising source in the direction of the BRCs. Fig. 7.3 shows the global distribution of clustered YSOs selected from the study of Koenig et al. (2008), in the whole W5 E region, which indicates an alignment of YSOs towards the

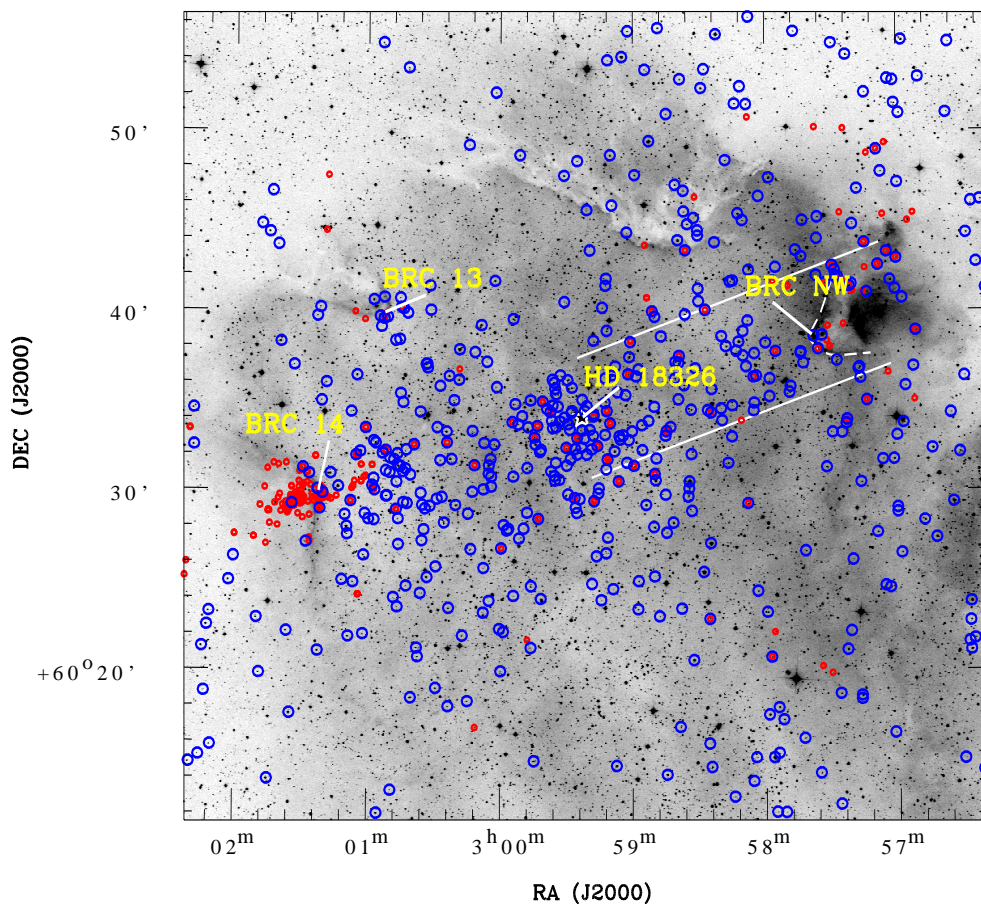


Figure 7.3: Global distribution of YSOs in the W5 E HII region. Small red circles show the location of NIR excess sources, whereas large blue circles show the YSOs identified using the *Spitzer* observations (see text).

direction of the BRCs. Fig. 7.4 shows the radial variation of $\Delta(H - K)$ and A_V , of the YSOs located within the strip towards the direction of BRC NW region. The distribution reveals higher A_V values near the BRC NW region.

On the basis of the global distribution of YSOs in the region and the radial distribution of the amount of NIR excess $\Delta(H - K)$ and A_V in the region (cf. Figs. 7.3, 7.4, 5.11, 5.12, 5.13) as well as the age distribution of YSOs, it seems that a series of RDI processes proceeded in the past from near the central O star towards the present locations of the BRCs.

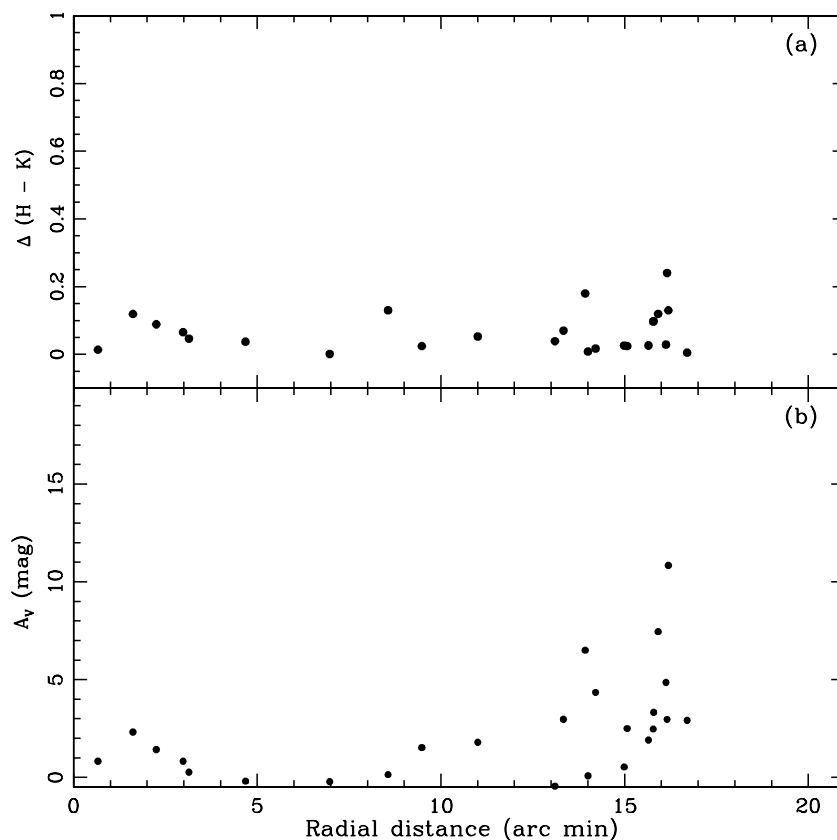


Figure 7.4: Variation of NIR excess $\Delta(H-K)$ (upper panel) and A_V (lower panel) for the IR excess stars in the strip toward BRC NW as a function of distance from the ionising source (HD 18326) of the W5 E HII region.

7.3.1 Small scale sequential star formation (S^4F)

In the Chapter 6 we have obtained a sample of YSOs associated with W5 HII region which is significantly larger as compared to that used in Chapters 4 & 5. Hence, it will be interesting to examine the S^4F hypothesis with the new sample of YSOs. To further verify the S^4F hypothesis we follow the approach as given in Chapters 4 & 5. We have divided the YSOs associated with BRCs into two groups: those lying inside/on the rim (i.e., stars embedded or projected onto the molecular cloud/lying on the rim) and outside the rim (i.e., stars lying outside the rim in the projected HII region) (see e.g., Figure 5.2 for BRCs 13 and 14). Mean age has been calculated for these regions. Since the ionising source of the

7.4 Nature and origin of the stars at the tip of ETLs

Table 7.1: Mean age inside/on the rim and outside rim in BRCs associated with W5 E.

Region	Mean age (Myr)	
	Inside/On the rim (number of sources)	Outside rim (number of sources)
BRC NW	0.92 ± 0.56 (12)	1.29 ± 0.54 (19)
BRC 13	1.61 ± 1.41 (10)	2.44 ± 1.37 (24)
BRC 14	1.01 ± 0.73 (18)	2.32 ± 1.22 (58)

BRCs studied here has a maximum MS lifetime of 4-5 Myr, therefore the sources having age greater than 5 Myr can not be expected as the products of triggered star formation. They might have formed spontaneously in the original molecular cloud prior to the formation of the HII region. Some of them may be background stars; larger distances make them look older in the CM diagram. Therefore, while calculating the mean age we have not included those stars. The results are given in Table 7.1, which shows that in all the BRCs, the YSOs lying on/inside the rim are younger than those located outside it. The above results are exactly the same as those obtained in Chapters 4 & 5. Therefore, the present results further confirm the S^4F hypothesis. As discussed in Chapters 4 and 5, we again find a large scatter in the stellar age in spite of a clear trend of the mean age.

7.4 Nature and origin of the stars at the tip of ETLs

In order to examine the PMS nature of the stars located at the tip of the *ETLs*, we carried out VI_c photometry of these stars and constructed a $V/V - I_c$ CMD. We also used NIR data from the 2MASS to construct a NIR -CC diagram as well as MIR data from *Spitzer Space Telescope* to make SED curves.

7.4.1 Target Selection, Observations and Data Reduction

BRCs are small clouds apparently with both width and length of several arcmin, corresponding to the physical size of a few pc typically (see, SFO 91, Sugitani & Ogura 1994). In these papers BRCs are morphologically classified into *types A, B*

7.4 Nature and origin of the stars at the tip of ETLs

Table 7.2: Stars at the tip of elephant trunk-like structures

Star ID	$\alpha_{(2000)}$ (h:m:s)	$\delta_{(2000)}$ ($^{\circ}$: ' : ")	identification & remarks	
1a	02:59:18.08	+60:08:37.7	brighter than 1a	
1b	02:59:18.61	+60:08:34.5		
2	02:59:23.28	+60:12:22.9		
3	02:59:32.93	+60:11:32.1		
4	02:59:42.33	+60:11:18.4		
5	02:59:46.25	+60:21:09.7		K14
6	02:59:47.75	+60:21:36.6		
7	02:59:49.66	+60:11:13.1		
8	03:00:08.01	+60:17:12.1		
9	03:00:12.21	+60:20:45.4		
10	03:00:23.54	+60:17:55.1	K15	
11	03:00:57.52	+60:21:44.0		
12	03:01:01.97	+60:21:57.7	K16	
13a	03:01:17.42	+60:24:13.4		
13b	03:01:17.55	+60:24:25.0	K17?	

Note – K numbers are identifications from Table 4 of Koenig et al. (2008). The coordinates of K17 are between those of 13a and 13b. There is another star 5.4 " NE of 13b. It is relatively bright in the optical, but presumably a field star unrelated to the *ETLS* in view of its positions on the $V/(V - I_c)$ CMD and $(J - H)/(H - K)$ NIR-CC diagram.

and *C* according to their length to width ratios with *type C* the most elongated. But many of the *ETLS*s found in Fig. 7.1 are much more elongated and of far smaller widths (typically a few tenths of *pc*) than most of the *type C* BRCs in SFO 91 and Sugitani & Ogura (1994). We searched for such peculiar *ETLS*s that have a star/stars at their tip on the *Spitzer* 3.6 μm , 4.5 μm and 8.0 μm images. Table 7.2 gives the results, listing such stars with running numbers identified in Fig. 7.1, the coordinates and some remarks. We refer to these stars as *ETLS* stars. Some of them are listed in Koenig et al. (2008)(see their Table 4).

For the *ETLS* stars that are visible in the *DSS 2 red* image, we carried out

7.4 Nature and origin of the stars at the tip of ETLs

Table 7.3: Log of observations

$\alpha_{(2000)}$ (h:m:s)	$\delta_{(2000)}$ ($^{\circ}$: ' : ")	Filter & Exposure(sec) \times no. of frames	Date of observa- tions (yr-mm-dd)
02:59:18.6	+60:08:34	V:600 \times 3; I:200 \times 3	2009-11-22
03:20:07.0	+60:18:47	V:600 \times 3; I:200 \times 3	2009-11-23
03:00:44.7	+60:20:45	V:600 \times 2; I:200 \times 3	2009-11-24

photometric observations in the VI_c bands using HFOSC in the imaging mode mounted on the 2.0-m HCT of the IAO, Hanle, India on 2009 November 22, 23 and 24. The details of the site, HCT and HFOSC are discussed in Section 2.2. The sky at the time of observations was photometric with a seeing size (FWHM) of $\sim 1''.5$. A number of bias and twilight flat frames were also taken during the observing runs. The log of the HCT observations is tabulated in table 7.3

The data processing and analyses were performed using the procedure discussed in Section 2.2.5. The data was standardised by using the secondary standards taken from Chapter 3. The photometric accuracies depend on the brightness of the stars, and the typical DAOPHOT errors in V and I_c bands at $V \sim 18$ are smaller than 0.01 mag. Near the limiting magnitude of $V \sim 22$ the DAOPHOT errors increase to 0.1 and 0.02 mag in the V and I_c bands, respectively.

Since YSOs often show NIR/MIR excesses caused by circumstellar disks, NIR/MIR photometric data are very important to know their nature and evolutionary status. NIR JHK_s data for the *ETLS* stars have been obtained from the 2MASS Point Source Catalog (PSC) (Cutri et al. 2003). Also we tried to collect IRAC 3.6 μm , 4.5 μm , 5.6 μm and 5.8 μm and MIPS 24 μm photometry for them from Koenig et al. (2008)'s list of stars in the W5 region. We searched for the 2MASS and *Spitzer* MIR counterparts of the *ETLS* stars and identified them using a search radius of $1''.2$. The photometric data for the stars are given in table 7.4.

Table 7.4: Photometric data for the *ETLS* stars

Star ID	$V \pm eV$ (mag)	$I_c \pm eI_c$ (mag)	$J \pm eJ$ (mag)	$H \pm eH$ (mag)	$K_s \pm eK_s$ (mag)	$[3.6] \pm e[3.6]$ (mag)	$[4.5] \pm e[4.5]$ (mag)	$[5.8] \pm e[5.8]$ (mag)	$[8.0] \pm e[8.0]$ (mag)	$[24] \pm e[24]$ (mag)	class et al. 2008)
1b	20.73 ± 0.08	17.59 ± 0.02	14.63 ± 0.04	12.72 ± 0.03	11.78 ± 0.03	11.04 ± 0.01	10.92 ± 0.01	10.74 ± 0.02	10.56 ± 0.06	-	III
5*	19.49 ± 0.02	17.25 ± 0.01	16.14 ± 0.11	15.22 ± 0.11	14.38 ± 0.1	12.65 ± 0.01	11.9 ± 0.01	11.04 ± 0.01	9.9 ± 0.03	6.68 ± 0.16	I
6	20.13 ± 0.02	17.35 ± 0.01	15.41 ± 0.08	14.07 ± 0.06	12.96 ± 0.04	11.93 ± 0.01	11.27 ± 0.01	10.59 ± 0.01	9.63 ± 0.01	6.11 ± 0.12	II
9*	19.81 ± 0.02	16.93 ± 0.01	15.08 ± 0.05	14.08 ± 0.05	13.5 ± 0.04	12.85 ± 0.01	12.41 ± 0.01	11.9 ± 0.02	10.99 ± 0.02	8.08 ± 0.06	II
10*	17.4 ± 0.01	15.05 ± 0.01	13.38 ± 0.03	12.48 ± 0.03	11.96 ± 0.03	11.29 ± 0.01	10.91 ± 0.01	10.48 ± 0.01	9.9 ± 0.01	7.16 ± 0.14	II
12	18.66 ± 0.01	16.03 ± 0.01	14.31 ± 0.03	13.24 ± 0.03	12.64 ± 0.03	11.59 ± 0.01	11.08 ± 0.01	10.56 ± 0.01	9.73 ± 0.01	7.08 ± 0.08	II
13b	22.08 ± 0.09	18.19 ± 0.01	16.09 ± 0.11	14.84 ± 0.08	14.14 ± 0.08	13.01 ± 0.01	12.61 ± 0.01	12.06 ± 0.02	11.12 ± 0.05	-	II

* V and I_c magnitudes are averages of those obtained from different nights.

7.4.2 Results

7.4.2.1 NIR colour-colour diagram

Figure 7.5a shows the $(J - H)/(H - K)$ NIR-CC diagram (see Sec. 2.5.2.2 for details) for the *ETLS* stars identified in the 2MASS catalogue. In figure 7.5a *ETLS* stars having a 2MASS counterpart, are plotted with different symbols according to the classifications by Koenig et al. (2008) based on the *Spitzer* data. Sources of class I, class II and class III are shown by filled circles, by triangles and by open circles, respectively. Figure 7.5a seems to indicate that most of the *ETLS* stars are low-mass PMS objects. We estimated A_V for each star by tracing them back to the intrinsic CTT line of Meyer et al. (1997) along the reddening vector (for details; see Section 2.5.3.1). The mean of the individual A_V values turned out to be $A_V = 2.4 \pm 1.2$ mag or $E(V - I_c) = 0.96 \pm 0.48$ mag, which we use in further discussions.

7.4.3 Optical colour magnitude diagram

In Fig. 7.5b we give the $V/(V - I_c)$ CMD of the *ETLS* stars listed in Table 7.4. The PMS isochrones of Siess et al. (2000) are overlaid after being shifted to the distance modulus 13.5 mag (distance of 2.1 *kpc*; see Chapter 3) and the mean reddening of $E(V - I_c) = 0.96$ mag. Note that the positions of the stars are not corrected for their reddening values. But the effect of variable reddenings on the age estimation is small, because the reddening vector is nearly parallel to the $V/(V - I_c)$ PMS isochrones, as is indicated in Fig. 7.5b. This CMD seems to manifest that these sources are actually PMS stars having the age of 0.5-5 *Myr*. We presume that these stars are physically related to the *ETLS*s because of their location at their very tip. However the possibility that they are field stars (foreground MS or background giant stars) can not be entirely rejected since the southern part of W5 E is located at a very low Galactic latitude ($l \sim 1.5^\circ$).

7.4.3.1 SED fitting

To understand the nature and evolutionary status of *ETLS* stars we construct their SEDs using the recently available grid of models and fitting tools of Ro-

7.4 Nature and origin of the stars at the tip of ETLs

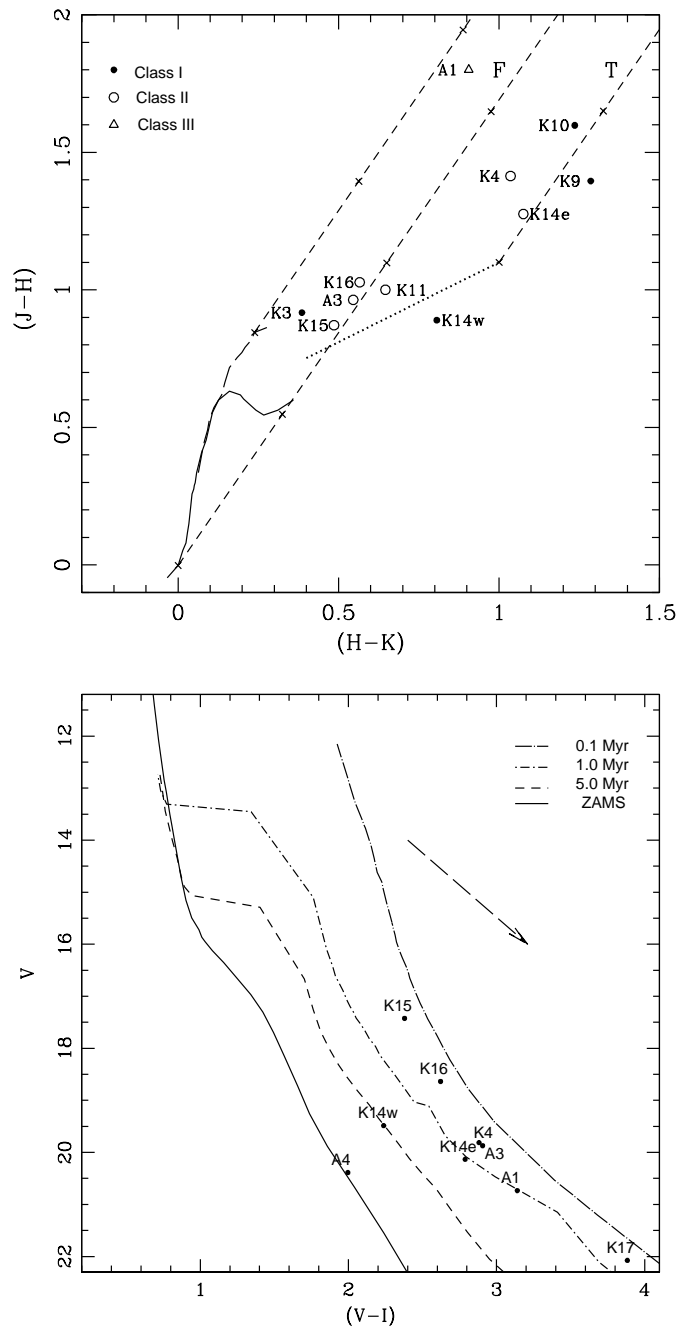


Figure 7.5: (a) NIR CC diagram for the *ETLS* stars. Their classification is taken from Koenig et al. (2008), which is based on the *Spitzer* data. (b) $V/(V - I_c)$ CMD for the *ETLS* stars. The thick continuous line is the ZAMS from Girardi et al. (2002). The PMS isochrones from Siess et al. (2000) for 0.1 Myr, 1 Myr and 5 Myr are also shown. The isochrones are corrected for the distance 2.1 kpc and the mean reddening $E(V - I_c) = 0.96$ mag (see the text). The dashed arrow shows the reddening vector corresponding to $A_V = 2$ mag.

7.4 Nature and origin of the stars at the tip of ETLs

bitaille et al. (2007, 2006). The models are computed using a Monte-Carlo based radiation transfer codes (Whitney et al. 2003b,c) assuming several combinations of a PMS central star, a flared accretion disk, a rotationally flattened in-falling envelope and a bipolar cavity for a reasonably large parameter space. Interpreting SEDs using radiative transfer codes is subject to degeneracies, which spatially-resolved multiwavelength observations can break. The SED fitting tools fit these models to observational data points assuming the distance and foreground reddening as free parameters. For IC 1848 the distance in literature varies from 1.9 to 2.3 *kpc* (Becker & Fenkart 1971; Hillwig et al. 2006; Moffat 1972). Hence we have taken distance in the range of 1.9 to 2.3 *kpc*. Based on the NIR CCD (Fig. 7.5a), we have assumed the visual absorption (A_V) ranges from 2 to 10 mag for these sources. We set the photometric uncertainties to be 10 to 15% error in the NIR and MIR flux estimates. We calculated a goodness-of-fit parameter χ^2 normalized by the number of data points (between 5 to 10) used in the fitting. The evolutionary parameters of each source were determined by using the average of all the “well-fitted” models. The well-fitted models of each source have been defined by

$$\chi^2 - \chi^2_{min} \leq 2N_{data}$$

where χ^2_{min} is the goodness-of-fit parameter for the best fit model. For each source we tabulate the average parameters, such as the interstellar extinction to the source (A_V , which does not include the extinction due to the circumstellar disk or envelope), the mass of the star (M_{star}), the disk accretion rate (\dot{M}_d), and the envelope accretion rate (\dot{M}_{env}). Here it is worthwhile to mention that these are robust values of the parameters, since there are a large number of parameters and the number of observational data points is limited. Figure 7.6 shows three examples of the SEDs fitting. The stellar ages given in table 7.5 should be considered only approximate due to the underlying assumptions in the models. Again the stars have ages ranging from 0.2 to 5 Myr, although the results for individual stars differ from the ages derived from the $V/(V - I_c)$ CMD.

7.4 Nature and origin of the stars at the tip of ETLs

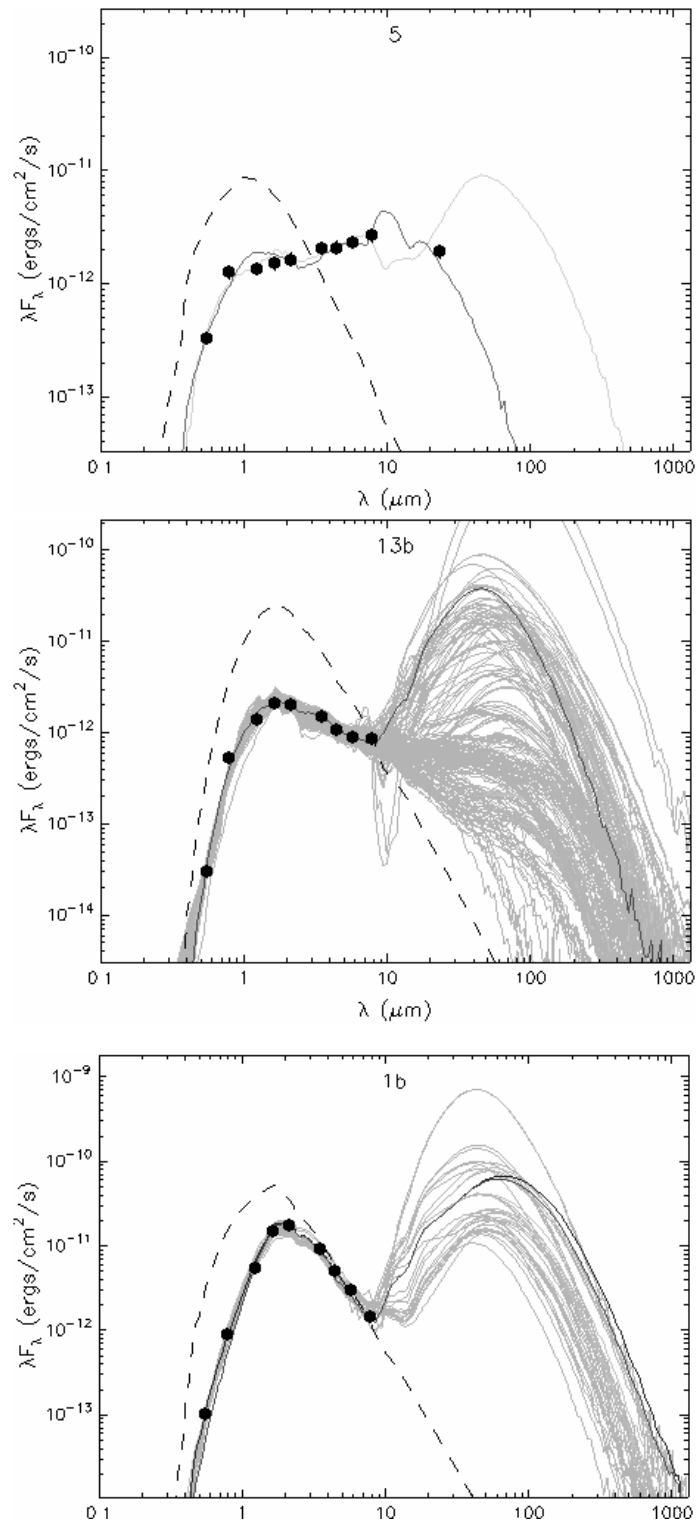


Figure 7.6: The SEDs for a Class I, Class II and Class III sources among the *ETLS* stars. The black line represents the best fit, and the gray lines subsequent good fits. The dashed lines show the stellar photosphere corresponding to the central source of the best fitted model. The filled circles are the input flux values.

7.4 Nature and origin of the stars at the tip of ETLs

Table 7.5: Physical parameters for the *ETLS* stars based on the SED fitting

Star ID	χ^2	A_V (mag)	Age (Myr)	M_{star} (M_\odot)	M_d (M_\odot)	\dot{M}_d ($10^{-8}M_\odot/\text{yr}$)	\dot{M}_{env} ($10^{-6}M_\odot/\text{yr}$)	N_{data}
1b	5.36	3.8 ± 0.8	0.2 ± 0.1	1.8 ± 1.2	0.01 ± 0.03	11.0 ± 11.0	14.0 ± 18.0	9
5	25.85	3.1 ± 0.6	4.4 ± 3.1	2.4 ± 0.3	0.02 ± 0.02	0.12 ± 0.12	1.3 ± 1.7	10
6	9.20	5.5 ± 1.5	5.5 ± 3.6	2.0 ± 1.3	0.01 ± 0.02	14.0 ± 1.8	1.1 ± 11.0	10
9	5.06	4.3 ± 0.8	2.8 ± 2.1	1.6 ± 0.5	0.01 ± 0.01	0.5 ± 0.5	0.03 ± 0.14	10
10	2.15	3.2 ± 0.6	1.0 ± 0.9	2.2 ± 0.8	0.01 ± 0.01	1.4 ± 1.3	0.57 ± 1.2	10
12	5.31	5.1 ± 0.8	4.8 ± 2.6	2.3 ± 0.6	0.01 ± 0.01	3.9 ± 3.6	0.1 ± 0.4	10
13b	7.44	5.4 ± 1.0	2.3 ± 2.3	2.1 ± 0.9	0.01 ± 0.01	1.6 ± 1.5	6.8 ± 16.9	9

7.4.4 Origin of Bright-Rimmed Clouds and Hydrodynamical Instability of Ionization Fronts

Effects of intense UV radiation from OB stars on star formation can be either constructive or destructive depending on the situation. As for the mechanisms with which it works constructively, two mechanisms have so far been proposed: *collect-and-collapse* and *radiation-driven implosion* (RDI). The former/latter is of larger/smaller size in space (~ 10 pc/ ~ 1 pc) and of longer/shorter timescale (\sim a few Myr/ ~ 0.5 Myr).

Collect-and-collapse was advocated by Elmegreen & Lada (1977) in their hypothesis of *Sequential Star Formation* (discussed in Section 1.4.2.1). However, it has never been convincingly confirmed for many years until very recently the Deharveng group (Deharveng et al. 2005; Pomarès et al. 2009, and references therein) presented the first persuasive examples. This mechanism is probably viable in relatively uniform molecular clouds.

RDI takes place in small molecular clouds which are often called as “BRCs”, “globules”, “elephant trunks” and so forth. Detailed observations of physical properties of BRCs cataloged in SFO 91 and Sugitani & Ogura (1994) were made by the British group (Morgan et al. 2008; Urquhart et al. 2009 and references therein) by means of sub-millimeter observations and radio continuum and CO/ ^{13}CO / C^{18}O line observations. They concluded that RDI is in progress in many (but not all) of these BRCs and that massive stars are being formed

there, based on the high luminosity of the embedded sources (Urquhart et al. 2009).

As for the origin of BRCs or elephant trunks, Rayleigh-Taylor instability of expanding HII regions was proposed first (e.g., Spitzer 1954), but Pottasch (1958) pointed out disagreements between their morphologies and theoretical predictions. In mid-1960s Axford (1964) investigated the stability of weak D-type I-Fronts, explicitly taking into account the effect of diffuse UV radiation caused by recombinations to the ground state of hydrogen atoms. He claimed that weak D-type I-Fronts, which correspond to the major part of the evolution of HII regions, are stable against the growth of wavelengths larger than $0.2 pc$, so hydrodynamical instability could not be the origin of elephant trunks. Given the fact that radio observations showed the clumpiness of molecular clouds, BRCs or elephant trunks have since then been considered usually as pre-existing clouds left over in expanding HII regions. Sysoev (1997) re-examined the stability of D-type I-fronts analytically and showed that, contrary to the conclusion by Axford (1964), they are *not* stable even with the effect of the recombination. This new result was confirmed by the numerical simulations of Williams (2002). Prior to these studies, Giuliani (1979) investigated the stability of the combined systems of a D-type IF and a preceding SF and reached a similar conclusion that there is a new regime of instability (longer wavelengths which are similar to the widths of the above structures) that grow rapidly in an oscillatory manner (overstability). Vishniac (1983) generalized this instability including SN/wind bubble S-fronts, and it is now called as “*thin shell instability*” or “*Vishniac instability*”. Its mechanism is simple, as shown, e.g., in Fig. 1 of Garcia-Segura & Franco (1996). The presence of an IF exacerbates the growth of the instability.

Thus BRCs or globules seem to be formed also via hydrodynamical instability without pre-existing molecular clumps. This was clearly shown in the numerical simulations (2-dimensional) of the evolution of HII regions by Garcia-Segura & Franco (1996); such structures arise in all of their models as HII regions expand. In their 3-D simulations Whalen & Norman (2008) obtained very similar results to those of Garcia-Segura & Franco (1996). Other recent numerical simulations of evolution of HII regions with turbulence (Dale et al. 2007; Gritschneider et al. 2010, 2009; Mellema et al. 2006) and without turbulence (Bisbas et al. 2009;

Mizuta et al. 2006) all show the formation of BRC- or globule-like structures. But, since molecular clouds are very clumpy, it is likely that both hydrodynamical instability and pre-existing clumps contribute in reality. As for *ETLSs*, we presume that they result from hydrodynamical instability in view of their very different morphology from that of BRCs.

7.4.5 Third Possible Mechanism of Triggered Star Formation

On the basis of the result that the *ETLS* stars in W5 E are of the PMS nature having ages of 0.5-5 *Myr*, we consider that they formed by the compressing effects of the HII gas from these small clouds which were created by hydrodynamical instability of the expanding HII region. Thus this process seems to make a third mode of triggered star formation associated with HII regions, in addition to *collect-and-collapse* and RDI.

This new mechanism of triggered star formation is somewhat similar to the RDI in BRCs, but it differs in that the cloud was not pre-existing but formed from accumulated and then fragmented gas in the process of expansion of an HII region. In addition we find only one star or at most a few stars at the tip of each *ETLS*, so the scale of star formation in each object is very small. But the total product can be considerable because a large number of these clouds exist in an HII region. In our recent studies on BRC star formation we noticed many IR-excess stars scattered inside HII regions besides W5 E (see Fig. 5.8). We suspect that some of these stars may have been formed by this mechanism. On the *Spitzer* IRAC images of the Carina Nebula Smith et al. (2010) also found a large number of scattered YSOs as well as many features morphologically similar to our *ETLSs*. Table 7.6 summarizes the differences of this mechanism from *collect-and-collapse* and usual RDI.

7.5 Conclusions

The main conclusions of the present chapter are as follows:

Table 7.6: Comparison of modes of triggered star formation

mode	cloud	scale	stars formed	timescale
collect & collapse	accumulated	large	> 300	a few Myr
RDI	pre-existing	small	< 100	< 1 Myr
HD instability	accumulated	small	\leq a few	< 1 Myr

The distribution of the YSOs in the W5 E region indicates that they are globally aligned from the ionising source towards the BRCs. A comparison of the average age of the YSOs lying on/inside and outside the bright rim indicates a quantitative age gradient in the sense that the YSOs located on/inside the rim are younger than those located outside the rim. These results confirm the S^4F hypothesis, which is same as found in Chapters 4 & 5 . The globally aligned distribution of the YSOs, indicate that a series of RDI events took place in the past from near the central ionising source to the periphery of the HII region.

We also paid attention to the numerous, elephant trunk-like clouds in W5 E and their positions on the $V/V - I_c$ CMD indicate that they are PMS stars of ages of mostly one *Myr* or less. The physical parameters for these stars, derived by using the SED fitting tools indicates that they are largely Class I or Class II PMS sources. The PMS nature of these stars strongly suggests that they must have formed from these *ETLSs*. We suspect that the *ETLSs* are created by the hydrodynamical instability of the IF/SF of the expanding HII region, and hypothesize that, in addition to the *collect-and-collapse* process and RDI, this mechanism makes a third mode of triggered star formation associated with HII regions. So particularly, in the case of W5 E, although BRCs are more likely formed due to RDI, the *ETLSs* may have been created by the hydrodynamical instability and some of the YSOs scattered inside HII region may have been formed by this mechanism.

Chapter 8

SUMMARY, CONCLUSIONS AND FUTURE WORK

This thesis presents the results of the multiwavelength investigations of BRCs and clusters associated with HII regions. As described in the chapter 1, the main objectives of the present thesis are to examine the star formation scenario in the HII region, to study the disk evolution of the TTSs and to compare the mass function of the YSOs in the BRCs and cluster region. The summary and conclusion of the work presented in this thesis and strategies for the future work are described in the ensuing sections:

8.1 Summary and conclusions

As our objects are associated with the HII regions created by the massive stars, in **chapter 3**, we studied the evolutionary status of the massive star and the basic properties of the cluster around the massive star as well as the influence of massive star on its immediate vicinity. In order to study the star formation and stellar content of the central cluster of the W5 E HII region, we have used optical, H α , 2MASS and *Spitzer* IRAC/MIPS data. Based on the optical spectroscopy of the massive star, we designated it as an O7 V star. The central cluster has a distance of ~ 2.1 kpc and a radius of $6'$. A mean age of the YSOs identified based on the H α emission activity and NIR/MIR excess is found to be ~ 1.3 Myr. The reddening law in the cluster region is found to be normal. The star

formation in the cluster region is found to be non-coeval, with an age spread of ~ 5 Myr and formation of low mass stars doesn't seem to cease after the formation of high mass star. The slope of the IMF within the cluster region in the mass range $0.4 \leq M/M_{\odot} \leq 30$ is found to be $\Gamma = -1.29 \pm 0.03$, which is comparable to the Salpeter value.

In **chapter 4**, the S^4F hypothesis in the case of BRC aggregates has been examined. For this purpose we undertook BVI_c photometry of four BRC aggregates, namely, BRC 11, BRC 12, BRC 14 and BRC 37. The optical data were complemented with the archive data from 2MASS and $H\alpha$ emission stars from Ogura et al. (2002). The amounts of interstellar extinction and reddening for each star have been estimated by using the JHK_s photometry. We constructed reddening-corrected $V/V-I_c$ CMDs, where the age of each star has been derived. All the stars turned out to be a few tenths to a few Myr old. We divided BRC regions into inside/on the bright rim, outside bright rim and estimated the mean ages and A_V values of the $H\alpha$ stars in these two regions for each BRC aggregate. The regions in each BRC aggregate show big scatters of the ages of the member stars in spite of a clear trend of the mean ages. Although the scatters were large and the numbers of the sample stars were small, we found a clear trend that the stars inside or in the immediate vicinity of the bright rim are younger than those outside it in all the four aggregates, confirming the hypothesis in question.

In **chapter 5** we have studied the S^4F as well as global star formation in HII regions associated with the BRCs. In order to fulfill our purpose we used optical BVI photometry of the BRCs 2, 11, 13, 14, 27, 38 and supplemented it with archival 2MASS data. Hence, in our sample of YSOs we included $H\alpha$ emission stars from Ogura et al. (2002), NIR excess stars from 2MASS NIR photometry. Visual extinction (A_V) and NIR excess ($\Delta(H - K)$) for individual YSO were calculated using the NIR $(J - H)/(H - K)$ CC diagram. We estimated the ages of individual YSOs associated with BRCs from the reddening-corrected $V_0, (V - I_c)_0$ CMDs. The comparison of the average ages of the YSOs lying on/inside and outside bright rim regions (except BRC 27) represents quantitative age gradients in the BRCs studied. The distribution of NIR-excess stars in the studied HII regions indicates that they are aligned from the ionizing source to the BRC direction. The age indicators, viz., infrared excess ($\Delta(H - K)$) and A_V as

well as the age itself of the YSOs manifest an age gradient toward the ionizing source. This global distribution indicates that a series of triggered star formation took place in the past from near the central O star(s) towards the peripheries of the HII region.

In **chapter 6**, the evolution of protoplanetary disks in TTSs and CMFs of the YSOs are studied. To study the disk evolution of TTSs in BRC regions, we used ages of the H α emission stars and their EWs in the above studied BRC regions. We found that in general WTTSs are somewhat older than CTTSs. Also the fraction of CTTSs among the TTSs associated with the BRCs is found to decrease with age. These facts are in accordance with the recent conclusion by Bertout et al. (2007) that CTTSs evolve into WTTSs. The variation of EW of H α emission stars, seems to support the idea that in general the $EW(H\alpha)$ in TTSs associated with the BRCs decreases with age.

To study the MF of the YSOs associated with the different morphological type BRCs, we estimated the masses of all the YSOs associated with studied BRCs. The CMF of the aggregates associated with the BRCs of the morphological type ‘A’ seems to follow that found in young open clusters, whereas ‘B/C’ type BRCs show significantly steeper MF.

Based on the age distribution of Class II and Class III sources in the cluster and BRC regions associated with W5 E HII region we found that, in general, the age distributions of the Class II (CTT) and Class III (WTT) sources are the same. This result is apparently in contradiction with the conclusion made above that CTTSs evolve to WTTSs. This difference may be due to fact that the classification of CTTS and WTTS in the BRCs and cluster associated with W5 E region is based on the *Spitzer* MIR observations, whereas in the different BRC regions the classification was based on the EWs of H α emission stars. H α surveys may fail to detect Class III sources which have smaller EWs whereas, those sources can be identified using the MIR observations. Similarly, we also used the masses of the YSOs in the cluster, BRC13, BRC 14 and BRC NW to compare the CMF of the YSOs in the cluster region and BRCs. We found that in the mass range $0.2 \leq M/M_{\odot} \leq 0.8$, the cluster region and BRC NW have more low mass YSOs in comparison to BRCs 13 and 14.

In **chapter 7** we discussed the star formation in BRCs and tiny globules associated with W5 E HII region. Based on the TCDs of the BRC 13, BRC 14 and BRC NW, we found higher total-to-selective extinctions in BRC NW (R_{BRCNW}) and in BRC 13 (R_{BRC13}), whereas the value of R_{BRC14} is found to be smaller than the normal value. This indicates that the evolution of dust grains in the W5 E region has not taken place in a homogeneous way. On the basis of the global distribution of YSOs in the region and the radial distribution of the amount of NIR excess $\Delta(H - K)$ and A_V in the region as well as the age distribution of YSOs, it seems that a series of RDI processes proceeded in the past from near the central O star towards the present locations of the BRCs. A comparison of the average age of the new sample of YSOs (which includes H α emission, NIR excess and MIR excess stars) further confirm the S^4F hypothesis in the BRC 13, BRC 14 and BRC NE. We also notices tiny globules (ETLSs) in the region and stars on the tips of many ETLSs. To study the nature of ETLS's stars, we constructed $V/V - I_c$ CMD for the stars obtained through deep VI observations of these regions. The positions of these stars on the CMD indicate that they are PMS stars having ages $\lesssim 1$ Myr. The physical parameters obtained by SED fittings also indicate their PMS nature. This suggests that they were formed from the elongated elephant trunk-like structures (ETLSs).

Hence, we also suspect that such ETLSs are caused by hydrodynamical instability of the I/S-front of the expanding HII region. Similar structures often show up in recent numerical simulations of the evolution of HII regions. We further hypothesize that this mechanism makes a third mode of triggered star formation associated with HII regions, in addition to the two known mechanisms, i.e., collect-and-collapse of the shell accumulated around an expanding HII region and RDI of BRCs originated from pre-existing cloud clumps.

8.2 Strategies for the Future Work

Sugitani et al. (1989) found that luminosity to cloud mass ratio is higher for the protostars in bright-rimmed globules than those in dark globules. This indicate that the RDI may affect the luminosity and accretion rates of the protostars. Also,

photo-evaporation of the disks of the young stellar objects through the intense ionising radiation may occur in the HII region. This effect will be dominating in the region closer to the massive star and will reduce as increasing distance from the ionising source. Eventually, we can see a significant enhancement in disk fraction as the distance from ionising source will increase.

Hence, there may be two competing effects of RDI on the star formation, either strong implosion may enhance the density of the material near core and hence accretion rates of protostars, leading to the formation of high to intermediate mass stars or the photo-evaporation of the parental core may result the low mass star formation.

Radio and MIR imaging survey of some BRCs by Morgan et al. (2004) show that some of the embedded clusters associated with the BRCs contain early-type ‘B’ stars, implying that at least some BRCs are intimately involved in intermediate- to high-mass star formation. Whereas, Valdetaro et al. (2005) argued that most BRCs host YSOs of low-luminosity, likely in an evolutionary phase later than the protostellar Class 0 sources, and that a significant contribution to the observed IRAS luminosity comes from warm dust heated by the radiation from the bright rim.

Although there are many observational studies on star formation in BRCs, still it is not well defined whether RDI favours low-mass star formation or high mass star formation in BRCs.

Also, it will be worthwhile to investigate following facts further:

1. How are the YSOs spatially distributed in the BRCs regions and their vicinity ? Is small scale sequential star formation is working in all BRCs ?
2. Whether RDI favours the formation of low-mass stars or high-mass stars and affect of RDI on accretion rate of YSOs inside different BRCs ?
3. Why there are distinct morphological types of BRCs even in the same environment and how the mass spectrum of BRCs is different for distinct morphological types ?

4. Why some BRCs showing cometary morphologies are still not showing any signatures of recent or ongoing star formation while type ‘A’ BRCs are showing the signatures of triggered star formation ?
5. How the disk fraction is varying with distance from the ionizing star and what is the disk survival time for the stars in different BRCs ?

8.2.1 Sample selection and observational Strategy

Recently, Morgan et al. (2009) and Urquhart et al. (2009) found that all the BRCs are not involved with triggered star formation. They refined the BRC and divided BRCs into three categories. In order to answer the above mentioned questions, we have selected a sample of nearby (within 2 kpc distance from the sun) BRCs for further study which are showing signatures of triggered star formation. The aim of the future study will be to have a detailed census of stars in their youth, using infrared to X-ray wavelengths. The SED shall be obtained to classify the YSOs.

8.2.1.1 Deep Near-IR imaging

Since mostly young stars are embedded inside BRCs and may be obscured through the optical window of electromagnetic spectrum. Deep near infrared imaging obtained through facilities like CFHT, NTT will enable to detect very low mass stars in highly extinguished ($A_V > 25$ mag) regions. For typical embedded cluster of 1-3 Myr ages, half of their members may be surrounded by circumstellar disks (Hernández et al. 2008). Circumstellar disks can be detected directly with infrared broad-band photometry as a excess emission above the expected normal stellar atmospheric emission.

8.2.1.2 Mid-IR imaging from Spitzer-IRAC

The excess emission in infrared wavelengths due to circumstellar disks and envelopes are most robustly measured at wavelengths longer than $2 \mu\text{m}$. The mid- and far-infrared data from *Spitzer* Space telescope (3.6 to $160 \mu\text{m}$) has provided

the capability to detect and measure infrared excess and circumstellar disk emission with the unprecedented sensitivity and resolution. We plan to use IRAC (3.6 - 8.0 μm) and MIPS (24 μm) data for our target BRCs.

8.2.1.3 X-ray data from Chandra

Although infrared observations are sufficiently sensitive to detect the disk bearing stars, there may be a population of stars that doesn't possess disks and any other accretion signatures. Young stars emit X-rays at levels 10^2 - 10^4 times that of normal stars, particularly during the first 10 Myr of their lives (Preibisch & Feigelson 2005). X-ray emission is detectable across almost the entire mass spectrum, whether or not the stars have disks (e.g. Telleschi et al. 2007). Hence, we plan to have X-ray observations of BRCs and associated clusters in order to detect diskless stars to complete the sample of pre-main sequence sources and remove the observational biases.

8.2.1.4 Slitless $\text{H}\alpha$ spectroscopy

$\text{H}\alpha$ emission in young stars is either produced by mass accretion or by chromospheric activity. Slitless grism spectroscopy enables to directly detect the $\text{H}\alpha$ emission from the YSOs. We plan to have slitless $\text{H}\alpha$ spectroscopy for those target BRCs for which it is not previously done.

8.2.1.5 Optical photometry

The association of YSOs selected based on the above methods can be confirmed by constructing optical $V/(V-I)$ CMDs. Deep optical VI photometric observations will be made to determine the nature of the associated cluster and massive star(s) responsible for the triggering of star formation activity. To identify and classify the evolutionary stages of the individual YSOs SED fitting tool of Robitaille et al. (2007) will be used. This will also give an estimation of many parameters like disk mass, age, disk accretion rate etc. of the YSOs.

Appendix A

CHAPTER 5

Table A.1: B , V and I_c photometric data for the stars along with their positions, EWs and corresponding 2MASS data.

S. N.	RA (2000)	DEC (2000)	$B \pm eB$ (mag)	$V \pm eV$ (mag)	$I_c \pm eI_c$ (mag)	$H\alpha$ EW (Å)	2MASS Name	$J \pm eJ$ (mag)	$H \pm eH$ (mag)	$K \pm eK$ (mag)	Q flag	C flag	ID (OSP 2000)
BRC 2													
1	00 03 57.1	+68 33 46.4	20.087 ± 0.009	18.049 ± 0.003	15.136 ± 0.004	16.3	00035705+6833465	13.067 ± 0.026	11.906 ± 0.031	11.220 ± 0.021	AAA	000	5
2	00 03 57.3	+68 33 23.0		22.450 ± 0.044	17.832 ± 0.004	274.4	00035728+6833229	14.863 ± 0.036	13.768 ± 0.035	13.174 ± 0.033	AAA	000	6
3	00 03 59.1	+68 32 47.4		21.134 ± 0.014	17.133 ± 0.005	28.1	00035905+6832472	14.681 ± 0.035	13.804 ± 0.042	13.315 ± 0.037	AAA	000	8
4	00 04 01.6	+68 34 14.2		17.975 ± 0.037	15.649 ± 0.014	2.7	00040165+6834137	13.737 ± 0.040	12.834 ± 0.037	12.447 ± 0.029	AAA	ccc	9
5	00 04 01.8	+68 34 00.1		22.786 ± 0.074	18.087 ± 0.007	21.7	00040176+6833599	15.423 ± 0.048	13.756 ± 0.035	12.639 ± 0.033	AAA	000	10
6	00 04 01.8	+68 34 34.3	18.906 ± 0.009	16.950 ± 0.005	13.991 ± 0.004	20.9	00040183+6834344	11.359 ± 0.049	10.059 ± 0.051	9.099 ± 0.039	EEE	000	12
7	00 04 02.6	+68 34 26.0		19.489 ± 0.036	16.795 ± 0.011	19.4	00040261+6834263	14.644 ± 0.045	13.355 ± 0.040	12.617 ± 0.033	AAA	ccc	14
8	00 04 07.6	+68 33 24.8	22.113 ± 0.046	19.673 ± 0.006	16.363 ± 0.002	18.2	00040758+6833250	14.158 ± 0.026	12.990 ± 0.032	12.539 ± 0.028	AAA	000	21
9	00 04 11.7	+68 33 25.2		20.455 ± 0.008	16.470 ± 0.003	18.2	00041165+6833253	14.104 ± 0.034	12.978 ± 0.030	12.461 ± 0.021	AAA	000	22
10	00 04 15.2	+68 33 01.8	18.424 ± 0.01	16.617 ± 0.004	14.148 ± 0.002	18.2	00041520+6833019	12.126 ± 0.032	11.019 ± 0.032	10.324 ± 0.023	AAA	000	25
11	00 03 58.4	+68 34 06.6		20.695 ± 0.040	17.521 ± 0.012	6.8	00035828+6834062	14.661 ± 0.034	13.175 ± 0.029	12.276 ± 0.023	AAA	000	7
12	00 04 04.6	+68 34 52.0	21.649 ± 0.033	19.356 ± 0.004	16.025 ± 0.004	23.2	00040454+6834519	13.599 ± 0.029	12.364 ± 0.029	11.625 ± 0.019	AAA	000	16
13	00 04 05.6	+68 33 44.3		17.352 ± 0.013	14.926 ± 0.003	804.5	00040563+6833442	12.867 ± 0.035	11.660 ± 0.032	10.787 ± 0.023	AAA	000	19
14	00 03 38.0	+68 34 55.6		21.268 ± 0.017	17.758 ± 0.006		00033798+6834554	15.120 ± 0.047	14.215 ± 0.048	13.660 ± 0.045	AAA	000	
15	00 03 54.5	+68 33 43.2		23.591 ± 0.127	18.730 ± 0.007		00035445+6833444	14.951 ± 0.047	13.762 ± 0.050	13.027 ± 0.044	AAA	000	
16	00 04 14.0	+68 32 21.5	21.74 ± 0.029	19.904 ± 0.005	17.020 ± 0.003	238.6	00041398+6832215	14.026 ± 0.031	12.709 ± 0.051	11.810 ± 0.033	AAA	000	23
17	00 04 14.7	+68 32 48.8		21.905 ± 0.025	18.924 ± 0.007		00041473+6832490	13.585 ± 0.026	12.480 ± 0.032	12.052 ± 0.021	AAA	000	24
BRC 11NE													
18	02 51 37.4	+60 06 26.6	20.088 ± 0.007	18.481 ± 0.002	16.268 ± 0.002	27.4	02513737+6006267	14.550 ± 0.042	13.527 ± 0.043	12.940 ± 0.033	AAA	000	1
19	02 51 54.5	+60 08 26.6	20.497 ± 0.010	18.837 ± 0.004	16.530 ± 0.003	50.9	02515451+6008266	14.582 ± 0.056	13.567 ± 0.043	12.825 ± 0.038	AAA	c0c	4
20	02 51 58.7	+60 08 05.8	21.109 ± 0.018	19.503 ± 0.004	16.996 ± 0.003	6.8	02515869+6008060	14.918 ± 0.029	14.016 ± 0.043	13.466 ± 0.040	AAA	000	5
21	02 52 11.1	+60 07 15.2	21.649 ± 0.029	19.860 ± 0.005	17.332 ± 0.002	25.5	02521113+6007154	15.634 ± 0.053	14.509 ± 0.058	13.988 ± 0.050	AAA	000	7
22	02 52 15.1	+60 05 18.5	21.220 ± 0.023	19.797 ± 0.008	17.153 ± 0.005	17.9	02521503+6005188	15.113 ± 0.047	14.089 ± 0.042	13.640 ± 0.044	AAA	000	8
23	02 51 54.2	+60 07 43.5	20.456 ± 0.012	18.598 ± 0.006	15.919 ± 0.003		02515419+6007437	14.116 ± 0.034	13.144 ± 0.037	12.791 ± 0.033	AAA	000	3
24	02 51 59.7	+60 06 39.3	20.803 ± 0.012	19.202 ± 0.004	16.893 ± 0.002	49.4	02515975+6006394	15.306 ± 0.048	14.236 ± 0.042	13.515 ± 0.038	AAA	000	6
25	02 51 52.1	+60 07 10.0	19.964 ± 0.009	18.334 ± 0.003	15.988 ± 0.002		02515212+6007102	14.131 ± 0.032	12.975 ± 0.033	12.136 ± 0.026	AAA	000	
26	02 52 01.3	+60 06 15.3		21.882 ± 0.028	18.491 ± 0.004		02520131+6006154	15.629 ± 0.053	14.406 ± 0.056	13.627 ± 0.042	AAA	000	
27	02 51 59.9	+60 05 32.0		21.713 ± 0.021	18.51 ± 0.006		02515993+6005323	16.155 ± 0.091	14.914 ± 0.081	14.142 ± 0.068	AAA	000	

Table A.1 cont.

BRC 11												
28	02 51 32.8	+60 03 54.3		19.871 ± 0.013	16.965 ± 0.012	7.2	02513283+6003542	13.005 ± 0.026	11.523 ± 0.032	10.447 ± 0.022	AAA 000	1
29	02 51 25.6	+60 06 04.8	19.816 ± 0.006	18.318 ± 0.002	15.967 ± 0.001		02512557+6006048	14.609 ± 0.038	13.142 ± 0.033	12.095 ± 0.019	AAA 000	
BRC 11E												
30	02 52 13.6	+60 03 26.2		20.991 ± 0.014	18.151 ± 0.015	136.4	02521362+6003262	15.592 ± 0.074	14.685 ± 0.064	14.157 ± 0.072	AAA ccc	1
31	02 52 14.2	+60 03 11.7	20.687 ± 0.016	19.129 ± 0.005	16.647 ± 0.008		02521422+6003114	14.311 ± 0.036	13.278 ± 0.038	12.532 ± 0.032	AAA 000	
BRC 13												
32	03 00 51.1	+60 39 36.3	20.129 ± 0.014	18.477 ± 0.022		99.2	03005107+6039360	13.508 ± 0.044	12.421 ± 0.043	11.804 ± 0.038	AAA ccc	6
33	03 00 51.6	+60 39 48.9		21.683 ± 0.031	17.783 ± 0.003	20.5	03005161+6039489	15.270 ± 0.055	14.176 ± 0.044	13.478 ± 0.068	AAA c00	7
34	03 00 52.7	+60 39 31.6	21.216 ± 0.018	19.667 ± 0.006	17.147 ± 0.003	602.3	03005265+6039317	15.043 ± 0.050	14.025 ± 0.050	13.291 ± 0.042	AAA 000	10
35	03 00 53.6	+60 40 24.9	21.955 ± 0.042	19.702 ± 0.013	16.893 ± 0.009		03005350+6040252	14.376 ± 0.042	13.157 ± 0.045	12.751 ± 0.038	AAA ccc	11
36	03 00 55.4	+60 39 42.7		20.841 ± 0.015	17.869 ± 0.004	180.5	03005542+6039427	15.789 ± 0.075	14.496 ± 0.059	13.935 ± 0.056	AAA 000	12
37	03 00 56.0	+60 40 26.3		20.713 ± 0.022	17.244 ± 0.008	8.0	03005601+6040265	14.695 ± 0.053	13.591 ± 0.057	12.945 ± 0.054	AAA cc0	13
38	03 00 44.8	+60 40 09.1	21.874 ± 0.038	19.923 ± 0.009	17.283 ± 0.015	16.7	03004476+6040092	14.683 ± 0.039	13.756 ± 0.039	13.008 ± 0.036	AAA 000	2
39	03 00 45.3	+60 40 39.5	20.536 ± 0.01	18.722 ± 0.005	16.399 ± 0.004	14.8	03004529+6040395	14.517 ± 0.038	13.672 ± 0.038	13.327 ± 0.040	AAA 000	3
BRC 14												
40	03 01 24.0	+60 30 42.2		21.397 ± 0.029	17.971 ± 0.005	125.4	03012400+6030423	15.940 ± 0.010	14.870 ± 0.010	14.410 ± 0.010		29
41	03 01 24.7	+60 30 09.6		21.998 ± 0.045	18.197 ± 0.006			15.680 ± 0.010	14.360 ± 0.010	13.780 ± 0.010		30
42	03 01 25.6	+60 29 39.0		19.644 ± 0.006	16.857 ± 0.003	9.5	03012556+6029392	14.730 ± 0.010	13.610 ± 0.010	13.080 ± 0.010		31
43	03 01 26.4	+60 30 53.9	20.374 ± 0.012	18.351 ± 0.003	15.816 ± 0.004	10.6	03012638+6030539	14.050 ± 0.010	13.030 ± 0.010	12.570 ± 0.010		32
44	03 01 27.2	+60 30 56.9		20.927 ± 0.018	18.063 ± 0.006	58.5	03012722+6030569	16.150 ± 0.020	15.090 ± 0.020	14.520 ± 0.020		33
45	03 01 27.4	+60 30 39.7	22.791 ± 0.092	20.661 ± 0.016	17.794 ± 0.006	21.3		15.510 ± 0.010	14.370 ± 0.010	13.820 ± 0.010		34
46	03 01 29.3	+60 31 13.6	20.097 ± 0.009	18.277 ± 0.003	15.866 ± 0.002	49.4	03012930+6031136	14.720 ± 0.010	13.420 ± 0.010	12.420 ± 0.010		35
47	03 01 34.0	+60 27 45.6	22.614 ± 0.076	20.349 ± 0.011	17.343 ± 0.003	11.4		15.200 ± 0.010	14.190 ± 0.010	13.700 ± 0.010		39
48	03 01 34.4	+60 30 08.5		20.462 ± 0.012	17.100 ± 0.003	19.4		14.750 ± 0.010	13.410 ± 0.010	12.680 ± 0.010		40
49	03 01 36.4	+60 29 06.1		21.481 ± 0.034	17.928 ± 0.005	54.7	03013640+6029061	15.660 ± 0.010	14.180 ± 0.010	13.120 ± 0.010		41
50	03 01 37.0	+60 31 00.2		20.347 ± 0.012	17.175 ± 0.017	17.1	03013695+603100	14.920 ± 0.010	13.880 ± 0.010	13.360 ± 0.010		42
51	03 01 37.1	+60 29 41.2		20.355 ± 0.010	17.228 ± 0.004	6.5		15.770 ± 0.010	15.160 ± 0.020	14.870 ± 0.020		43

Table A.1 cont.

52	03 01 43.3	+60 28 51.5		22.110 ± 0.051	18.337 ± 0.012	13.3		15.530 ± 0.010	14.030 ± 0.010	13.240 ± 0.010		46
53	03 01 50.0	+60 28 50.5		21.694 ± 0.032	18.183 ± 0.006			15.650 ± 0.010	14.310 ± 0.010	13.800 ± 0.010		47
54	03 01 04.2	+60 31 25.3		20.579 ± 0.016	17.760 ± 0.004	44.8	03010418+6031252	15.640 ± 0.010	14.460 ± 0.010	13.800 ± 0.010		1
55	03 01 06.2	+60 30 17.6	22.387 ± 0.062	20.709 ± 0.017	17.481 ± 0.008	79.8	03010623+6030176	15.670 ± 0.010	14.610 ± 0.010	14.070 ± 0.010		3
56	03 01 06.6	+60 30 36.0		22.287 ± 0.067	18.596 ± 0.006			16.420 ± 0.020	15.420 ± 0.020	14.900 ± 0.020		4
57	03 01 07.7	+60 29 21.8	20.223 ± 0.011	18.335 ± 0.002	15.968 ± 0.003	31.5	03010774+6029218	14.300 ± 0.010	13.150 ± 0.010	12.340 ± 0.010		5
58	03 01 11.5	+60 30 46.3		20.875 ± 0.024	17.987 ± 0.018	86.6	03011150+6030464	16.100 ± 0.020	15.070 ± 0.020	14.490 ± 0.010		6
59	03 01 13.4	+60 29 31.9		21.807 ± 0.040	18.383 ± 0.006	13.7		15.550 ± 0.010	14.350 ± 0.010	13.690 ± 0.010		8
60	03 01 16.1	+60 29 47.1		21.138 ± 0.023	17.779 ± 0.004	25.8	03011610+6029470	15.820 ± 0.010	14.770 ± 0.010	14.280 ± 0.010		10
61	03 01 17.0	+60 29 23.2	22.261 ± 0.058	19.904 ± 0.008	17.179 ± 0.003	16.0	03011705+6029232	15.350 ± 0.010	14.360 ± 0.010	13.970 ± 0.010		12
62	03 01 20.3	+60 30 02.3		20.338 ± 0.012	17.666 ± 0.003	38.4	03012024+6030024	15.580 ± 0.010	14.310 ± 0.010	13.330 ± 0.010		18
63	03 01 20.6	+60 29 31.7	22.594 ± 0.079	20.767 ± 0.019	17.990 ± 0.004	9.1		15.750 ± 0.010	14.690 ± 0.010	14.150 ± 0.010		20
64	03 01 21.2	+60 29 44.3		20.297 ± 0.017	17.608 ± 0.005			15.790 ± 0.010	14.670 ± 0.010	14.040 ± 0.010		23
65	03 01 21.2	+60 30 10.5		20.969 ± 0.018	17.774 ± 0.004	24.3		15.880 ± 0.010	14.750 ± 0.010	13.970 ± 0.010		24
66	03 01 32.0	+60 29 36.3		21.907 ± 0.046	19.193 ± 0.015			17.600 ± 0.020	16.550 ± 0.030	15.720 ± 0.030		
67	03 01 21.9	+60 29 29.5		20.588 ± 0.013	17.660 ± 0.004		03012186+6029296	15.630 ± 0.070	14.700 ± 0.070	14.150 ± 0.070	AAA	000
68	03 01 51.4	+60 27 22.7		22.305 ± 0.059	18.613 ± 0.008		03015137+6027224	15.590 ± 0.073	14.560 ± 0.070	13.900 ± 0.050	AAA	000
69	03 01 19.4	+60 29 38.9		21.924 ± 0.042	19.621 ± 0.016			17.730 ± 0.020	16.71 ± 0.010	15.930 ± 0.010		
70	03 00 47.1	+60 28 53.6		20.298 ± 0.011	17.664 ± 0.019		03004713+6028535	15.030 ± 0.050	14.05 ± 0.060	13.386 ± 0.053	AAA	ccc
71	03 01 20.3	+60 29 49.3	15.932 ± 0.008	14.746 ± 0.015	13.256 ± 0.026		03012029+6029493	11.910 ± 0.028	10.97 ± 0.030	10.171 ± 0.023	AAA	000
72	03 01 23.5	+60 31 50.6		20.853 ± 0.021	18.096 ± 0.005		03012352+6031507	16.070 ± 0.100	15.02 ± 0.090	14.330 ± 0.072	AAA	000
73	03 01 14.1	+60 29 37.4		21.553 ± 0.034	19.196 ± 0.017			17.370 ± 0.010	16.39 ± 0.010	15.590 ± 0.010		
74	03 01 01.1	+60 30 45.2		21.045 ± 0.024	19.013 ± 0.020			16.770 ± 0.010	15.64 ± 0.010	14.840 ± 0.010		
75	03 00 58.0	+60 30 13.4		19.776 ± 0.012	17.100 ± 0.021		03005792+6030133	14.930 ± 0.046	13.89 ± 0.050	13.158 ± 0.039	AAA	000
76	03 01 00.9	+60 33 26.7		20.708 ± 0.021	17.603 ± 0.005		03010092+6033265	15.680 ± 0.076	14.85 ± 0.090	14.324 ± 0.098	AAA	000
77	03 01 02.9	+60 31 22.4		21.023 ± 0.025	18.045 ± 0.005		03010291+6031223	15.880 ± 0.093	15.02 ± 0.104	14.438 ± 0.097	AAA	000
78	03 00 57.9	+60 31 21.7		20.848 ± 0.021	17.721 ± 0.004		03005798+6031217	15.970 ± 0.090	15.10 ± 0.092	14.550 ± 0.099	AAA	000
79	03 00 51.8	+60 32 10.8		20.733 ± 0.019	17.931 ± 0.004		03005180+6032106	15.830 ± 0.097	14.89 ± 0.101	14.270 ± 0.089	AAA	ccc
80	03 01 05.2	+60 31 55.4	17.823 ± 0.002	16.269 ± 0.001	14.261 ± 0.005		03010520+6031552	12.780 ± 0.020	11.88 ± 0.030	11.312 ± 0.022	AAA	000
BRC 27												
81	07 03 52.8	-11 23 13.2	18.954 ± 0.018	17.465 ± 0.015	15.313 ± 0.028	4.6	07035271-1123132	13.801 ± 0.047	13.026 ± 0.050	12.848 ± 0.039	AAA	000 2
82	07 03 53.8	-11 24 28.4		20.018 ± 0.009	16.761 ± 0.002	27.7	07035372-1124285	15.008 ± 0.043	14.211 ± 0.051	13.960 ± 0.057	AAA	000 4

Table A.1 cont.

83	07 03 57.1	-11 24 32.8	20.764±0.069	19.139 ± 0.005	16.476 ± 0.004	6.1	07035712-1124327	14.789 ± 0.033	13.968 ± 0.021	13.756 ± 0.053	AAA	000	7
84	07 04 02.9	-11 23 37.3	20.678±0.085	19.011 ± 0.014	16.327 ± 0.015	8.4	07040290-1123375	13.489 ± 0.043	12.400 ± 0.049	11.875 ± 0.033	AAA	000	8
85	07 04 03.1	-11 23 50.6		20.176 ± 0.011	17.398 ± 0.003	72.6	07040308-1123504	15.583 ± 0.060	14.303 ± 0.043	13.567 ± 0.040	AAA	000	10
86	07 04 04.3	-11 23 55.7	20.895±0.074	19.616 ± 0.011	16.722 ± 0.004	168.3	07040426-1123556	14.949 ± 0.044	13.995 ± 0.042	13.559 ± 0.047	AAA	000	12
87	07 04 04.8	-11 23 39.8	20.026±0.036	18.318 ± 0.003	15.970 ± 0.003	26.6	07040470-1123397	14.089 ± 0.040	13.060 ± 0.043	12.527 ± 0.037	AAA	000	14
88	07 04 05.3	-11 23 13.2	20.508±0.049	19.095 ± 0.004	16.546 ± 0.003	38.8	07040519-1123132	14.393 ± 0.071	13.226 ± 0.073	12.472 ± 0.040	AAA	000	15
89	07 04 06.0	-11 23 58.9	19.815±0.030	18.224 ± 0.006	15.925 ± 0.004	22.0	07040593-1123587	14.360 ± 0.033	13.444 ± 0.026	12.951 ± 0.031	AAA	000	16
90	07 04 06.0	-11 23 15.7		20.053 ± 0.008	17.314 ± 0.003	4.2	07040603-1123156	15.030 ± 0.062	13.933 ± 0.044	13.264 ± 0.035	AAA	000	17
91	07 04 06.5	-11 23 36.2		20.585 ± 0.013	16.839 ± 0.003	318.1	07040644-1123360	14.652 ± 0.049	13.788 ± 0.050	13.381 ± 0.072	AAA	ccc	18
92	07 04 06.5	-11 23 16.4	19.70±0.026	18.083 ± 0.003	15.744 ± 0.002	33.8	07040656-1123163	13.851 ± 0.062	12.932 ± 0.043	12.543 ± 0.031	AAA	c00	19
93	07 03 52.6	-11 26 16.8	18.311 ± 0.010	16.865 ± 0.002	15.109 ± 0.002	19.8	07035249-1126168	13.657 ± 0.027	12.855 ± 0.030	12.588± 0.029	AAA	000	1
94	07 03 55.0	-11 25 14.5	20.349 ± 0.045	18.769 ± 0.004	16.153 ± 0.009	4.6	07035499-1125145	14.593 ± 0.030	13.817 ± 0.040	13.600± 0.047	AAA	000	5
95	07 03 56.4	-11 25 41.5		20.435 ± 0.019	17.396 ± 0.008	11.0	07035638-1125413	15.671 ± 0.073	14.931 ± 0.070	14.439± 0.088	AAA	000	6
96	07 04 04.1	-11 26 35.5		20.515 ± 0.091	17.267 ± 0.021	36.1	07040408-1126354	15.349 ± 0.048	14.595 ± 0.070	14.146± 0.062	AAA	000	11
97	07 04 08.2	-11 23 54.6	17.168 ± 0.006	15.949 ± 0.003	14.346 ± 0.002	39.1	07040803-1123547	13.094 ± 0.033	12.430 ± 0.037	12.216± 0.030	AAA	000	22
98	07 04 08.2	-11 23 09.6	21.783± 0.144	20.338 ± 0.008	17.413 ± 0.003	926.8	07040816-1123097	15.411 ± 0.111	14.568 ± 0.055	14.205± 0.075	EAA	ccc	23
99	07 04 09.4	-11 24 38.1		21.053 ± 0.013	17.261 ± 0.003	137.2	07040925-1124381	15.003 ± 0.039	14.222 ± 0.054	13.729± 0.053	AAA	ccc	24
100	07 04 09.8	-11 23 16.4	16.234± 0.004	15.106 ± 0.002	13.525 ± 0.003	53.2	07040995-1123164	11.698 ± 0.024	10.663 ± 0.021	9.849 ± 0.021	AAA	ccc	25
101	07 04 12.0	-11 24 23.0		20.330 ± 0.014	16.850 ± 0.004	69.5	07041195-1124227	14.658 ± 0.047	13.866 ± 0.054	13.473± 0.047	AAA	ccc	27
102	07 04 13.0	-11 24 03.2	19.017± 0.016	17.570 ± 0.002	15.695 ± 0.003	293.7	07041292-1124031	15.317 ± 0.060	14.369 ± 0.047	13.931± 0.047	AAA	000	28
103	07 04 13.4	-11 24 55.8	16.822± 0.005	15.519 ± 0.003	13.742 ± 0.004	17.5	07041352-1124557	12.135 ± 0.028	11.269 ± 0.024	10.795± 0.023	AAA	000	29
104	07 04 14.2	-11 23 17.2	18.986± 0.016	17.596 ± 0.002	15.548 ± 0.002	33.1	07041424-1123169	13.833 ± 0.028	12.949 ± 0.022	12.358± 0.026	AAA	000	31
105	07 04 14.2	-11 23 37.3		20.843 ± 0.025	17.507 ± 0.004		07041427-1123371	15.435 ± 0.064	14.551 ± 0.060	14.034 ± 0.059	AAA	000	32
106	07 04 08.4	-11 20 05.3	13.529± 0.028	12.533 ± 0.026	11.936 ± 0.024		07040831-1120052	13.600 ± 0.028	12.564 ± 0.026	11.919 ± 0.024	AAA	000	
107	07 04 03.1	-11 23 27.6	12.919± 0.038	11.533 ± 0.037	10.710 ± 0.026		07040314-1123275	13.033 ± 0.038	11.573 ± 0.037	10.694 ± 0.026	AAA	000	
108	07 03 54.7	-11 20 11.0	15.869± 0.074	14.946± 0.076	14.385 ± 0.074		07035465-1120110	15.933 ± 0.074	14.976 ± 0.076	14.368 ± 0.074	AAA	000	
109	07 03 52.3	-11 21 01.1	15.618 ± 0.065	14.546 ± 0.068	13.794 ± 0.050		07035228-1121009	15.705 ± 0.065	14.586 ± 0.068	13.777 ± 0.050	AAA	000	
110	07 04 12.2	-11 20 20.8	15.618 ± 0.065	14.546 ± 0.068	13.794 ± 0.050		07041215-1120205	15.848 ± 0.072	14.463 ± 0.049	13.640 ± 0.040	AAA	000	
111	07 04 05.8	-11 20 03.8	15.743 ± 0.072	14.426 ± 0.049	13.656 ± 0.040		07040576-1120038	14.827 ± 0.048	13.459 ± 0.037	12.631 ± 0.030	AAA	000	
112	07 04 16.8	-11 24 32.4	14.723± 0.048	13.421 ± 0.037	12.647 ± 0.030		07041680-1124324	14.123 ± 0.026	13.213 ± 0.028	12.595 ± 0.024	AAA	000	
113	07 04 15.1	-11 26 22.6	14.062± 0.026	13.182 ± 0.028	12.612 ± 0.024		07041508-1126224	14.151 ± 0.033	13.094 ± 0.032	12.441 ± 0.027	AAA	000	
114	07 04 19.9	-11 22 22.4	14.078± 0.033	13.063 ± 0.032	12.458 ± 0.027		07041999-1122224	14.352 ± 0.029	13.340 ± 0.024	12.666 ± 0.029	AAA	000	
115	07 04 15.1	-11 23 39.8	16.111± 0.086	15.008 ± 0.076	14.249 ± 0.075		07041500-1123398	16.200 ± 0.086	15.049 ± 0.076	14.232 ± 0.075	AAA	c00	

Table A.1 cont.

BRC 38													
116	21 40 26.2	+58 14 24.7	22.249 ± 0.032	20.232 ± 0.014	17.812 ± 0.012		21402612+5814243	15.182 ± 0.076	14.262 ± 0.051	14.004 ± 0.062	AAA	000	1
117	21 40 28.1	+58 15 14.4	0 ± 0	20.2 ± 0.011	17.296 ± 0.013	23.94	21402800+5815142	14.506 ± 0.038	13.411 ± 0.035	12.939 ± 0.035	AAA	000	3
118	21 40 31.7	+58 17 55.3	22.632 ± 0.047	20.275 ± 0.012	17.054 ± 0.008	3.04	21403159+5817551	14.028 ± 0.032	12.889 ± 0.031	12.393 ± 0.028	AAA	000	4
119	21 40 37.0	+58 14 38.0	18.448 ± 0.012	16.664 ± 0.004	14.441 ± 0.015	55.86	21403691+5814378	11.902 ± 0.024	10.886 ± 0.030	10.234 ± 0.018	AAA	000	6
120	21 40 37.0	+58 15 03.2	21.957 ± 0.027	20.142 ± 0.011	17.069 ± 0.01	25.84	21403704+5815029	14.269 ± 0.029	13.284 ± 0.041	12.821 ± 0.029	AAA	000	7
121	21 40 41.3	+58 15 11.5	19.971 ± 0.011	18.055 ± 0.005	15.403 ± 0.011	25.08	21404116+5815112	12.968 ± 0.031	11.614 ± 0.035	10.676 ± 0.019	AAA	000	9
122	21 40 41.5	+58 14 25.8	22.43 ± 0.046	20.582 ± 0.016	17.642 ± 0.015	14.06	21404156+5814255	13.650 ± 0.029	12.618 ± 0.032	12.166 ± 0.028	AAA	000	10
123	21 40 44.9	+58 15 03.6	0	21.232 ± 0.023	17.95 ± 0.015	113.24	21404485+5815033	14.617 ± 0.038	13.347 ± 0.040	12.658 ± 0.030	AAA	000	11
124	21 40 48.0	+58 15 37.8	22.524 ± 0.037	20.546 ± 0.015	16.845 ± 0.01	16.34	21404803+5815376	13.894 ± 0.026	12.954 ± 0.033	12.667 ± 0.028	AAA	000	12
125	21 40 49.0	+58 17 09.6	0	21.541 ± 0.033	17.932 ± 0.012	59.66	21404908+5817093	14.141 ± 0.031	12.859 ± 0.038	12.133 ± 0.018	AAA	000	15
126	21 40 27.4	+58 14 21.5	21.205 ± 0.02	19.702 ± 0.013	17.041 ± 0.017	57.00	21402732+5814212	14.303 ± 0.042	13.303 ± 0.040	12.878 ± 0.039	AAA	000	2
127	21 40 36.5	+58 13 46.2	21.377 ± 0.016	19.213 ± 0.007	16.289 ± 0.024	4.18	21403655+5813458	13.514 ± 0.024	12.582 ± 0.032	12.245 ± 0.026	AAA	000	5
128	21 40 42.7	+58 19 37.6	0.	21.135 ± 0.021	17.456 ± 0.014		21404282+5819373	13.935 ± 0.032	12.545 ± 0.036	11.640 ± 0.024	AAA	000	
129	21 41 12.0	+58 20 33.7	0.	21.726 ± 0.037	18.972 ± 0.021		21411208+5820336	16.171 ± 0.098	15.152 ± 0.089	14.523 ± 0.090	AAA	000	
130	21 40 45.1	+58 19 50.2	0.	22.364 ± 0.093	18.643 ± 0.011		21404517+5819506	14.668 ± 0.026	13.121 ± 0.030	12.214 ± 0.019	AAA	000	
131	21 39 49.2	+58 14 37.0	23.277 ± 0.176	21.125 ± 0.029	17.511 ± 0.024		21394918+5814365	14.592 ± 0.026	13.607 ± 0.037	12.934 ± 0.023	AAA	000	
132	21 39 56.4	+58 13 47.7	20.981 ± 0.021	19.037 ± 0.014	16.289 ± 0.024		21395635+5813475	13.338 ± 0.028	12.273 ± 0.036	11.528 ± 0.023	AAA	000	
133	21 40 21.8	+58 14 45.6	23.012 ± 0.068	21.092 ± 0.023	17.536 ± 0.007		21402176+5814454	14.784 ± 0.036	13.775 ± 0.047	13.043 ± 0.028	AAA	000	

Table A.2: J , H and K magnitudes of the sources used in the analysis (cf. section 5.6.2).

RA (J2000)	DEC (J2000)	2MASS Name	$J \pm eJ$ (mag)	$H \pm eH$ (mag)	$K \pm eK$ (mag)	Q flag	C flag	A_V (mag)	$\Delta(H - K)$ (mag)	2MASS/Matsuyanagi et al. 2006(M06)
IC 1848W										
02 51 12.63	+60 24 00.1	02511262+6024000	13.719 \pm 0.050	12.912 \pm 0.051	12.361 \pm 0.035	AAA	000	0.00	0.05	2MASS
02 51 24.86	+60 21 40.2	02512485+6021402	14.305 \pm 0.038	13.545 \pm 0.043	13.017 \pm 0.031	AAA	000	0.00	0.05	2MASS
02 51 12.27	+60 25 51.3	02511226+6025512	15.955 \pm 0.086	15.189 \pm 0.103	14.630 \pm 0.099	AAA	c00	0.00	0.08	2MASS
02 51 08.31	+60 26 09.9	02510831+6026099	14.390 \pm 0.075	13.636 \pm 0.065	13.160 \pm 0.062	AAA	000	0.00	0.01	2MASS
02 50 56.55	+60 20 53.1	02505654+6020530	15.257 \pm 0.060	14.296 \pm 0.066	13.646 \pm 0.043	AAA	ccc	0.69	0.07	2MASS
02 50 48.48	+60 23 02.1	02504848+6023020	16.032 \pm 0.072	15.269 \pm 0.084	14.691 \pm 0.095	AAA	000	0.00	0.10	2MASS
02 51 01.47	+60 25 58.9	02510147+6025589	15.908 \pm 0.087	15.131 \pm 0.088	14.618 \pm 0.092	AAA	c00	0.00	0.03	2MASS
02 50 58.77	+60 25 53.7	02505876+6025536	15.497 \pm 0.074	14.396 \pm 0.065	13.687 \pm 0.067	AAA	ccc	2.00	0.05	2MASS
02 50 49.41	+60 24 38.4	02504941+6024384	14.625 \pm 0.055	13.629 \pm 0.042	12.767 \pm 0.026	AAA	000	0.00	0.26	2MASS
02 50 59.84	+60 26 10.6	02505983+6026105	15.258 \pm 0.080	14.224 \pm 0.074	13.555 \pm 0.051	AAA	000	1.47	0.05	2MASS
02 51 22.13	+60 26 51.2	02512213+6026512	14.030 \pm 0.042	12.804 \pm 0.030	12.007 \pm 0.021	AAA	000	2.89	0.07	2MASS
02 51 49.74	+60 21 28.5	02514973+6021285	14.941 \pm 0.032	14.059 \pm 0.040	13.455 \pm 0.034	AAA	ccc	0.06	0.06	2MASS
02 51 05.64	+60 18 40.7	02510563+6018406	15.072 \pm 0.025	13.820 \pm 0.041	12.967 \pm 0.030	AAA	000	2.77	0.11	2MASS
02 51 56.56	+60 22 35.8	02515655+6022358	15.669 \pm 0.070	14.766 \pm 0.079	14.208 \pm 0.066	AAA	ccc	0.69	0.01	2MASS
02 51 58.31	+60 23 59.2	02515831+6023591	15.386 \pm 0.045	14.358 \pm 0.045	13.569 \pm 0.047	AAA	000	0.43	0.17	2MASS
02 51 25.03	+60 17 32.9	02512502+6017329	14.732 \pm 0.035	13.639 \pm 0.036	12.967 \pm 0.027	AAA	000	2.20	0.02	2MASS
02 50 45.22	+60 27 21.6	02504522+6027216	15.651 \pm 0.088	14.433 \pm 0.072	13.507 \pm 0.062	AAA	cc0	1.75	0.20	2MASS
02 51 25.44	+60 17 23.2	02512544+6017231	15.603 \pm 0.070	14.313 \pm 0.038	13.281 \pm 0.034	AAA	000	1.81	0.27	2MASS
02 50 49.61	+60 27 55.3	02504960+6027553	15.067 \pm 0.048	13.981 \pm 0.068	13.295 \pm 0.057	AAA	ccc	1.99	0.03	2MASS
02 52 00.71	+60 25 49.8	02520071+6025497	15.998 \pm 0.081	15.223 \pm 0.098	14.700 \pm 0.098	AAA	c00	0.66	0.04	2MASS
02 52 05.71	+60 18 28.1	02520571+6018281	15.513 \pm 0.070	14.744 \pm 0.066	14.233 \pm 0.076	AAA	cc0	0.00	0.03	2MASS
02 52 19.20	+60 23 48.1	02521920+6023481	15.478 \pm 0.072	14.562 \pm 0.079	13.835 \pm 0.058	AAA	000	0.00	0.17	2MASS
02 51 44.25	+60 15 51.7	02514424+6015517	15.911 \pm 0.092	15.040 \pm 0.093	14.489 \pm 0.092	AAA	000	0.34	0.02	2MASS
02 51 38.48	+60 15 18.1	02513847+6015181	16.121 \pm 0.091	15.214 \pm 0.083	14.564 \pm 0.088	AAA	000	0.01	0.10	2MASS
02 51 26.18	+60 12 57.7	02512618+6012576	15.985 \pm 0.071	15.208 \pm 0.099	14.662 \pm 0.088	AAA	000	0.00	0.06	2MASS
02 52 07.87	+60 14 55.6	02520787+6014556	14.372 \pm 0.026	13.354 \pm 0.036	12.574 \pm 0.028	AAA	000	0.00	0.16	2MASS
02 51 54.52	+60 08 26.6	02515451+6008266	14.582 \pm 0.056	13.567 \pm 0.043	12.825 \pm 0.038	AAA	c0c	0.64	0.13	2MASS
02 51 52.12	+60 07 10.2	02515212+6007102	14.131 \pm 0.032	12.975 \pm 0.033	12.136 \pm 0.026	AAA	000	1.66	0.15	2MASS
02 51 25.58	+60 06 04.8	02512557+6006048	14.609 \pm 0.038	13.142 \pm 0.033	12.095 \pm 0.019	AAA	000	3.95	0.19	2MASS
02 51 59.76	+60 06 39.5	02515975+6006394	15.306 \pm 0.048	14.236 \pm 0.042	13.515 \pm 0.038	AAA	000	1.51	0.08	2MASS
02 52 01.32	+60 06 15.4	02520131+6006154	15.629 \pm 0.053	14.406 \pm 0.056	13.627 \pm 0.042	AAA	000	2.99	0.05	2MASS

Table A.2 cont.

02 51 59.93	+60 05 32.3	02515993+6005323	16.155 ± 0.091	14.914 ± 0.081	14.142 ± 0.068	AAA	000	3.28	0.04	2MASS
02 51 32.84	+60 03 54.2	02513283+6003542	13.005 ± 0.026	11.523 ± 0.032	10.447 ± 0.022	AAA	000	3.90	0.21	2MASS
02 52 14.22	+60 03 11.4	02521422+6003114	14.311 ± 0.036	13.278 ± 0.038	12.532 ± 0.032	AAA	000	0.84	0.12	2MASS
02 52 18.56	+60 02 27.4	02521856+6002274	16.212 ± 0.107	15.204 ± 0.095	14.272 ± 0.069	AAA	000	0.00	0.32	2MASS
02 51 43.36	+59 58 59.7	02514336+5958597	16.005 ± 0.089	15.139 ± 0.096	14.583 ± 0.092	AAA	000	0.24	0.02	2MASS
IC 1848E										
03 01 33.0	+60 29 04		17.25 ± 0.02	15.85 ± 0.02	14.82 ± 0.02			3.91	0.20	M06
03 01 33.9	+60 29 09		14.35 ± 0.01	13.25 ± 0.01	12.54 ± 0.01			2.33	0.06	M06
03 01 36.4	+60 29 06		15.66 ± <0.01	14.18 ± 0.01	13.12 ± <0.01			4.78	0.18	M06
03 01 33.2	+60 29 08		17.37 ± 0.07	15.64 ± 0.04	14.37 ± 0.03			6.55	0.25	M06
03 01 34.3	+60 29 08		16.16 ± 0.03	15.07 ± 0.03	14.13 ± 0.03			0.34	0.29	M06
03 01 34.0	+60 29 10		14.81 ± 0.01	13.69 ± 0.01	12.95 ± 0.01			2.36	0.08	M06
03 01 35.4	+60 29 11		16.76 ± 0.04	14.88 ± 0.03	13.49 ± 0.02			7.66	0.28	M06
03 01 30.1	+60 29 12		14.52 ± 0.01	13.41 ± 0.02	12.61 ± 0.02			1.74	0.14	M06
03 01 33.0	+60 29 12		16.97 ± 0.04	15.65 ± 0.04	14.59 ± 0.05			2.56	0.28	M06
03 01 33.4	+60 29 13		16.60 ± 0.02	15.49 ± 0.02	14.70 ± 0.04			1.82	0.13	M06
03 01 35.4	+60 29 15		17.62 ± 0.09	16.22 ± 0.04	15.05 ± 0.01			2.79	0.34	M06
03 01 32.7	+60 29 16		17.53 ± 0.08	15.17 ± 0.03	13.54 ± 0.02			12.37	0.23	M06
03 01 34.9	+60 29 16		15.10 ± 0.01	13.23 ± <0.01	11.68 ± <0.01			6.24	0.44	M06
03 01 29.8	+60 29 19		16.80 ± 0.04	15.61 ± 0.05	14.70 ± 0.05			1.97	0.20	M06
03 01 29.1	+60 29 18		17.63 ± 0.06	16.60 ± 0.07	15.72 ± 0.08			0.00	0.27	M06
03 01 30.9	+60 29 19		14.30 ± 0.01	12.89 ± 0.01	11.86 ± <0.01			4.05	0.20	M06
03 01 26.8	+60 29 17		18.80 ± 0.09	16.31 ± 0.01	14.56 ± 0.01			13.21	0.28	M06
03 01 33.2	+60 29 26		17.15 ± 0.03	15.63 ± 0.02	14.53 ± 0.01			5.01	0.20	M06
03 01 31.9	+60 29 26		15.27 ± <0.01	12.87 ± <0.01	11.26 ± <0.01			13.09	0.19	M06
03 01 29.6	+60 29 28		17.69 ± 0.03	16.39 ± 0.02	15.46 ± 0.04			3.33	0.16	M06
03 01 34.8	+60 29 31		16.85 ± 0.01	15.72 ± 0.01	14.87 ± 0.01			1.62	0.18	M06
03 01 29.6	+60 29 35		17.28 ± 0.03	15.97 ± 0.04	15.05 ± 0.05			3.55	0.14	M06
03 01 23.3	+60 29 34		18.35 ± 0.04	16.66 ± 0.02	15.28 ± 0.01			5.11	0.38	M06
03 01 32.0	+60 29 36		17.60 ± 0.02	16.55 ± 0.03	15.72 ± 0.03			0.67	0.21	M06
03 01 30.2	+60 29 37		16.95 ± 0.02	14.55 ± 0.01	12.88 ± 0.01			12.61	0.25	M06
03 01 34.7	+60 29 39		18.62 ± 0.04	17.62 ± 0.03	16.86 ± 0.04			0.54	0.17	M06
03 01 30.2	+60 29 39		16.86 ± 0.02	14.45 ± 0.01	12.86 ± <0.01			13.39	0.16	M06
03 01 30.9	+60 29 40		19.33 ± 0.10	17.76 ± 0.06	16.64 ± 0.07			5.54	0.19	M06
03 01 32.0	+60 29 41		18.70 ± 0.05	16.12 ± 0.02	14.33 ± 0.01			14.13	0.26	M06

Table A.2 cont.

03 01 29.8	+60 29 43		18.23 ± 0.03	16.59 ± 0.02	15.41 ± 0.01	6.03	0.21	M06
03 01 25.1	+60 29 44		17.31 ± 0.01	15.42 ± <0.01	14.14 ± <0.01	8.68	0.16	M06
03 01 32.6	+60 29 48		18.20 ± 0.03	15.87 ± 0.01	14.14 ± 0.01	11.16	0.35	M06
03 01 30.1	+60 29 55	03013009+6029554	14.64 ± <0.01	12.86 ± <0.01	11.69 ± <0.01	8.04	0.12	M06
03 01 23.8	+60 29 59	0301238+6029587	16.15 ± 0.01	14.95 ± <0.01	14.16 ± <0.01	3.07	0.08	M06
03 01 31.0	+60 30 07		19.27 ± 0.06	17.81 ± 0.04	16.79 ± 0.03	4.82	0.16	M06
03 01 29.2	+60 30 10		16.35 ± <0.01	14.64 ± <0.01	13.54 ± <0.01	7.64	0.09	M06
03 01 28.9	+60 30 18		19.09 ± 0.05	18.04 ± 0.04	17.27 ± 0.04	1.15	0.15	M06
03 01 31.0	+60 30 27		16.33 ± 0.01	15.10 ± 0.01	14.29 ± <0.01	3.32	0.08	M06
03 01 30.7	+60 30 60		17.96 ± 0.02	16.54 ± 0.01	15.60 ± 0.01	4.91	0.10	M06
03 01 29.3	+60 31 13		14.72 ± <0.01	13.42 ± <0.01	12.42 ± <0.01	2.77	0.23	M06
03 01 45.9	+60 26 59		19.64 ± 0.10	18.46 ± 0.08	17.54 ± 0.07	1.75	0.22	M06
03 01 40.7	+60 28 00		18.80 ± 0.05	17.51 ± 0.04	16.58 ± 0.04	3.19	0.17	M06
03 01 45.0	+60 28 47		16.76 ± 0.01	15.24 ± 0.01	14.13 ± 0.01	4.93	0.21	M06
03 01 39.2	+60 28 47		17.81 ± 0.02	16.44 ± 0.01	15.54 ± 0.01	4.54	0.09	M06
03 01 44.5	+60 28 48		17.97 ± 0.03	16.45 ± 0.02	15.34 ± 0.02	4.93	0.21	M06
03 01 36.7	+60 28 48		16.72 ± 0.02	15.57 ± 0.01	14.82 ± 0.01	2.70	0.07	M06
03 01 44.8	+60 28 50	03014484+6028496	15.96 ± 0.01	13.98 ± 0.01	12.55 ± <0.01	8.72	0.26	M06
03 01 48.5	+60 29 06		17.38 ± 0.02	15.83 ± 0.01	14.30 ± 0.01	1.97	0.61	M06
03 01 37.0	+60 29 07		16.51 ± 0.01	14.95 ± 0.01	13.86 ± <0.01	5.64	0.17	M06
03 01 38.4	+60 29 08		18.67 ± 0.05	17.28 ± 0.04	16.13 ± 0.03	2.81	0.33	M06
03 01 41.9	+60 29 14		17.73 ± 0.03	15.97 ± 0.01	14.77 ± 0.01	7.52	0.16	M06
03 01 37.0	+60 29 17		18.66 ± 0.05	16.12 ± 0.01	14.44 ± 0.01	14.46	0.18	M06
03 01 40.4	+60 29 30		18.04 ± 0.03	16.43 ± 0.02	15.15 ± 0.01	4.81	0.33	M06
03 01 39.7	+60 29 43		17.36 ± 0.02	15.47 ± 0.01	14.24 ± <0.01	9.08	0.11	M06
03 01 46.5	+60 30 07		19.27 ± 0.07	18.23 ± 0.06	17.40 ± 0.06	0.53	0.21	M06
03 01 27.2	+60 30 23		19.49 ± 0.09	17.69 ± 0.04	16.44 ± 0.03	7.68	0.18	M06
03 01 45.2	+60 31 09		18.51 ± 0.04	16.62 ± 0.02	15.28 ± 0.01	8.20	0.22	M06
03 01 42.4	+60 31 28		18.04 ± 0.04	16.88 ± 0.03	15.99 ± 0.02	1.71	0.20	M06
03 01 30.6	+60 29 12		13.85 ± 0.05	12.79 ± 0.05	11.89 ± 0.04	0.25	0.27	M06
03 01 30.9	+60 29 19		14.30 ± 0.01	12.89 ± 0.01	11.86 ± <0.01	2.22	0.13	M06
03 00 57.2	+60 29 59		17.53 ± 0.03	16.19 ± 0.02	15.28 ± 0.01	4.04	0.12	M06
03 01 06.6	+60 30 11		18.15 ± 0.03	17.29 ± 0.03	16.68 ± 0.03	0.00	0.10	M06
03 01 06.0	+60 30 28		17.25 ± 0.01	16.26 ± 0.01	15.61 ± 0.01	1.29	0.06	M06
03 01 01.7	+60 30 41		16.81 ± 0.01	15.79 ± 0.01	15.06 ± 0.01	1.06	0.13	M06
03 01 00.9	+60 30 45		16.77 ± 0.01	15.64 ± 0.01	14.84 ± 0.01	2.02	0.13	M06

Table A.2 cont.

03 01 21.2	+60 30 11	03012120+6030105	15.88 \pm <0.01	14.75 \pm <0.01	13.97 \pm <0.01			2.18	0.11	M06
03 01 20.2	+60 30 03		15.58 \pm <0.01	14.31 \pm <0.01	13.33 \pm <0.01			2.51	0.23	M06
03 01 14.1	+60 29 38		17.37 \pm 0.01	16.39 \pm 0.01	15.59 \pm 0.01			0.00	0.22	M06
03 01 16.5	+60 29 28		18.39 \pm 0.03	17.39 \pm 0.02	16.66 \pm 0.02			0.78	0.14	M06
03 01 20.6	+60 29 28	03012059+6029280	17.02 \pm 0.01	15.74 \pm 0.01	14.82 \pm 0.01			3.13	0.16	M06
03 01 19.1	+60 29 45		17.54 \pm 0.01	16.27 \pm 0.01	15.25 \pm 0.01			2.19	0.27	M06
03 01 19.4	+60 29 39		17.73 \pm 0.02	16.71 \pm 0.01	15.93 \pm 0.01			0.66	0.18	M06
03 01 19.1	+60 29 32		16.72 \pm 0.01	15.69 \pm 0.01	15.02 \pm 0.01			1.68	0.06	M06
03 01 24.16	+60 29 21.3		18.52 \pm 0.04	17.26 \pm 0.04	16.47 \pm 0.03			3.90	0.04	M06
03 01 24.90	+60 29 31.8		18.48 \pm 0.04	17.02 \pm 0.04	16.14 \pm 0.03			5.94	0.02	M06
03 01 25.83	+60 30 15.1		19.26 \pm 0.07	18.01 \pm 0.06	17.20 \pm 0.06			3.60	0.07	M06
03 01 26.13	+60 27 05.0		18.77 \pm 0.05	17.96 \pm 0.04	17.39 \pm 0.06			0.00	0.09	M06
03 01 26.28	+60 28 34.5		19.44 \pm 0.09	18.32 \pm 0.06	17.63 \pm 0.06			2.76	0.03	M06
03 01 28.85	+60 29 34.6		18.84 \pm 0.05	17.55 \pm 0.04	16.69 \pm 0.03			3.75	0.10	M06
03 01 29.32	+60 29 23.9		17.27 \pm 0.02	16.26 \pm 0.01	15.60 \pm 0.01			1.49	0.06	M06
03 01 29.38	+60 28 25.4		18.40 \pm 0.03	17.38 \pm 0.04	16.76 \pm 0.03			1.94	0.02	M06
03 01 33.26	+60 29 33.7		18.44 \pm 0.03	16.94 \pm 0.03	16.05 \pm 0.02			6.41	0.002	M06
03 01 33.92	+60 26 56.2		18.19 \pm 0.03	17.33 \pm 0.04	16.44 \pm 0.03			0.00	0.38	M06
03 01 34.05	+60 29 28.6		18.20 \pm 0.03	15.60 \pm 0.01	14.00 \pm <0.01			15.93	0.06	M06
03 01 34.92	+60 29 27.5		16.91 \pm 0.01	15.06 \pm 0.01	13.92 \pm <0.01			9.25	0.05	M06
03 01 35.24	+60 28 55.7		17.65 \pm 0.02	15.46 \pm 0.01	14.15 \pm <0.01			12.59	0.01	M06
03 01 36.16	+60 28 41.0		16.58 \pm 0.01	15.70 \pm 0.01	15.17 \pm 0.01			0.73	0.01	M06
03 01 36.79	+60 31 27.8		18.29 \pm 0.03	17.38 \pm 0.04	16.78 \pm 0.03			0.58	0.06	M06
03 01 07.18	+60 30 04.0		18.84 \pm 0.05	18.00 \pm 0.06	17.37 \pm 0.06			0.00	0.13	M06
03 01 23.53	+60 31 50.7	03012352+6031507	16.154 \pm 0.100	15.059 \pm 0.088	14.313 \pm 0.072	AAA	000	1.63	0.09	2MASS
03 01 05.21	+60 31 55.2	03010520+6031552	12.845 \pm 0.023	11.905 \pm 0.028	11.295 \pm 0.022	AAA	000	0.75	0.04	2MASS
03 01 02.91	+60 31 22.4	03010291+6031223	15.942 \pm 0.093	15.047 \pm 0.104	14.421 \pm 0.097	AAA	000	0.05	0.08	2MASS
03 01 27.22	+60 30 57.0	03012722+6030569	16.013 \pm 0.084	15.047 \pm 0.089	14.237 \pm 0.057	AAA	cc0	0.00	0.22	2MASS
03 01 02.92	+60 30 26.6	03010292+6030266	15.954 \pm 0.086	15.062 \pm 0.094	14.458 \pm 0.103	AAA	000	0.18	0.06	2MASS
03 01 20.30	+60 29 49.3	03012029+6029493	11.991 \pm 0.028	11.015 \pm 0.030	10.154 \pm 0.023	AAA	000	0.00	0.27	2MASS
03 01 18.60	+60 29 37.4	03011859+6029373	15.550 \pm 0.081	14.785 \pm 0.103	14.300 \pm 0.084	AAA	000	0.00	0.01	2MASS
03 01 29.30	+60 31 13.6	03012930+6031136	14.346 \pm 0.031	13.131 \pm 0.037	12.320 \pm 0.026	AAA	000	2.63	0.09	2MASS
03 01 17.70	+60 29 32.2	03011770+6029322	15.884 \pm 0.084	15.112 \pm 0.094	14.580 \pm 0.091	AAA	000	0.00	0.05	2MASS
03 00 57.98	+60 31 21.8	03005798+6031217	16.033 \pm 0.090	15.127 \pm 0.092	14.533 \pm 0.099	AAA	000	0.44	0.04	2MASS
03 01 21.86	+60 29 29.6	03012186+6029296	15.697 \pm 0.065	14.734 \pm 0.070	14.131 \pm 0.071	AAA	000	1.10	0.02	2MASS
03 01 07.75	+60 29 21.9	03010774+6029218	14.249 \pm 0.030	13.039 \pm 0.033	12.212 \pm 0.024	AAA	000	2.44	0.11	2MASS

Table A.2 cont.

03 00 57.92	+60 30 13.3	03005792+6030133	15.014 ± 0.046	13.931 ± 0.046	13.141 ± 0.039	AAA	000	1.12	0.14	2MASS
03 01 30.10	+60 29 55.5	03013009+6029554	14.529 ± 0.082	12.597 ± 0.062	11.379 ± 0.042	AAA	ccc	8.49	0.11	2MASS
03 01 21.60	+60 28 56.7	03012159+6028566	11.788 ± 0.026	10.805 ± 0.030	9.869 ± 0.020	AAA	000	0.00	0.34	2MASS
03 01 00.92	+60 33 26.6	03010092+6033265	15.735 ± 0.076	14.863 ± 0.089	14.306 ± 0.098	AAA	000	0.31	0.02	2MASS
03 01 34.35	+60 30 08.7	03013435+6030087	14.782 ± 0.038	13.427 ± 0.035	12.560 ± 0.025	AAA	000	3.97	0.07	2MASS
03 01 31.88	+60 29 25.7	03013187+6029256	15.400 ± 0.049	12.921 ± 0.027	11.379 ± 0.018	AAA	000	12.85	0.13	2MASS
03 00 51.81	+60 32 10.7	03005180+6032106	15.903 ± 0.097	14.923 ± 0.101	14.253 ± 0.089	AAA	ccc	0.77	0.08	2MASS
03 01 35.73	+60 28 49.0	03013572+6028490	14.867 ± 0.085	13.065 ± 0.060	12.017 ± 0.040	AAA	cc0	8.20	0.01	2MASS
03 00 47.13	+60 28 53.5	03004713+6028535	15.105 ± 0.045	14.083 ± 0.057	13.369 ± 0.053	AAA	ccc	0.96	0.10	2MASS
03 00 38.96	+60 32 29.6	03003896+6032295	15.893 ± 0.087	14.840 ± 0.081	14.185 ± 0.089	AAA	000	1.82	0.02	2MASS
03 01 44.84	+60 28 49.7	03014484+6028496	15.883 ± 0.105	13.863 ± 0.063	12.485 ± 0.045	AAA	000	8.33	0.22	2MASS
03 01 51.38	+60 27 22.5	03015137+6027224	15.672 ± 0.073	14.599 ± 0.071	13.885 ± 0.054	AAA	000	1.60	0.07	2MASS
03 00 24.11	+60 32 36.3	03002411+6032363	16.195 ± 0.107	15.027 ± 0.104	14.213 ± 0.078	BAA	000	2.01	0.12	2MASS
03 02 00.11	+60 27 31.0	03020010+6027309	15.401 ± 0.056	14.244 ± 0.053	13.447 ± 0.042	AAA	000	2.01	0.11	2MASS
03 00 11.65	+60 31 20.2	03001164+6031202	16.000 ± 0.103	14.982 ± 0.082	14.258 ± 0.073	AAA	000	0.82	0.11	2MASS
03 01 01.33	+60 39 28.5	03010133+6039285	15.860 ± 0.092	14.942 ± 0.095	14.272 ± 0.093	AAA	000	0.00	0.11	2MASS
03 00 52.66	+60 39 31.8	03005265+6039317	15.043 ± 0.050	14.025 ± 0.050	13.291 ± 0.042	AAA	000	0.74	0.12	2MASS
03 01 05.81	+60 39 54.1	03010581+6039541	15.868 ± 0.088	15.040 ± 0.092	14.526 ± 0.092	AAA	000	0.09	0.002	2MASS
03 00 18.43	+60 36 41.9	03001843+6036419	15.687 ± 0.078	14.891 ± 0.080	14.272 ± 0.082	AAA	c00	0.00	0.13	2MASS
03 00 51.61	+60 39 48.9	03005161+6039489	15.270 ± 0.055	14.176 ± 0.044	13.478 ± 0.068	AAA	c00	2.00	0.04	2MASS
03 00 44.77	+60 40 09.2	03004476+6040092	14.683 ± 0.039	13.756 ± 0.039	13.008 ± 0.036	AAA	000	0.00	0.18	2MASS
02 59 54.51	+60 33 44.7	02595451+6033447	14.373 ± 0.047	13.387 ± 0.053	12.672 ± 0.040	AAA	000	0.49	0.12	2MASS
02 59 59.49	+60 26 42.1	02595949+6026421	15.212 ± 0.077	14.342 ± 0.081	13.777 ± 0.085	AAA	c0c	0.22	0.03	2MASS
02 59 44.48	+60 32 52.8	02594448+6032528	14.142 ± 0.035	13.216 ± 0.045	12.547 ± 0.033	AAA	000	0.09	0.10	2MASS
02 59 43.18	+60 33 32.0	02594317+6033319	15.851 ± 0.098	15.025 ± 0.095	14.390 ± 0.101	AAA	000	0.00	0.12	2MASS
02 59 42.82	+60 28 21.2	02594281+6028212	15.593 ± 0.075	14.647 ± 0.074	13.951 ± 0.080	AAA	c00	0.13	0.12	2MASS
02 59 40.85	+60 34 53.6	02594084+6034535	15.073 ± 0.050	13.995 ± 0.046	13.285 ± 0.039	AAA	000	1.70	0.06	2MASS
02 59 37.27	+60 34 18.4	02593726+6034183	15.666 ± 0.068	14.628 ± 0.087	13.886 ± 0.054	AAA	000	0.93	0.12	2MASS
02 59 30.10	+60 32 19.2	02593010+6032191	15.768 ± 0.086	14.852 ± 0.083	14.015 ± 0.072	AAA	000	0.00	0.28	2MASS
03 01 18.94	+60 44 25.7	03011894+6044257	9.597 ± 0.023	8.102 ± 0.040	7.204 ± 0.021	AAA	000	5.50	0.02	2MASS
02 59 26.32	+60 29 31.4	02592632+6029314	14.080 ± 0.031	13.042 ± 0.039	12.401 ± 0.023	AAA	000	1.74	0.02	2MASS
02 59 25.24	+60 32 51.9	02592523+6032518	14.001 ± 0.034	13.129 ± 0.035	12.514 ± 0.029	AAA	000	0.00	0.08	2MASS
02 59 17.55	+60 29 20.9	02591754+6029209	15.362 ± 0.050	14.589 ± 0.066	14.085 ± 0.069	AAA	ccc	0.00	0.02	2MASS
02 59 17.74	+60 34 03.6	02591773+6034035	15.526 ± 0.078	14.599 ± 0.082	14.020 ± 0.059	AAA	ccc	0.83	0.01	2MASS
02 59 16.00	+60 32 24.7	02591600+6032247	15.545 ± 0.067	14.475 ± 0.063	13.743 ± 0.056	AAA	000	1.42	0.09	2MASS
02 59 11.38	+60 31 40.2	02591138+6031401	14.289 ± 0.034	13.397 ± 0.037	12.804 ± 0.029	AAA	0c0	0.27	0.05	2MASS

Table A.2 cont.

02 59 11.73	+60 34 21.5	02591173+6034215	15.693 ± 0.079	14.805 ± 0.078	14.024 ± 0.057	AAA	000	0.00	0.24	2MASS
02 59 10.22	+60 33 40.8	02591022+6033408	15.320 ± 0.058	14.113 ± 0.049	13.276 ± 0.051	AAA	000	2.32	0.12	2MASS
02 59 06.34	+60 30 26.8	02590634+6030268	15.095 ± 0.059	14.253 ± 0.062	13.725 ± 0.055	AAA	ccc	0.16	0.01	2MASS
02 58 59.45	+60 31 18.6	02585944+6031185	14.081 ± 0.029	13.163 ± 0.035	12.596 ± 0.028	AAA	000	0.81	0.01	2MASS
02 59 02.05	+60 36 24.4	02590205+6036243	14.703 ± 0.037	13.726 ± 0.040	13.068 ± 0.033	AAA	000	0.83	0.07	2MASS
02 59 01.04	+60 38 15.0	02590104+6038149	15.557 ± 0.071	14.449 ± 0.077	13.735 ± 0.049	AAA	s00	2.05	0.05	2MASS
02 58 50.05	+60 30 51.6	02585004+6030516	13.505 ± 0.025	12.474 ± 0.033	11.639 ± 0.023	AAA	000	0.00	0.21	2MASS
02 58 44.68	+60 33 14.4	02584468+6033144	15.721 ± 0.075	14.893 ± 0.085	14.344 ± 0.074	AAA	000	0.00	0.04	2MASS
02 58 51.21	+60 39 54.4	02585120+6039544	15.218 ± 0.064	14.184 ± 0.062	13.487 ± 0.047	AAA	000	1.24	0.07	2MASS
02 58 53.70	+60 40 40.2	02585369+6040402	15.655 ± 0.080	14.601 ± 0.079	13.768 ± 0.058	AAA	000	0.41	0.20	2MASS
CMa R1										
07 04 01.24	-11 22 42.6	07040123-1122426	16.274 ± 0.094	14.936 ± 0.083	13.822 ± 0.054	AAA	000	1.77	0.33	2MASS
07 04 03.14	-11 23 27.6	07040314-1123275	13.033 ± 0.038	11.573 ± 0.037	10.694 ± 0.026	AAA	000	5.20	0.02	2MASS
07 04 05.19	-11 23 13.3	07040519-1123132	14.486 ± 0.071	13.265 ± 0.073	12.455 ± 0.040	AAA	000	2.72	0.09	2MASS
07 04 06.04	-11 23 15.6	07040603-1123156	15.113 ± 0.062	13.967 ± 0.044	13.247 ± 0.035	AAA	000	2.49	0.04	2MASS
07 04 01.21	-11 25 31.1	07040121-1125311	14.258 ± 0.032	12.963 ± 0.024	11.979 ± 0.021	AAA	000	2.26	0.22	2MASS
07 03 56.39	-11 25 41.4	07035638-1125413	15.717 ± 0.073	14.959 ± 0.070	14.422 ± 0.088	AAA	000	0.00	0.06	2MASS
07 04 09.96	-11 23 16.4	07040995-1123164	11.786 ± 0.024	10.709 ± 0.021	9.832 ± 0.021	AAA	000	0.35	0.23	2MASS
07 03 52.29	-11 21 00.9	07035228-1121009	15.705 ± 0.065	14.586 ± 0.068	13.777 ± 0.050	AAA	000	1.43	0.14	2MASS
07 04 09.26	-11 24 38.1	07040925-1124381	15.052 ± 0.039	14.250 ± 0.054	13.712 ± 0.053	AAA	000	0.00	0.04	2MASS
07 03 54.65	-11 20 11.0	07035465-1120110	15.933 ± 0.074	14.976 ± 0.076	14.368 ± 0.074	AAA	000	0.98	0.03	2MASS
07 04 05.77	-11 20 03.9	07040576-1120038	14.827 ± 0.048	13.459 ± 0.037	12.631 ± 0.030	AAA	000	4.44	0.02	2MASS
07 04 14.25	-11 23 16.9	07041424-1123169	13.896 ± 0.028	12.982 ± 0.022	12.341 ± 0.026	AAA	000	0.17	0.08	2MASS
07 04 14.28	-11 23 37.1	07041427-1123371	15.493 ± 0.064	14.579 ± 0.060	14.017 ± 0.059	AAA	000	0.80	0.003	2MASS
07 04 08.31	-11 20 05.3	07040831-1120052	13.600 ± 0.028	12.564 ± 0.026	11.919 ± 0.024	AAA	000	1.69	0.02	2MASS
07 04 15.00	-11 23 39.8	07041500-1123398	16.200 ± 0.086	15.049 ± 0.076	14.232 ± 0.075	AAA	c00	1.77	0.13	2MASS
07 04 12.16	-11 20 20.5	07041215-1120205	15.848 ± 0.072	14.463 ± 0.049	13.640 ± 0.040	AAA	000	4.70	0.01	2MASS
07 04 16.80	-11 24 32.4	07041680-1124324	14.123 ± 0.026	13.213 ± 0.028	12.595 ± 0.024	AAA	000	0.30	0.06	2MASS
07 04 05.98	-11 19 03.9	07040597-1119038	12.438 ± 0.029	11.045 ± 0.024	10.105 ± 0.019	AAA	000	3.86	0.12	2MASS
07 04 17.74	-11 24 03.8	07041774-1124037	15.108 ± 0.039	14.152 ± 0.038	13.567 ± 0.043	AAA	000	1.15	0.004	2MASS
07 04 09.22	-11 19 18.1	07040921-1119181	15.970 ± 0.068	14.526 ± 0.043	13.353 ± 0.035	AAA	000	2.64	0.33	2MASS
07 04 15.09	-11 26 22.4	07041508-1126224	14.151 ± 0.033	13.094 ± 0.032	12.441 ± 0.027	AAA	000	1.89	0.02	2MASS
07 04 19.99	-11 22 22.4	07041999-1122224	14.352 ± 0.029	13.340 ± 0.024	12.666 ± 0.029	AAA	000	1.15	0.06	2MASS
07 04 09.95	-11 18 25.2	07040994-1118251	12.995 ± 0.039	11.691 ± 0.034	10.503 ± 0.024	AAA	000	0.74	0.42	2MASS
07 04 12.33	-11 17 59.0	07041232-1117590	14.346 ± 0.029	13.309 ± 0.032	12.620 ± 0.030	AAA	000	1.35	0.06	2MASS

Table A.2 cont.

07 03 53.03	-11 29 35.3	07035303-1129352	12.356 ± 0.024	11.540 ± 0.022	10.947 ± 0.021	AAA	000	0.00	0.09	2MASS
07 04 13.46	-11 30 07.3	07041345-1130073	16.032 ± 0.079	15.048 ± 0.094	14.321 ± 0.084	AAA	000	0.37	0.13	2MASS
07 03 38.74	-11 29 16.4	07033874-1129163	15.395 ± 0.042	14.526 ± 0.070	13.976 ± 0.068	AAA	000	0.32	0.02	2MASS
07 04 20.87	-11 29 36.2	07042086-1129361	13.801 ± 0.024	12.883 ± 0.022	12.286 ± 0.024	AAA	000	0.57	0.04	2MASS
07 04 17.06	-11 30 37.0	07041706-1130370	13.705 ± 0.022	12.802 ± 0.026	12.247 ± 0.024	AAA	000	0.72	0.002	2MASS
07 04 34.08	-11 20 24.5	07043407-1120244	14.026 ± 0.035	13.038 ± 0.024	12.422 ± 0.027	AAA	000	1.31	0.02	2MASS
07 03 50.34	-11 32 51.4	07035034-1132514	15.812 ± 0.061	14.916 ± 0.086	14.297 ± 0.069	AAA	000	0.11	0.07	2MASS
07 03 50.43	-11 33 42.5	07035043-1133425	15.238 ± 0.056	14.395 ± 0.065	13.806 ± 0.057	AAA	000	0.00	0.07	2MASS
07 03 45.54	-11 33 28.6	07034554-1133286	15.968 ± 0.079	14.597 ± 0.065	13.488 ± 0.038	AAA	ccc	2.23	0.30	2MASS
07 04 00.41	-11 33 59.6	07040041-1133596	12.099 ± 0.030	10.916 ± 0.028	10.190 ± 0.026	AAA	000	2.91	0.02	2MASS
07 04 01.60	-11 34 13.3	07040160-1134133	15.430 ± 0.052	12.449 ± 0.030	9.997 ± 0.026	AAA	000	11.94	0.77	2MASS
07 04 05.85	-11 34 10.0	07040584-1134099	16.174 ± 0.086	13.780 ± 0.043	12.195 ± 0.030	AAA	000	11.43	0.22	2MASS
07 03 58.50	-11 34 42.7	07035849-1134426	15.671 ± 0.070	14.552 ± 0.087	13.837 ± 0.055	AAA	000	2.18	0.05	2MASS
07 03 48.69	-11 34 30.3	07034869-1134303	15.658 ± 0.062	14.772 ± 0.066	14.182 ± 0.068	AAA	0cc	0.22	0.05	2MASS
07 03 56.67	-11 34 55.4	07035666-1134553	12.938 ± 0.024	11.872 ± 0.027	11.169 ± 0.023	AAA	000	1.60	0.06	2MASS
07 04 06.48	-11 34 47.1	07040648-1134470	15.009 ± 0.051	13.352 ± 0.065	12.365 ± 0.035	AAA	000	6.85	0.03	2MASS
07 04 36.12	-11 15 52.2	07043612-1115521	14.548 ± 0.037	13.237 ± 0.024	12.451 ± 0.027	AAA	000	4.06	0.01	2MASS
07 03 56.71	-11 35 09.6	07035670-1135095	14.336 ± 0.024	12.951 ± 0.027	12.114 ± 0.026	AAA	000	4.59	0.02	2MASS
07 03 55.43	-11 35 14.9	07035542-1135149	12.949 ± 0.026	11.970 ± 0.031	11.361 ± 0.027	AAA	000	1.25	0.02	2MASS
07 04 39.48	-11 32 35.6	07043947-1132356	15.023 ± 0.052	14.233 ± 0.045	13.688 ± 0.053	AAA	000	0.00	0.05	2MASS
07 04 33.95	-11 34 25.8	07043395-1134258	9.663 ± 0.024	8.295 ± 0.051	7.464 ± 0.023	AAA	000	4.42	0.03	2MASS
07 04 52.30	-11 14 30.6	07045230-1114306	12.720 ± 0.023	11.834 ± 0.024	11.285 ± 0.023	AAA	000	0.12	0.24	2MASS
07 04 01.80	-11 38 45.7	07040180-1138456	14.288 ± 0.030	13.263 ± 0.036	12.532 ± 0.025	AAA	000	0.55	0.01	2MASS
07 05 05.93	-11 17 45.8	07050593-1117458	14.220 ± 0.036	13.430 ± 0.042	12.896 ± 0.039	AAA	000	0.00	0.04	2MASS
07 05 16.42	-11 10 45.7	07051641-1110456	14.091 ± 0.076	12.691 ± 0.071	11.866 ± 0.054	AAA	ccc	4.87	0.002	2MASS
07 05 16.86	-11 10 43.8	07051685-1110437	12.153 ± 0.037	10.846 ± 0.036	9.806 ± 0.029	AAA	000	1.97	0.27	2MASS
07 05 18.78	-11 10 50.1	07051878-1110500	14.823 ± 0.038	13.940 ± 0.035	13.271 ± 0.032	AAA	000	0.00	0.13	2MASS
07 05 19.11	-11 10 26.9	07051911-1110269	15.305 ± 0.061	13.255 ± 0.039	12.022 ± 0.030	AAA	000	9.87	0.06	2MASS
07 02 27.04	-11 31 06.7	07022704-1131067	15.696 ± 0.065	14.842 ± 0.085	14.281 ± 0.080	AAA	000	0.00	0.09	2MASS
07 05 47.99	-11 17 43.7	07054798-1117436	15.877 ± 0.092	15.012 ± 0.075	14.466 ± 0.098	AAA	000	0.31	0.01	2MASS
07 05 45.29	-11 14 55.2	07054528-1114552	13.691 ± 0.030	12.857 ± 0.032	12.338 ± 0.026	AAA	000	0.13	0.004	2MASS
07 05 46.62	-11 15 45.2	07054662-1115452	15.890 ± 0.083	15.010 ± 0.071	14.459 ± 0.099	AAA	000	0.46	0.01	2MASS
07 06 00.79	-11 20 32.4	07060079-1120323	15.625 ± 0.091	14.740 ± 0.079	14.148 ± 0.084	AAA	000	0.19	0.05	2MASS
07 06 02.38	-11 26 54.2	07060238-1126541	12.302 ± 0.026	11.531 ± 0.028	10.974 ± 0.023	AAA	000	0.00	0.08	2MASS
07 06 12.23	-11 11 54.0	07061222-1111540	15.368 ± 0.050	14.538 ± 0.055	13.961 ± 0.055	AAA	000	0.00	0.06	2MASS

Table A.3: IRAC photometric magnitudes of the disk bearing candidates in BRCs 2, 27 and 13/14.

RA (J2000)	DEC (J2000)	[3.6]	e[3.6]	[4.5]	e[4.5]	[5.8]	e[4.5]	[8.0]	e[8.0]	IRAC type
BRC 2										
00 04 14.69	+68 32 49.8	11.899	0.033	10.97	0.03	10.095	0.052	8.985	0.028	0/I
00 03 57.27	+68 33 24.4	12.231	0.038	11.74	0.042	11.100	0.087	9.996	0.075	0/I
00 04 03.83	+68 32 49.6	13.316	0.064	12.57	0.062	11.749	0.123	10.57	0.117	0/I
00 03 59.71	+68 35 06.9	7.237	0.004	5.778	0.004	4.558	0.004	3.586	0.002	0/I
00 04 37.79	+68 35 07.4	10.274	0.015	9.342	0.014	8.595	0.027	7.630	0.026	0/I
00 03 57.78	+68 35 01.6	10.344	0.021	9.414	0.021	8.707	0.034	7.725	0.035	0/I
00 03 54.41	+68 35 17.8	11.283	0.024	9.973	0.019	8.938	0.031	8.048	0.021	0/I
00 04 03.90	+68 35 01.9	11.129	0.025	10.05	0.021	9.311	0.046	8.544	0.044	0/I
00 04 11.51	+68 36 01.0	11.481	0.027	10.38	0.023	9.602	0.042	8.748	0.032	0/I
00 03 56.17	+68 34 42.4	11.815	0.033	10.65	0.026	9.924	0.051	9.236	0.056	0/I
00 04 01.83	+68 34 35.2	7.925	0.006	7.318	0.006	6.815	0.012	5.996	0.008	II
00 04 15.21	+68 33 02.8	9.342	0.010	8.882	0.012	8.427	0.024	7.804	0.015	II
00 04 05.58	+68 33 45.0	9.231	0.010	8.604	0.011	8.129	0.021	7.318	0.016	II
00 03 33.24	+68 39 56.7	9.741	0.012	9.366	0.014	9.152	0.034	8.684	0.031	II
00 04 13.89	+68 32 22.5	10.119	0.014	9.532	0.015	9.101	0.033	8.461	0.020	II
00 03 57.05	+68 33 47.2	10.234	0.015	9.791	0.017	9.430	0.038	8.874	0.025	II
00 04 04.49	+68 34 53.2	10.477	0.017	9.997	0.020	9.546	0.043	8.830	0.036	II
00 04 12.17	+68 32 49.6	10.884	0.020	10.470	0.024	9.988	0.049	9.153	0.033	II
00 04 01.71	+68 34 01.1	10.897	0.020	10.460	0.024	10.002	0.050	9.258	0.034	II
00 03 58.26	+68 34 07.6	10.974	0.021	10.390	0.023	9.948	0.049	9.287	0.041	II
00 04 02.52	+68 34 27.5	10.970	0.025	10.480	0.028	10.033	0.056	9.097	0.035	II
00 04 35.38	+68 36 58.9	11.378	0.026	10.770	0.027	10.252	0.061	9.420	0.076	II
00 04 15.36	+68 34 06.4	11.532	0.028	11.050	0.031	10.626	0.069	9.861	0.060	II
00 04 11.63	+68 33 26.2	11.664	0.029	11.230	0.034	10.655	0.067	9.827	0.040	II
00 04 04.60	+68 33 49.8	11.089	0.031	10.330	0.028	9.702	0.049	8.777	0.049	II
00 03 55.64	+68 41 06.4	11.829	0.031	11.290	0.034	10.897	0.075	10.465	0.052	II
00 03 58.79	+68 34 49.7	11.640	0.033	11.090	0.037	10.521	0.105	9.940	0.097	II
00 03 54.42	+68 33 45.8	11.920	0.033	11.360	0.036	10.759	0.072	9.742	0.046	II
00 04 09.67	+68 32 33.1	11.988	0.034	11.910	0.046	11.782	0.113	11.287	0.084	II
00 04 07.31	+68 33 43.6	12.215	0.040	11.700	0.044	11.086	0.088	10.080	0.077	II
00 03 59.02	+68 32 48.4	12.370	0.041	11.910	0.046	11.353	0.103	10.612	0.150	II
00 03 53.69	+68 35 53.8	12.423	0.043	11.700	0.042	11.290	0.104	10.622	0.159	II
00 03 55.95	+68 33 35.1	12.629	0.046	12.270	0.054	11.846	0.124	10.906	0.093	II
00 03 54.86	+68 32 43.6	12.983	0.054	12.250	0.053	11.681	0.109	11.212	0.088	II
00 04 04.61	+68 34 44.1	12.85	0.057	12.280	0.073	11.672	0.121	11.089	0.165	II

Table A.3 cont.

BRC 27											
07 04 01.21	-11 22 43.2	8.412	0.007	7.614	0.007	6.874	0.012	5.166	0.005	0/I	
07 04 12.56	-11 26 34.3	12.843	0.051	12.210	0.053	11.561	0.104	10.424	0.076	0/I	
07 04 01.38	-11 23 35.5	9.419	0.011	9.076	0.013	8.627	0.035	7.839	0.051	II	
07 04 03.14	-11 23 28.3	9.653	0.014	9.282	0.015	8.830	0.046	7.903	0.088	II	
07 04 01.21	-11 25 31.9	10.587	0.018	10.201	0.021	9.964	0.049	9.368	0.032	II	
07 04 02.89	-11 23 37.9	10.931	0.023	10.537	0.026	10.073	0.070	9.065	0.109	II	
07 04 02.74	-11 23 25.9	11.135	0.026	10.657	0.027	10.038	0.078	9.050	0.124	II	
07 04 05.21	-11 23 13.9	11.371	0.026	10.914	0.029	10.384	0.062	9.415	0.051	II	
07 04 05.95	-11 23 59.5	11.620	0.029	11.097	0.031	10.621	0.066	9.691	0.050	II	
07 04 04.71	-11 23 40.3	11.631	0.030	11.238	0.034	10.971	0.101	10.239	0.184	II	
07 04 08.04	-11 23 55.3	11.908	0.033	11.773	0.043	11.680	0.109	11.225	0.091	II	
07 04 01.62	-11 21 33.0	11.968	0.034	11.623	0.040	11.174	0.092	10.545	0.113	II	
07 04 06.57	-11 23 16.7	12.08	0.039	11.802	0.045	11.231	0.111	10.179	0.132	II	
07 04 03.09	-11 23 51.1	12.021	0.041	11.720	0.044	10.559	0.094	9.671	0.210	II	
07 04 02.14	-11 25 12.7	12.504	0.043	12.071	0.049	11.864	0.117	11.145	0.077	II	
07 04 06.44	-11 23 36.7	12.635	0.047	12.405	0.058	12.049	0.131	11.631	0.160	II	
07 04 06.03	-11 23 16.3	12.668	0.048	12.096	0.05	11.508	0.109	10.499	0.109	II	
07 04 01.28	-11 22 34.2	12.969	0.055	12.65	0.066	12.247	0.149	11.421	0.167	II	
BRC 14											
03 01 21.66	+60 28 55.6	8.563	0.007	8.080	0.008	7.378	0.015	6.259	0.008	0/I	
03 02 21.76	+60 25 57.3	10.643	0.018	10.164	0.020	9.562	0.041	8.163	0.018	0/I	
03 00 27.55	+60 27 35.2	10.864	0.020	10.452	0.023	9.873	0.047	8.579	0.021	0/I	
03 01 34.55	+60 28 48.9	11.154	0.031	10.538	0.030	9.907	0.110	8.713	0.111	0/I	
03 00 52.78	+60 40 15.4	12.264	0.041	11.665	0.042	10.807	0.090	9.551	0.082	0/I	
03 00 56.49	+60 40 11.0	10.087	0.047	9.568	0.034	7.799	0.095	6.098	0.095	0/I	
03 00 56.85	+60 40 29.0	11.307	0.053	10.625	0.043	9.929	0.076	8.622	0.075	0/I	
03 01 32.14	+60 26 48.9	13.510	0.073	13.064	0.079	12.478	0.215	11.100	0.234	0/I	
03 00 55.39	+60 45 21.8	13.864	0.081	13.322	0.088	11.816	0.115	9.827	0.042	0/I	
03 01 48.00	+60 35 22.9	13.194	0.088	12.325	0.059	11.115	0.131	9.658	0.144	0/I	
03 00 53.09	+60 40 36.5	13.176	0.093	12.375	0.065	11.151	0.139	9.229	0.095	0/I	
03 01 32.47	+60 25 53.7	10.677	0.019	9.344	0.015	8.289	0.023	7.266	0.013	0/I	
03 01 48.54	+60 29 05.1	10.980	0.021	10.109	0.020	9.219	0.035	8.442	0.021	0/I	
03 01 43.43	+60 28 50.2	11.130	0.025	10.327	0.025	9.835	0.046	9.098	0.041	0/I	
03 01 32.10	+60 29 40.5	11.271	0.035	10.262	0.030	9.418	0.067	8.620	0.071	0/I	
03 01 36.08	+60 28 37.4	11.875	0.038	10.768	0.030	9.922	0.052	9.341	0.044	0/I	
03 01 52.90	+60 24 48.3	12.354	0.040	11.231	0.033	10.245	0.056	9.333	0.032	0/I	
03 01 39.41	+60 29 27.7	12.352	0.043	11.224	0.034	10.374	0.062	9.634	0.061	0/I	
03 01 20.86	+60 31 23.5	14.230	0.094	13.261	0.085	12.674	0.172	11.694	0.091	0/I	
03 01 20.31	+60 29 48.3	9.109	0.009	8.615	0.010	8.209	0.022	7.503	0.013	II	

Table A.3 cont.

03 01 30.15	+60 29 54.6	10.099	0.015	9.497	0.016	9.186	0.036	8.637	0.050	II
03 01 05.24	+60 31 54.4	10.126	0.015	9.756	0.017	9.410	0.038	8.514	0.021	II
03 01 41.20	+60 29 15.3	10.556	0.018	10.491	0.024	10.462	0.071	9.611	0.057	II
03 01 44.92	+60 28 48.9	10.611	0.019	9.993	0.020	9.451	0.040	8.867	0.032	II
03 00 51.08	+60 39 34.9	10.811	0.020	10.328	0.022	10.030	0.050	9.344	0.032	II
03 01 29.32	+60 31 12.8	10.956	0.021	10.433	0.023	9.969	0.049	9.279	0.036	II
03 01 07.75	+60 29 20.9	11.087	0.022	10.665	0.026	10.35	0.058	9.794	0.038	II
03 00 25.58	+60 28 08.7	11.302	0.024	10.984	0.030	10.709	0.069	9.691	0.035	II
03 01 34.37	+60 30 07.7	11.230	0.025	10.751	0.027	10.167	0.065	9.246	0.078	II
03 01 16.63	+60 30 53.5	11.402	0.026	11.128	0.032	10.885	0.075	10.343	0.048	II
03 02 22.56	+60 25 09.3	11.490	0.027	11.053	0.031	10.682	0.068	9.617	0.040	II
03 00 44.78	+60 40 08.3	11.624	0.028	11.084	0.031	10.611	0.066	9.880	0.039	II
03 01 04.37	+60 24 08.7	11.654	0.029	11.260	0.034	10.912	0.075	10.249	0.046	II
03 01 38.96	+60 25 31.0	11.677	0.029	11.647	0.040	11.448	0.105	10.814	0.129	II
03 01 25.80	+60 29 18.1	11.367	0.030	10.922	0.034	9.894	0.113	8.917	0.088	II
03 00 54.43	+60 39 38.1	11.734	0.031	11.521	0.039	11.066	0.099	10.057	0.109	II
03 01 30.22	+60 29 36.9	10.655	0.031	9.955	0.031	9.611	0.08	9.081	0.108	II
03 00 57.25	+60 32 42.2	11.845	0.032	11.451	0.037	11.139	0.084	10.640	0.056	II
03 00 56.28	+60 32 34.4	11.842	0.032	11.614	0.04	11.401	0.095	10.896	0.063	II
03 01 54.81	+60 24 21.4	11.925	0.033	11.493	0.038	11.002	0.079	10.354	0.050	II
03 01 26.40	+60 30 52.9	11.901	0.033	11.667	0.041	11.267	0.093	10.525	0.089	II
03 01 20.27	+60 30 01.4	11.961	0.034	11.361	0.036	10.940	0.078	10.238	0.052	II
03 01 03.09	+60 41 30.4	11.963	0.034	11.874	0.045	11.557	0.124	10.856	0.204	II
03 00 57.98	+60 30 12.2	12.158	0.036	11.729	0.042	11.389	0.094	10.736	0.061	II
03 01 01.27	+60 28 38.6	12.192	0.037	11.853	0.045	11.415	0.095	10.660	0.056	II
03 00 56.85	+60 29 57.8	12.246	0.038	11.962	0.047	11.655	0.108	11.194	0.094	II
03 00 24.06	+60 26 15.7	12.262	0.038	12.258	0.054	11.958	0.123	11.342	0.077	II
03 01 18.78	+60 29 55.6	12.275	0.039	11.778	0.044	11.301	0.092	10.693	0.065	II
03 00 46.48	+60 39 51.5	12.421	0.041	11.914	0.046	11.548	0.101	10.759	0.059	II
03 00 45.33	+60 40 38.3	12.427	0.041	12.064	0.049	11.665	0.107	10.825	0.061	II
03 00 47.14	+60 28 52.7	12.407	0.041	12.084	0.049	11.777	0.112	11.131	0.070	II
03 01 22.84	+60 39 39.2	12.425	0.041	12.086	0.049	11.831	0.116	10.850	0.061	II
03 01 22.45	+60 30 02.0	12.337	0.040	11.968	0.048	11.590	0.109	10.903	0.098	II
03 00 45.26	+60 31 16.7	12.485	0.042	12.123	0.050	11.725	0.110	11.073	0.068	II
03 00 48.19	+60 31 08.4	12.455	0.042	12.226	0.053	11.991	0.125	11.323	0.078	II
03 01 21.21	+60 30 09.2	12.544	0.044	12.021	0.049	11.780	0.116	11.147	0.087	II
03 01 35.05	+60 27 56.0	12.478	0.044	12.372	0.057	12.515	0.193	11.722	0.209	II
03 00 48.68	+60 39 33.6	12.589	0.044	12.408	0.058	12.075	0.132	11.672	0.096	II
03 01 59.87	+60 24 18.2	12.592	0.044	12.539	0.061	12.373	0.154	11.905	0.181	II
03 00 41.93	+60 39 48.6	12.628	0.046	12.184	0.053	11.708	0.109	10.835	0.061	II

Table A.3 cont.

03 01 04.22	+60 31 24.4	12.673	0.046	12.200	0.052	11.943	0.122	11.259	0.074	II
03 01 31.72	+60 34 02.1	12.686	0.046	12.361	0.056	11.930	0.121	11.246	0.073	II
03 00 48.23	+60 39 33.0	12.635	0.046	12.395	0.057	12.047	0.130	11.541	0.091	II
03 01 54.04	+60 32 48.1	12.720	0.047	12.369	0.057	11.994	0.127	11.324	0.099	II
03 01 47.49	+60 28 10.6	12.754	0.048	12.289	0.054	11.874	0.120	11.129	0.088	II
03 00 42.59	+60 24 36.5	12.776	0.048	12.418	0.058	12.159	0.134	11.338	0.075	II
03 00 22.65	+60 31 42.1	12.691	0.048	12.486	0.060	12.194	0.140	11.616	0.089	II
03 01 40.78	+60 43 37.5	12.775	0.048	12.691	0.065	12.465	0.161	11.859	0.136	II
03 00 54.35	+60 36 49.9	12.745	0.048	12.721	0.066	12.719	0.176	12.140	0.186	II
03 00 57.31	+60 30 35.3	12.822	0.049	12.470	0.059	12.204	0.137	11.516	0.084	II
03 00 42.25	+60 29 12.7	12.895	0.051	12.419	0.058	12.201	0.138	11.623	0.097	II
03 01 12.99	+60 28 50.9	12.913	0.051	12.493	0.060	12.128	0.132	11.424	0.081	II
03 00 24.85	+60 33 13.5	12.888	0.051	12.653	0.065	12.492	0.159	11.800	0.108	II
03 01 35.79	+60 22 23.6	12.856	0.050	12.303	0.055	11.761	0.112	11.092	0.079	II
03 01 17.64	+60 24 24.3	12.857	0.050	12.502	0.060	11.948	0.124	10.977	0.070	II
03 02 26.07	+60 33 02.8	12.837	0.050	12.819	0.070	12.613	0.179	11.726	0.192	II
03 01 31.04	+60 30 26.1	12.750	0.052	12.322	0.056	11.634	0.129	10.575	0.154	II
03 01 06.26	+60 30 16.8	12.962	0.052	12.536	0.061	12.177	0.135	11.566	0.084	II
03 01 49.97	+60 28 49.3	12.902	0.053	12.367	0.057	11.797	0.117	10.758	0.092	II
03 01 07.27	+60 25 25.7	13.011	0.054	12.520	0.061	11.887	0.119	11.122	0.076	II
03 01 08.16	+60 39 00.5	13.070	0.055	12.627	0.063	12.271	0.142	11.639	0.106	II
03 02 28.02	+60 32 21.2	13.074	0.055	13.035	0.077	12.920	0.200	12.362	0.193	II
03 00 46.58	+60 31 58.4	13.122	0.056	12.615	0.063	12.410	0.152	11.718	0.095	II
03 01 12.21	+60 38 40.2	13.118	0.057	12.458	0.059	12.034	0.127	11.468	0.090	II
03 00 52.69	+60 39 21.7	13.093	0.057	13.069	0.079	13.028	0.219	12.568	0.201	II
03 00 27.63	+60 28 46.3	13.159	0.058	12.968	0.074	12.938	0.196	12.236	0.125	II
03 00 53.24	+60 32 01.3	13.295	0.061	13.027	0.076	12.743	0.177	12.202	0.116	II
03 01 10.59	+60 25 55.8	13.253	0.060	12.701	0.066	12.203	0.138	11.753	0.094	II
03 00 36.20	+60 34 17.7	13.281	0.062	13.048	0.078	12.721	0.176	12.050	0.111	II
03 01 16.15	+60 29 46.3	13.327	0.063	13.002	0.076	12.769	0.182	12.173	0.124	II
03 01 10.75	+60 32 45.0	13.357	0.063	13.057	0.078	12.844	0.186	12.273	0.135	II
03 00 24.14	+60 32 35.1	13.337	0.064	12.869	0.071	12.302	0.145	11.383	0.080	II
03 02 01.70	+60 39 27.4	13.352	0.064	12.996	0.076	12.588	0.174	11.634	0.127	II
03 00 43.96	+60 34 50.2	13.415	0.065	12.964	0.074	12.828	0.184	12.178	0.124	II
03 01 22.23	+60 39 28.3	13.438	0.066	13.287	0.087	12.963	0.198	12.400	0.134	II
03 01 59.06	+60 22 57.4	13.494	0.067	13.342	0.089	13.208	0.230	12.579	0.243	II
03 00 44.00	+60 30 58.2	13.506	0.068	13.347	0.089	13.317	0.240	12.822	0.185	II
03 01 02.67	+60 31 00.9	13.533	0.069	13.506	0.096	13.396	0.247	12.776	0.184	II
03 00 30.81	+60 31 01.7	13.597	0.071	13.088	0.079	12.701	0.174	11.902	0.102	II
03 00 23.45	+60 31 50.6	13.527	0.071	13.111	0.081	13.042	0.213	12.438	0.138	II
03 01 40.12	+60 22 17.3	13.540	0.070	13.116	0.080	12.590	0.179	11.619	0.162	II

Table A.3 cont.

03 01 04.04	+60 28 23.2	13.588	0.070	13.243	0.084	12.989	0.199	12.446	0.154	II
03 00 46.60	+60 23 26.4	13.587	0.070	13.301	0.087	12.973	0.197	12.343	0.127	II
03 00 22.81	+60 28 26.6	13.678	0.074	13.482	0.095	13.309	0.242	12.805	0.166	II
03 01 17.14	+60 30 45.1	13.737	0.076	13.348	0.089	13.386	0.244	12.783	0.156	II
03 00 36.16	+60 24 12.2	13.757	0.076	13.658	0.103	13.438	0.247	12.947	0.180	II
03 00 50.07	+60 30 55.0	13.775	0.077	13.412	0.092	12.966	0.198	12.118	0.112	II
03 01 18.46	+60 29 47.5	13.365	0.079	12.91	0.085	12.421	0.162	11.869	0.136	II
03 00 46.71	+60 31 40.2	13.792	0.079	13.086	0.079	12.662	0.174	11.973	0.111	II
03 00 34.68	+60 27 43.9	13.831	0.079	13.481	0.094	13.326	0.235	12.827	0.156	II
03 00 45.01	+60 35 19.8	13.867	0.081	13.299	0.088	12.680	0.176	11.814	0.135	II
03 01 16.15	+60 31 30.7	13.888	0.080	13.321	0.087	12.959	0.196	12.319	0.122	II
03 00 27.18	+60 35 44.2	13.935	0.082	13.618	0.101	13.137	0.214	12.640	0.157	II
03 01 53.77	+60 29 21.4	13.892	0.082	13.729	0.107	13.303	0.241	12.219	0.194	II
03 01 05.84	+60 28 02.0	13.955	0.085	13.506	0.096	12.987	0.202	12.232	0.118	II
03 00 43.01	+60 31 08.3	14.013	0.086	13.612	0.100	13.058	0.207	12.098	0.114	II
03 01 31.55	+60 34 11.7	13.899	0.087	13.458	0.094	13.157	0.215	12.666	0.150	II
03 00 57.52	+60 29 18.2	14.044	0.087	13.477	0.094	12.851	0.186	11.931	0.108	II
03 01 45.15	+60 40 02.2	14.032	0.087	13.628	0.101	13.377	0.250	12.461	0.216	II
03 01 06.66	+60 30 35.3	14.045	0.087	13.632	0.101	13.337	0.234	12.618	0.159	II
03 01 25.74	+60 31 17.1	14.117	0.090	13.763	0.107	13.348	0.243	12.920	0.242	II
03 01 05.23	+60 29 20.6	14.169	0.092	13.589	0.099	13.196	0.225	12.689	0.160	II
03 00 42.87	+60 34 22.6	14.228	0.094	13.677	0.103	13.335	0.234	12.900	0.182	II
03 00 30.47	+60 31 16.5	14.244	0.096	13.830	0.111	13.297	0.230	12.456	0.136	II
03 00 39.02	+60 37 09.6	14.387	0.101	13.988	0.119	13.457	0.248	12.831	0.182	II

References

- Allen, L. E., et al. 2004, *ApJS*, 154, 363–60, 116, 120
- Allen, L. E., Hora, J. L., Megeath, S. T., Deutsch, L. K., Fazio, G. G., Chavarria, L., & dell, R. W. 2005, in *IAU Symposium*, Vol. 227, *Massive Star Birth: A Crossroads of Astrophysics*, ed. R. Cesaroni, M. Felli, E. Churchwell, & M. Walmsley, 352–120
- Allen, P. R., Luhman, K. L., Myers, P. C., Megeath, S. T., Allen, L. E., Hartmann, L., & Fazio, G. G. 2007, *ApJ*, 655, 1095–60
- Armitage, P. J., Clarke, C. J., & Palla, F. 2003, *MNRAS*, 342, 1139–132, 136, 147
- Axford, W. I. 1964, *ApJ*, 140, 112–165
- Becker, W., & Fenkart, R. 1971, *A&AS*, 4, 241–75, 162
- Becker, W., & Stock, J. 1954, *Z. Astrophys.*, 34, 1–55
- Bernasconi, P. A. 1996, *A&AS*, 120, 57–7
- Bertoldi, F. 1989, *ApJ*, 346, 735–19, 23, 124
- Bertoldi, F., & Draine, B. T. 1996, *ApJ*, 458, 222–16, 17
- Bertout, C., Siess, L., & Cabrit, S. 2007, *A&A*, 473, L21–26, 132, 135, 144, 145, 147, 171
- Bessell, M. S., & Brett, J. M. 1988, *PASP*, 100, 1134–58, 59, 90, 107

REFERENCES

- Bisbas, T. G., Wünsch, R., Whitworth, A. P., & Hubber, D. A. 2009, *A&A*, 497, 649–665
- Blitz, L. 1993, in *Protostars and Planets III*, ed. E. H. Levy & J. I. Lunine, 125–27
- 1991, *CCD astronomy. Construction and use of an astronomical CCD camera*, ed. Buil, C. 35
- Burki, G. 1975, *A&A*, 43, 37–55
- Carpenter, J. M., Heyer, M. H., & Snell, R. L. 2000, *ApJS*, 130, 381–404
- Chauhan, N., Pandey, A. K., Ogura, K., Ojha, D. K., Bhatt, B. C., Ghosh, S. K., & Rawat, P. S. 2009, *MNRAS*, 396, 964–966, 150
- Chini, R., & Wargau, W. F. 1990, *A&A*, 227, 213–215, 74, 81
- Cohen, J. G., Persson, S. E., Elias, J. H., & Frogel, J. A. 1981, *ApJ*, 249, 481–483, 59, 79
- Cohen, M., Megeath, S. T., Hammersley, P. L., Martín-Luis, F., & Stauffer, J. 2003, *AJ*, 125, 2645–2650
- Conti, P. S., & Leep, E. M. 1974, *ApJ*, 193, 113–115, 75
- Contreras, M. E., Sicilia-Aguilar, A., Muzerolle, J., Calvet, N., Berlind, P., & Hartmann, L. 2002, *AJ*, 124, 1585–1587, 106, 128
- 2003, *2MASS All Sky Catalog of point sources.*, ed. Cutri, R. M., Skrutskie, M. F., van Dyk, S., Beichman, C. A., Carpenter, J. M., Chester, T., Cambresy, L., Evans, T., Fowler, J., Gizis, J., Howard, E., Huchra, J., Jarrett, T., Kopan, E. L., Kirkpatrick, J. D., Light, R. M., Marsh, K. A., McCallon, H., Schneider, S., Stiening, R., Sykes, M., Weinberg, M., Wheaton, W. A., Wheelock, S., & Zacarias, N. 69, 102, 158
- Dale, J. E., Clark, P. C., & Bonnell, I. A. 2007, *MNRAS*, 377, 535–540, 165
- Deharveng, L., Zavagno, A., & Caplan, J. 2005, *A&A*, 433, 565–567, 164

- Deharveng, L., Zavagno, A., Cruz-Gonzalez, I., Salas, L., Caplan, J., & Carrasco, L. 1997, *A&A*, 317, 459–88, 104
- Deharveng, L., Zavagno, A., Salas, L., Porras, A., Caplan, J., & Cruz-González, I. 2003, *A&A*, 399, 1135–18, 114
- Duvert, G., Guilloteau, S., Ménard, F., Simon, M., & Dutrey, A. 2000, *A&A*, 355, 165–26
- Edwards, S., Hartigan, P., Ghandour, L., & Andrulis, C. 1994, *AJ*, 108, 1056–131
- Elmegreen, B. G. 1998, in *Astronomical Society of the Pacific Conference Series*, Vol. 148, *Origins*, ed. C. E. Woodward, J. M. Shull, & H. A. Thronson Jr., 150–13, 14, 114
- Elmegreen, B. G., & Lada, C. J. 1977, *ApJ*, 214, 725–18, 114, 164
- Fazio, G. G., et al. 2004, *ApJS*, 154, 10–46
- Feinstein, A., Vazquez, R. A., & Benvenuto, O. G. 1986, *A&A*, 159, 223–104
- Forte, J. C. 1978, *AJ*, 83, 1199–54
- Furlan, E., et al. 2006, *ApJS*, 165, 568–26, 132
- Garcia-Segura, G., & Franco, J. 1996, *ApJ*, 469, 171–20, 165
- Georgelin, Y. M., & Georgelin, Y. P. 1976, *A&A*, 49, 57–75
- Getman, K. V., Feigelson, E. D., Garmire, G., Broos, P., & Wang, J. 2007, *ApJ*, 654, 316–105, 120, 134
- Girardi, L., Bertelli, G., Bressan, A., Chiosi, C., Groenewegen, M. A. T., Marigo, P., Salasnich, B., & Weiss, A. 2002, *A&A*, 391, 195–73, 74, 75, 76, 77, 80, 81, 83, 84, 106, 111, 142, 161
- Giuliani, J. L., Jr. 1979, *ApJ*, 233, 280–165
- Goodman, A. A., Barranco, J. A., Wilner, D. J., & Heyer, M. H. 1998, *Astrophysical Letters Communications*, 37, 109–2

- Gras-Velázquez, À., & Ray, T. P. 2005, *A&A*, 443, 541 26, 132, 147
- Gritschneider, M., Burkert, A., Naab, T., & Walch, S. 2010, *ApJ*, 723, 971 165
- Gritschneider, M., Naab, T., Walch, S., Burkert, A., & Heitsch, F. 2009, *ApJL*, 694, L26 165
- Haisch, K. E., Jr., Lada, E. A., & Lada, C. J. 2001, *AJ*, 121, 2065 132
- Hamann, F., & Persson, S. E. 1992, *ApJS*, 82, 247 6
- Hartmann, L. 2001, *AJ*, 121, 1030 12, 132
- Hartmann, L. 2003, *ApJ*, 585, 398 135
- Hartmann, L., Hewett, R., & Calvet, N. 1994, *ApJ*, 426, 669 131
- He, L., Whittet, D. C. B., Kilkenny, D., & Spencer Jones, J. H. 1995, *ApJS*, 101, 335 54
- Herbst, W., & Assousa, G. E. 1977, *ApJ*, 217, 473 105
- Hernández, J., Hartmann, L., Calvet, N., Jeffries, R. D., Gutermuth, R., Muzerolle, J., & Stauffer, J. 2008, *ApJ*, 686, 1195 174
- Hill, J. K., & Hollenbach, D. J. 1978, *ApJ*, 225, 390 17
- Hillenbrand, L. A. 2005, *ArXiv Astrophysics e-prints* 62
- Hillenbrand, L. A., Bauermeister, A., & White, R. J. 2008, in *Astronomical Society of the Pacific Conference Series*, Vol. 384, 14th Cambridge Workshop on Cool Stars, Stellar Systems, and the Sun, ed. G. van Belle, 200 62, 78
- Hillenbrand, L. A., Strom, S. E., Vrba, F. J., & Keene, J. 1992, *ApJ*, 397, 613 59
- Hillwig, T. C., Gies, D. R., Bagnuolo, W. G., Jr., Huang, W., McSwain, M. V., & Wingert, D. W. 2006, *ApJ*, 639, 1069 75, 162
- Hogerheijde, M. 1998, Ph.D. thesis, Department of Astronomy, University of California, Campbell Hall, Berkeley, CA 94720, USA; `¡EMAIL¡michiel@strw.leidenuniv.nl¡/EMAIL¡` 5

- Horne, K. 1986, *PASP*, 98, 609 44
- Houck, J. R., et al. 2004, *ApJS*, 154, 18 46
- Ikeda, H., et al. 2008, *AJ*, 135, 2323 105, 133
- Johnson, H. L., & Morgan, W. W. 1953, *ApJ*, 117, 313 55, 74
- Johnstone, D., Matsuyama, I., McCarthy, I. G., & Font, A. S. 2004, in *Revista Mexicana de Astronomia y Astrofisica*, vol. 27, Vol. 22, *Revista Mexicana de Astronomia y Astrofisica Conference Series*, ed. G. Garcia-Segura, G. Tenorio-Tagle, J. Franco, & H. W. Yorke , 38 133
- Jones, B. F., & Herbig, G. H. 1979, *AJ*, 84, 1872 96
- Jose, J., et al. 2008, *MNRAS*, 384, 1675 85
- Kahn, F. D. 1958, *Reviews of Modern Physics*, 30, 1058 15
- Kaluzny, J., & Udalski, A. 1992, *Acta Astronomica*, 42, 29 52
- Karr, J. L., & Martin, P. G. 2003, *ApJ*, 595, 900 65, 104, 149, 150
- Kassis, M., Friel, E. D., & Phelps, R. L. 1996, *AJ*, 111, 820 51
- Kenyon, S. J., & Hartmann, L. 1995, *ApJS*, 101, 117 131, 132
- Kessel-Deynet, O., & Burkert, A. 2003, *MNRAS*, 338, 545 19, 152
- King, I. 1962, *AJ*, 67, 471 52, 72, 73
- King, I. R. 1966, *AJ*, 71, 64 52
- Koenig, X. P., Allen, L. E., Gutermuth, R. A., Hora, J. L., Brunt, C. M., & Muzerolle, J. 2008, *ApJ*, 688, 1142 xvi, 65, 66, 70, 78, 80, 104, 123, 124, 125, 129, 140, 145, 150, 153, 157, 158, 160, 161
- Kroupa, P. 2001, *MNRAS*, 322, 231 139, 145
- Kroupa, P. 2002, *Science*, 295, 82 27, 139, 145

- Lada, C. J. 1987, in IAU Symposium, Vol. 115, Star Forming Regions, ed. M. Peimbert & J. Jugaku, 1–8
- Lada, C. J. 2010, RSPTA, 368, 713–12
- Lada, C. J., & Wilking, B. A. 1984, ApJ, 287, 610–8
- Landolt, A. U. 1992, AJ, 104, 340–39, 43, 67, 100, 124, 127
- Larson, R. B. 2003, in Astronomical Society of the Pacific Conference Series, Vol. 287, Galactic Star Formation Across the Stellar Mass Spectrum, ed. J. M. De Buizer & N. S. van der Bliik, 65–13
- Lawson, W. A., Feigelson, E. D., & Huenemoerder, D. P. 1996, MNRAS, 280, 1071–26, 132, 147
- Lee, H., Chen, W. P., Zhang, Z., & Hu, J. 2005, ApJ, 624, 808–95
- Lefloch, B., & Lazareff, B. 1994, A&A, 289, 559–23, 96, 124
- Lefloch, B., & Lazareff, B. 1995, A&A, 301, 522–19
- Mac Low, M. 1999, in Lecture Notes in Physics, Berlin Springer Verlag, Vol. 523, IAU Colloq. 169: Variable and Non-spherical Stellar Winds in Luminous Hot Stars, ed. B. Wolf, O. Stahl, & A. W. Fullerton, 391–21
- Mac Low, M., & Klessen, R. S. 2004, Reviews of Modern Physics, 76, 125–2
- Mac Low, M., & Norman, M. L. 1993, ApJ, 407, 207–20
- Makovoz, D., & Marleau, F. R. 2005, PASP, 117, 1113–49
- Manoj, P., Bhatt, H. C., Maheswar, G., & Muneer, S. 2006, ApJ, 653, 657–133
- Martín, E. L. 1998, AJ, 115, 351–131
- Martins, F., & Plez, B. 2006, A&A, 457, 637–75
- Matsuyanagi, I., Itoh, Y., Sugitani, K., Oasa, Y., Mukai, T., & Tamura, M. 2006, PASJ, 58, L29–25, 26, 88, 91, 95, 102, 104, 115, 124, 126, 141

- Megeath, S. T., et al. 2004, *ApJS*, 154, 367–60, 104, 116, 117, 120
- Mellema, G., Arthur, S. J., Henney, W. J., Iliev, I. T., & Shapiro, P. R. 2006, *ApJ*, 647, 397–165
- Meyer, M. R., Calvet, N., & Hillenbrand, L. A. 1997, *AJ*, 114, 288–58, 59, 61, 90, 106, 107, 140, 160
- Miao, J., White, G. J., Nelson, R., Thompson, M., & Morgan, L. 2006, *MNRAS*, 369, 143–19, 23, 24
- Miao, J., White, G. J., Thompson, M. A., & Nelson, R. P. 2009, *ApJ*, 692, 382–23
- Miller, G. E., & Scalo, J. M. 1979, *ApJS*, 41, 513–11
- Milligan, S., Cranton, B. W., & Skrutskie, M. F. 1996, in *Society of Photo-Optical Instrumentation Engineers (SPIE) Conference Series*, Vol. 2863, *Society of Photo-Optical Instrumentation Engineers (SPIE) Conference Series*, ed. R. E. Fischer & W. J. Smith, 2–45
- Mizuta, A., Kane, J. O., Pound, M. W., Remington, B. A., Ryutov, D. D., & Takabe, H. 2006, *ApJ*, 647, 1151–21, 166
- Moffat, A. F. J. 1972, *A&AS*, 7, 355–162
- Moitinho, A., Alfaro, E. J., Yun, J. L., & Phelps, R. L. 1997, *AJ*, 113, 1359–51
- Morgan, L. K., Thompson, M. A., Urquhart, J. S., & White, G. J. 2008, *A&A*, 477, 557–129, 132, 136, 137, 138, 164
- Morgan, L. K., Thompson, M. A., Urquhart, J. S., White, G. J., & Miao, J. 2004, *A&A*, 426, 535–22, 173
- Morgan, L. K., Urquhart, J. S., & Thompson, M. A. 2009, *MNRAS*, 400, 1726–174
- Munari, U., & Carraro, G. 1996, *A&A*, 314, 108–91

- Muzerolle, J., Calvet, N., & Hartmann, L. 2001, *ApJ*, 550, 944 131
- Nakano, M., Sugitani, K., Niwa, T., Itoh, Y., & Watanabe, M. 2008, *PASJ*, 60, 739 71, 78, 79, 85, 125, 129, 149, 150
- Niwa, T., Tachihara, K., Itoh, Y., Oasa, Y., Sunada, K., Sugitani, K., & Mukai, T. 2009, *A&A*, 500, 1119 66, 149
- Ogura, K., Chauhan, N., Pandey, A. K., Bhatt, B. C., Ojha, D., & Itoh, Y. 2007, *PASJ*, 59, 199 150
- Ogura, K., & Sugitani, K. 1998, *Publications Astronomical Society of Australia*, 15, 91 23
- Ogura, K., Sugitani, K., & Pickles, A. 2002, *AJ*, 123, 2597 25, 26, 58, 87, 88, 89, 90, 104, 106, 115, 133, 135, 140, 141, 170
- Ojha, D. K., et al. 2004a, *ApJ*, 608, 797 58
- Ojha, D. K., et al. 2004b, *ApJ*, 616, 1042 59
- Palla, F., & Stahler, S. W. 1999, *ApJ*, 525, 772 85
- Pandey, A. K., Nilakshi, Ogura, K., Sagar, R., & Tarusawa, K. 2001, *A&A*, 374, 504 12
- Pandey, A. K., Ogura, K., & Sekiguchi, K. 2000, *PASJ*, 52, 847 54, 74, 81
- Pandey, A. K., Sharma, S., & Ogura, K. 2006, *MNRAS*, 373, 255 74, 75
- Pandey, A. K., Sharma, S., Ogura, K., Ojha, D. K., Chen, W. P., Bhatt, B. C., & Ghosh, S. K. 2008, *MNRAS*, 383, 1241 61, 62, 85, 103, 106
- Pandey, A. K., Upadhyay, K., Nakada, Y., & Ogura, K. 2003, *A&A*, 397, 191 54, 80, 82, 152
- Pandey, A. K., Upadhyay, K., Ogura, K., Sagar, R., Mohan, V., Mito, H., Bhatt, H. C., & Bhatt, B. C. 2005, *MNRAS*, 358, 1290 12, 56

REFERENCES

- Patel, N. A., Goldsmith, P. F., Heyer, M. H., Snell, R. L., & Pratap, P. 1998, *ApJ*, 507, 241–105
- Patel, N. A., Heyer, M. H., Goldsmith, P. F., Snell, R. L., Hezel, T., & Pratap, P. 1994, in *Astronomical Society of the Pacific Conference Series*, Vol. 65, *Clouds, Cores, and Low Mass Stars*, ed. D. P. Clemens & R. Barvainis, 81–105
- Pomarès, M., et al. 2009, *A&A*, 494, 987–164
- Pottasch, S. R. 1958, *Bulletin of the Astronomical Institutes of the Netherlands*, 14, 29–165
- Preibisch, T., & Feigelson, E. D. 2005, *ApJS*, 160, 390–175
- Rieke, G. H., et al. 2004, *ApJS*, 154, 25–46
- Roberts, M. S. 1957, *PASP*, 69, 59–11
- Robitaille, T. P., Whitney, B. A., Indebetouw, R., & Wood, K. 2007, *ApJS*, 169, 328–160, 175
- Robitaille, T. P., Whitney, B. A., Indebetouw, R., Wood, K., & Denzmore, P. 2006, *ApJS*, 167, 256–59, 106, 162
- Roger, R. S., & Dewdney, P. E. 1992, *ApJ*, 385, 536–17, 18
- Sagar, R., Miakutin, V. I., Piskunov, A. E., & Dluzhnevskaja, O. B. 1988, *MNRAS*, 234, 831–51
- Sagar, R., & Richtler, T. 1991, *A&A*, 250, 324–57
- Salpeter, E. E. 1955, *ApJ*, 121, 161–27, 83
- Schaller, G., Schaerer, D., Meynet, G., & Maeder, A. 1992, *A&AS*, 96, 269–124, 127
- 2005, *From Dust To Stars Studies of the Formation and Early Evolution of Stars*, ed. Schulz, N. S. xviii, 6, 7, 8

-
- Sharma, S., Pandey, A. K., Ojha, D. K., Chen, W. P., Ghosh, S. K., Bhatt, B. C., Maheswar, G., & Sagar, R. 2007, MNRAS, 380, 1141–124
- Shevchenko, V. S., Ezhkova, O. V., Ibrahimov, M. A., van den Ancker, M. E., & Tjin A Dje, H. R. E. 1999, MNRAS, 310, 210–105
- Sicilia-Aguilar, A., Hartmann, L. W., Briceño, C., Muzerolle, J., & Calvet, N. 2004, AJ, 128, 805–105, 127
- Sicilia-Aguilar, A., Hartmann, L. W., Hernández, J., Briceño, C., & Calvet, N. 2005, AJ, 130, 188–105, 127, 128, 135
- Siess, L., Dufour, E., & Forestini, M. 2000, A&A, 358, 593–62, 76, 77, 80, 81, 83, 84, 85, 91, 94, 106, 111, 142, 160, 161
- 2004, *The origin of stars*, ed. Smith, M. D. 9
- Smith, N., et al. 2010, MNRAS, 406, 952–166
- Spitzer, L., Jr. 1954, ApJ, 120, 1–165
- 2005, *The Formation of Stars*, ed. Stahler, S. W. & Palla, F. 11
- Stetson, P. B. 1987, PASP, 99, 191–37, 41, 68, 89, 101
- Stetson, P. B. 1989, *Highlights of Astronomy*, 8, 635–40
- Stetson, P. B. 1990, PASP, 102, 932–42
- Stetson, P. B. 1992, in *Astronomical Society of the Pacific Conference Series*, Vol. 25, *Astronomical Data Analysis Software and Systems I*, ed. D. M. Worrall, C. Biemesderfer, & J. Barnes, 297–68
- Strom, K. M., Strom, S. E., Edwards, S., Cabrit, S., & Skrutskie, M. F. 1989, AJ, 97, 1451–6
- Sugitani, K., Fukui, Y., Mizuni, A., & Ohashi, N. 1989, ApJ, 342, L87–172
- Sugitani, K., Fukui, Y., & Ogura, K. 1991, ApJS, 77, 59–23, 28, 66, 91, 96, 103, 104, 105, 106, 129, 132, 138, 149, 150, 156, 157, 164

- Sugitani, K., & Ogura, K. 1994, *ApJS*, 92, 163 23, 156, 157, 164
- Sugitani, K., Tamura, M., & Ogura, K. 1995, *ApJL*, 455, L39 24
- Sung, H., Chun, M., & Bessell, M. S. 2000, *AJ*, 120, 333 62
- Sysoev, N. E. 1997, *Astronomy Letters*, 23, 409 165
- Tapia, M., Costero, R., Echevarria, J., & Roth, M. 1991, *MNRAS*, 253, 649 54, 74
- Telleschi, A., Güdel, M., Briggs, K. R., Audard, M., & Palla, F. 2007, *A&A*, 468, 425 175
- The, P. S., & Groot, M. 1983, *A&A*, 125, 75 54
- Thompson, M. A., White, G. J., Morgan, L. K., Miao, J., Fridlund, C. V. M., & Hultgren-White, M. 2004, *A&A*, 414, 1017 124
- Turner, N. H., ten Brummelaar, T. A., Roberts, L. C., Mason, B. D., Hartkopf, W. I., & Gies, D. R. 2008, *AJ*, 136, 554 75
- Urquhart, J. S., Morgan, L. K., & Thompson, M. A. 2009, *A&A*, 497, 789 164, 165, 174
- Valdettaro, R., Palla, F., Brand, J., & Cesaroni, R. 2005, *A&A*, 443, 535 173
- Vallee, J. P., Hughes, V. A., & Viner, M. R. 1979, *A&A*, 80, 186 104
- Vanhala, H. A. T., & Cameron, A. G. W. 1998, *ApJ*, 508, 291 23
- Vishniac, E. T. 1983, *ApJ*, 274, 152 20, 165
- von Hoerner, S. 1960, *Z. Astrophys.*, 50, 184 51
- von Hoerner, S. 1963, *Z. Astrophys.*, 57, 47 51
- Walborn, N. R. 1973, *AJ*, 78, 1067 75
- Walter, F. M., Brown, A., Mathieu, R. D., Myers, P. C., & Vrba, F. J. 1988, *AJ*, 96, 297 26, 131, 132, 147

- Wegner, W. 1993, *Acta Astronomica*, 43, 209 54
- Whalen, D. J., & Norman, M. L. 2008, *ApJ*, 672, 287 165
- Whitney, B. A., Wood, K., Bjorkman, J. E., & Cohen, M. 2003a, *ApJ*, 598, 1079 60, 116
- Whitney, B. A., Wood, K., Bjorkman, J. E., & Cohen, M. 2003b, *ApJ*, 598, 1079 162
- Whitney, B. A., Wood, K., Bjorkman, J. E., & Wolff, M. J. 2003c, *ApJ*, 591, 1049 162
- Williams, J. P., Blitz, L., & McKee, C. F. 2000, *Protostars and Planets IV*, 97 2
- Williams, R. J. R. 2002, *MNRAS*, 331, 693 165
- Winkler, H. 1997, *MNRAS*, 292, 273 54
- Yang, J., & Fukui, Y. 1992, *ApJ*, 386, 618 103
- Zavagno, A., Pomarès, M., Deharveng, L., Hosokawa, T., Russeil, D., & Caplan, J. 2007, *A&A*, 472, 835 152